Adaptive Structural Health Monitoring Framework for Bridges using Vehicle-Carried Sensors

Adaptive Structural Health Monitoring Framework for Bridges using Vehicle-Carried Sensors

by

Soheil Sadeghi Eshkevari

Presented to the Graduate and Research Committee

of Lehigh University

in Candidacy for the Degree of

Doctor of Philosophy

in

Structural Engineering

Lehigh University

January 2021

Approved and recommended for acceptance as a dissertation in partial fulfillment of the requirements for the degree of Doctor of Philosophy.

Date

Dr. Shamim Pakzad
Dissertation Advisor

Committee Members:

Dr. Ethan Yang
Committee Chair

Dr. Martin Takáč
Committee Member

Dr. Shalinee Kishore
Committee Member

Dr. Richard Sause
Committee Member

"We can only see a short distance ahead,

but we can see plenty there that needs to be done."

- Alan Turing

Acknowledgements

I indeed would like to acknowledge people who were directly or indirectly influential in my professional career so far. First, I want to express my sincerest gratitude to my Ph.D. advisor, Professor Shamim Pakzad for giving me the chance to experience this wonderful journey. I really enjoyed to be a part of his team and work under his supervision and fruitful guidance. Most importantly, I appreciate the opportunity of working on a topic with such high impact on economy well-being and with worldwide application. After that, I have to thank Professor Martin Takac for not just being a supportive committee member, but being a great contributor, friend, and role model for my professional career. I cannot imagine finishing my Ph.D. degree with its current quality without his intellectual contributions. I also would like to kindly thank Professors Sause, Kishore, and Yang for their helpful feedback and guidance.

I would love to take this opportunity and express my gratitude to my lovely family. Setareh, my kinder and way better half, has been a strong and extremely patient companion in our way for professional success. Once again, I feel lucky to know you and share a life with you, dear Setareh. How can I really appreciate my parents' sacrifices, love, and efforts with words? I will try poorly to send my warmest appreciation to my lovely parents, Narges and Mojtaba for literally everything. I see my parents as superheros way ahead of their time and society and great examples for myself. Thank you for supporting our dreams and always believing in us. And last but not least, my little sister who is a perfect example of unconditional love and

support. I love you dear.

I also should thank to my friends in ATLSS with whom I spent probably more time than home and with my wife over the last four years. First I would like to thank to My colleagues in Dr. Pakzad's reseach group, Sila, Bhavana, and Rosalin for their helps and kindness. I would like to thank my officemates, in particular Alia, for bearing my grumpy attitude over these years. I really appreciate the support and friendship I received from my other colleagues, Mohannad, Vasilious, Liang, Qi, Bryan, Jeong-Joo, and all other ATLSS graduate students. I would also love to send my gratitude to my friends in Iran, mostly from *Allameh Helli* high school, who have major impact in who I am today: Amirsaman Babaei, Sadjad Falahatkar, Ashkan Forootan, Babak Jamali, Omid Hoseinzadeh, Mohammadreza Esalat, and Navid Siami, Also I would like to thank to my friends from University of Tehran and Sharif University of Technology: Mahdi Akbari, Mohammad Hossein Ohadi, Ehsan Bafandeh, Farzad Haghi, Mohammad Attary, Araz Shabestari, and many more.

My Ph.D. experience would be less significant if it was not the help of my great research collaborators. On top of the list is indeed Dr. Thomas Matarazzo. He has been an exemplary mentor and fellow over the last few years and we have had such fruitful collaborations. I would like to recognize his knowledge, patience, and selflessness. I also like to thank Liam Cronin for being a great researcher and collaborator and I am looking forward to our future works. And finally, I should appreciate the supports from Majid Jahani not only as a research collaborator, but also as a great friend. It would be my privilege to continue collaborating with you all.

Contents

List of Tables

List of Figures

Abstract

In order to sustain a smoothly-operating economy, reliable and healthy infrastructure is critical. Civil infrastructure including bridges, roads, buildings, and many more are designed for long time operation with minimal interruption. However, in developed countries, the strong majority of operating structures were built decades ago and have already passed their designated lifespan, while their operation rate has not been discounted but even boosted. This concerning trend is now a global economic challenge that requires drastic financial investments if supposed to be addressed traditionally. The financial burden of such solutions is extremely high so that it has encouraged scientists to distribute resources attentively between monitoring and repairing costs. Structural health monitoring is a collective term for any advanced engineering technique that is able to estimate the existing status of structures given sensory data. By advancements in sensor technology, dense sensor networks have been installed for detailed monitoring of structures. Despite its promising achievements, the method is yet expensive and cannot be upscaled to a large number of structures. Mobile sensing as an alternative paradigm strives to dramatically reduce the sensor setup costs while maintaining the data information as high and dense as possible. The idea of mobile sensing is promising and feasible, yet further developments are required to establish industry-friendly solutions. In this thesis, practical and scalable solutions based on realistic mobile sensing data are developed in order to shrink the gap between theory and applied scenarios.

Chapter 1

Introduction

1.1 Motivations

American Society of Civil Engineers (ASCE) has recently reported that nearly one out of every nine bridges in the US is structurally deficient [ASCE, 2017]. The report estimated that it would cost nearly $123 billion to fix the bridges if we take immediate actions. This cost is the minimum and probably unrealistic, considering the fact that a detailed map of bridges with their structural health conditions does not exist. this technological gap is critical because a healthy and operational infrastructure is a key requirement for a prolific and leading economy. Official agencies such as Departments of Transportation (DOTs) and Federal Emergency Management Agency (FEMA) have repeatedly reported that transportation infrastructure in the US suffer from aging and substantial deterioration. For instance, PennDOT published that the average age of bridges in the state system is over 50 years old. Citizens have great reliance on operating bridges, buildings, and highways to maintain their daily activities. When a large body of infrastructure is at risk of damage or loss of serviceability, this risk directly affects the public. In the COVID-19 pandemic era, we have realized the importance of having a sustainable and strong medical infrastruc-

ture. Civil infrastructure is of the same level of importance and require inspection, monitoring, and maintenance. In this dissertation, the goal is to develop practical and inexpensive solutions to monitor structural health of bridges which benefit from enabling technologies such as smartphones.

The state of practice for bridge health monitoring consists of periodic inspections by human agents who collect qualitative information using visual assessments and limited measurements. For bridges with higher traffic demands or importance, the inspection plan may include some sensors in fixed locations that collect structural vibrations over a limited time frame. These approaches are slow and manual, meaning that each bridge requires its own planning and implementations. They also could conflict with the regular operation of the bridge. Most importantly, the information is limited to the bridges under inspection and the date they were inspected, and also bounded to a few sensing locations. Utilization of mobile sensors for bridge health monitoring has potentials to address the majority of these challenges at once. Ultimately, in the mobile sensing paradigm, smartphones that are located within vehicles perform as the primary sensing devices. Smartphones are equipped with a complete set of motion sensors including accelerometers. The ubiquity of smartphone data that collect vibrations while crossing bridges creates a unique potential for comprehensive and large-scale bridge inspection frameworks.

1.2 Thesis Statement

The topic has been of great interest over recent years. In particular, indirect bridge health monitoring and damage detection is one of the most active research domains in the field of infrastructure health monitoring. The objective of mobile sensing research is to develop mathematical frameworks that enable processing of vibration data that are functions of time and space, as opposed to the traditional fixed sensing

in which the sensor data is merely a time function [Matarazzo and Pakzad, 2018, Sadeghi Eshkevari et al., 2020a]. The interaction of the vehicle and the bridge is also a difficult challenge when considering vehicles as sensor carriers. Over the past few decades, researchers have developed methodologies for processing data collected by individual vehicles that interact with simple and short-span bridges [Yang et al., 2004a,b, González et al., 2012, Marulanda et al., 2016, OBrien and Malekjafarian, 2016]. The methods have been a step towards a practical mobile sensing solution; nevertheless, the application has been limited to controlled vehicle-bridge interaction scenarios. In addition, the studies have been more focused on partial modal information (i.e., natural frequencies), rather than a complete bridge modal identification.

To reach further to a realistic and general solution, it is desired to develop methodologies that can incorporate data from a network of vehicle fleet and also enable comprehensive modal identification. The motivation is that when a large pool of vehicles are sensing simultaneously, the extracted information is a consensus of all individual sensors which is more reliable and informative compared to an individual moving agent. In this regard, Matarazzo and Pakzad [2016a] proposed truncated physical model for bridges and further, developed the STRIDEX algorithm that enables utilization of a group of mobile sensor carriers for comprehensive bridge modal identification [Matarazzo and Pakzad, 2018]. The method has been numerically and experimentally validated. Despite its generality and wider application, the method employs a simplified approach to convert mobile sensing data to virtual stationary measurements. In addition, the method was verified for vehicle networks with planned motions. This presumption complicates the application of the method since in practice, vehicles in a network maintain random motions. In this dissertation, developing alternative methods with more practicality has been one of the objectives.

The other challenge for a realistic and generalized framework is the fact that the data collected by smartphones within vehicles is not a pure version of structural vi-

brations, but a highly contaminated variant of it. In particular, vehicle contact point experiences the roughness of the road pavement and the vehicle suspension system responds to it. This vibration response is fully manifested in the signal collected by the smartphone. In literature, the main approach to circumvent this challenge has been setting some specifications for mobile sensing with vehicles. For instance, Yang et al. [2004b], OBrien et al. [2010] suggest that as the speed of the sensing vehicle increases, the rate of contamination intensifies. Alternatively, in some research it is recommended to utilize task-specific sensor carriers (i.e., carts or pulleys) to minimize the impact of the vehicle suspension. Still, looking forward to the ultimate idea of crowdsensing, in this dissertation a significant effort has been invested in proposing algorithms to decontaminate these sensor measurements with feasible solutions. Signal decontamination methods enable the exploitation of raw smartphone data which is a substantial step toward a human-based collaborative framework for bridge health monitoring.

1.3 Approaches

Considering the state of research in the field of mobile sensing, in this thesis, studies are divided in two categories. Each category has been studied from different perspective to maximally address the substantial remaining challenges for reaching to a practical crowd-based and collaborative bridge health monitoring paradigm.

1.3.1 Practical Mobile Sensing Methodologies

The objective is to develop frameworks for collaborative mobile sensing. Previous works have demonstrated the inspiring potentials of mobile data aggregation for bridge system identification. Yet, the reality of crowdsensing using smartphones differs from the building assumptions of these methods. In this phase, some algorithms

are designed that enable more realistic data collection schemes such as random vehicle fleet. Chapters 2, 4, and 5 are attributed to this phase of the research.

- In Chapter 2, an alternative viewpoint to the mobile sensing problem is presented. In summary, it is argued that individual mobile sensors sparsely observe a huge matrix of bridge vibration responses. Given this sparse representation, optimization solutions are proposed that enable comprehensive modal identification.

- Numerical analysis of bridges subjected to a random traffic load is computationally laborious and restricting, so that there are very few available studies considering networks of vehicles interacting with long bridges. In Chapter 4, a simplified algorithm for this numerical analysis is proposed and then validated with a theoretical proof as well as a multiple numerical trials.

- To the best of our knowledge, all available methods for mobile sensing using crowd data are based on synchronous data collection. In Chapter 5, an intuitive approach for asynchronous data acquisition is presented. In this method, by aggregation of vibrations collected by independent and unconnected vehicles, natural frequencies and absolute mode shapes of the bridge are reconstructed.

1.3.2 Bridge Vibration Retrieval from Noisy Vehicle Measurements

Data acquisition practices in structural health monitoring are susceptible to high noise. Likewise, the vibration signal collected by mobile phones contains unsought contents triggered by the vehicle suspension as well as the pavement roughness. In fact, there is a theoretical gap in this research community regarding this challenge and practical approaches to address it. In this dissertation, multiple recommendations

and methodologies are proposed to minimize the noise effect. Chapters 3, 6, and 7 are focused on this phase of research.

- In Chapter 3, a detailed investigation of vehicle-road-bridge interactions is presented and the sources of noise are characterized. In addition, two blind source separation techniques are proposed in order to mitigate the undesired vibration contents from raw data. In this research, the primary assumption is that the vehicle suspension responds linearly to the input.

- Linearity assumption is valid when vehicle motion is controlled and slow, or when customized sensing vehicles are utilized. In order to expand the extent of our ultimate solution, in Chapter 6 we investigate data-driven approaches to predict responses of nonlinear dynamic systems to a given input. A physics-based neural network architecture is proposed that is able to quickly learn the dynamics of the nonlinear system. The trained network is then useful for future response predictions.

- In Chapter 7, inspired by the neural network architecture proposed in Chapter 6, the inverse problem of dynamic systems is explored. By training a neural net that is able to predict a vehicle's input given its cabin measurements, the vehicle turns into a useful sensing device with no suspension-caused contamination. To validate this idea, an experimental study is conducted and results are presented in this chapter.

Chapter 2

Mobile Sensing with Sparse Vibration Data

2.1 Abstract

Dynamic sensor networks have the potential to significantly increase the speed and scale of infrastructure monitoring. Structural health monitoring (SHM) methods have been long developed under the premise of utilizing fixed sensor networks for data acquisition. Over the past decade, applications of mobile sensor networks have emerged for bridge health monitoring. Yet, when it comes to modal identification, there remain gaps in knowledge that have ultimately prevented implementations on large structural systems. This study presents a structural modal identification methodology based on sensors in a network of moving vehicles: a large-scale data collection mechanism that is already in place. Vehicular sensor networks scan the bridge's vibrations in space and time to build a sparse representation of the full response, i.e., an incomplete data matrix with a low rank. This research introduces modal identification using matrix completion (MIMC) methods to extract dynamic properties (frequencies, damping, and mode shapes) from data collected by a large number of mobile

sensors. A dense matrix is first constructed from sparse observations using alternating least-square (ALS), then decomposed for structural modal identification. This study shows that the completed data matrix is the product of a spatial matrix and a temporal matrix from which modal properties can be extracted via methods such as principal component analysis (PCA). Alternatively, an impulse-response structure can be embedded into the temporal matrix then, natural frequencies and damping ratios are determined using Newton's method with an inverse Hessian approximation. For the case of ambient vibrations, the natural excitation technique (NExT) is applied and then, structured optimization (Newton's method) is performed. Both approaches are evaluated numerically and results are compared in terms of data sparsity, modal property accuracy, and post-processing complexity. Results show that both techniques extract accurate modal properties, including high-resolution mode shapes, from sparse dynamic sensor network data; they are the first to provide a complete modal identification using data from a large-scale dynamic sensor network.

2.2 List of Symbols

x_k	state vector at time step k
A	state matrix
η_k	systematic noise at time step k (bridge random load)
y_k	observation vector at time step k
C	observation matrix
ν_k	sensing noise at time step k
Q	covariance matrix of the systematic noise
R	covariance matrix of the sensing noise
p	model order
N_α	number of virtual probing nodes
N_0	number of observation nodes
Ω_k	mode shape regression function at time step k
s_k^0	position vector of sensing nodes at time step k
s_i^α	location of the ith virtual probing location
Δs^α	uniform distance between virtual probing locations
y_k, y_k^{br}	pure bridge dynamic response at time step k
y_k^{act}	actual response recieved by the sensor at time step k
y_k^{if}	bridge response to the vehicle-bridge interaction force at time step k
y_k^{vbi}	actual bridge response including vehicle-bridge interaction at time step k
y_k^{act}	actual response recieved by the sensor at time step k
y_k^{rgh}	road profile roughness displacement under the tire at time step k
y_k^{eng}	engine-induced vibration at time step k
y_k^{obs}	observed vibration within the vehicle at time step k
y_k^{inp}	displacement input of the vehicle at the tire level at time step k
$Y(\omega)$	frequency representation of y_k
$H(\omega)$	vehicle transfer function
$\alpha(\omega)$	frequency response function
Φ	vehicle mode shapes
m_s	vehicle sprung mass
m_{us}	vehicle unsprung mass
c_s	vehicle sprung damping
c_{us}	vehicle unsprung damping
k_s	vehicle suspension stifness
k_{us}	vehicle tire stiffness

2.3 Introduction

Dynamic sensor networks are an element of modern society. Humans are increasingly relying on ubiquitous smartphones, internet-of-things devices, and data-driven services in their daily lives. This phenomenon has given life to massive amounts of data, which have driven an entire field of studies [Barabasi, 2005, Wang et al., 2010, 2012, Alexander et al., 2015, Tachet et al., 2017] on human activity in the urban environment and the development of smart city applications [Tachet et al., 2016, Anjomshoaa et al., 2018, Vazifeh et al., 2018]. Sensors carried by humans create an inexpensive, large-scale mobile sensor network and as smart and self-driving cars continue to emerge, vehicles will become a growing source for sensory data on the built environment [Gurney et al., 2015, Massaro et al., 2017]. Throughout hundreds of millions of trajectories each day, humans capture data on bridges and other infrastructure routinely and comprehensively.

This has sparked a massive interest in the use of mobile sensors for structural health monitoring (SHM), a field that has exclusively relied on datasets collected by networks of fixed sensors [Sony et al., 2019, Pakzad et al., 2008, Lynch and Loh, 2006, Kurata et al., 2011, Matarazzo and Pakzad, 2016a]. Mobile sensor networks have low setup costs and address major shortcomings of fixed sensor networks. Mobile sensor data contain a denser spatial resolution when compared to data collected by the same number of distributed fixed sensors. Overall, mobile sensor networks are scalable and produce significantly more spatial information per sensor. The development of SHM approaches that are able to incorporate crowdsensed mobile sensor data [Matarazzo and Pakzad, 2018, Matarazzo et al., 2018, Mei et al., 2019, Mei and Gül, 2018] accelerates the rate at which engineers acquire knowledge on the true conditions of infrastructure; the corresponding boom in information would prove invaluable to bridge monitoring and management [Kleywegt and Sinha, 1994, Smith, 2016]. Early work on mobile sensors in SHM demonstrated that a sensor within a moving vehicle

can be used to detect the fundamental frequency of a bridge [Yang et al., 2004a, Lin and Yang, 2005, Yang and Chang, 2009]. Subsequent studies built on the theory and application of vehicle-bridge interaction in order to estimate damping using various "drive-by" setups [González et al., 2012, Keenahan et al., 2014, McGetrick et al., 2015] or stiffness information [Li et al., 2014] whose variations may be indicative of structural damage. Very recent studies have theoretically and experimentally developed methodologies for damage detection using aggregation of passing-by vehicles on bridges [Mei et al., 2019, Mei and Gül, 2018].

Modern system identification (SID) algorithms for civil structures are reliable, repeatable, and often have a formidable mathematical foundation, e.g., frequency domain decomposition (FDD) [Brincker et al., 2001], eigensystem realization analysis (ERA) [Juang and Pappa, 1985, James et al., 1995], stochastic system identification (SSI) [Peeters and De Roeck, 2001], fast Bayesian FFT method [Au, 2011], distributed modal identification [Pakzad et al., 2011], Kalman filter-based SID [Chang and Pakzad, 2013a], and stochastic iterative SID [Dorvash and Pakzad, 2013]. As with SHM, classical SID methods were formulated under the premise of fixed sensor network data and are incompatible with mobile sensor data. Recently, there has been progress in the development of SID methods that are designed for mobile sensor data. Matarazzo and Pakzad [2016b] proposed an updated version of the structural modal identification using expectation maximization (STRIDE) algorithm to recognize incomplete datasets and mobile sensor network data. A method proposed by Marulanda et al. [2016] enabled the identification of spatially dense mode shapes using a hybrid sensor network: one mobile and one fixed. Matarazzo and Pakzad [2016a] derived three state-space models that expect data from dynamic sensor networks and recommended the truncated physical model based on its configurable model complexity and ability to distinguish between sensing nodes and model DOF. Matarazzo and Pakzad [2018] introduced a new version of the STRIDE algorithm called STRIDEX, which

is able to identify the parameters of the truncated physical state-space model and therefore produce comprehensive estimates of structural modal properties using data from a mobile sensor network. In an initial experimental application, STRIDEX produced an accurate mode shape with 248 points using data from two mobile sensors. Subsequent experimental applications demonstrated accurate identification of higher modes, complete with dense mode shapes, based exclusively on mobile sensor data [Matarazzo et al., 2018].

This study focuses on bridge SID based on random vehicular sensor networks, an especially widespread dynamic sensor network with increasing sensing capabilities. In everyday traffic, connected vehicles with embedded sensors scan the bridge's vibrations in space and time. The vehicular sensor network data is a sparse representation of the full response - more specifically, an incomplete data matrix with a low rank. The sparsity of the data matrix depends on attributes of the vehicular sensor network, such as the number of mobile sensors, position time-series, sampling rates, etc. This study presents modal identification using matrix completion (MIMC) methods for SID of bridges based on data collected by a large number of mobile sensors.

2.4 Background Theory and Scope

2.4.1 Mathematical Model for Dynamic Sensor Networks

Dynamic sensor network data are produced when some aspect of the sensor network varies during measurement. For instance, mobile sensor data are classified as dynamic because the positions of the sensors change throughout discrete-time sampling. Dynamic sensor networks were introduced in Matarazzo and Pakzad [2016a] along with state-space models that were designed to analyze the resulting datasets for structural dynamics applications; the stochastic truncated physical state-space model is the primary model for the case of ambient vibrations (for complete mathematical details

see Matarazzo and Pakzad [2016a] and Matarazzo and Pakzad [2018]). The model is given in Equation 2.1:

$$\begin{aligned} x_k &= Ax_{k-1} + \eta_k \\ y_k &= G_k C x_k + \nu_k \end{aligned} \tag{2.1}$$

where $x_1 \sim N(\hat{\mu}, \hat{V})$, $\eta_k \sim N(0, Q)$ and $\nu_k \sim N(0, R)$. $A \in \mathbb{R}^{pN_\alpha \times pN_\alpha}$ is the state matrix, $C \in \mathbb{R}^{N_0 \times pN_\alpha}$ is the observation matrix, $x_k \in \mathbb{R}^{pN_\alpha}$ and $y_k \in \mathbb{R}^{N_0}$ are the state and observation vectors, respectively. η_k and ν_k are the input excitation and measurement noises, which are both modeled as Gaussian white noise with covariance matrices Q and R, respectively. N_α is the number of virtual probing locations and N_0 is the size of the observation vectors and p is the model order. G_k is the mode shape regression (MSR) function (here, G_k is identical to Ω_k in Matarazzo and Pakzad [2016a]), which maps structural responses at the locations of the mobile sensors to responses at virtual probing locations (VPLs). In one definition, VPLs are the structural DOF of interest and are the points at which mode shapes are computed. In theory, the MSR function is a product of two matrices, which are based on the exact structural mode shapes. Matarazzo and Pakzad [2016a] showed that the MSR function could be approximated adequately using *sinc* basis functions with $\hat{G}_k$, as shown in Equation 2.2:

$$\hat{G}_k = \left[sinc(\frac{1}{\Delta s^\alpha}(s_k^O - s_1^\alpha)), sinc(\frac{1}{\Delta s^\alpha}(s_k^O - s_2^\alpha)), ..., sinc(\frac{1}{\Delta s^\alpha}(s_k^O - s_N^\alpha)) \right] \tag{2.2}$$

In this equation s_k^O is a vector of sensors' positions at time step k, s_i^α is the location of the ith VPL, and Δs^α is the uniform distance between the VPLs. In spatial signal reconstruction, the role of $sinc(x) = \frac{sin(x)}{x}$ is to map measurements from an observed

location to a different unobserved location based on an ideal low-pass filter [Gensun, 1996, Schanze, 1995, Moheimani et al., 2003].

In this mathematical framework, the STRIDEX method has been successful in both numerical and experimental applications where the VPLs were set to be uniformly spaced (as recommended by Matarazzo and Pakzad [2016a]). Yet, the applications to date have considered a relatively small number of mobile sensors (less than ten). In addition, signal reconstruction literature shows the errors associated with nonuniform sampling [Jerri, 1977, Maymon and Oppenheim, 2011]; yet, further research is needed to quantify how the spacing of the VPLs, or the mobile sensors, influences the accuracy of the *sinc* MSR approximations used in STRIDEX, which ultimately impact modal property estimates. When relying on vehicular sensor networks, it is prudent to consider the following: (i) a very large number of sensors collecting data simultaneously; (ii) a variable number of participating sensors during data collection; and (iii) vehicle-bridge interaction and pavement roughness effects. The approach described in this study addresses the first two considerations (Throughout the study, the dynamic effect of the vehicles are ignored and road surface is assumed to be smooth); topic (iii) is studied in Sadeghi Eshkevari et al. [2020b] and Eshkevari and Pakzad [2019a] and will be discussed in the following chapters. In addition, the effect of vehicle dynamics and roughness-caused vibrations has been broadly studied in recent years [Lin and Yang, 2005, Malekjafarian et al., 2015, Malekjafarian and OBrien, 2014a].

2.4.2 Dynamic Sensor Networks with Sparse Data

The structural responses recorded by a vehicular sensor network are both sparse and dynamic. At each instant, the vast majority of the bridge is not sampled in space (sparse) and the sensing configuration is time variant (dynamic). Consider a large response matrix with temporal and spatial dimensions. Since the data collected by a

moving sensor is a function of both time and space, the entries build in two directions simultaneously, i.e., not just in single a row or a column. In case of a constant speed, the mobile sensor data is a diagonal band within the response matrix.

Figure 2.1 shows an illustration of a generic sparse data matrix produced by a large vehicular sensor network. The response matrix is three-dimensional with two spatial dimensions on the bridge (longitudinal and transverse directions) and one temporal dimension (time). A 2D slice of this matrix removes the dimension along the cross section (transverse) of the bridge and shows the data collected for a given traffic lane. There are two key observations: (i) this data matrix is mostly empty; and (ii) while there are some visible patterns among the available entries in the data matrix, ultimately there is an unknown stochastic structure that governs. The methods presented in this study are evaluated based on this 2D slice of the full 3D response matrix, both of which are sparse tensors.

The general approach is to "complete" the unobserved parts of this matrix given the sparse entries, i.e., the matrix completion problem. For example, in Eshkevari and Pakzad [2020a], the alternating least-squares (ALS) method [Jain et al., 2013, Zachariah et al., 2012] was implemented to complete a sparse structural response matrix, which resulted in responses at all considered DOFs. Using ALS, the sparse matrix is estimated as the product of two matrices with rank K, which is much smaller than the dimensions of the original matrix. Further details of this method are discussed later in this study.

2.4.3 Contributions

This study presents a set of Modal Identification using Matrix Completion (MIMC) methods which enables a comprehensive bridge SID based solely on data collected by a large-scale vehicular sensor network. As mentioned previously, vehicular sensor network data are unique for SHM because they are both sparse and dynamic. Two

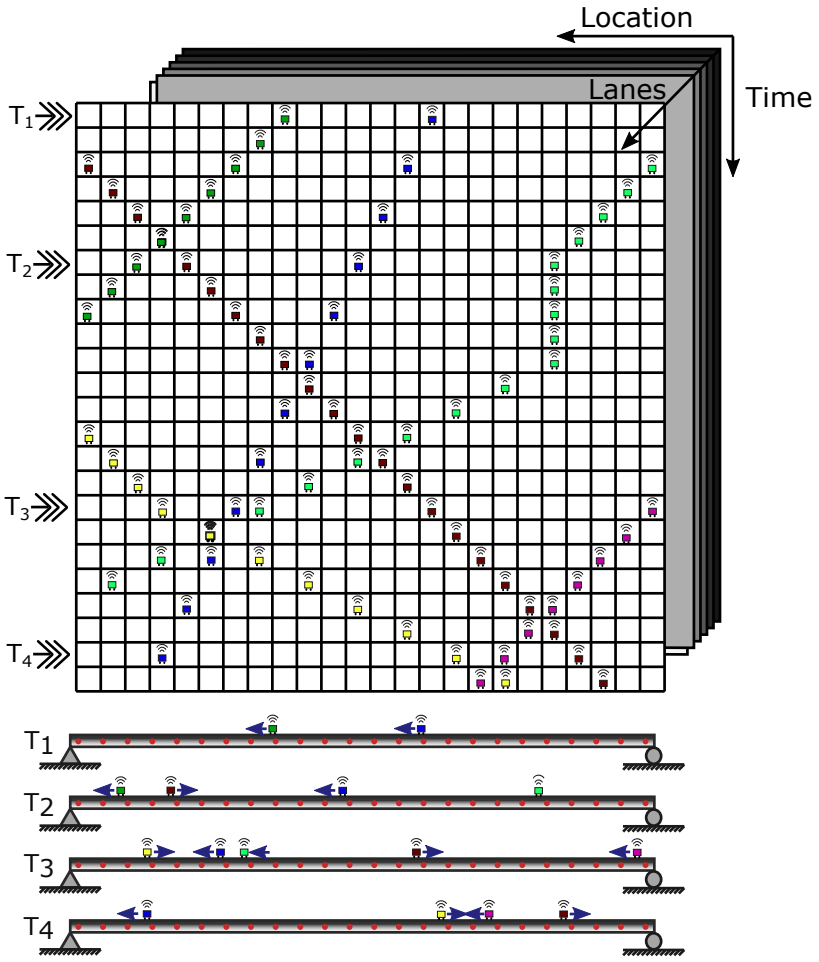

Figure 2.1: Illustration of a sparse matrix produced by a large vehicular sensor network. The full bridge response is represented by a 3D data matrix: two spatial dimensions and one temporal dimension. A 2D matrix shows the response along the bridge length for a given traffic lane. The methods in this study consider the problem of completing such a sparse 2D data matrix and extracting bridge modal properties. The instantaneous vehicle configurations corresponding to time samples T_1, T_2, T_3, and T_4 are depicted.

approaches, principal component analysis (PCA) and structured matrix optimization (SOA) are proposed to transform a completed response matrix into structural modal properties. The MIMC methods have the following novelties:

1. The MIMC methods are the first SID algorithms designed to process data collected by a large network of mobile sensors and are immediately applicable to vehicular sensor networks.

2. MIMC methods are able to process unstructured mobile sensor data, which include records from vehicles that have random and independent trajectories, e.g., different speeds, sampling rates, etc.

3. MIMC methods are able to estimate very high-resolution mode shapes after one computational run (no iterations are necessary).

4. Within the MIMC methods, a new optimization technique for the structured matrix completion problem that uses an approximate Newton's method is proposed and validated.

5. MIMC methods adapt to the availability of the observed data. The procedure is successful in identifying structural modes even when the original data matrix is very sparse, e.g., 0.5% completeness.

In the next section, the matrix completion problem is presented with respect to incomplete structural response data. Then in Section 2.6 three MIMC methods are proposed and described in detail. In Section 2.7 three mobile sensing simulations based on finite element models are presented to evaluate the performance of the MIMC methods. In Section 2.8, the simulation results are discussed. Section 2.9 provides the conclusions.

2.5 Completion of a Sparse Structural Response Matrix

In this matrix completion problem, the full structure response matrix Y is represented as the product of two matrices A and B (see Equation 2.3). Within alternating least squares (ALS), the problem reduces to determining the optimal values of decomposition matrices A and B [Jain et al., 2013, Zachariah et al., 2012]. Note that Y is

the true complete response matrix which is not available; only a subset of it is observed (Y_{obs}) during data collection. As a result, the mathematical expression of the objective function is described in Equation 2.5

$$Y = AB \tag{2.3}$$

$$Y_{obs} = \Phi(Y) \tag{2.4}$$

$$\min_{A,B} \frac{1}{2}||Y_{obs} - \Phi(AB)||^2 + \frac{\lambda}{2}(||A||^2 + ||B||^2) \tag{2.5}$$

where Y_{obs} is a sparse matrix, which is a subset of the original time-space matrix Y. The matrix Φ is a mapping function that selects observed entries from the full matrix Y. In the ALS method, the objective function shown in Equation 2.5 is minimized using alternating gradient descent steps on matrices A and B (the goal is to find matrices A and B that minimize the objective function). Conventionally, a regularization term is added to the objective function to prohibit overfitting.

So far, the algorithm provides a solution to complete the response matrix using sparse observations. Next step is to process this matrix in order to extract modal properties of the bridge. The first approach could be to apply ERA [Juang and Pappa, 1985] for modal identification. Despite its broad application, ERA is computationally impractical when the number of output channels is large [Kramer and Gugercin, 2016, Krishnan et al., 2011, Kramer and Gorodetsky, 2018]. In addition, no distributed implementation of ERA-based algorithms are known to the authors. To address this concern, and since the focus of this study is not on the system identification methods, alternative approaches have to be proposed that are computationally affordable and

can adequately demonstrate the efficiency and accuracy of this approach.

ALS requires that the original matrix (here Y) has a low-rank. From structural dynamics, it is known that in a multi degrees of freedom (MDOF) system, the response at each location can be represented in modal coordinates as shown in Equation 2.6. In this equation, Ω is a matrix of stacked mode shapes and Q is a matrix of stacked single-degree-of-freedom (SDOF) responses of modal coordinates.

$$Y = \Omega Q \approx \tilde{\Omega}\tilde{Q} \tag{2.6}$$

The dimensionality of this equation can be reduced through modal truncation. For many structures, the dynamic responses can be estimated accurately using only the most significant modes, e.g., the first K modes. The truncated matrices of the mode shapes and modal coordinates are presented as $\tilde{\Omega}$ and $\tilde{Q}$ with the ranks equal to K (model order). From Equations 2.3 and 2.6, $AB \approx \tilde{\Omega}\tilde{Q}$. This suggests that matrices A and B are the transformed versions of the matrix of mode shapes ($\tilde{\Omega}$) and modal coordinates ($\tilde{Q}$), respectively.

From modal analysis, it is known that the modal coordinates are orthogonal with respect to the mass and stiffness matrices, while there is no orthogonality condition when matrices A and B are optimized using ALS (unconditional optimization). The normalized mass matrix of a large and homogeneous bridge converges to an identity matrix. This fact simplifies the mass orthogonality condition to a simple orthogonality condition. Therefore, to mass-orthogonalize components of matrices A and B, a simple approach is to transform them using principal component analysis (PCA). PCA extract orthogonal principal components from a set of data (note that it is nearly equivalent to apply PCA over the reconstructed matrix with significantly more computational cost). It is expected that after orthogonalization of A and B, these new

matrices are better estimations of the actual modal components. However, it is known that the mass and stiffness orthogonality between two modes does not guarantee that these modes are natural mode shapes. For instance, Ritz modes [Wilson et al., 1982] are orthogonal but not natural (Ritz modes may contain an exclusive set of natural modes). To address this problem, an alternative approach is proposed to estimate modal components from matrices A and B in which the structure of matrix B is prefixed.

2.5.1 Impulse Response Analysis using Structured Optimization

The impulse response of each mode in a MDOF system has a certain structure. In fact, in this response, $\tilde{Q}$ contains the free vibration responses of the modal coordinates as presented in Equation 2.7 for undamped and Equation 2.8 for damped problems

$$
\begin{aligned}
Y(x,t) &= \sum_{n=1}^{K} \Omega_n(x) \sin(\omega_n t + \psi_n) \qquad (2.7)\\
&= \Omega_1(x) \sin(\omega_1 t + \psi_1) + \cdots + \Omega_K(x) \sin(\omega_K t + \psi_K)\\
&= \begin{bmatrix} \Omega_1(x) & \Omega_2(x) & \cdots & \Omega_K(x) \end{bmatrix} \begin{bmatrix} sin(\omega_1 t + \psi_1) \\ sin(\omega_2 t + \psi_2) \\ \vdots \\ \sin(\omega_K t + \psi_K) \end{bmatrix}\\
&= \tilde{\Omega}\tilde{Q}
\end{aligned}
$$

$$
\begin{aligned}
Y(x,t) &= \sum_{n=1}^{K} \Omega_n(x) e^{-\xi_n \omega_n t} \sin(\omega_n t + \psi_n) \\
&= \begin{bmatrix} \Omega_1(x) & \Omega_2(x) & \cdots & \Omega_K(x) \end{bmatrix} \begin{bmatrix} e^{-\xi_1\omega_1 t} sin(\omega_1 t + \psi_1) \\ e^{-\xi_2\omega_2 t} sin(\omega_2 t + \psi_2) \\ \vdots \\ e^{-\xi_K\omega_K t} \sin(\omega_K t + \psi_K) \end{bmatrix} \\
&= \tilde{\Omega}\tilde{Q}
\end{aligned}
\tag{2.8}
$$

where $\Omega_i(x)$ is the ith mode shape magnitude at location x and ξ_i, ω_i, and ϕ_i are modal damping, frequency, and phase angle for mode i. This reiterates the fact that the dense time and space response matrix Y can be decomposed into two sub-matrices that include modal information. The rows of the matrix $\tilde{Q}$ are decaying harmonics.

In this study, as an alternative for the PCA method for extracting modal components from ALS step results, the following optimization problem is considered. Say matrix Y is estimated from Y_{obs} using the ALS method; the new objective function is expressed as Equation 2.9, in which optimization variables are shown in Equation 2.10.

$$
\min_{\hat{\Omega},\hat{Q}} \frac{1}{2} ||Y - \hat{\Omega}\hat{Q}||^2 \tag{2.9}
$$

$$\hat{Q} = \begin{bmatrix} e^{-\omega_{11}\omega_{12}t} sin(\omega_{12}t + \omega_{13}) \\ e^{-\omega_{21}\omega_{22}t} sin(\omega_{22}t + \omega_{23}) \\ \vdots \\ e^{-\omega_{K1}\omega_{K2}t} sin(\omega_{K2}t + \omega_{K3}) \end{bmatrix}_{K \times N}$$

$$\hat{\Omega} = \begin{bmatrix} \vdots & \vdots & & \vdots \\ V_1 & V_2 & \cdots & V_K \\ \vdots & \vdots & & \vdots \end{bmatrix}_{M \times K} \tag{2.10}$$

Matrix $\hat{\Omega}$ is unknown in all components, while $\hat{Q}$ has only three unknowns per row (ω_{i1}, ω_{i2}, ω_{i3}). This optimization problem aims to find the best parameters for ω_{ij} and V_k in order to minimize the objective function. A visualization of this decomposition is given in Figure 2.2.

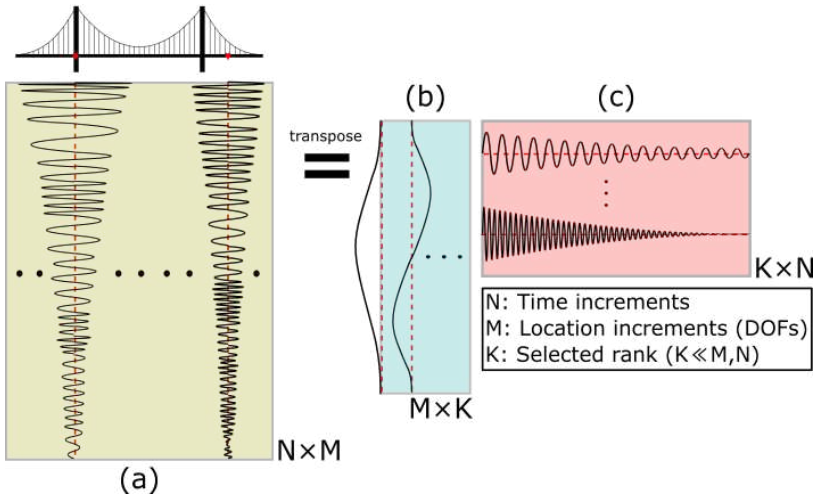

Figure 2.2: The concept of matrix decomposition from free vibration response: In this case, a bridge is subjected to impulsive loading and its vibration responses at all DOFs are stacked and form matrix (a). This response matrix can be accurately approximated as a multiplication of two matrices (b) and (c), both with rank K (model order). The vertical matrix contains natural mode shapes, while the horizontal matrix includes natural modal fluctuations.

By imposing the structure, it is guaranteed that if the optimal parameters can

be found, they will provide modal property estimates, i.e., frequency, damping, and mode shapes. The ALS method, like other common linear optimization methods for matrix completion [Cai et al., 2010, Candès and Recht, 2009], is inapplicable to such a highly-constrained optimization problem. Therefore, in this study, Newton's optimization method is incorporated for estimating parameters. The main challenge in applying Newton's method to high dimensional data is the numerical calculation of Hessian inverse [Zhu et al., 1997]. An approximate approach is utilized here to do this task more efficiently.

2.5.2 Ambient Response Analysis using NExT

The structured optimization technique is suitable only when the impulse responses of an MDOF system are available. In order to generalize this method for random structural vibrations, the natural excitation technique (NExT) [James et al., 1995] is embedded into the proposed method. In short, this technique converts the response of a structure under ambient loading into impulse responses in cross-correlational coordinates. The equation of motion for a damped system under ambient loading is shown in Equation 2.11:

$$M\ddot{y}(t) + C\dot{y}(t) + Ky = F(t) \tag{2.11}$$

where M, C, and K are mass, damping, and stiffness matrices of the system, respectively. $y(t)$ is the response vector at time t and $F(t)$ is a random loading vector. In case of a random ambient load (e.g., white noise), the cross-correlation function of the response vector with an arbitrary reference response channel results in a free vibration equation of motion, as in Equation 2.12

$$M\ddot{R}_{\ddot{y}_i\ddot{y}_{ref}}(t) + C\dot{R}_{\ddot{y}_i\ddot{y}_{ref}}(t) + KR_{\ddot{y}_i\ddot{y}_{ref}}(t) = 0 \tag{2.12}$$

where $R_{\ddot{y}_i\ddot{y}_{ref}}(t)$ is the cross-correlation between the response signal y_i at DOF i and a reference response signal $\ddot{y}_{ref}$ (could be any chosen DOF, with minimal constrains). Note that this technique was developed to use with measurements from a fixed sensor network. Yet, in this case, after matrix completion, the columns of the response matrix Y, i.e., time histories at the DOFs, are available. Therefore, it is possible to apply NExT on the columns of Y to produce a response matrix with the necessary structure, i.e., free vibration of a damped SDOF system. A demonstration of how to incorporate NExT with structured optimization analysis (SOA) is given in Figure 2.3.

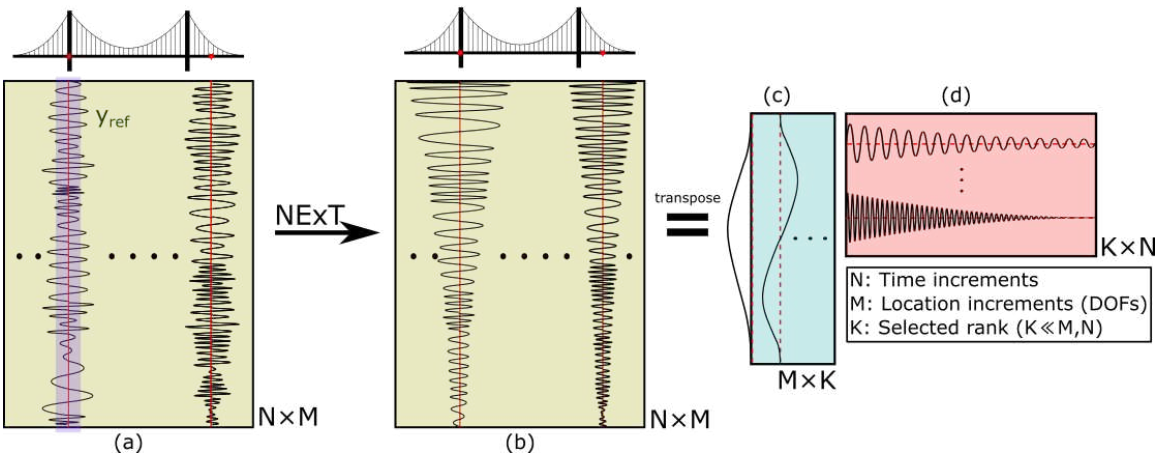

Figure 2.3: The concept of matrix decomposition from ambient loading response: in this case, a bridge is subjected to ambient loading and its vibration response is shown as matrix (a). The vibration responses at each DOF is not decaying, therefore, these random responses are mapped into decaying signals, matrix (b), using NExT. Once this matrix is formed, the rest of the process is identical to the free vibration case (Figure 2.2).

2.6 Modal Identification using Matrix Completion (MIMC) Methods

In this section, the proposed procedure (MIMC) is explained in its three possible forms: 1) Matrix completion with PCA; 2) Matrix completion with structured optimization analysis; and 3) Matrix completion with structured optimization analysis integrated with NExT method. In all three methods, the preliminary step is to complete the bridge response matrix using the ALS method. The first two methods are designated for bridges subjected to impulsive loads (free vibration response), while the third method is generalized for structures responding to ambient white noise excitations.

2.6.1 Method 1: Matrix Completion with PCA

This method includes two main steps; i) use ALS to complete the response matrix based on the observed mobile sensor data, and ii) apply PCA to the decomposition matrices to produce orthogonal modes. In order to complete the highly sparse response matrix, the objective function shown in Equation 2.5 should be minimized by tuning variable matrices A and B. This task can be done by taking gradient steps towards optimality as expressed in Algorithm 1 [Jain et al., 2013].

Algorithm 1 Alternating minimization for matrix completion.

1: **Input**: $Y_{obs}, \Phi(.), T$
2: Initialize $A^1_{M,K}, B^1_{K,N}$ to be random matrices
3: **for** t = 1, $\cdots$, T **do**
4: $\quad A^{t+1} = argmin_A(||Y_{obs} - \Phi(A^t B^t)||_2^2)$ ▷ Gradient Descent
5: $\quad B^{t+1} = argmin_B(||Y_{obs} - \Phi(A^{t+1} B^t)||_2^2)$ ▷ Gradient Descent
6: **Return** A^T, B^T

In this algorithm, $Y_{obs}^{M \times N}$ is a sparse matrix with an assumed model order K, $\Phi(.)$ is a binary location matrix with ones at observed coordinates and zeros elsewhere, and T is the desired number of iterations. Within the $argmin(.)$ function, the variable

matrices are updated using a magnitude proportional to their gradients and with a certain step size. For brevity, these common steps are summarized into the $argmin(.)$ function.

After this step, the PCA algorithm is applied on K columns (or rows) of matrix A (or B) to decouple its components into estimations of modal coordinates. A similar task was done by Poncelet et al. [2007] using PCA, independent component analysis (ICA), and second-order blind identification (SOBI). These tools are all able to extract uncoupled sources from mixed data by assuming different characteristics for separated sources (e.g., orthogonality, statistical independence, and uncorrelatedness for the three mentioned methods). In this study, the simplest method (PCA) is incorporated for the separation task. In PCA, a matrix is decomposed into its singular vectors and values and then, based on a desired level of accuracy, multiple singular terms with the most participation are used to repopulate an estimation of the original matrix. We say that the estimated matrix $Y = A^T \times B^T$ has a rank equal to the model order K. Therefore, by applying PCA, K orthogonal modes are expected that are estimations of the natural mode shapes.

2.6.2 Method 2: Matrix Completion with Structured Optimization Analysis

The second MIMC method can be viewed as a variation of Method 1. In the second step of Method 1, PCA may not produce the expected results, i.e., natural modal coordinates. There are multiple modal coordinates among which, each pair satisfies the orthogonality condition; however, they are not necessarily true structural modes. In fact, PCA performs ideally on regular and symmetric structures with a uniform mass distribution. In these cases, the mass matrix is approximated as a scaled identity matrix and mass orthogonality condition is simplified to the regular orthogonality condition which is guaranteed in PCA. To force this step of the algorithm to produce

the natural modes, structured optimization analysis (SOA) is proposed, as shown in Equation 2.10.

To estimate parameters of the structured decomposition matrices ($\hat{Q}$ and $\hat{\Omega}$ in Equation 2.10), an approximate Newton's optimization method is adopted from Eisen et al. [2017]. In principle, Newton's optimization method takes the step shown in Equation 2.13 towards the optimal point, using second order information from the Hessian:

$$\omega_{n+1} = \omega_n - \lambda H[f(\omega_n)]^{-1} \nabla f(\omega_n) \tag{2.13}$$

where $H(.)$ is the Hessian of a function $f(\omega)$, λ is a step size that ensures the step satisfies Wolfe conditions [Wright and Nocedal, 1999] (a requirement for line search algorithms). The inverse calculation for the Hessian is a computationally expensive task for high-dimensional data. In this problem, the dimension includes all entries of matrix $\hat{Q}$ and three parameters for each columns of matrix $\hat{\Omega}$, in total $(M+3) \times K$. Despite its lower dimension with respect to the matrix completion problem using ALS, the problem is still high dimensional and the inverse Hessian calculation is a bottleneck. To circumvent this issue, k-truncated adoptive Newton's method (k-TAN) is implemented as shown in Algorithms 2 and 3:

In this algorithm, *eps* is a threshold for eigenvalue truncation, *threshold* is the acceptable accuracy indicator, and $f(.)$ is a function that converts ξ, ω and ϕ into decaying oscillations and stack them to form matrix A. The $LineSearch(.)$ function is adopted from Wright and Nocedal [1999] to calculate valid step sizes a_{new} and produce $H(loss)^{-1}\nabla loss$ for each time step. Note that $\Phi(.)$ is the binary matrix that activates available entries of Y_{obs} in AB. However, since this step (Newton's optimizer) is implemented following ALS, after all entries of Y_{obs} have been estimated, $\Phi(.)$ is

Algorithm 2 Newton Algorithm using Approximated Hessian Inverse.

Input: $Y_{obs}, \Phi(.), eps, threshold$
$d = 1, w_1 = random$;
procedure LOSSFUNCTION(W)
    $\xi, \omega, \phi, B := w$ ▷ w is flattened vector of variables
    $A = f(\xi, \omega, \phi)$
    return $loss(w) := |\Phi(AB) - Y_{obs}|$
while $d > threshold$ **do**
    $a_{new}, P_k = LineSearch(eps)$ ▷ Based on strong Wolfe conditions
    $w_2 = w_1 + a_{new} P_k$
    $d = \mid loss(w_2) - loss(w_1) \mid$
    $w_1 = w_2$
Return w_1

Algorithm 3 Hessian Inverse Approximation using Truncated Absolute Eigenvalues.

procedure INVERSEHESSIAN
    Input: H, eps
    $U^T V U := H$ ▷ Eigenvalue decomposition of Hessian
    $\lambda_i = diag(V)$
    If $|\lambda_i| > eps$: ▷ Eigenvalue truncation
        $\gamma_i := 1/|\lambda_i|$
    Else:
        $\gamma_i := 0$
    $V_{new} := diag(\gamma_i)$
    $H_{inv} := U^T V_{new} U$ ▷ Inverse Hessian approximation
    Return H_{inv}

equal to a matrix of all ones. Most importantly, $H(.)^{-1}$ is calculated according to Algorithm 3. This algorithm uses truncated absolute values of the Hessian eigenvalues to approximate its inverse. The proposed method using ALS and SOA is illustrated visually in Figures 2.4 and 2.5.

SOA is a nonconvex optimization problem and is sensitive to the initial values of the variables. Accordingly, an appropriate initialization of the frequencies is possible by detecting peaks in the PSD estimate of a random scan. This "warm start" of the frequency variables proved to be sufficient for the algorithm to find the optimal parameters.

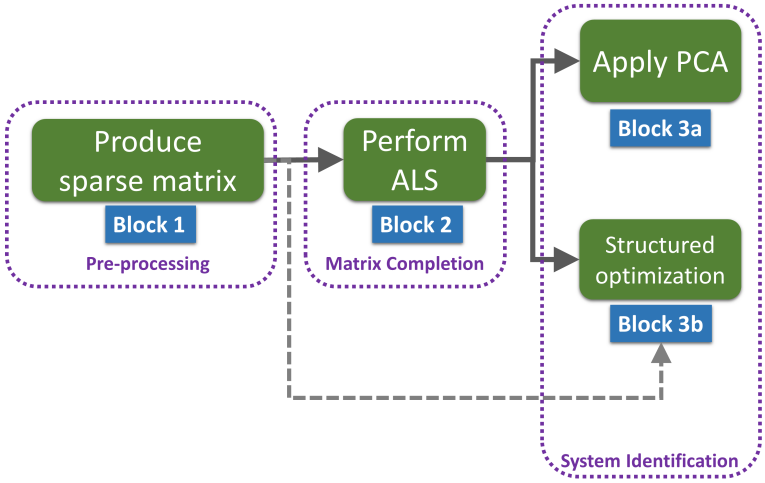

Figure 2.4: Process of the methods for free vibration-based identification. the method consists of three main phases: Block 1: pre-processing, Block 2: matrix completion, and Block 3: system identification. The third phases can be performed using PCA (Block 3a) or structured optimization (Block 3b).

Method 2b: Structured Optimization Only

Method 2 can proceed without the matrix completion step in advance. In Algorithm 2, the objective function still includes $\Phi(.)$ which is an element-wise multiplication of a binary matrix. In Method 2, the binary matrix $\Phi(.)$ is all ones, since the unobserved entries of the response matrix are estimated. Alternatively, instead of minimizing the objective function calculated over the entire matrix, Y_{obs} (sparse matrix) can be fed into the algorithm along with its corresponding binary matrix $\Phi(.)$ to tailor this algorithm for an SOA-only method. In other words, SOA has this possibility to be applied directly on the original sparse matrix of the observations, in contrast to PCA in which a preliminary matrix completion step is necessary. This approach is successful in SID when impulse responses are considered; however, for a generalized, random structural response, it is beneficial to integrate NExT into the process. For that case, ALS as a preliminary step is required.

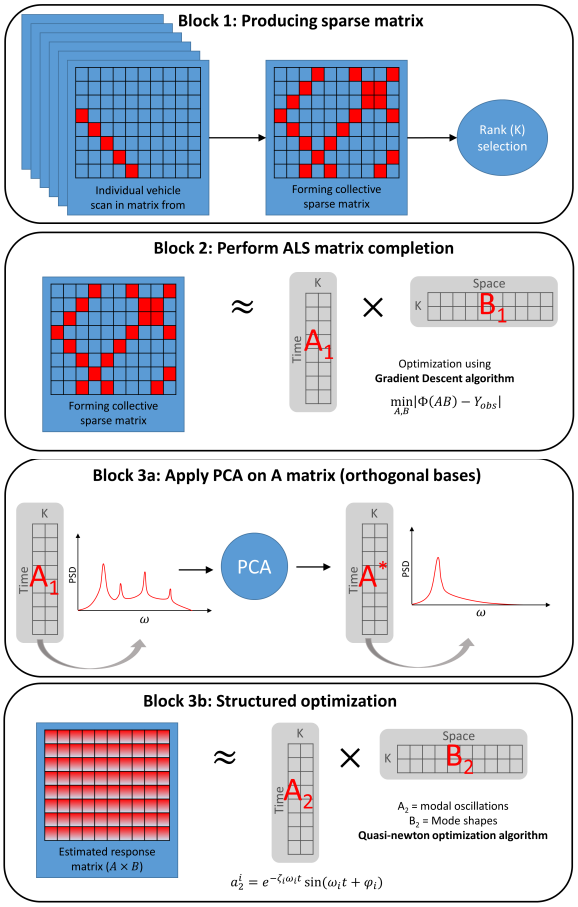

Figure 2.5: Components of the free vibration-based methods. Block 1: superposing dynamic mobile scans into a global response matrix. Block 2: Applying ALS to complete matrix from the sparse matrix. Block 3a: Applying PCA to extract uncoupled components from matrices A and B. Block 3b: Applying structured optimization to fit free vibration signal parameters for each mode from the completed matrix.

2.6.3 Method 3: Matrix Completion with Structured Optimization Analysis Integrated with NExT

The third method combines Method 2 with the natural excitation technique (NExT) in order to process response data from a randomly excited structure, which is the most commonly considered scenario in SID. Figure 2.6 shows that in this approach, after completing the partially observed response matrix Y_{obs}, one DOF is selected as the reference signal (y_{ref} in Figure 2.3) and a new matrix of cross-correlated signals with respect to the reference signal is produced. Then, this matrix is estimated using the SOA technique to produce modal property estimates.

The critical hyper-parameter here is the index of the reference signal (DOF). According to literature on NExT, the best selection for $\ddot{y}_{ref}$ is a location whose response is influenced by the structural modes of interest (i.e., it is not at or near a modal node for modes of interest). This method needs the matrix completion step to be performed before SOA, since the completed matrix after Block 2 (Figure 2.6) does not have the presumed decaying structure in its columns. A better illustration of this proposed method is given in Figure 2.7.

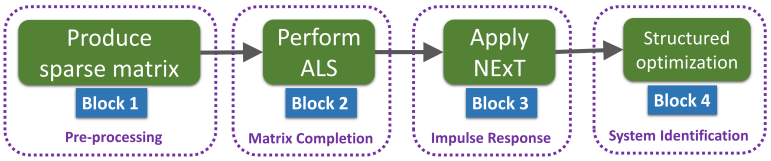

Figure 2.6: Process of the method for ambient vibration-based identification. The identification phase can be performed by structured optimization after applying NExT to the completed matrix.

To evaluate the proposed methods, in the next section they are validated in multiple simulated numerical case studies.

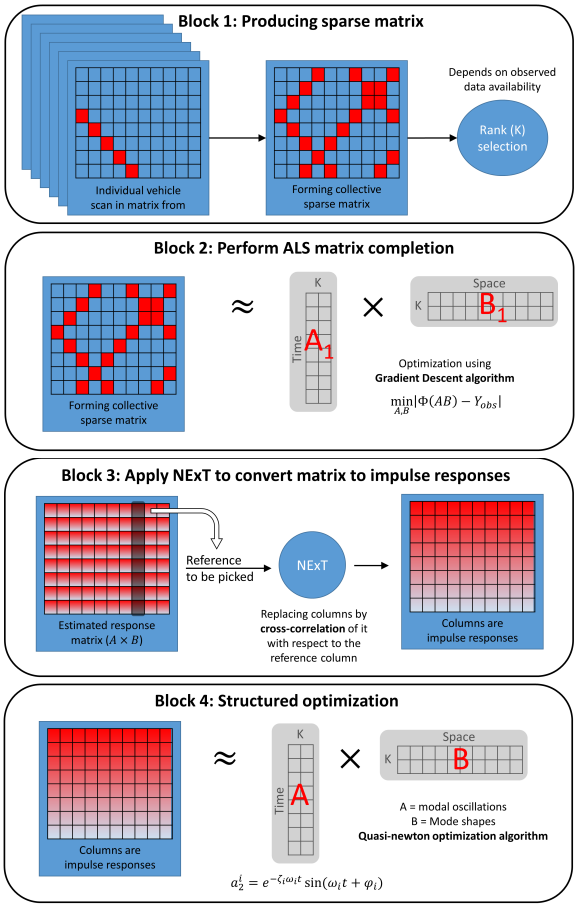

Figure 2.7: Components of the ambient vibration-based method. Block 1: superposing dynamic mobile scans into a global response matrix. Block 2: Applying ALS to complete matrix from the sparse matrix. Block 3: Applying NExT to convert non-decaying signals to decaying signals. Block 4: Applying structured optimization for modal properties extraction.

2.7 Simulation and Results

In this section, three simulations of the MIMC methods are presented to demonstrate their performances for SID: 1) undamped structure subjected to an impulsive load, 2) damped structure subjected to an impulsive load, and 3) damped structure subjected to a random ambient load. The goal of the simulations is to accurately identify the first four modes of a bridge using mobile sensors scanning data. In the first two simulations, Method 1 (ALS+PCA) and Method 2 (ALS+SOA) are implemented and their performances are compared for three different levels of data availability, which are directly related to the total number of vehicles that contribute to the mobile sensor dataset: 75 scans, 100 scans, and 125 scans (cases A, B, and C, respectively). The completeness of the corresponding data matrices in these cases are 0.75%, 1.00%, and 1.25%, respectively. These cases are presented first as a reference to better understand the methods in order to present comprehensively in the third simulation case. Moreover, in bridges with potholes or construction/expansion joints, impulsive loads are a proper way of modeling large trucks and buses passing through these irregularities. In Simulation III, ambient vibrations are considered along with four data completion levels (0.50%,0.75%, 1.00%, and 1.25%) for which Method 3 is implemented.

2.7.1 Finite Element Model and Mobile Sensing Setup

The simulations are based on a 500-meter single-span bridge, whose linear responses are modeled using OpenSees. The responses at $5,000$ equally-spaced DOFs of the bridge are considered, which are sampled at 50 Hz and have a duration of 100 seconds. Forces are applied at nine evenly-spaced nodes along the bridge with random magnitudes. The response data at all DOFs form a $5,000 \times 5,000$ dense response matrix from which a sparse response matrix Y_{obs} can be subsampled based on the paths of the simulated mobile sensors. Rayleigh damping is assigned by setting damping

ratios equal to 2% for modes one and eight. A modal analysis of the structure shows the natural frequencies of the first four modes: 0.2655 Hz, 0.7322 Hz, 1.4356 Hz, and 2.3731 Hz. Since the bridge is modeled in 2D, all modes are vertical. After data generation in OpenSees, the matrix database is exported to Python for further analyses.

The mobile scanning data are generated by selecting appropriate entries from the dense response matrix – a process that is illustrated in Block 1 of Figure 2.5. To simulate the random nature of vehicles scanning the bridge, the starting times and locations of each vehicle are selected randomly. This process is repeated n times to mimic a sensing scenario including n vehicular sensors, which scan the bridge's response within a 100-second period. Note the lengths of the individual datasets (diagonals) vary among the vehicles, since their trajectories begin at a random point in the data matrix. In other words, the mobile sensors collect data independently. Finally, for simplicity, the speeds of all the sensors are set to 5.0 m/s to allow just enough time (100 seconds) for a vehicle starting at one end to complete one full-length bridge scan, meaning that most scans only cover a portion of the bridge.

2.7.2 Simulation I: Undamped Bridge Subjected to Impulsive Load

The first step in all the proposed methods is to complete the matrix using the ALS method, for which Algorithm 1 is implemented in Python using TensorFlow framework and performed on the sparse matrix. For applying the algorithm, a value for K (desired model order of the decomposition matrices) must be selected. In all three cases, a K value between four and six yields the best performance - further details about this selection are discussed later. Figure 2.8 shows the ALS results for cases A, B, and C: top plots display the components of the A matrix and bottom plots show the power spectral density (PSD) estimates of the components of the B matrix. The

components of the matrix A are similar to the expected mode shapes of the bridge; however they are not exactly the natural modes. The peaks of the PSD estimates of the components of the B matrix correspond to the modal frequencies. Note that these components are coupled, i.e., each component contains multiple peaks. PCA is used to make these components orthogonal to one another.

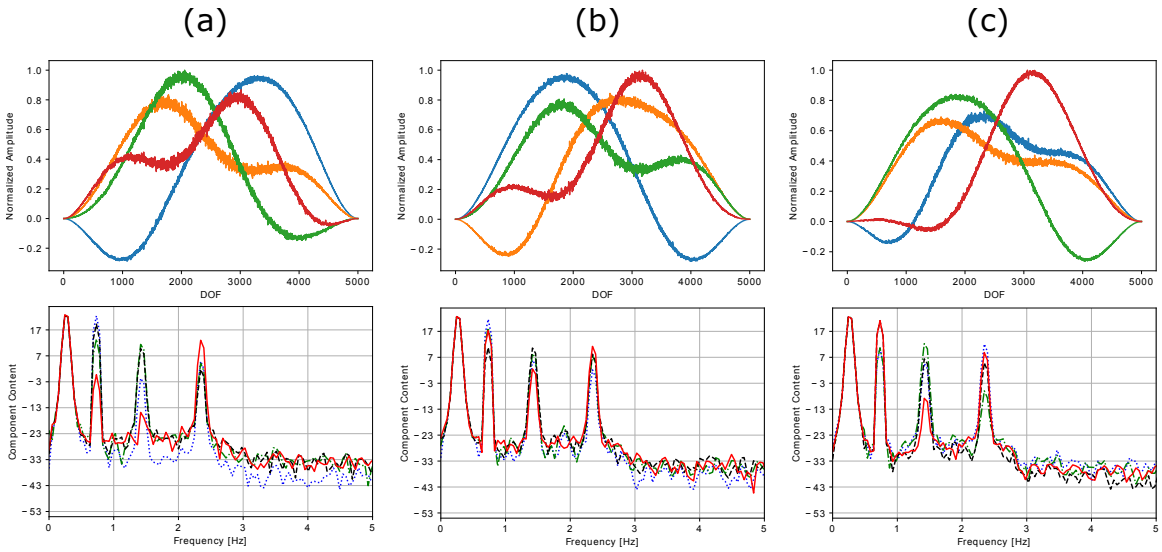

Figure 2.8: Simulation I: ALS results for three cases: (a) Case A, (b) Case B, (c) Case C. Top plots show matrix A components in space and bottom plots show Welch PSD estimates of matrix B components.

PCA is performed on columns of matrix A as well as rows of matrix B to produce orthogonal modes. Figure 2.9 shows the mode shapes resulting from PCA for cases A, B, and C, respectively. The estimated mode shapes for the first four modes are consistent with the true mode shapes of the bridge as indicated by the modal assurance criteria (MAC) [Allemang and Brown, 1982] values in Table 1, which are all greater than 0.95. The first and second mode shapes were perfectly identified in all cases. The PSD estimates of these extracted modes for all three cases are presented in Figure 2.10. In this figure, each mode shows only one peak in its frequency representation, which means PCA is successful in decoupling the modes.

It is important to notice that the identified mode shapes contain $5,000$ points; a very high resolution - in fact, these are the densest mode shapes that are extracted

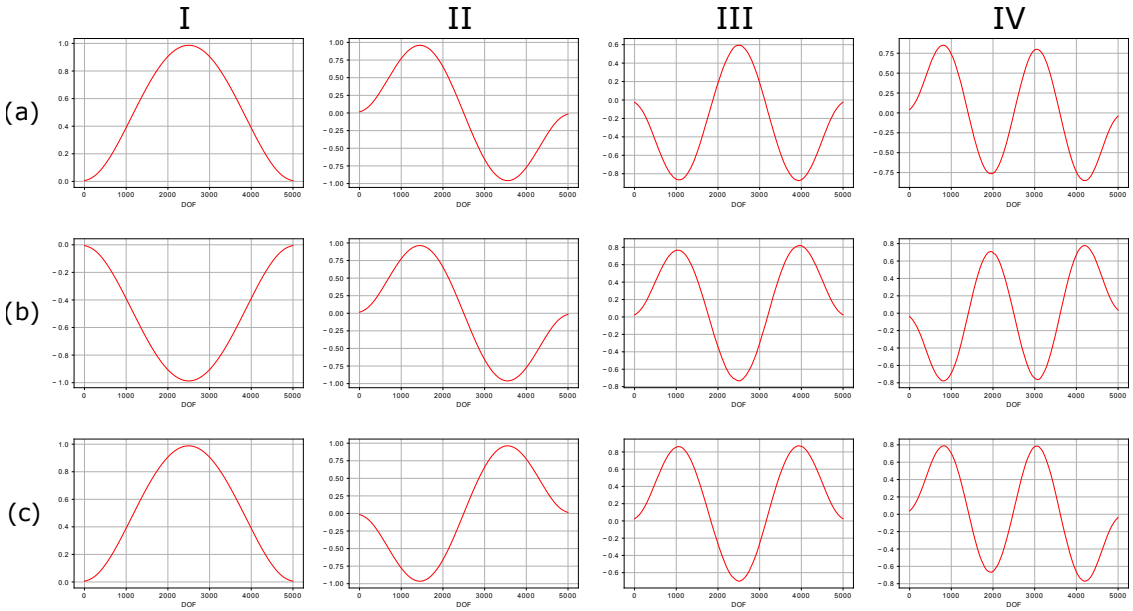

Figure 2.9: Simulation I: mode shapes resulted from method 1: (a) Case A, (b) Case B, and (c) Case C.

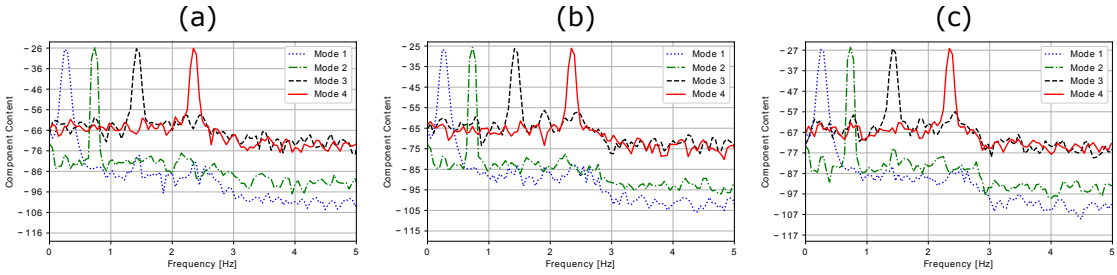

Figure 2.10: Simulation I: Welch PSD estimates of identified modes for (a) Case A, (b) Case B, and (c) Case C using Method 1.

from accelerometer data in the literature of the field. The implication is that, in case A, on average, each mobile sensor scan produced about 66 points.

The same problem is approached using Method 2 (matrix completion with structured optimization). In this method, after the matrix completion step, the response matrix is reformed into a structured matrix to approximate modal properties of each mode. Likewise, Algorithm 2 is implemented in Python to tune unknown variables. The estimated mode shapes for cases A, B, and C are shown in Figure 2.11. In Method 2, the number of points in the identified mode shapes is reduced to 100, a user-defined value. This particular selection enables a quick solution to the optimization problem while maintaining a dense mode shape.

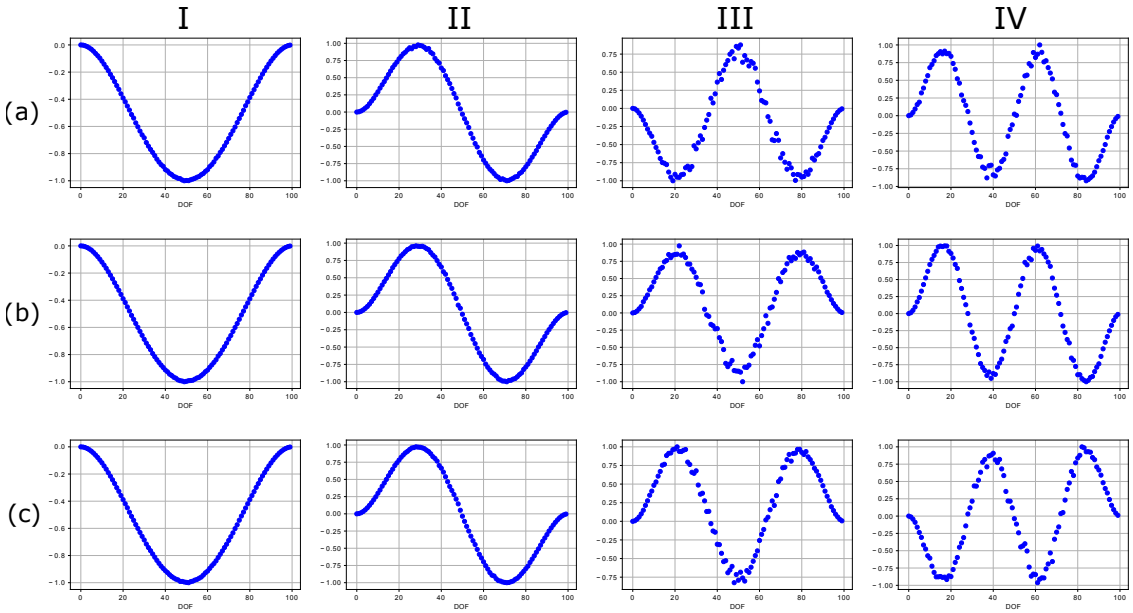

Figure 2.11: Simulation I: mode shapes resulted from method 2: (a) Case A, (b) Case B, and (c) Case C.

The accuracy of the identified mode shapes are quantified using MAC values and displayed in Table 2.1. The MAC values for all four modes are above 0.94 in all three cases, which indicates the identified shapes are consistent with the true mode shapes. In addition, the mode shape estimates are insensitive to data completion levels (from case A to case C). MAC values for two first modes using both PCA and SOA are

above 0.99. This accuracy is especially significant considering the high resolution of the identified mode shapes. Comparing two methods in natural frequency estimation shows that PCA has 2% error in the worst case, while SOA estimates are within 1% of the true values. Regarding the frequency representation of the modes identified with SOA, Figure 2.12 shows that in all three cases, modes are independent and without spectral leakage. By comparing this results with Figure 2.10, the advantages of SOA are noticeable; SOA includes a constraint that guarantees natural mode extraction, which is different from PCA. This special feature is demonstrated again in the following simulation.

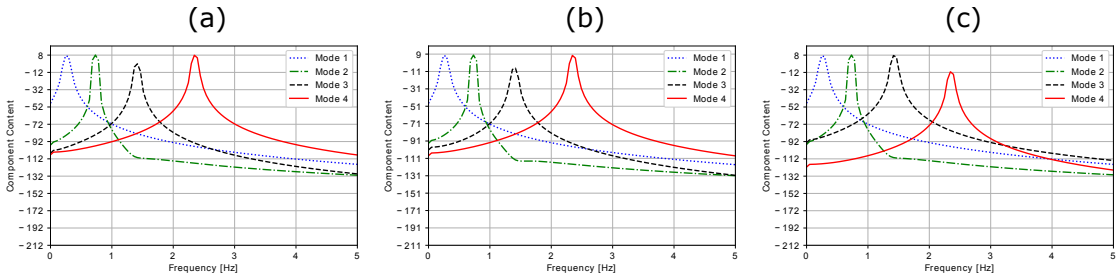

Figure 2.12: Simulation I: Welch PSD estimates of identified modes for (a) Case A, (b) Case B, and (c) Case C using Method 2.

Table 2.1 summarizes the estimated modal frequencies from both methods and all three cases; the results confirm that both methods produce accurate modal property estimates. Overall, SOA provided more accurate frequency estimates than PCA. It is important to keep in mind that while successful, this simulation was basic; a damped structure is considered in simulation II.

2.7.3 Simulation II: Damped Bridge Subjected to Impulsive Load

Simulation II is the same as simulation I except damping is considered. After forming a sparse matrix of the damped bridge response subjected to an impulsive load from finite element analysis, the matrix is completed using the ALS algorithm; the results

Table 2.1: Identification results for simulation I.

Case	Method	Mode 1	Mode 2	Mode 3	Mode 4
		MAC values			
A	PCA	0.9999	0.9993	0.9408	0.9585
	SOA	0.9995	0.9987	0.9575	0.9511
B	PCA	0.9999	0.9996	0.9577	0.963
	SOA	0.9995	0.9985	0.9418	0.9543
C	PCA	0.9999	0.9993	0.9533	0.9566
	SOA	0.9995	0.9988	0.9485	0.9519
		Natural frequencies [Hz]			
A	PCA	0.2562	0.7291	1.4187	2.3498
	SOA	0.2656	0.7317	1.4066	2.3554
B	PCA	0.2704	0.7375	1.4356	2.3451
	SOA	0.2656	0.7316	1.4322	2.3553
C	PCA	0.2653	0.7274	1.4305	2.3499
	SOA	0.2656	0.7317	1.4313	2.3553
	Actual	0.2655	0.7322	1.4356	2.3731

are shown in Figure 2.13. These plots are different when compared with ALS results of the undamped case; for instance, the components of the A matrix are noisy and contain outliers. In addition, the peaks in the PSD estimates are less prominent. One explanation for this difference is that the matrix completion algorithm performs more desirably when the values of the matrix do not decay significantly. In the damped case, the rapid decays of the signal interfere with the algorithm's ability to properly estimate the tails. Despite this, Table 2.2 shows that Method 1 is still successful in identifying highly dense mode shapes. A comparison between Figures 2.12 (undamped) and 2.14 (damped) highlights the spectral leakage among the modes in frequency domain in the damped case, which influences the amplitudes of each peak.

Regarding three sparsity cases, it was observed that as the amount of available data increased, the estimated components of matrix A are less noisy. However, to

address this noise (unwanted high frequency content), a moving average window is applied to the mode shapes resulting from PCA to filter out high frequency noises.

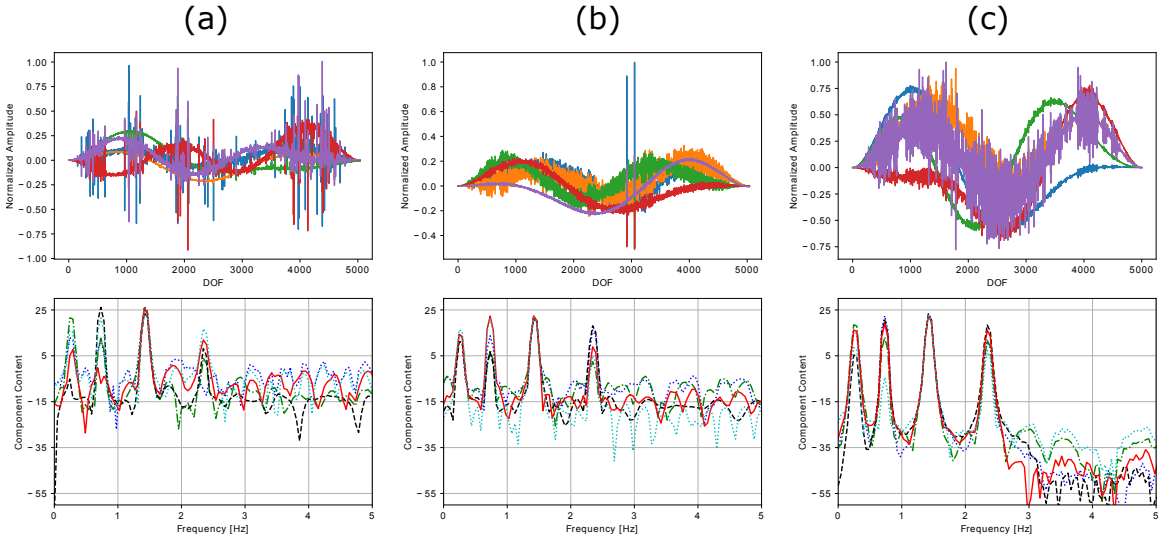

Figure 2.13: Simulation II: ALS results for three cases: (a) Case A, (b) Case B, and (c) Case C. Top plots show matrix A components in space and bottom plots show Welch PSD estimates of matrix B components.

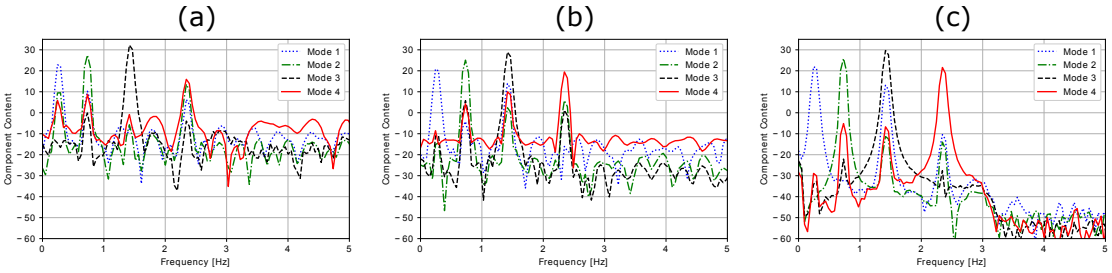

Figure 2.14: Simulation II: Welch PSD estimates of identified modes for (a) Case A, (b) Case B, and (c) Case C using Method 1.

In Method 1 (matrix completion with PCA), the damping ratios for each mode are calculated based on free vibration decay [Chopra, 2017]. After applying PCA, the corresponding modal coordinates are plotted in time and the amplitude decay within a certain number of cycles are measured and the modal damping is estimated. The results shown in Table 2.2 indicate that the damping ratios are estimated properly.

Next, Method 2 is used, in which SOA is implemented after matrix completion. This algorithm is very fast and converges in fewer than 20 iterations. In contrast

to Method 1, after convergence, the mode shapes, damping ratios, and frequencies are all calculated separately and there is no need for post processing. The identified modes are not presented for brevity; however, the MAC values, damping ratios, and frequencies are presented in Table 2.2.

Overall, the mode shapes are estimated accurately; MAC values in Table 2.2 exceed 0.92 in all cases (except for the fourth mode in case A). Note that the identified modes from Method 1 consist of $5,000$ points, while Method 2 results in 100 points. In terms of natural frequency estimates, Table 2.2 shows that both methods were equally successful. Estimated damping ratios shown in Table 2.2 indicate that both algorithms are successful in this aspect. SOA results in almost exact estimations for first three modes while PCA estimates are not as accurate. The PSD estimates in Figure 2.15 display four independent and smooth frequency plots for the structural modes. In terms of the damping ratio estimates (presented in Table 2.2), those from SOA are nearly exact.

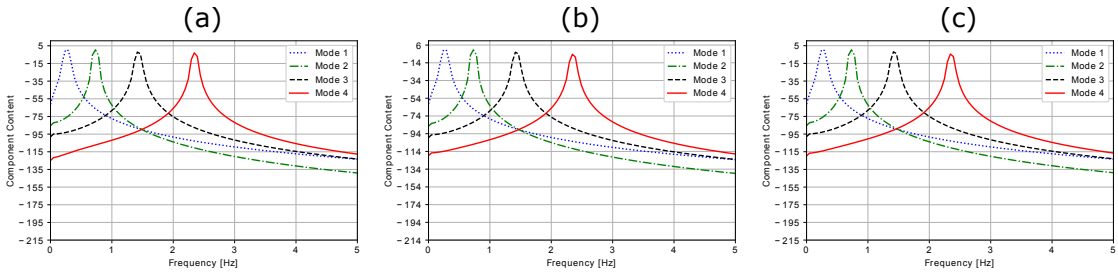

Figure 2.15: Simulation II: Welch PSD estimates of identified modes for (a) Case A, (b) Case B, and (c) Case C using Method 2.

Until now, we showed that the proposed methods are successful for estimating modal characteristics of a bridge (damped or undamped) subjected to the impulsive load and using mobile sensors data. In the next simulation, a more realistic loading case (ambient random load) is investigated.

Table 2.2: Identification results for simulation II.

Case	Method	Mode 1	Mode 2	Mode 3	Mode 4
			MAC		
A	PCA	0.9993	0.9986	0.9578	0.9582
	SOA	0.9902	0.9948	0.9555	0.7996
B	PCA	0.9959	0.9260	0.9579	0.9426
	SOA	0.9875	0.9994	0.9554	0.9246
C	PCA	0.9933	0.9929	0.9579	0.9700
	SOA	0.9831	0.9988	0.9557	0.9572
			Natural frequencies [Hz]		
A	PCA	0.2655	0.7325	1.4258	2.3500
	SOA	0.2657	0.7318	1.4313	2.3495
B	PCA	0.2606	0.7325	1.4307	2.3599
	SOA	0.2655	0.7319	1.4313	2.3539
C	PCA	0.2706	0.7429	1.4315	2.3653
	SOA	0.2657	0.7319	1.4316	2.3550
	Actual	0.2655	0.7322	1.4356	2.3731
			Damping ratios [%]		
A	PCA	2.048	1.004	0.707	0.473
	SOA	1.886	0.777	0.576	0.450
B	PCA	2.101	0.976	0.619	0.521
	SOA	1.783	0.751	0.574	0.535
C	PCA	2.155	0.923	0.735	0.933
	SOA	1.882	0.792	0.576	0.539
	Actual	2.000	0.800	0.600	0.700

2.7.4 Simulation III: Damped Bridge Subjected to Ambient Load (Operational Condition)

In this section, Method 3 is used for SID using ambient vibration data. Based on the results in the previous two simulations, it is concluded that SOA produces more consistent SID results. Simultaneously, PCA excels at determining modes that are orthogonal to one another; yet, it does not automatically produce true structural modes as the condition for these is orthogonality with respect to the mass and stiffness matrices. As a result, PCA performs ideally on single-span bridges with a uniform mass because in these cases, the condition for component orthogonality is equivalent to that for mass-stiffness orthogonality. SOA, on the other hand, is not built on this assumption and is widely applicable to more generic structures. Based on these considerations, SOA is recommended to be used with NExT for ambient vibrations and was selected for this simulation. In this example, to further test the limits of sparse data, a lower level of data completion case is added. The four cases, 50 scans, 75 scans, 100 scans, and 125 scans, correspond to data completion levels 0.50%, 0.75%, 1.00%, and 1.25%, respectively.

The bridge is excited randomly at nine locations while the mobile sensors scan the response. This case is simulating the passage of a network of moving sensors over evenly spaced potholes or expansion joints. However, other random loading patterns with more loading points can be assigned with no loss of generality in the performance. In addition, 5% white measurement noise is added to the mobile sensing data. The first step is to apply ALS to complete the response matrix. To demonstrate this process, Figure 2.16 compares the PSD estimates of the true responses at the $1,000^{th}$ DOF with the ALS approximations for two extreme sparsity cases. Overall, the ALS responses contain accurate frequency content - especially below 3 Hz. These plots do not indicate any significant differences among the data completion levels.

After the matrix completion step, NExT is applied to the estimated signals (ac-

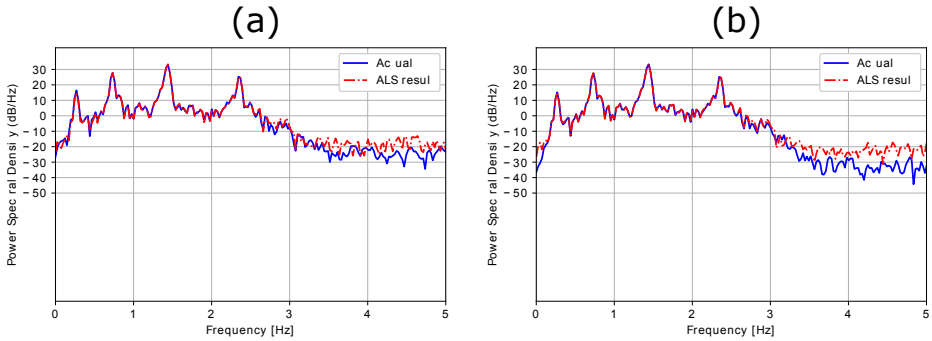

Figure 2.16: Simulation III: Welch PSD estimates of completed vs. actual bridge response signals: (a) 50 scans, (b) 125 scans.

cording to the procedure in Figure 2.6). Out of the 100 DOF available (reduced from $5,000$ to improve CPU speed), the 40^{th} is selected as the reference signal since it includes contributions from all four modes. then, a response matrix with decaying signals in each column is constructed for SOA. Figure 2.17 shows the estimated modes for each of the data availability levels. In general, the modal property estimates from this simulation are more accurate than those from Simulation II.

The estimated mode shapes are evaluated using MAC values in Table 2.3. The MAC values for the identified mode shapes, for all modes and all sparsity cases are greater than 0.95, which indicates a strong agreement with the true mode shapes. In particular, the shapes for the first and second modes were perfectly identified in all incomplete data cases, as measured by MAC values over 0.99. Furthermore, it is worth reiterating that Method 3 is successful in estimating high resolution mode shapes (100 points each). Figure 2.18 illustrates the method's accuracy in extracting clear and independent modal frequencies without spectral leakage. This result can be attributed to the structure imposed by SOA.

Lastly, by superposing identified modes and comparing with the completed response matrix results, Figure 2.19 is created. This figure demonstrates that the combined reconstructed signal from SOA ideally resembles the underlying natural frequency contents of the bridge. In addition, by comparing figures, different cases

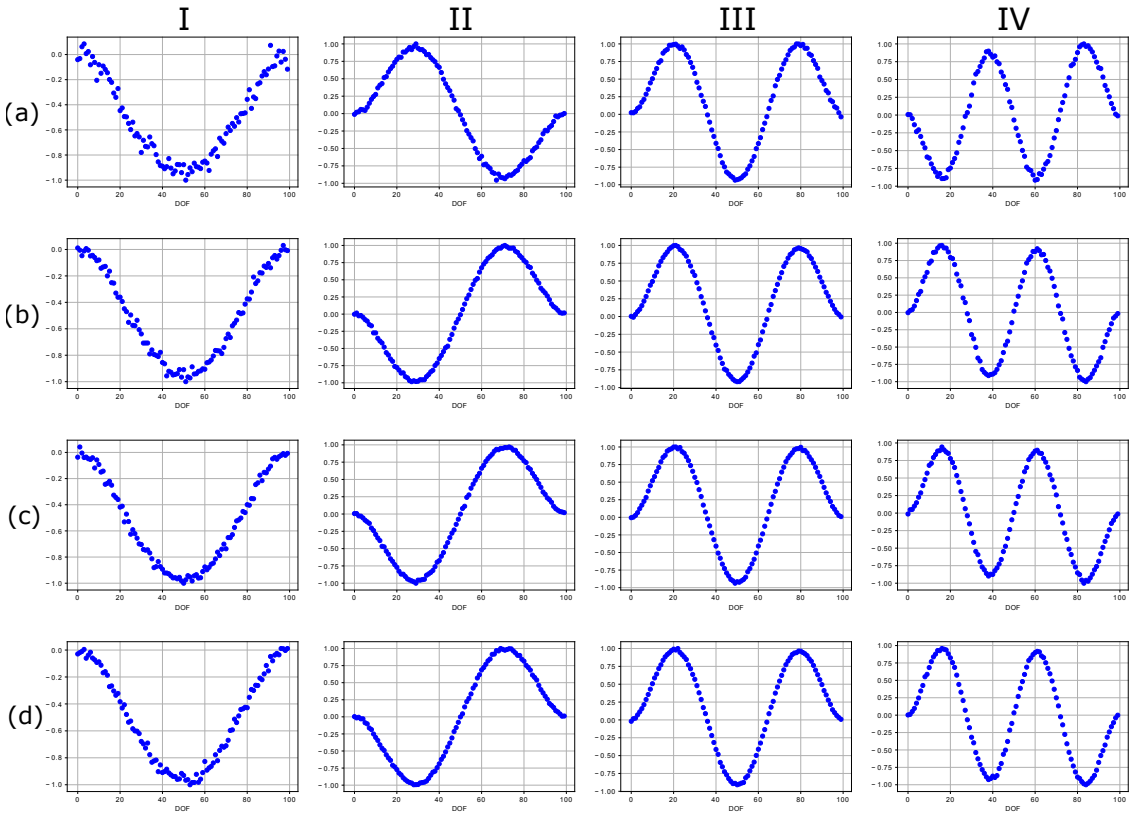

Figure 2.17: Simulation III: mode shapes resulted from method 3: (a) 50 scans, (b) 75 scans, and (c) 100 scans, and (d) 125 scans.

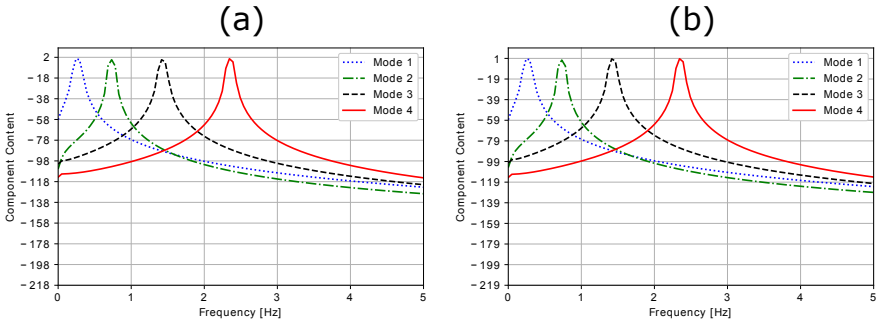

Figure 2.18: Simulation III: Welch PSD estimates of identified modes using Method 3: (a) 50 scans, (b) 125 scans.

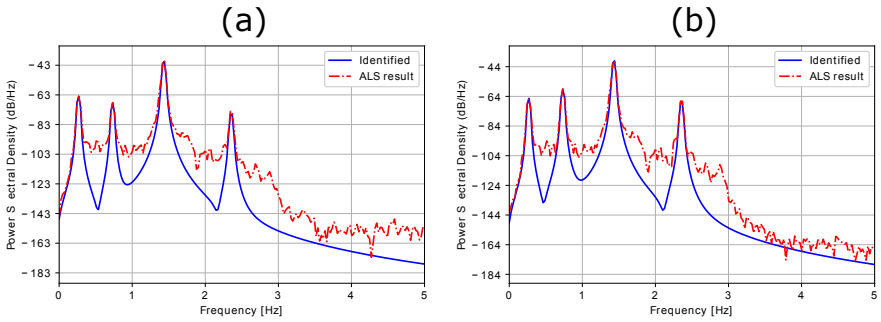

Figure 2.19: Simulation III: Welch PSD estimates of optimal structured response vs. ALS estimated signal: (a) 50 scans, (b) 125 scans.

(data availability variations) result in the same level of modal estimation accuracy. Table 2.3 shows that the natural frequency estimations are all within 0.7% error range which is promising. Damping ratio estimations from Table 2.3 agree closely with the actual values, specially in the first three modes. The same level of accuracy is also evident from MAC values of the estimated mode shapes presented in Table 2.3 (two first modes are identified with MAC values higher than 0.99). By comparing accuracy of the estimated parameters in different data availability cases, it is evident that MIMC performs consistently well within the tested range (50 to 125 scans). This is important since it shows the robustness of the proposed method for different mobile data availability. This robustness was also observed in two former cases and in SOA results. In fact, in SOA the number of unknown variables reduces from $(M+N)\times K$ for ALS step to $(M+3)\times K$ ($M\times K$ for mode shape estimations and $3\times K$ for modal coordinate estimates), and this lowers the sensitivity of the algorithm to the observed data availability.

2.8 Discussion

In the previous sections, the proposed MIMC methods were applied to a set of examples for demonstration and validation. This section provides further information to assist users with proper implementations of MIMC methods.

Table 2.3: Identification results from simulation III.

Scans	Mode 1	Mode 2	Mode 3	Mode 4
		MAC		
50	0.9932	0.9981	0.9546	0.9527
75	0.9965	0.9978	0.9552	0.9542
100	0.9978	0.9980	0.9552	0.9549
125	0.9976	0.9972	0.9555	0.9573
		Natural frequencies [Hz]		
50	0.2654	0.7316	1.4311	2.3549
75	0.2654	0.7333	1.4312	2.3555
100	0.2654	0.7331	1.4311	2.3554
125	0.2654	0.7330	1.4311	2.3553
Actual	0.2655	0.7322	1.4356	2.3731
		Damping ratios [%]		
50	1.855	0.894	0.421	0.214
75	1.857	1.004	0.426	0.213
100	1.867	0.996	0.422	0.213
125	1.867	0.993	0.349	0.213
Actual	2.000	0.800	0.600	0.700

Operations on high dimensional data are vulnerable to computational instabilities. ALS and SOA are two optimization techniques based on sparse data whose performances depend on a number of parameters. In the matrix completion with ALS, a decaying step size was tuned for the gradient descent optimization provided an adequate performance. A decaying step size is generally suitable for smooth and convex objective functions. The SOA objective function is nonconvex; thus a line search algorithm with strong Wolfe conditions [Wright and Nocedal, 1999] was implemented, as presented in Algorithm 2.

In the optimization process (ALS step), the sparse matrix is more accurately estimated if the model order K is slightly more than the expected rank of the response matrix ($K = 5, 6$). In general, the rank of the decomposition matrix is close to the target number of modes to be identified (e.g., four in this study). However, increasing the rank (model order) marginally can improve ALS optimization based on the sparse data and produce beneficial SID results [Eshkevari and Pakzad, 2020a]. In all simulations, K is tuned to produce the best performance.

In Simulation II, Figure 2.14 shows that despite the fair accuracy of the identified modes (shown in Table 2.2), the modes from PCA are not as well separated as the first simulation (modal interactions are present). Figure 2.15 shows that this problem does not exist in the modes identified with SOA. In SOA, modal interactions or spectral leakage are unlikely, because the structure only accepts one set of frequency, damping ratio, and phase shift parameters for each component; this constraint guarantees the extraction of distinct and independent modes.

For a matrix completion problem, a range of data completion between 0.5% to 2.0% is reasonable [Candès and Recht, 2009]. This ratio is convertible to different numbers of mobile scans according to the dimension of the response matrix. For instance, in this study the response matrix is $5,000 \times 5,000$ which needs nearly 100 mobile scans to suffice 1.0% data completion rate. These 100 scans are divided in the

number of lanes over the bridge (e.g., for the numerical case study, we can assume three lanes in each direction). Therefore for each lane, 17 scans are needed within the monitoring duration (25 scans for a four-lane bridge). Considering the sampling rate, the vehicle speed, and the length of the bridge, this number is easily practical. Important note here is that these 17 scans do not need to visit all DOFs within the time frame, e.g., partial scans are acceptable. For crowded bridges, the number of mobile scans are significantly more than this range, however, the operator can randomly pick sufficient measurements and use for the matrix completion and modal identification tasks.

To better understand the effect of model order K with respect to the data availability levels, various K values and scan levels were considered by Method 3. Table 2.4 shows the corresponding final objective function values of ALS and SOA and documents the runtimes and number of identified modes. In this table, ALS objective function values are reported per observed matrix entry and SOA values are reported over the entire response matrix after completion with normalization. A smaller ALS objective function value indicates a more successful fit based on the observed entries and suggests a more accurate signal reconstruction. Generally, as K increases, the ALS objective function decreases. At the lowest data availability (50 scans), when K grew from 5 to 6, the ALS objective function value increased slightly - which implies that a limit had been reached. For the more complete data cases, the ALS objective function always decreased as K increased. Similarly, the SOA objective function value measures the success in imposing a structure over the response matrix; however, this value was much less sensitive to changes in K or data availability.

The runtimes of each technique are compared in Table 2.4; while these are subject to the processing units, the relative metrics are informative. At the lowest data level (50 scans) and with K equal to 6, five modes were identified; however, the runtime for ALS was significant. Alternatively, five modes can be identified over ten times

faster, and about four times more accurately, when 100 or 150 scans were available (see Table 2.4). Generally, when the number of scans increased from 100 to 150 there was no improvement in SID. These points demonstrate some of the trade-offs between K, data availability, and the target number of identified modes. In certain circumstances, more data does not improve the SID results.

There are numerous variables that influence the data collected by a vehicular sensor network. In this study, the MIMC methods proposed were shown to produce accurate SID results in the case of a random monitoring process. The speed of the mobile sensors is an influential parameter that was not explicitly studied in this study - instead it was linked to a particular data duration and the bridge's length. It is important to clarify that this example was presented for demonstration purposes and to show that there are no aspects of the MIMC algorithms that restrict speed variations of the mobile sensors. The velocities of the individual vehicles affect the locations of the observed entries in the response matrix and, in turn, the shape of the available data (see the first block of the proposed methods shown in Figures 2.5 and 2.7). Matrix completion literature [Candès and Recht, 2009] discusses how sparse matrices with randomly arranged entries provide an ideal starting point for reaching the global optimum, i.e., yielding the most accurate full response matrix. Thus, a stochastic vehicular sensor network with various speeds, sampling rates, scanning intervals, etc. is better suited to achieve this condition. In addition, speed variations can help to better facilitate the proposed methods for shorter span bridges. For instance, if the bridge span is 300 meters and vehicle network cross the bridge with speed 10 km/hr, the same level of spatial discretization could be achieved. This means that the response matrix will have the same dimensions and consequently, the conclusions of the current case studies (e.g., high resolution natural mode shape identification) are achievable.

Table 2.4: Runtimes, number of identified modes, and objective functions for various K and data availability.

Measure	Scans	K = 2	3	4	5	6
Runtime [sec]	50	155	161	>1000	>1000	>1000
	100	31	30	55	93	162
	150	46	31	57	31	233
Identified Modes	50	2	3	3	4	5
	100	0	3	4	5	5
	150	2	3	4	5	5
Objective function values						
ALS step	50	77.1751	40.6841	23.9679	11.0315	12.7113
	100	90.8833	51.8795	29.3165	7.3299	3.6893
	150	93.5409	51.0089	26.5513	9.0379	4.6717
SOA step	50	0.0221	0.0479	0.0535	0.0025	0.0159
	100	0.1313	0.0483	0.0476	0.0446	0.0404
	150	0.0378	0.0549	0.0807	0.0469	0.0461

2.9 Conclusion

In this study, novel methods were proposed for a comprehensive modal identification of a bridge based on data collected by a large number of moving sensors (vehicles). Bridge response data collected by a vehicular sensor network are both sparse and dynamic. The full (unobserved) bridge response is viewed as a very large data matrix of which the aggregated mobile sensing data provide a sparse representation. The modal identification using matrix completion (MIMC) methods proposed utilizing matrix completion, i.e., alternating least square (ALS) [Jain et al., 2013], to complete the full matrix based on sparse entries. Then, the completed matrix was analyzed to extract a complete set of modal properties, e.g., frequencies, damping ratios, and high-resolution mode shapes. For this, two algorithms, principal component analysis (PCA) [Jolliffe, 2011] and structured optimization analysis (SOA) were proposed (the latter was developed by the authors) and applied on the completed matrix (Methods 1 and 2, respectively). To extend the applicability of this technique to ambient

structural vibrations, a third method was proposed based on the natural excitation technique (NExT) [James et al., 1995] (Method 3).

The proposed methods were evaluated numerically in three different case studies and results were presented. Method 1 was able to extract natural mode shapes of the bridge under impulsive loading with $5,000$ points which are the densest identified mode shapes in the existing literature. Alternatively, Method 2 can extract mode shapes with a user-defined number of points. In Simulation III, Method 3 showed that it is a robust and accurate SID solution for bridges using mobile sensor network with minimal sensitivity to the data completion rate. However, the methods generally improve in terms of computational costs and SID results when more data completion rate is available. It was also shown that Method 2 and 3 could extract fully decoupled modal components while Method 1 suffered from modal leakage in some modes. A sensitivity study on the user-defined model order K (rank of the decomposition matrices) was performed. The study showed that while larger K's usually lead to better signal reconstruction results, it will increase the computational costs. A balanced configuration of K and data completion rate yielded the best performance.

The accuracy of estimated modal properties are promising in all three simulations and methods (within 2% error in most cases). Method 1 was able to identify very high-resolution fundamental mode with MAC value equals to 0.9999. Frequency estimated in all three simulations are very accurate (e.g., Method 3 resulted in 0.07% estimation error in the worst case on Simulation III). Method 2 and 3 showed a desired performance in damping ratio estimation, especially on the first three modes. This work further supports the practice of dynamic sensor networks for SHM applications, especially system identification. MIMC methods are applicable to data collected by vehicular sensor networks, which present new opportunities to monitor bridge vibrations at unprecedented rates and scales. This proposed methodology paves the way towards a fully autonomous and real-time bridge health monitoring platform

using crowd-sourced data provided by smart devices.

Chapter 3

Processing Acceleration Measurements within Moving Vehicles

3.1 Abstract

Vehicles commuting over bridge structures respond dynamically to the bridge's vibrations. An acceleration signal collected within a moving vehicle contains a trace of the bridge's structural response, but also includes other sources such as the vehicle suspension system and surface roughness-induced vibrations. This study introduces two general methods for the bridge system identification using data exclusively collected by a network of moving vehicles. The contributions of the vehicle suspension system are removed by deconvolving the vehicle response in frequency domain. The first approach utilizes the vehicle transfer function, and the second uses ensemble empirical modal decomposition (EEMD). EEMD is a geometric based blind source separation (BSS) tool that is able to extract sources out of a statically or convolutionally mixed signal. Next, roughness-induced vibrations are extracted through a novel

application of second-order blind identification (SOBI) method. After these two processes the resulting signal is equivalent to the readings of mobile sensors that scan the bridge's dynamic response. Structural modal identification using mobile sensor data has been recently made possible with the extended structural modal identification using expectation maximization (STRIDEX) algorithm. The processed mobile sensor data is analyzed using STRIDEX to identify the modal properties of the bridge. The performance of the methods are validated on numerical case studies of a long single-span bridge with a network of moving vehicles collecting data while in motion. The analyses consider three road surface roughness patterns. Results show that for long-span bridges with medium- to high-ongoing traffic volume, the proposed algorithms are successful in extracting pure bridge vibrations, and produce accurate and comprehensive modal properties of the bridge. The study shows that the proposed transfer function method can efficiently deconvolve the linear dynamics of a moving vehicle. EEMD method is able to extract vehicle dynamic response without a-priori information about the vehicle. In addition, proposed identification methods provide secondary information about the roughness pattern and the vehicle. This study is the first proposed methodology for complete bridge modal identification, including operational natural frequencies, mode shapes and damping ratios using *moving vehicle sensory data*.

3.2 Introduction

Advancements in sensor technology and data acquisition techniques have played a major role in bringing the civil engineering community towards more frequent and more accurate condition assessments of structures. Structural health monitoring (SHM) methods have been quick to evolve with technologies; most notably, wireless sensor networks became promising alternatives to wired precedents [Lynch and Loh, 2006,

Ni et al., 2009, Pakzad et al., 2008]. In terms of system identification techniques, many statistical frameworks have been proposed and verified [Andersen et al., 1999, Juang and Pappa, 1985, Gul and Catbas, 2009]. Yet, the measurement process in SHM still adheres to the fixed sensor paradigm. In this framework, sensors are installed at certain locations on the structure, thus the spatial information in the data is restricted to these particular points. Ultimately, this measurement approach can limit researchers' ability to understand structural condition and performance. For example, in system identification (SID), it is known that the spatial resolution of the identified mode shapes is directly impacted by the number of sensing nodes and their arrangement [Matarazzo and Pakzad, 2016b].

SID applications that target higher resolution mode shapes have used dense arrays of fixed sensor networks [Pakzad et al., 2008, Dorvash et al., 2014, Zhu et al., 2012]; while such networks are able to provide an improvement in spatial information, the equipment, setup, and maintenance costs associated with dense sensor networks effectively make this type of information inaccessible. In addition, complex networks have more complicated communication and processing tasks since more data need to be transmitted and analyzed, requiring more advanced communication technologies. Recently, real-time monitoring has been studied using internet of things (IoT) for data transmission and storage clouding [Smarsly et al., 2011, Kijewski-Correa et al., 2012, Zhang et al., 2016]. These technologies have eased the application of complex sensing networks, while the spatial resolution problem is not addressed yet.

The cost inefficiency of highly dense sensor networks has motivated researchers to determine more optimal sensor layouts, e.g., those that minimize network complexity while attaining a level of information that is appropriate for the application. This approach has been taken for both damage detection [Guo et al., 2004, Kim et al., 2000] and structural modal identification [Chang and Pakzad, 2015, Meo and Zumpano, 2005] purposes. While important and highly practical, this strategy does not resolve

the scalability problems that are inherent to fixed sensor networks because of two concerns: requiring more sensors for more spatial information and requiring dedicated sensor networks for each structure to be assessed.

Mobile sensor networks offer numerous advantages compared to the conventional stationary sensing scenario. Overall, mobile sensors have low setup costs, collect spatial information efficiently, and no dedicated sensors to any particular structure. Most importantly, mobile sensors can capture comprehensive spatial information using few sensors.

3.2.1 Toward Infrastructure Vibration Crowdsourcing

The advantages of mobile sensing combined with the ubiquity of smartphones with IoT connectivity have motivated researchers to think of automobiles as large-scale sensor networks. Recently, studies were conducted to show the suitability of mobile sensors and smartphones for environmental assessment in urban areas. Recent researches [Eriksson et al., 2008, Alessandroni et al., 2014, Kumar et al., 2016, Anjomshoaa et al., 2018] have incorporated smartphone vibration data for road pothole detection and road surface condition assessment purposes, and successfully examined their platform experimentally. Feng et al. [2015] studied substitution of stationary sensors with smartphones for identifying dynamic characteristics of structures. However, the sensing network consisted of fixed nodes. Matarazzo et al. [2018] studied crowdsensing possibilities created by smartphone abundance. In this study, smartphones were used for data collection while driving over a bridge and by frequency-domain analysis, bridge natural frequencies were identified. They showed that smartphones are viable moving sensors and easy to use; however, the result was limited to frequency informations and was not a comprehensive SID. The study emphasized on the huge information potential offered by ubiquitous smartphones in moving vehicles.

Despite the promises of scalability, there remains a need to develop practical

analytical procedures for a comprehensive SID that are applicable to mobile sensor and smartphone data. The recent studies considering mobile sensor networks have mostly demonstrated partial modal identification(either frequency, damping, or mode shapes). At this time, STRIDEX by Matarazzo and Pakzad [2018] is the one of the procedure that is capable of performing a complete identification using mobile sensor data. Sadeghi Eshkevari et al. [2020a] has recently proposed an alternative approach as well with a different sensing setting.

3.2.2 Review of System Identification using Mobile Sensor Networks

Mobile sensor networks offer more scalable and flexible data acquisition when compared to fixed sensor networks; yet the resulting datasets are fundamentally different and require special consideration [Matarazzo and Pakzad, 2016a]. Mobile sensing data fall under the dynamic sensor network (DSN) data classification and can be mapped exactly to the equation of motion through the truncated physical state-space model (TPM). In a TPM, the fundamental assumption is that the measurements at physical locations are truncated results of a coordinate transform from modal coordinates at every time sample. Equation 3.1 shows the state-space model of a dynamic structure:

$$\begin{aligned} x_k &= Ax_{k-1} + \eta_k \\ y_k &= \Omega_k C x_k + \nu_k \end{aligned} \tag{3.1}$$

In this equation, x_k (with $x_1 \sim N(\hat{\mu}, \hat{V})$) is the state vector containing the structural response at all degrees of freedom (DOFs), y_k is the observation vector which includes the structural responses at a subset of all DOFs. $A \in \mathbb{R}^{pN_\alpha \times pN_\alpha}$ and $C \in \mathbb{R}^{N_0 \times pN_\alpha}$ are state and observation matrices, respectively. N_α is the number of

virtual probing nodes and N_0 is the size of observation vectors. p is a user-defined model order, expanding number of observation channels to a desired number of states. $\eta_k \sim N(0, Q)$ and $\nu_k \sim N(0, R)$ are systematic and sensing noises, which are commonly modeled as uncorrelated Gaussian white noise with covariance matrices Q and R. Finally, Ω_k is called mode shape regression (MSR) function, and essentially is a known 3D array that for each time step, maps moving sensors data to virtual probing data by an approximation. Further mathematical details for MSR function can be found in Matarazzo and Pakzad [2016a]. In addition, a more advanced signal reconstruction method is proposed by Eshkevari and Pakzad [2020b] which enables data estimation on probing locations under high irregularities in the mobile sensors network.

The governing state-space model (Equation 3.1) of the system is time variant with six time-invariant parameters $\{A, C, \hat{\mu}, \hat{V}, Q, R\}$ and one time variant parameter $\{\Omega_k\}$, which can be approximated using a *sinc* basis function. The structural identification using expectation maximization (STRIDEX) method was proposed to identify the parameters of the TPM and extract modal properties of the structural system, which include high-resolution mode shapes. The accuracy and performance of STRIDEX was validated using both synthetic and experimental data [Matarazzo and Pakzad, 2018]. Most notably, it was shown that two mobile sensors can produce a mode shape estimation with over 240 points.

The STRIDEX [Matarazzo and Pakzad, 2018] was developed to determine the maximum likelihood estimates (MLE) of the TPM (Equation 3.1). This is achieved using the expectation maximization, a method which computes iteratively the conditional expectation of the unobserved state variable and its covariance matrices. In STRIDEX, the time invariant parameters are combined into one *super-parameter*. In the expectation (E) step, given the observed measurement data, state vectors are estimated using Kalman filtering [Ristic et al., 2004] and Rauch-Tung-Striebel (RTS)

smoothing [Särkkä, 2008]. Then the conditional expectation of the log-likelihood function of TPM is maximized to yield an updated super-parameter estimate (maximization (M) step). This procedure continues until log-likelihood function value changes less than a predefined threshold. Detailed explanations and mathematical proofs are available in Matarazzo and Pakzad [2018].

While successful, in previous applications of STRIDEX, it was assumed that the mobility mechanism did not contaminate the measurement process. In other words, considering the case of a sensor within a moving vehicle, the vehicle dynamics and road profile effects were not considered. In practice, a sensor within a moving carrier cannot capture the pure dynamic response of the bridge. These are a mixture from several sources, primarily roughness-induced vibrations and vehicle suspension vibrations. The following section presents an overview of relevant studies considered real-world data subjected to the vehicle-bridge interaction problem.

3.2.3 Bridge System Identification using Dynamic Sensor Network Data

Realistically, moving sensors are placed into a carrier, which itself is a mechanical system. Vehicle-carried sensors in fact are collecting responses of a vehicle suspension system under bridge vibrations entering via tires. Researchers have been studying vehicle-bridge interaction, mostly assuming one passing vehicle as the loading of the bridge [Cantero et al., 2019, Chang et al., 2014]. Indirect bridge monitoring considers the extraction of bridge properties, in a general sense, from the response of a moving vehicle; however, the specific objectives have varied throughout these studies. Some have aimed to obtain partial modal information, e.g., frequencies only [Yang et al., 2004a, Lin and Yang, 2005, Yang and Chang, 2009, Siringoringo and Fujino, 2012], or mode shapes [Malekjafarian and OBrien, 2014b], or damping ratio of the fundamental mode [González et al., 2012] given a special bridge excitation. Others have targeted

attributes that are related to modal properties such as mode shape squares [Zhang et al., 2012] and stiffness indicators [Malekjafarian and OBrien, 2017]. Very limited studied have been done on bridge identification using mobile data under ambient loading [Marulanda et al., 2016], with some constraints.

A frequency-domain bridge identification based on mobile sensor data was introduced by Yang et al. [2004a], which used the acceleration time history of a vehicle crossing a bridge to determine its fundamental frequency. A parametric study was done to capture effects of vehicle speed and bridge mechanical properties and numerically verified by finite element analysis. The bridge loading was moving point loads applied by the data collector vehicle. The research was experimentally validated by Lin and Yang [2005], in which a moving setup, consisting of a tractor and trailers passing with various speeds over a bridge and further investigations were conducted by Yang and Chang [2009]. A comprehensive finite element study was performed by Siringoringo and Fujino [2012], in which a detailed bridge-vehicle interaction model (VBI) was built and vehicle vibrations caused by bridge dynamic motions were used for frequency-domain SID. The study also was backed up by an experiment on a bridge in Japan. However, the methodology was only able to capture the first natural frequency and limited to a given moving load scenario.

The same framework (VBI) was studied by González et al. [2012] in order to estimate bridge damping ratios using moving acceleration records, assuming Rayleigh damping. The bridge was loaded by a passing sensor carrier. The study suggests an optimization procedure to tune the most fit damping ratio for the first mode of a bridge based on its geometry and mechanical properties. A SID procedure to refine identified mode shapes using time-frequency signal representation between fixed and mobile sensors was proposed by Marulanda et al. [2016]. The algorithm showed high resolution mode shapes extraction under numerical noise-free and experimental data. However, mobile sensing data were assumed to be pure structural vibrations in both

numerical and experimental cases. This study required stationary nodes, however, it was assuming a more general loading scenario.

Zhang et al. [2012] proposed a method to extract mode shapes of a plate and beam structures from acceleration response of a traveling device with a tapping instrument as a loading apparatus. In this study, a single sensor was used and good mode shape resolution could be achieved. The mode shapes are found by exciting the bridge by frequencies close to known natural frequencies. In addition, the method does not assume any contamination caused by other sources.

As a more realistic case, Malekjafarian and OBrien [2014b] used short time frequency domain decomposition for estimating bridge mode shapes using vehicle-carried sensing data. This study also considered the bridge under a special moving load resulted by a passing vehicle. The method showed promising results in the case of a very smooth roadway (no roughness considered). For the second phase, to eliminate roughness-caused vibrations, the residual of axle signals from two successive trailers was used as the input. The approach was successful for identifying mode shapes of first two modes. However, the spatial resolution was low and vehicle properties were not fully given. Alternatively, the same researchers extended the idea by adding a tapping device exciting the bridge with the frequency close to the bridge natural frequencies [Malekjafarian and OBrien, 2017]. For diminishing road roughness effect, the same technique of subtracting measurements of two axles was used and higher resolution mode shapes were identified. The method needs specialized vehicles that are pulling auxiliary parts, which are not common. In addition, the study aimed to identify mode shapes, not a complete modal identification. Note that neither of these studies considered ambient bridge excitation.

3.2.4 Problem Definition

Bridge vibrations are transmitted into the vehicle cabin as it travels across the bridge. The goal is to extract bridge dynamic information from vehicle accelerations; however, these measurements are subject to the vehicle-bridge interaction problem, i.e., polluted by undesired signals. Mathematically, the TPM developed for the mobile sensing problem shown in Equation 3.1 can be formulated to consider this particular measurement process as shown in Equation 3.2:

$$\begin{aligned} x_k &= Ax_{k-1} + \eta_k \\ y_k = y_k^{br} &= \Omega_k C x_k + \nu_k \\ y_k^{vbi} &= y_{br}^k + y_k^{if} \\ y_k^{act} &= f(y_k^{vbi} + y_k^{rgh}, y_k^{eng}) \end{aligned} \tag{3.2}$$

where $y_k = y_k^{br}$ and y_k^{if} are the pure bridge response and bridge response under vehicle-bridge interacting force, respectively. The algebraic sum of these two components constitute y_k^{vbi}, when the bridge interacts with the vehicle. The bridge-vehicle interaction in long span bridges can be modeled in detail as proposed in Zhou and Chen [2015], Camara et al. [2019]. In this study since a bridge under ambient load is considered, the vehicle-bridge interaction part y_k^{if} is significantly smaller that y_k^{br}, resulting $y_k^{vbi} \simeq y_k^{br}$. This approximation has been demonstrated by comparing coupled and uncoupled responses of the bridge and the vehicle in the preliminary stage of the analysis. In fact, as demonstrated in Sadeghi Eshkevari et al. [2020c], for long-span bridges with random traffic load, the simplified uncoupled approach is very accurate and computationally dramatically faster. However, as the sensing vehicle speed or weight increases, the simplified simulation approach becomes less accurate. In this study, the sensing vehicle is lightweight and moves with low speed, conforming with the assumptions for an accurate estimation. Note that the low speed assumption is a

widely-accepted practice for indirect bridge SHM [Yang and Chang, 2009]. The mobile sensor measurement y_k^{act} is a complex mixture of multiple simultaneous phenomena which includes the idealized mobile sensor data y_k^{br}. y_k^{rgh} is the profile roughness displacements at time k. y_k^{eng} is the engine-induced vibration, which presents in the vehicle response, is often actively controlled and not sensible [Elliott and Nelson, 1990], thus is neglected in this study. Most importantly, the final response y_k^{act} is a nonlinear function of the linear mixture of these three components. The function $f(\cdot)$ is the *convolution* of the vehicle impulse response by the input signal.

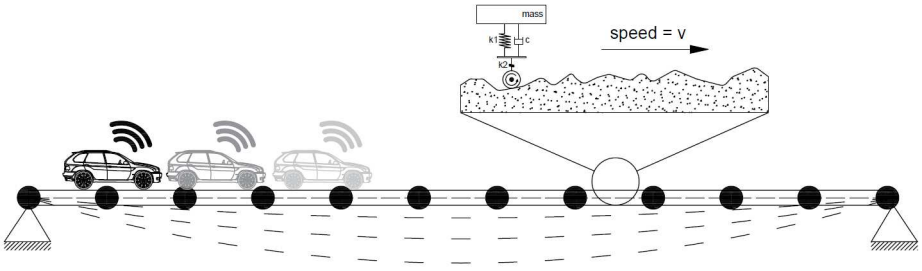

Figure 3.1: Schematic illustration of vehicle-carried sensing

The objective is to extract y_k^{br} from the actual vehicle response y_k^{act} and implement STRIDEX to provide a complete bridge SID.

3.2.5 Motivation

Given the state of the literature, a method that can simultaneously process data from multiple moving sensors within vehicles makes an important contribution to crowd-based systems. Note that the study intends to propose methodologies for bridge modal identification which are suitable for long and crowded bridges which have the potential for crowdsensing. We found that the significant challenge in large-scale "crowdsensing" campaigns is a methodological gap: the lack of an "end-to-end" system identification process that accounts for unwanted vehicle vibrations. Therefore the goal of this study is to present a set of methodologies that decompose the measurements recorded within the vehicle cabin into individual components. Blind source

separation (BSS) as a signal processing tool provides methodologies to decompose statically or convolutionally mixed signals to original sources without any knowledge about them in advance [Cardoso, 1998]. The BSS problem is ill-conditioned, since both sources and mixing matrix are unknown; however, many assumptions have been made to constrain the problem.

Recently, Eshkevari and Pakzad [2019a] showed that for a vehicle with a rigid suspension system, second-order blind identification (SOBI) is capable of separating roughness-induced vibration and bridge dynamics. That is, the bridge vibrations were extracted from a pair of vehicle measurements collected over a certain portion of the bridge length. However, the study did not consider realistic vehicle dynamics. This study incorporates a vehicle dynamics model and the technical goal is to remove both vehicle and roughness effects from raw acceleration measurements using signal deconvolution and blind source separation (BSS) techniques, e.g., EEMD [Huang et al., 1998] and SOBI [Belouchrani et al., 1997]. The objective of this phase is to decompose the highly contaminated raw signal collected by the vehicle sensor and extract bridge vibrations. Next, STRIDEX is implemented to process the mobile sensing data extracted and determine the structural modal properties (frequencies, damping ratios, and mode shapes).

In this study, two approaches are proposed to extract the bridge response from vehicle measurements (as shown in Figure 3.2): the transfer function (TF) approach and the EEMD approach. Each procedure consists of two phases: deconvolution of the vehicle dynamical effect and removal of roughness-induced vibrations. The key difference between the two approaches is the method by which the vehicle vibrations are separated. The TF approach uses the vehicle's frequency response function (FRF) for the deconvolution, while the EEMD approach estimates the sources of a signal by using trend extraction.

In either case, after deconvolution, the nonlinear function $f(\cdot)$ of Equation 3.2 is

inverted, so that the remainder is the argument of the function i.e. a linear mixture of the bridge dynamic vibrations y_k^{br} and roughness profile y_k^{rgh}, neglecting engine-induced noises. Therefore, the signal still needs to be separated to extract y_k^{br}. This objective is being done by applying SOBI which is a robust solution for un-mixing linearly superposed sources.

In the following sections, these procedures are detailed and their performances are evaluated using realistic numerical simulations. The main contributions of this study are as follows:

1. The proposed approaches are the first that provide a comprehensive modal identification of a bridge using acceleration measurements from moving vehicles.

2. The approaches are proposed to be used for bridges under ambient loading, with minimal assumptions on bridge type and vehicle characteristics.

3. The solution is potentially able to provide some insights regarding the road roughness condition as a byproduct of the process.

4. These approaches are robust for severely rough road profiles as long as the vehicle acts linearly within the frequency band considered.

In Sections 3.3 and 3.4, a simulation that has been used for numerical assessment is demonstrated and processing methods are presented. Later in Section 3.5, the procedures for signal decontamination are performed step by step and results are presented. In the next section, the purified signals are fed into the SID algorithm, STRIDEX, and results are discussed. In Section 3.7 the vehicle properties are changed from a vehicle with customized mechanical properties that is suitable for sensing (in terms of having disjoint frequency contents with the bridge) to a vehicle with regular mechanical properties and results are presented. Finally, in Section 3.8 a more practical version of the first method (deconvolution using vehicle FRF) is proposed and evaluated.

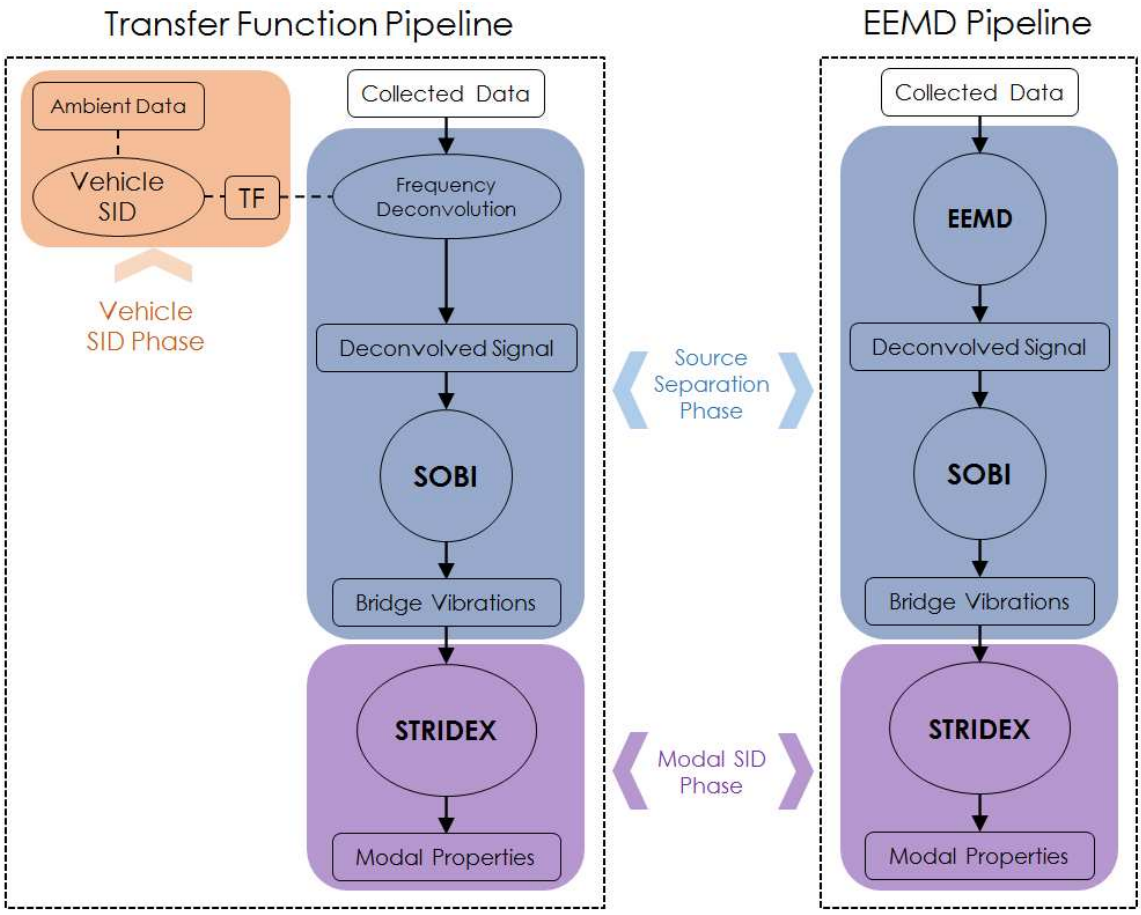

Figure 3.2: Flowcharts for two proposed pipelines

3.3 Approaches to Extract the Bridge Response from Measurements within Moving Vehicles

This section presents two general approaches to extract the bridge acceleration response from measurements within a moving vehicle. The primary differences in the approaches lie within the deconvolution process. Both approaches implement second-order blind identification (SOBI) after signal deconvolution. In addition to the system transfer function approach, a modified version of that is presented in which the deconvolution phase is eased significantly.

3.3.1 Method 1: Deconvolution using the System Transfer Function

To remove vehicle dynamics effect from the collected response, the direct approach is to apply deconvolution in frequency domain, for which an accurate description of the vehicle suspension system is needed. In cases where this information is not readily available a vehicle SID must be performed. The vehicle suspension system can be modeled efficiently as a linear quarter-car system, shown in Figure 3.3 [Cebon, 1999].

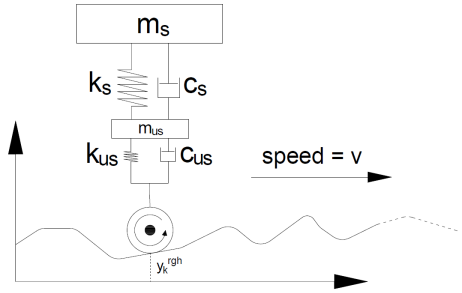

Figure 3.3: Quarter-car model for vehicle suspension system

where m_s and m_{us} are sprung and unsprung mass of a quarter-car. c_s, c_{us} and k_s, k_{us} are corresponding damping and stiffness for masses, respectively. At each time step, y_k^{rgh} is the displacement input of the system caused by the road profile roughness and vehicle response is collected while attached to the m_s. For a regular road, y_k^{rgh} is the input of the vehicle system, while for a vehicle-bridge interacting model, the vehicle input also contains the bridge vibrations y_k^{brg}. The model is a two DOF dynamic problem and a full description of the system can be expressed by a two DOF state space equation set.

Equations 3.3 and 3.4 show the governing dynamic equations of a vehicle with respect to the bridge vibrations and road profile roughness. In Equation 3.3, h_k is the quarter-car model impulse response in time domain, which in frequency representation is equivalent to the system transfer function (TF). Given system model and responses at both DOFs, the system can be identified using an output-only SID algorithm. After

determining the vehicle's modal properties, the TF can be generated in frequency domain ($H(\omega)$) and then using Equation 3.5, the vehicle input can be estimated. This input is yet to be processed for extracting y_k^{brg}, however, it is now a linear mixture of two components shown in Equation 3.4. Note that the TF here is equivalent to the frequency response function (FRF) in the structural dynamics control literature.

$$y_k^{obs} = h_k * (y_k^{brg} + y_k^{rgh}) \tag{3.3}$$

$$y_k^{inp} = y_k^{brg} + y_k^{rgh} \tag{3.4}$$

$$Y^{obs}(\omega) = H(\omega) \times Y^{inp}(\omega) \tag{3.5}$$

3.3.2 Deconvolution using the Approximated System Transfer Function

In Method 1, a complete description of the vehicle system is possible only when the system response at all DOFs are collected. This means that in order to construct the identified TF, measurements collect vehicle response not only inside the vehicle (sprung channel), but on the unsprung mass level (tire channel), which is a hard task. An alternative approach is to assuming vehicle suspension mode shapes as given, collect data only inside the vehicle. In this scenario, the sprung channel is adequate to generate vehicle TF, since output-only SID tools can identify natural frequencies and damping ratios using only one data channel. This approach is practically more desirable and will be analyzed in Section 3.8.

3.3.3 Method 2: Deconvolution using Ensemble Empirical Modal Decomposition

Separation of mixed signals to sources is the primary focus in the field of blind source separation (BSS). BSS is a signal processing topic that has been widely studied for both static and convolved mixtures [Cardoso, 1998]. The process of BSS was used for structural dynamics application in Poncelet et al. [2007] and Kerschen et al. [2007] and theoretical equivalence of the application to the classical signal un-mixing problem was explained. Empirical modal decomposition (EMD) [Huang et al., 1998] is a single-channel source separation technique that ideally is able to extract convoluted mixtures, as well as linear mixtures. The method is a geometrical based process for single-channel source separation which in some special circumstances, is successfully able to separate even non-stationary or nonlinearly mixed sources. Components extracted from EMD out of the signal represent embedded oscillatory trends in the original signal. EMD in its initial form suffers from frequency leakage and aliasing between components [Huang et al., 1998]. As an extension, an ensemble of EMDs (EEMD) is proposed and is more common for blind source separation applications. EEMD introduces additional noise to the signal and perform EMD procedure, and repeat these steps multiple times. By averaging EMD results, final components are found. In this study, EEMD is being used for extracting the vehicle dynamic response out of the mixture. Methods 1 and 2 will be performed and discussed further in Section 3.5.

3.3.4 Source Separation on the Linear Mixture

Following the implementation of one of the methods above, the residual signal is a linear mixture of two sources, y_k^{rgh} and y_k^{brg}, as shown in Equation 3.4. At this point, the goal is to extract the bridge response from this signal to enable SID. BSS

techniques for linear/static mixtures are thoroughly studied in different scenarios [Sadhu et al., 2017, Cichocki and Amari, 2002, Choi et al., 2005, Hyvärinen and Oja, 2000]. Second order blind identification (SOBI) [Tong et al., 1990, Belouchrani et al., 1997] is a successful BSS technique for separation of linear mixtures, especially for spectrally uncorrelated sources. The general mathematical description of a linear mixture is demonstrated in Equation 3.6.

$$x(t) = As(t) + \sigma(t) = y(t) + \sigma(t) \tag{3.6}$$

where A is a constant mixing matrix, $s(t)$ is a vector matrix of sources and $x(t)$ is a vector matrix of mixed signals. $\sigma(t)$ is also the additive noise in the observations. SOBI assume source uncorrelatedness, i.e., $R_s(\tau)$ is diagonal. In addition, for simplicity, the covariance matrix of the sources is presumed to be an identity matrix. The mathematical process is shown at the flowchart presented in Figure 3.4. In the first step, a whitening matrix W should be calculated to diagonalize the observation covariance matrix. In the second phase, unitary matrix U shall be found to satisfy $R_z^w(\tau) = UR_x(\tau)R_z^w(\tau)$. Given W and U, the mixing matrix can be found as $A = W^{-1}U$.

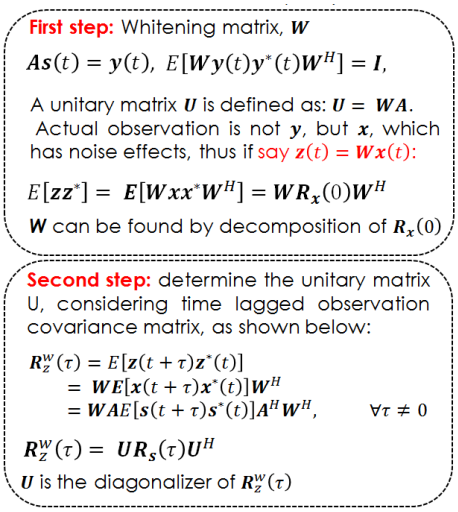

Figure 3.4: SOBI process flowchart

In the SOBI formulation, τ is an arbitrary time-lag. For a more robust solution, a set of time-lags is recommended [Belouchrani et al., 1997] to be considered for diagonalization. In this manner, the unitary matrix U that maximally diagonalizes all time-lagged covariance matrices in the set, is selected. In this study, SOBI is applied to separate the bridge vibrations from the road surface effects so that STRIDEX can be implemented as illustrated in Figure 3.2.

3.4 Generation of Vehicle Scanning Data

3.4.1 Bridge Finite Element Analysis

A $500m$ long bridge with rigid constraints at both ends is studied to evaluate the performance of the proposed methods. The criteria for selecting the bridge model are as follows: (1) maximum consistency in modal characteristics with the real-world long-span bridges, (2) simplification of the analysis, and (3) generalization of the model. The goal is to identify modal properties of this bridge from signals collected by a mobile sensor network comprised of eight vehicles as shown in Figure 3.5. The bridge is numerically modeled with elastic beam elements with 1728Kg nodal mass at each DOF, $17.28m^2$ cross-sectional area, and $85.81m^4$ moment of inertia. These characteristics are set in a way that the bridge shows realistic modal properties (i.e., operational natural frequencies, mode shapes, and damping ratios) compared to existing bridges [Abdel-Ghaffar and Khalifa, 1991, Weng et al., 2008]. Therefore, the model yields four natural modes at 0.1357Hz, 0.3714Hz, 0.7213Hz, and 1.1710Hz for the bridge. Simultaneously, three different road surface cases are analyzed: sinusoidal, expansion joints, and random. The bridge is excited by random white noise acting on nine point equally spaced along the bridge to simulate collective effect of random ongoing traffic. Numerical analysis of the bridge is performed in *OpenSees* finite element (FE) program [McKenna et al., 2000]. The damping for the first and

sixth modes are set as 2% using Rayleigh's method. Numerically, the model has been discretized into $10,000$ degrees of freedom, so will be called as $10K$ DOF model. As demonstrated in Figure 3.5, the sensing scenario consists of eight vehicles, each traveling 70% of the bridge span. Half of the vehicles travel right-to-left and the other half go the opposite. The vehicles travel with $2.5\frac{m}{s}$ velocity. This low speed has set in order to minimize excitations of the vehicle suspension system, as suggested in Siringoringo and Fujino [2012], Yang and Chang [2009]. Note that the vehicles shown in Figure 3.5 are located in different lanes to demonstrate the vehicle layout possibilities, however, since the 2D model of the bridge is considered, torsional modes are not estimated in this study. In these figures (and many other figures in this chapter), the x-axis is labeled by the number of the DOF within the length of the bridge from the numerical model. In fact, DOFs associate with different locations over the modeled bridge.

In order to produce signals collected by vehicles from the vehicle-bridge interaction (VBI), the approach is to first, produce vehicle input as shown in Equation 3.4 and then, pass the input through a two DOF vehicle quarter-car model to generate its response. In Equation 3.4, the vehicle input contains two components: bridge response, and roughness displacement at vehicle locations. For the bridge part, at the end of the FE analysis, a dense matrix of the bridge response at all 10K DOFs and time steps is computed. Next, for each vehicle, the values of bridge response at some DOFs and times are collected in accordance to the moving vehicle locations at any time. After finding a vector of the bridge response according to the location, corresponding roughness displacements are added location-wise to complete vehicle input generation phase. Once the compounded input signal is generated, the vehicle is subjected to it for vehicle response simulation. Figure 3.6 shows a displacement time signal felt by one of the vehicles while traveling over different types of road profiles.

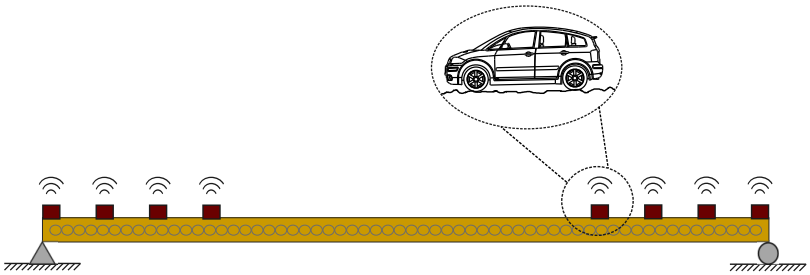

(a) side view of the sensing scenario

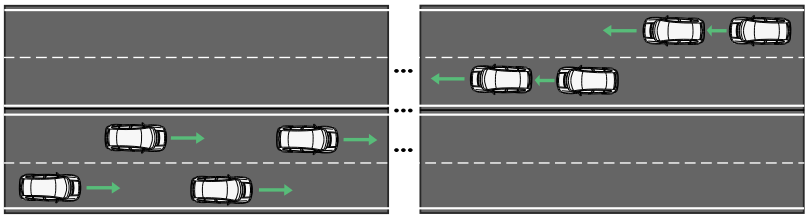

(b) Illustrative plan of the sensing scenario

Figure 3.5: Sensing vehicles layout

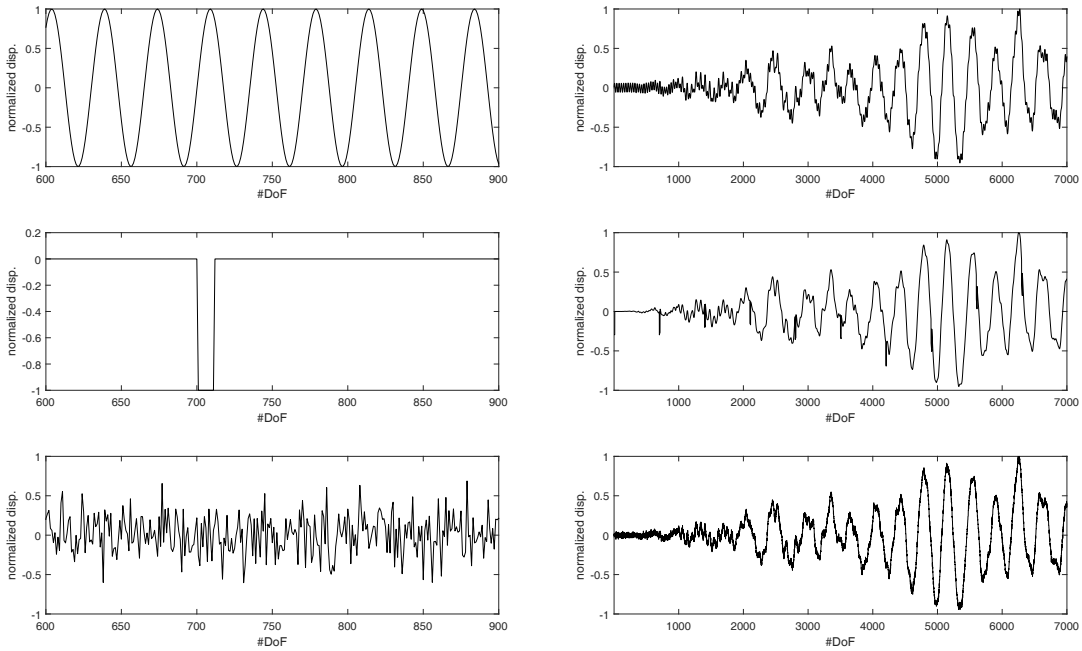

Figure 3.6: Left) Road roughness profile, Right) Total displacement felt by tires. From top to bottom: sinusoidal, expansion joints, and random white noise roughness profiles.

Three roughness patterns are investigated to examine robustness of the suggested methods. The first is a simple sinusoidal function; the second is a random white noise sequence, and the last is an expansion joint (EJ) model consisting of a white noise

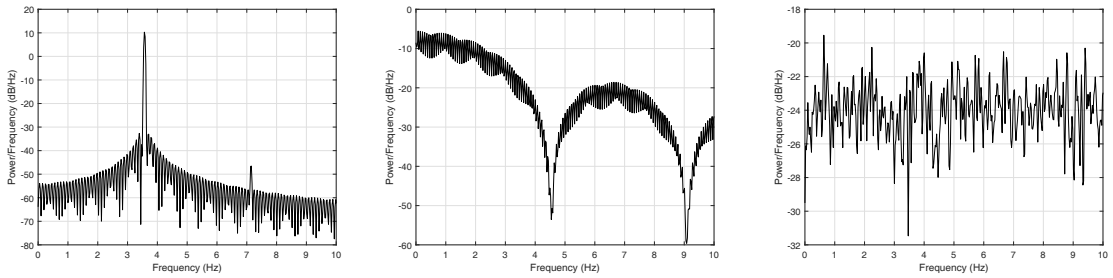

(a) Sinusoidal roughness (b) Expansion joints roughness (c) Random roughness

Figure 3.7: DFT of roughness cases - (b) indicates high amplitude fluctuations, will be propagated later

signal with a series of impulses (0.5 meter wide drops). The sinusoidal roughness is selected due to its simplicity in frequency domain, to verify the methods plausibility. The second case is an estimation of a real pavement profile and the latest is designed to simulate bridge expansion joints. This case also can be a representation of any possible road obstacles, such as potholes or speed bumps. In the following sections, the third pattern will be noted as EJ for brevity. The Welch's power spectral density (PSD) functions of the roughness profiles are also shown in Figure 3.7. The PSD of sinusoidal roughness shows a single spike, while two other cases have more complex frequency representations. Note that in the PSD of the expansion joints case, high energy fluctuations are superimposed over a relatively smooth hill series. This effect is intrinsic caused by the sudden drops in the time signal, and will be propagated and observable later.

Note that in Figure 3.5 the mobile sensors are synchronized and start collecting data simultaneously. In addition, roughness extraction using SOBI needs at least two channels of data from the same portion of the bridge scanned by each vehicle to produce two sources. These signals do not need to be synced. As a result, at least one addition mobile sensing data for each vehicle path is needed. These additional measurements can be collected before or after the main experiment (synchronized data collection of eight vehicle, Figure 3.5), resulting minimal operational difficulties.

3.4.2 Simulation of the Vehicle System

After generating the displacement input of the vehicles, these vectors are applied to a quarter-car model of the vehicle, which is a simplified and common model of the vehicular suspension system. Two factors are important for vehicle properties: frequency band separation between vehicle and the bridge, and relatively low damping for the vehicle. The first is a common preference for BSS methods, such as EEMD. In fact, as per Rilling and Flandrin [2008], EEMD is not able to separate harmonics with frequency ratio of greater than 0.6 (small frequency over the large frequency). The second criterion also enables the SID of the vehicle in the preprocessing phase. Qualitatively, for long-span bridges, stiff cars and for short bridges, flexible cars are appropriate choices in terms of frequency bands separation, For example, for a bridge with frequencies in the range of 8 - 25 Hz inspected by a vehicle with a frequency of 4 Hz or below, EEMD would successfully separate the vehicle dynamics. To demonstrate this approach, a vehicle with properties shown in Table 3.1 is considered. The dynamic response of the vehicle is assumed to remain linear throughout data collection. In the following section, another vehicle, with more common dynamical properties is analyzed. Note that these examples are generated using a generic vehicle model and are presented to validate the proposed methods; this is not a comprehensive report on how vehicle parameters influence identification results. The quarter-car suspension model is attached to the ground via a point, meaning that the tire touches every samples of the displacement input signal.

The quarter-car model for the vehicle is simulated using a state-space model with inputs linked to the road profiles as shown in Figure 3.6. The simulation outputs for three roughness profiles are shown in Figure 3.8 (plots show vehicle responses at both DOF's, tire and cabin levels).

The figure shows that the vehicle response of the vehicle under identical bridge load cases, is highly sensitive to the road roughness profile. In the next step, these

Table 3.1: Vehicle properties

Property Name	Value	Units
Unsprung Mass	49.8	Kg
Sprung Mass	466.5	Kg
Tire Damping	0.0	Ns/m
Suspension Damping	1400	Ns/m
Tire Stiffness	720	kN/m
Suspension Stiffness	1,800	kN/m
Fundamental Frequency	5.14	Hz

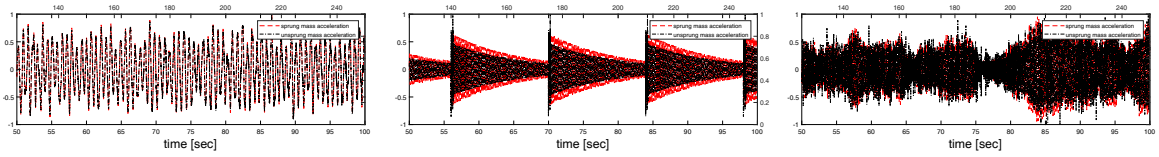

(a) Sinusoidal (b) Expansion joints (c) Random

Figure 3.8: Vehicle normalized outputs resulted from simulation

vehicle responses are used as the input for the separation phases and will be processed further to extract bridge modal properties.

3.5 Extraction of Bridge Vibrations from Vehicle Scanning Data

3.5.1 Method 1 - Signal Deconvolution with FRF

In general, the problem can be revisited as two cascaded blocks; first a bridge which is responding linearly to ambient random loads; the second, a vehicle which is excited by both the instantaneous vertical vibrations of the bridge as well as the road surface roughness, as illustrated in Figures 3.1 and 3.5.For vehicle simulation, the properties shown in Table 3.1 has been introduced. The objective in this section is to remove the effect of the vehicle suspension system on the signal and retrieve the vehicle input, which is a linear mixture of other sources. As the most direct approach, deconvolution of vehicle output using vehicle frequency response function is examined. FRF is a

function of system dynamic properties and has to be identified in advance, knowing that the existing conditions and properties of vehicles are different. With this in mind, a preprocessing phase is adopted to identify the vehicle using output-only SID methods.

Vehicle System Identification and Frequency Response Function

Output-only system identification is a well-studied field and there are many successful methods that can identify linear systems under ambient random loads. A toolsuite is developed by Chang and Pakzad [2013b] that has integrated some of these algorithms for SID. In the application of vehicle SID, it has been assumed that the vehicle response is recorded at both degrees of freedom (tire level and the cabin) while it is passing over a rough pavement with a random Gaussian pattern. Figure 3.9 shows the results of vehicle identification using its ambient response under random roughness. Exact natural frequencies of the vehicle are 5.14 Hz and 36.78 Hz. The identified frequencies shown in the table match well with these natural frequencies.

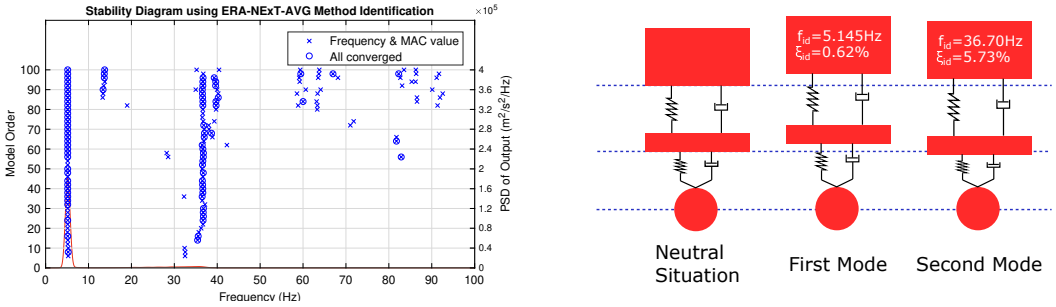

Figure 3.9: vehicle identification results - SMIT package outputs

The next step is to construct the vehicle FRF from identified characteristics found in the previous part. For this purpose, Equations 3.7 and 3.8 below are used [Bilošová, 2011]:

$$[\alpha(\omega)] = \left[K + i\omega C - \omega^2 M\right] \tag{3.7}$$

$$\alpha_{jk}(\omega) = \sum_{r=1}^{N} \frac{\Phi_{rj}.\Phi_{rk}}{\Omega_r^2 - \omega^2 + 2i\omega\Omega_r\xi_r} \tag{3.8}$$

where α_{jk} is the FRF that maps an input load at DOF j to the response at DOF k. Φ's are mode shapes and Ω_r is the undamped frequency of mode r. Equation 3.8 produces the vehicle FRF which is useful to find the vehicle input from its response collected in the cabin (can reproduce the vehicle input). Using this equation, the corresponding FRF is generated to be used for deconvolution, shown in Figure 3.10. As pointed out, the first frequency spike happens at $5.142Hz$ which is very close to the actual frequency of the car.

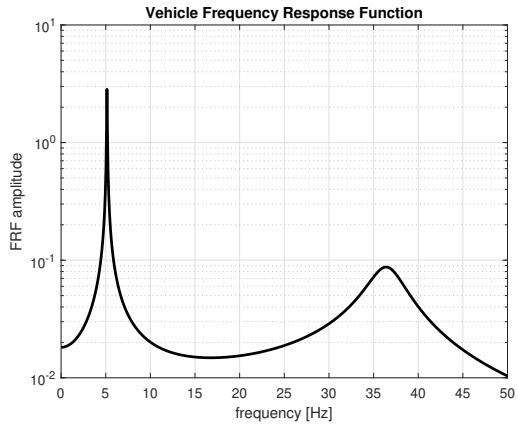

Figure 3.10: vehicle FRF from inputs at tire level to response inside the room

Note that the transfer function can be derived in closed-form as well if the manufactured properties of the vehicle is available. For instance, Sun et al. [2001] and Bogsjö et al. [2012] have provided two sets of equations for the transfer function of the sprung and unsprung DOF's of a vehicle. Using the transfer function $H(\omega)$ (FRF), simulation outputs can be deconvolved by Equation 3.5 via element-wise division of the discrete Fourier transform (DFT). Figures 3.11 and 3.12 show the results of deconvolution using the identified FRF.

Figure 3.12 shows that after deconvolution, the vehicle frequency content has been perfectly removed (the sharp spike around $5Hz$). In addition, a comparison of time signals in Figures 3.8b and 3.11b (and other cases with less clarity) shows that the

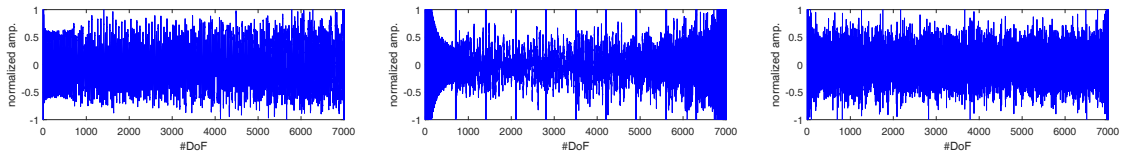

(a) Sinusoidal (b) Expansion (c) Random

Figure 3.11: Time signals after deconvolution

impulse effects caused by roughness shocks in the vehicle response have also been discarded. The remaining signal is a linear mixture of two sources; bridge vibrations and roughness profile displacements. The next step is to apply second order blind identification (SOBI) to separate these sources and extract the bridge vibrations.

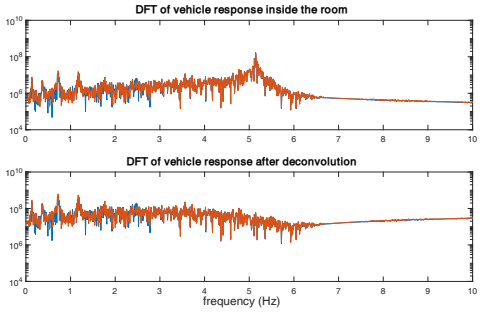

Figure 3.12: DFT of signals before and after deconvolution using FRF for random roughness

3.5.2 Method 2 - Signal Deconvolution with EEMD

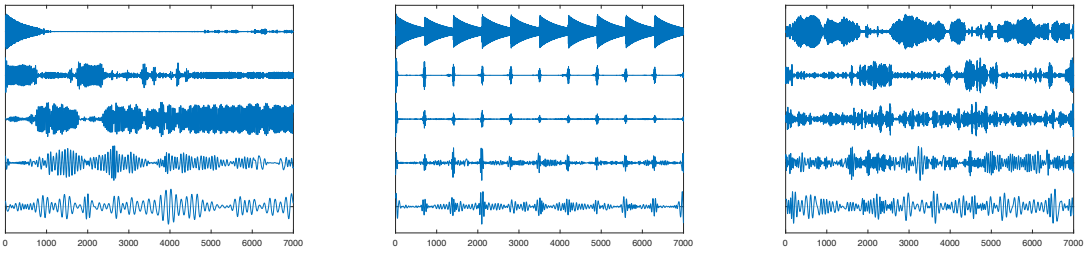

(a) Sinusoidal roughness (b) EJ roughness (c) Random roughness

Figure 3.13: IMFs in time domain

In this section, EEMD is applied to eliminate vehicle effects. Figure 3.13 shows the oscillatory components of the signal called intrinsic mode functions (IMF). IMFs are

the building components of a mixed signal that are extracted by the EEMD algorithm [Huang et al., 1998]. In summary, EEMD algorithm detects the most major building oscillation in a mixed signal by finding the envelope of the time signal. Then the major oscillation which is the first IMF is removed from the original signal and the process is repeated on the remaining signal to extract all IMFs. The frequency representation of IMFs are presented in Figure 3.14. The first IMF is able to capture vehicle effect and is presented in both time and frequency domains. This vehicle extraction is ideal for the case with EJ roughness, shown in Figure 3.14b, yet is not as perfect for two other cases. Figure 3.14a and 3.14c show traces of the vehicle response in their second IMF as well (frequency content around $5Hz$ is high). Therefore, in order to remove the vehicle effect from the signal, two first IMFs are subtracted from the original signal; the resultant signals are represented in Figure 3.15. The deconvolution using EEMD could not perfectly remove the vehicle frequency content, as shown in Figure 3.15, however, the remainder contains considerably less energy now. It will be seen in the following sections that despite this imperfect deconvolution, it is adequate for bridge modal identification purposes.

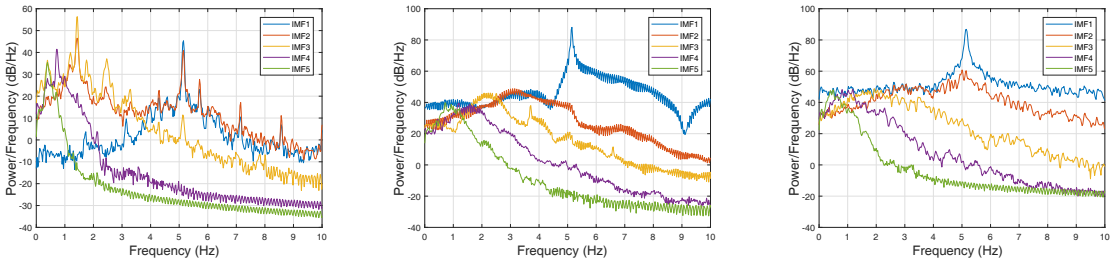

(a) Sinusoidal roughness (b) EJ roughness (c) Random roughness

Figure 3.14: IMFs in frequency domain

Note that the method is easier to perform compared to FRF method, since in this approach, there is no need for a preprocessing step for identifying the vehicle in advance. In fact, this method gives an estimate of the pure vehicle response (which is equivalent to the vehicle identification) as one of the extracted IMFs. A drawback

of this method is its inability to extract closely-spaced frequencies [Flandrin et al., 2004]. However, in a general setting, the frequency contents of the vehicle and the bridge may overlap. Thus, while EEMD is advantageous in its ease of use, it is not a universal solution.

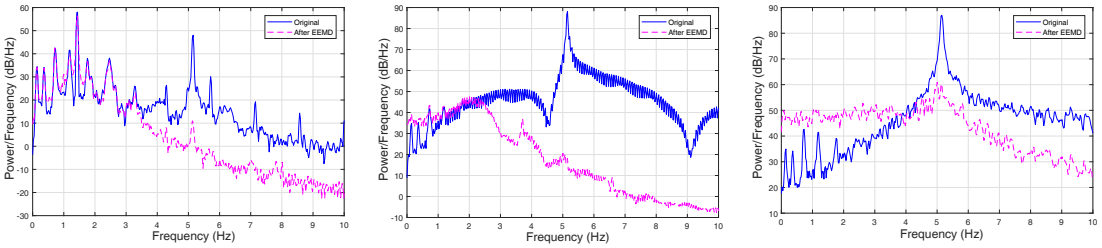

(a) Sinusoidal roughness (b) EJ roughness (c) Random roughness

Figure 3.15: Original signal before and after EEMD

In this case, the spatial frequency contents of the roughness cases are located mostly within the same region as the bridge frequency content and EEMD was not able to extract them as a separate source because of its disability for extracting contents with closely-spaced frequencies. Thus, for roughness separation (regardless of vehicle separation method), an extra step is necessary.

3.5.3 SOBI for Linear Un-mixing

Second order blind identification (SOBI) [Poncelet et al., 2007] is a method for unmixing linearly mixed signals. In this problem, the remaining sources, bridge vibrations and road profile roughness displacements are assumed to be unknown, however, some assumptions regarding them hold, such as being uncorrelated. The SOBI algorithm is implemented in MATLAB and used for separating roughness and bridge contents of the signals derived from deconvolution. Results of SOBI applied on outputs of both methods are shown in Figures 3.16 and 3.17 (bottom plots show the extracted source corresponding to the bridge only). SOBI is successful in diminishing roughness-induced peaks from the signal in both methods. The remaining signal is bridge vi-

brations and can further be utilized for system identification using STRIDEX. Note that the PSD of the signal resulted from FRF (Figure 3.16) has higher spectral resolution comparing to the other approach. This is because that in the FRF method, there is a possibility to enhance the deconvolution quality by refining the frequency range. However, it has been realized by authors that the technique is insensitive in the EEMD method.

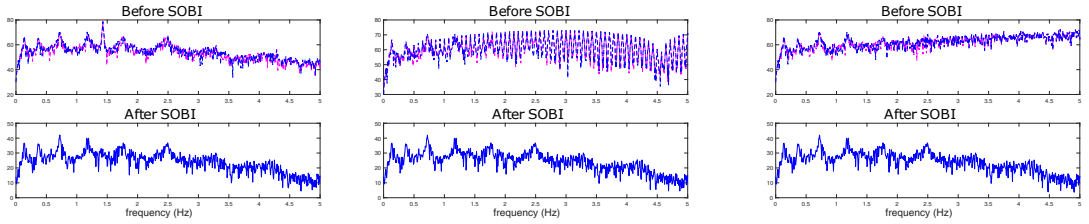

(a) Sinusoidal roughness (b) EJ roughness (c) Random roughness

Figure 3.16: SOBI on FRF output

To summarize, throughout these steps, the signal collected by a moving vehicle over a bridge has been processed to extract the bridge vibration signal. In the next step, these signals are analyzed by the system identification algorithm, STRIDEX, for bridge modal identification. Note that while the extraction approaches discussed were applied on the channels individually, STRIDEX can operate on multiple sensor channels simultaneously.

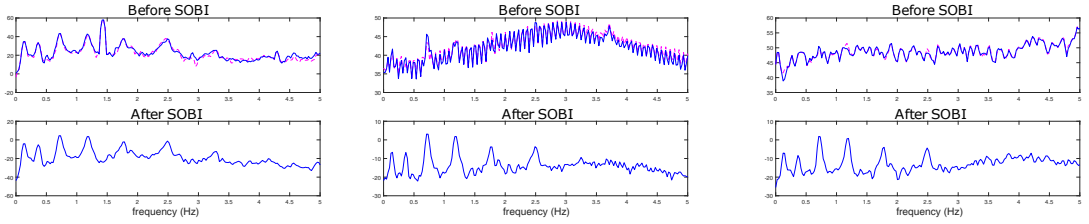

(a) Sinusoidal roughness (b) EJ roughness (c) Random roughness

Figure 3.17: SOBI on EEMD output

3.6 Bridge Modal Identification

In this simulated case, eight vehicles travel over a bridge modeled by 10K degrees of freedom. Each vehicle trip (one direction) scans 7K of DOFs in one direction as presented in Figure 3.5a. In this section, given extracted bridge dynamic vibration signals from mobile sensors, the procedure of STRIDEX [Matarazzo and Pakzad, 2018] for bridge system identification is performed.

The methods create many outputs among which, mode shapes were selected manually, which was a tedious task [Matarazzo and Pakzad, 2018]. As a contribution of this study, an algorithm is proposed in Appendix B to do the process of mode selection and superposition in an automated way and is implemented here. Identified modal parameters from this algorithm are shown in Figure 3.18.

Table 3.2: Identified frequencies

values in Hz		*EEMD+SOBI*			*FRF+SOBI*		
Mode ID	**Actual**	Sinusoidal	EJ	Random	Sinusoidal	EJ	Random
1	**0.1357**	0.1345	0.1343	0.1366	0.1360	0.1354	0.1361
2	**0.3714**	0.3689	0.3689	0.3677	0.3691	0.3687	0.3689
3	**0.7213**	0.7218	0.7195	0.7204	0.7214	0.7227	0.7204
4	**1.1710**	1.1832	1.1804	1.1861	1.1836	1.1850	1.1782

Table 3.3: Identified damping ratios

values in %		*EEMD+SOBI*			*FRF+SOBI*		
Mode ID	**Actual**	Sinusoidal	EJ	Random	Sinusoidal	EJ	Random
1	**2.00**	3.26	1.49	2.04	4.30	3.91	4.18
2	**0.80**	0.92	0.76	0.94	0.82	0.78	0.84
3	**0.60**	0.69	0.55	0.14	1.59	2.00	0.70
4	**0.70**	0.95	0.32	0.35	0.90	1.46	0.31

3.6.1 Modal Property Results

Tables 3.2, 3.3 and 3.4 show natural frequencies and damping ratios comparing to the actual values, and modal assurance criteria (MAC) values respectively. MAC is an

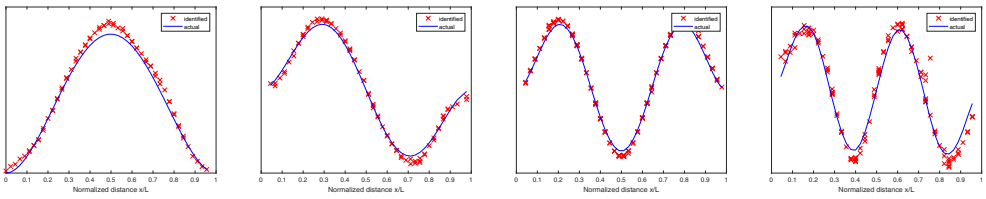

Case A: STRIDEX output on EEMD+SOBI with sinusoidal roughness

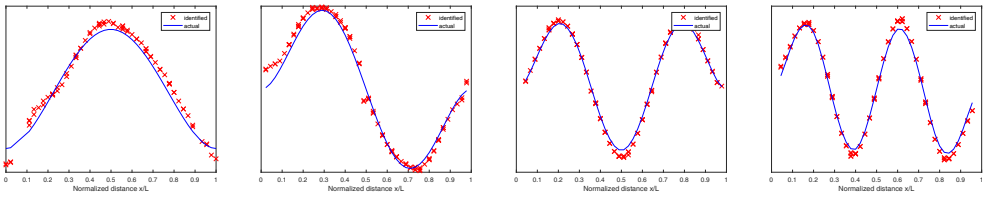

Case B: STRIDEX output on EEMD+SOBI with WN+EJs roughness

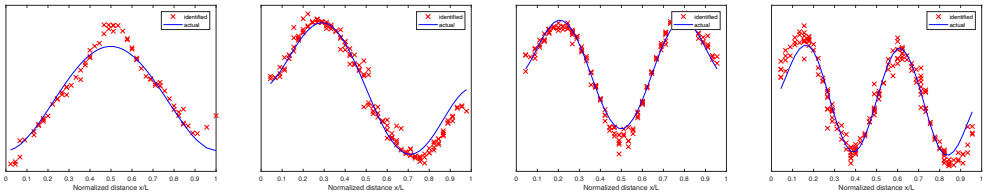

Case C: STRIDEX output on EEMD+SOBI with random roughness

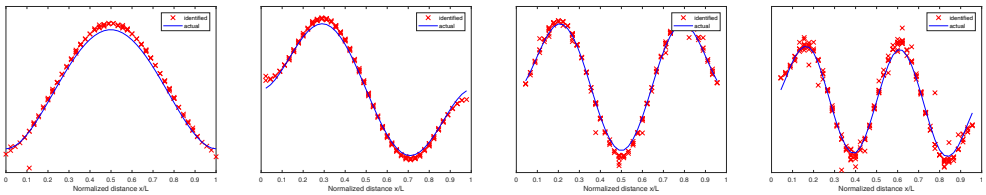

Case D: STRIDEX output on FRF+SOBI with sinusoidal roughness

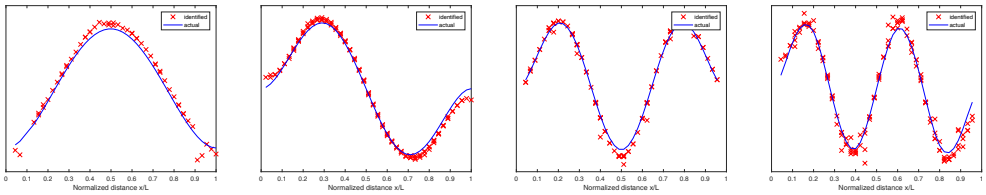

Case E: STRIDEX output on FRF+SOBI with WN+EJs roughness

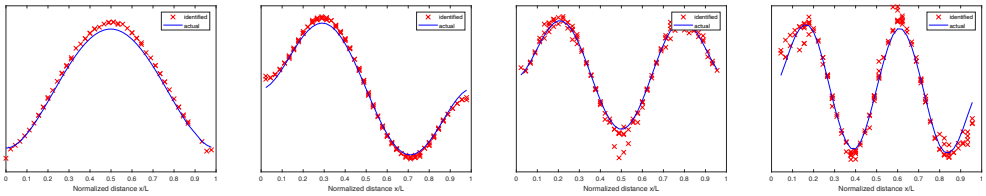

Case F: STRIDEX output on FRF+SOBI with random roughness

Figure 3.18: Model identification results

indicator of fitting accuracy between estimated mode shapes and actual ones [Pastor et al., 2012]. It is demonstrated in Table 3.2 and Figure 3.18 that both proposed

Table 3.4: Identified modal assurance criteria (MAC)

values in %	EEMD+SOBI			FRF+SOBI		
Mode ID	Sinusoidal	EJ	Random	Sinusoidal	EJ	Random
1	0.9991	0.9944	0.9829	0.9997	0.9996	0.9997
2	0.9914	0.9856	0.9640	0.9942	0.9922	0.9934
3	0.9825	0.9806	0.9612	0.9806	0.9816	0.9689
4	0.9605	0.9802	0.9443	0.9628	0.9612	0.9536

methods are successful in estimating natural frequencies and mode shapes of the bridge. As Figure 3.18 case C demonstrates, in the case of random roughness, the first mode is not ideally obtained, however, FRF method has extracted four modes from data collected over this road condition. Table 3.3 shows that the damping values are estimated precisely in most cases. Two methods (EEMD and FRF) are relatively as successful in damping estimation. In the case of the first mode identified with FRF method, damping values are not as close as others with respect to the exact values. All estimated modes have MAC value within 0.9443 to 0.9997 range (Table 3.4), which indicate the methods strength. In terms of mode shape accuracy, a comparison between methods shows that the FRF method outperformed slightly. Note that the identified MAC values are dependent to the threshold set for the automated mode aggregation algorithm (Appendix B); if lower threshold is selected, higher MAC can be found, however, the identified modes would have less resolution.

While the primary goal of this study is bridge modal identification using mobile sensor measurements, the proposed methods are able to estimate other important characteristics of the problem, e.g., the road surface roughness or the vehicle dynamical properties. These capabilities are discussed and presented in Appendix C.

3.7 Application using Mechanical Properties of Commercial Vehicles

Regular vehicles commonly have a frequency range between 0.5 Hz to 1.5 Hz, as recommended by Olley Criteria [Milliken et al., 2002] for a comfortable ride. This frequency range is highly possible to overlap with bridge frequency band. In fact, some special types of automobiles, e.g., heavy trucks, bicycles and sports cars [Giaraffa, 2017, Esmailzadeh and Taghirad, 1995, Champoux et al., 2007] have high fundamental frequency close to the one derived from Table 3.1. The proposed methods work best when the vehicle's frequency do not overlap with the bridge frequency band of interest. The vehicle with mechanical properties shown in Table 3.1 has a fundamental mode with about 5 Hz frequency. Therefore, such a stiff vehicle is perfectly suitable for sensing long and flexible bridges with first few natural frequencies below 3 Hz. In contrast, the fundamental frequency of a commercial car is about 1.0 Hz which is a good match for shorter and stiffer bridges with fundamental frequency above 2.0 Hz. In this section, a more common vehicle property set as shown in Table 3.5 is considered to investigate the case of an overlapping frequency (The properties are scaled for a unit sprung mass). Note that in this study, the scope considers flexible bridges with stiff and commercial vehicles to emphasize the impact of various road profiles as well as vehicle types on bridge modal identification. However, the generality of the methods with respect to the bridge length has also been verified by considering shorter bridges (e.g. Appendix A). By eigenvalue analysis of the vehicle properties shown in Table 3.5, the natural frequencies are calculated as $1.64Hz$ and $11.01Hz$. For the brevity, the analyses plots are only shown for the case of random roughness pattern. However, identification results for all three cases are illustrated.

First, the vehicle deconvolution is performed. In the FRF method (Method 1), the frequency representation of the signal before and after deconvolution is shown

Table 3.5: Common vehicle properties

Property Name	**Value**	**Units**
Unsprung Mass	0.162	Kg
Sprung Mass	1.0	Kg
Tire Damping	0.0	Ns/m
Suspension Damping	1.86	Ns/m
Tire Stiffness	643	N/m
Suspension Stiffness	128.7	N/m
Fundamental Frequency	1.6	Hz

in Figure 3.19. Note that the vehicle transfer function was identified using output-only methods, as explained before. A similar task is done in EEMD (Method 2) by subtracting corresponding IMFs from the original signal to remove vehicle effects. EEMD IMFs are presented in both time and frequency in Figure 3.20. The second IMF shows the vehicle content at $1.64Hz$, and is removed from the original signal. The next step is to extract roughness-induced vibrations using SOBI. Results for both methods are shown in Figure 3.21 (Top plots show SOBI inputs, while bottom ones show the extracted bridge vibration source). Boxes in the plots are pointing to the fundamental frequency of the vehicle. Since the bands are closely spaced, both methods were not completely able to remove the vehicle content. However, the content is significantly weakened and is suitable for the bridge identification purposes, as shown in Figure 3.22 and Tables 3.6 to 3.8.

The identification results show accurate estimations of the mode shapes and natural frequencies, promising that the suggested methods are suitable for more general types of vehicles. A comparison between the results of this vehicle and the previous one indicate that as expected, the frequencies were estimated more accurately in the previous case. In particular, the identified properties of the first mode (frequency, damping ratio, and MAC value) are less desirable. An explanation for this observation is that since the energy carried by the first mode is less than others (lower power compared to other peaks in PSD plots (Figure 3.21)), it is affected more by

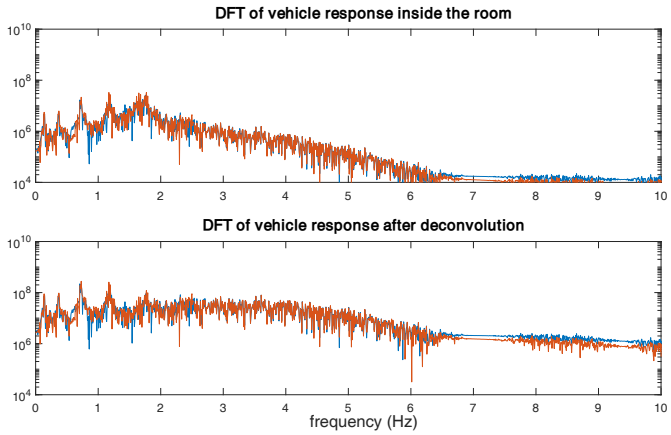

Figure 3.19: FRF deconvolution on common vehicle

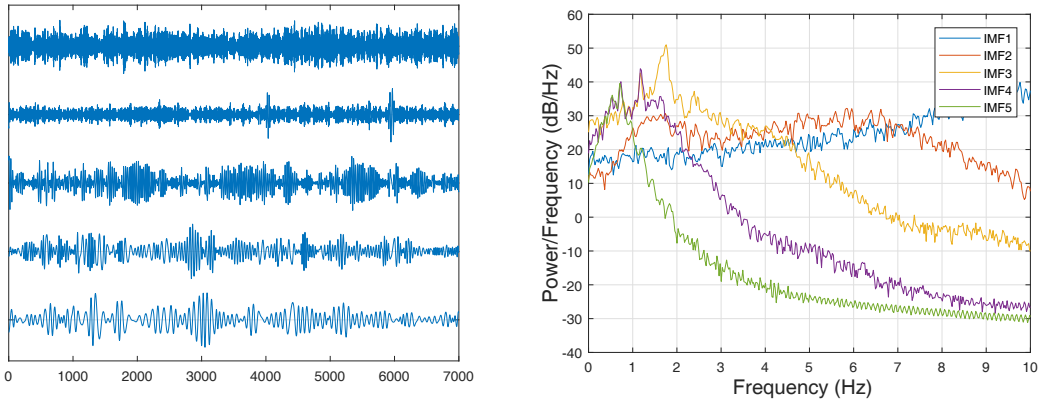

Figure 3.20: EEMD results on common vehicle

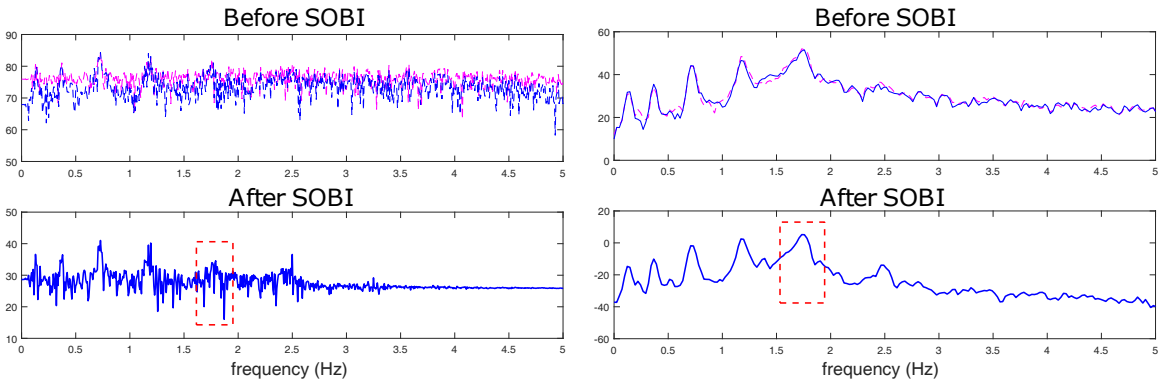

Figure 3.21: SOBI on common vehicle

the vehicle contamination. The range of MAC values in Table 3.8 is 0.9656 to 0.9987 which is desirable. By comparing Figure 3.17 and Figure 3.21, it is noticeable that

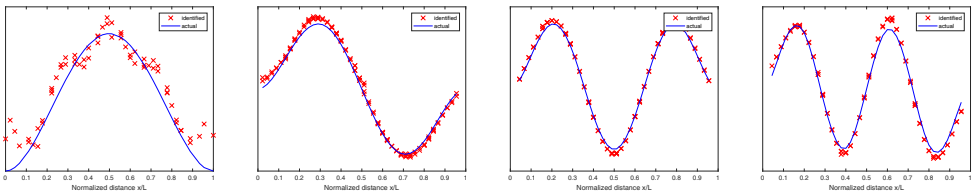

Case A: STRIDEX output on EEMD+SOBI with sinusoidal roughness

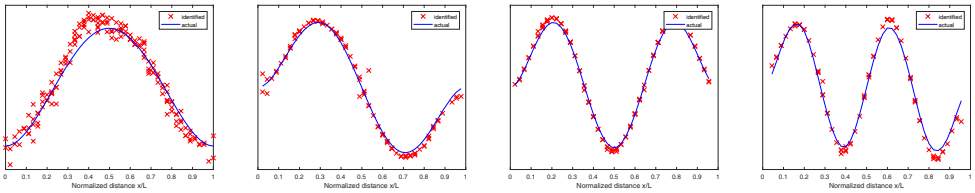

Case B: STRIDEX output on EEMD+SOBI with WN+EJs roughness

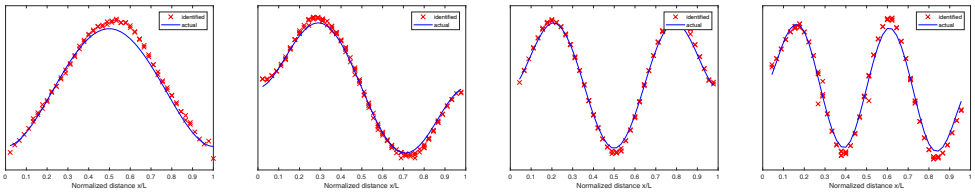

Case C: STRIDEX output on EEMD+SOBI with random roughness

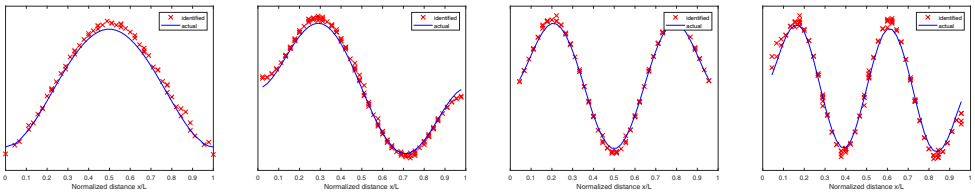

Case D: STRIDEX output on FRF+SOBI with sinusoidal roughness

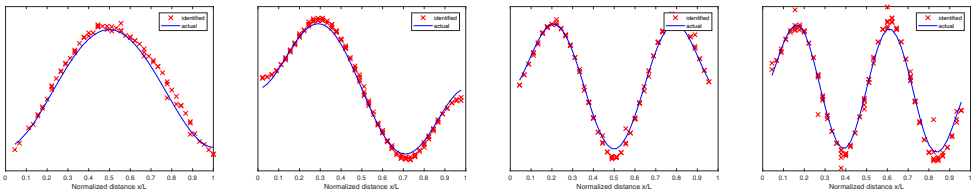

Case E: STRIDEX output on FRF+SOBI with WN+EJs roughness

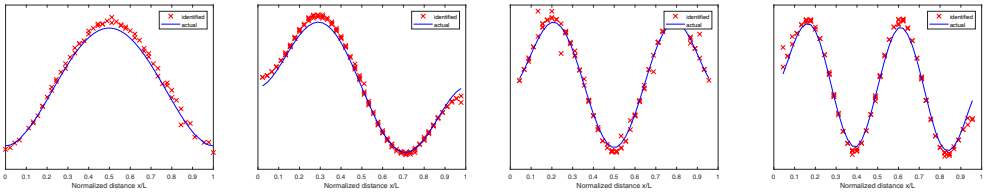

Case F: STRIDEX output on FRF+SOBI with random roughness

Figure 3.22: Modal identification results - common vehicle

the first peak is wider in the second case. This wideness results in very high estimated damping ratios for the first mode, as shown in Table 3.7. The relatively lower accuracy of this case compared to the previous case is originated as a result of the

frequency band proximity issue and was expected.

Table 3.6: Identified frequencies using common vehicle

values in Hz		*EEMD+SOBI*			*FRF+SOBI*		
Mode ID	**Actual**	Sinusoidal	EJ	Random	Sinusoidal	EJ	Random
1	**0.1357**	0.1286	0.1250	0.1381	0.1423	0.1372	0.1404
2	**0.3714**	0.3686	0.3684	0.3688	0.3696	0.3696	0.3695
3	**0.7213**	0.7213	0.7213	0.7207	0.7196	0.7209	0.7211
4	**1.1710**	1.1800	1.1809	1.1801	1.1791	1.1923	1.1800

Table 3.7: Identified damping ratios using common vehicle

values in %		*EEMD+SOBI*			*FRF+SOBI*		
Mode ID	**Actual**	Sinusoidal	EJ	Random	Sinusoidal	EJ	Random
1	**2.00**	14.44	N.A.	7.14	15.85	14.36	14.95
2	**0.80**	0.70	0.82	0.40	1.01	1.43	1.02
3	**0.60**	0.47	0.72	0.29	0.45	0.77	0.54
4	**0.70**	0.37	0.46	0.51	0.33	1.11	0.38

Table 3.8: Identified modal assurance criteria (MAC) using common vehicle

values in %	EEMD+SOBI			FRF+SOBI		
Mode ID	Sinusoidal	EJ	Random	Sinusoidal	EJ	Random
1	0.9724	0.9883	0.9977	0.9987	0.9969	0.9987
2	0.9924	0.9921	0.9933	0.9920	0.9918	0.9909
3	0.9836	0.9822	0.9812	0.9836	0.9783	0.9726
4	0.9769	0.9779	0.9760	0.9743	0.9709	0.9656

3.8 System Identification using Approximated Vehicle Transfer Function

As a preprocessing part of the proposed method using FRF, sensing vehicles have to be identified in advance, as shown in Figure 3.2. For this identification, a complete description of the vehicle is needed for producing vehicle transfer function, hence the

vehicle responses at both DOFs are collected and fed into the output-only SID toolbox. The need to record the vehicle response at two locations simultaneously is a potential drawback. For example, in a crowdsensing scenario, it may be impractical to retrieve data at the tire level (unsprung mass) of the vehicle. Moreover, as mentioned in the former section, common vehicle suspension systems can have similar modal properties, specifically natural frequencies and mode shapes. The mechanical characteristics of various vehicles are shown in Table 3.9, and their tabulated modal responses and their average are presented in Table 3.10. The properties shown in Table 3.9 are selected from reference vehicles commonly used in the literature, which covers a wide range of linear vehicles [Sun et al., 2001, Bogsjö et al., 2012, Florin et al., 2013, Gillespie and Sayers, 1985]. The fundamental frequency range of the vehicles also covers from 0.54 Hz to 36.78 Hz as shown in Table 3.10, which is considerable, suggesting that these mode shapes are a good representation of available automobiles. As a simple demonstration, the average mode shapes are set as the identified values in the FRF. According to Equation 3.8, natural frequencies are also needed to produce a vehicle TF, as well as the mode shapes. The frequencies can be identified from the peaks of the PSD of the vehicle response at either DOF. In this section, bridge identification is performed using averaged mode shapes for the common vehicle by using FRF method.

Table 3.9: Mechanical properties of various vehicles

	Vehicle ID					
	v1	**v2**	**v3**	**v4**	**v5**	**Units**
Suspension Stiffness	1.8e6	62.30	128.7	2.7e5	5700	N/m
Suspension Damping	1400	6.0	3.86	6000	290	Ns/m
Sprung Mass	466.5	1.0	1.0	3400	466.5	Kg
Unsprung Mass	49.8	0.15	0.162	350	49.8	Kg
Tire Stiffness	7.2e5	653	643	9.5e5	1.35e5	N/m
Tire Damping	0	0	0	300	1400	Ns/m

In addition to the natural frequencies and the mode shapes, Equation 3.8 requires

damping ratio entries. In case of linear vehicles, like frequencies, these values are also identifiable by output-only SID of the system using only one channel vibration (sprung mass accelerations). A comparison between results shown in Figure 3.23 with Figure 3.22 confirm that the approximated transfer function is as successful as the actual one for the identification purposes. Identified frequencies shown in Table 3.11 show a very good match between estimated frequencies and actual ones. Estimated dampings presented in Table 3.12 are acceptably accurate for modes 2 to 4, while the first mode still is far large. A comparison between Tables 3.7 and 3.12 show that the approximation for the mode shape slightly impacted negatively on the damping estimations. MAC values of the identified modes are also introduced in Table 3.13. The range of MAC values are as desirable as the former case, promising that the approximation is generally successful.

These results show that using an approximated mode shape, the vehicle response can be characterized sufficiently using only one sensor in the vehicle cabin. Of course, it is preferable to utilize the mechanical properties provided by the manufacturer whenever possible.

Table 3.10: Vehicle modal characteristics

	1st mode		2nd mode		Natural Frequencies	
	DOF1	**DOF2**	**DOF1**	**DOF2**	**f1**	**f2**
v1	0.73	1.00	-1.00	0.08	5.14	36.78
v2	0.09	1.00	-1.00	0.01	1.20	11.00
v3	0.17	1.00	-1.00	0.03	1.64	11.01
v4	0.23	1.00	-1.00	0.02	1.25	9.42
v5	0.04	1.00	-1.00	0.00	0.54	8.46
Average	**0.25**	**1.00**	**-1.00**	**0.03**	**1.96**	**15.33**

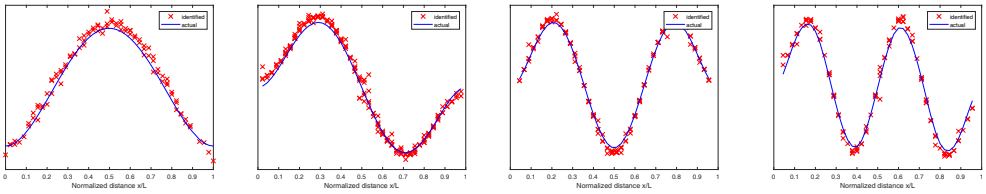

Figure 3.23: Modal identification results - approximated common car

Table 3.11: Identified frequencies using approximated common car

values in Hz		FRF+SOBI		
Mode ID	**Actual**	Sinusoidal	EJ	Random
1	**0.1357**	0.1324	0.1421	0.1327
2	**0.3714**	0.3687	0.3686	0.3702
3	**0.7213**	0.7211	0.7215	0.7196
4	**1.1710**	1.1861	1.1839	1.1793

Table 3.12: Identified damping ratios using approximated common car

values in %		FRF+SOBI		
Mode ID	**Actual**	Sinusoidal	EJ	Random
1	**2.00**	21.79	26.07	14.18
2	**0.80**	1.75	1.70	1.67
3	**0.60**	1.59	0.53	0.47
4	**0.70**	1.04	0.79	0.35

Table 3.13: Identified modal assurance criteria (MAC) using approximated common car

values in %	FRF+SOBI		
Mode ID	Sinusoidal	EJ	Random
1	0.9915	0.9888	0.9966
2	0.9922	0.9904	0.9893
3	0.9806	0.9737	0.9803
4	0.9722	0.9723	0.9761

3.9 Conclusion

In this study, two methods were proposed for the comprehensive bridge system identification using vehicle-carried sensor data. In the first approach, vehicle deconvolution using the vehicle frequency response function (FRF), along with second order blind identification (SOBI) extracted bridge vibration from mixed signals collected by drive-by vehicles. Empirical modal decomposition was proposed as an alternative approach for vehicle deconvolution. Throughout the extraction phase, vehicle suspension effects and roughness-induced vibrations were removed. Finally, for bridge system identification (SID), resulting signal (from either the FRF or the EEMD method) represents pure mobile sensing data and was processed by the extended structural identification using expectation maximization (STRIDEX) algorithm for bridge modal identification. Numerical case studies from a $500m$ long bridge were used to validate proposed methods.

The methods were both successful in estimating first four modes of the bridge. Modal assurance criteria (MAC) values for the estimated mode shapes from both methods were all above 0.94. In terms of the estimated frequencies, estimated values of FRF and EEMD methods had all less than 1.2% and 1.3% error from the actual values, respectively. The accuracy of the damping ratios was generally on par with traditional SID methods; in some cases, the estimates were near exact, e.g., the second mode.

In order to investigate methods' robustness to the sensing vehicle properties, a second property set (properties of common vehicles) was evaluated. Both identification methods were applied on the measured data from this vehicle. In this case, modal identification results were not considerably affected with respect to the case of the designated vehicle property. However, estimated damping ratios of the first mode were affected significantly. The possible reasons were discussed.

The EEMD-based method operates without vehicle property information. Over-

all, the FRF approach yielded more accurate SID results of the bridge. As a means to circumvent the vehicle SID phase in the FRF method, a simplified procedure was proposed to approximate vehicle transfer function using data exclusively collected from within the cabin. The results showed that this method was successful in producing accurate modal property estimate; the frequency error was at max 1.2% and the MAC values were above 0.97.

The rate at which the SHM community can incorporate information extracted from crowdsourced data depends on how its analytical tools can adopt to new, more readily available data formats, e.g., mobile sensing data. The proposed methods enable robust extraction of important bridge information using data types that are compatible with large-scale vehicles networks. An ability to turn everyday vehicle-based datasets into core SHM information fuels more regular observations on the operational behavior of the bridge, which in turn supports more frequent condition reports.

Chapter 4

Simplified Vehicle-Bridge Interaction for Medium to Long-span Bridges Subject to Random Traffic Load

4.1 Abstract

This study introduces a simplified model for bridge-vehicle interaction for medium- to long-span bridges subject to random traffic loads. Previous studies have focused on calculating the exact response of the vehicle or the bridge based on an interaction force derived from the compatibility between two systems. This process requires multiple iterations per time step per vehicle until the compatibility is reached. When a network of vehicles is considered, the compatibility equation turns to a system of coupled equations which dramatically increases the complexity of the convergence process. In this study, we simplify the problem into two sub-problems that are decoupled: (a) a bridge subject to a random excitation, and (b) individual sensing agents that are

subject to linear superposition of the bridge response and the road profile roughness. The study provides sufficient evidences to confirm that the simulation approach is valid with minimal error when the bridge span is medium to long, and the spatio-temporal load pattern can be modeled as random white noise. The latter assumption is verified using a comparative study on a random traffic network. Quantitatively, the proposed approach is over 1,000 times more computationally efficient when compared to the conventional approach for a 500 m long bridge, with response prediction errors below 0.1%.

4.2 Introduction

The problem of vehicle-bridge interaction (VBI) has been studied widely over recent years due to the broad applications spanning from fatigue analysis and bridge mobile sensing [Chen and Cai, 2007, Zhu and Law, 2015, 2016, Yang and Yang, 2018, Sadeghi Eshkevari et al., 2020b] to ride comfort and safety analysis [Zhou and Chen, 2016, Camara et al., 2019]. The complexity of the problem has resulted in a reliance on numerical modeling to evaluate research hypotheses [Yang et al., 2004b, Malekjafarian and OBrien, 2014b, Sadeghi Eshkevari et al., 2020d]. Consequently, today various numerical tools for VBI modeling are available, yet the majority are geared towards problems concerning individual vehicle dynamics, e.g., a single vehicle's interaction with a simple bridge. Recent applications on vehicle fleets and crowdsensing methods [O'Keeffe et al., 2019, Matarazzo et al., 2018] have provided insight into the wealth of SHM information that can be produced by ubiquitous mobile sensors. Such large-scale analyses call for interaction methods that can incorporate vehicular networks and everyday traffic scenarios, and are computationally efficient.

4.2.1 Crowdsensing the Built Environment with Mobile Sensors

The growing adaptation of *internet of things* technologies and connected devices in smart cities suggest a new sensing paradigm in which new information is regularly gathered from the crowd, e.g., individual smartphones, vehicular sensor networks, etc. Calabrese et al. [2010] proposed a real-time data aggregation solution for constructing a dynamic urban map of large cities using crowdsourced smartphone data. Wang et al. [2012] quantified traffic patterns and proposed management applications based on large-scale mobile phone data. Yu et al. [2015] successfully utilized smartphone sensors for structural health monitoring application due to its availability and inexpensive data acquisition. Feng et al. [2015], Ozer et al. [2015] also suggested novel applications in post-event bridge vibration analysis using stationary smartphones as sensors.

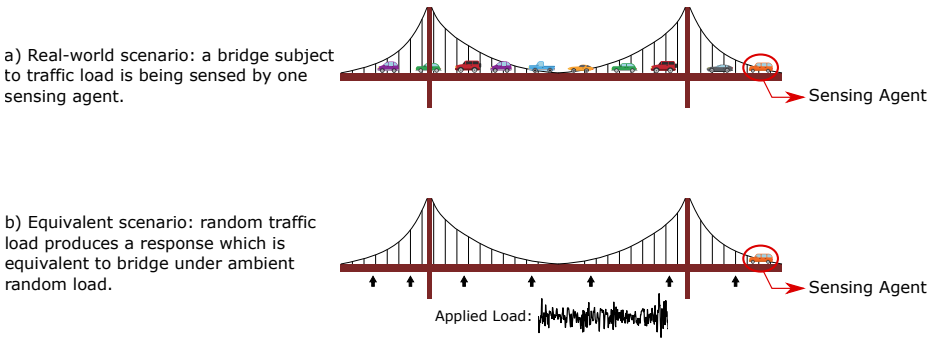

Figure 4.1: Crowdsourcing framework. The sensing agent is one (or more) particular vehicle within a large pool of crossing vehicles. The problem is equivalent to a case in which the bridge is subject to ambient random load while being scanned by the sensing agent.

Crowdsensing inherently relies on *mobile sensor networks*, which is an emerging data acquisition technique in structural health monitoring (SHM). Historically, observations of structural dynamics have been based on measurements collected by *fixed sensor networks*. Alternatively, Figure 4.1 illustrates how a vehicle can act as a sensing agent amongst bridge traffic. Matarazzo and Pakzad [2016c] presented the STRIDE

modal identification algorithm and verified that mobile sensor data was suitable for a comprehensive modal identification (frequencies, damping ratios, and mode shapes). They proposed the truncated physical state-space model as an efficient approach for representing time-space observations from a mobile sensor network. Later, Matarazzo and Pakzad [2018] presented an identification algorithm called STRIDEX to identify truncated physical model parameters, which enabled efficient and scalable modal identification using mobile sensors; the study showed that in an experimental case, one mobile sensor provided a mode shape density comparable to 120 fixed sensors. As a versatile alternative for STRIDEX, Sadeghi Eshkevari et al. [2020d], Eshkevari and Pakzad [2020b] proposed a method called MIMC to consider vibration data collected by multiple mobile sensors with uncontrolled motions which successfully identified comprehensive bridge modal properties in different simulated applications.

The idea of smartphone data crowdsourcing for bridge system identification has been recently tested on real bridges. Matarazzo et al. [2018] presented a real-world application of mobile sensors, in the form of smartphones in moving vehicles. Significant indicators of the first three modal frequencies of the Harvard Bridge were found by aggregating data from about forty bridge trips. This study shows promising results for the use of crowdsensing in bridge health monitoring. Yet further development is needed, in particular, analytical and experimental studies on mobile sensing using data crowdsourcing, to attain the sophistication and robustness of the traditional modal identification methods based on fixed sensor data.

4.2.2 Vehicle-Bridge Interaction Modeling

More practical approaches for bridge health monitoring such as crowdsensing require a computationally scalable numerical framework. A comprehensive literature review of common VBI simulation approaches is provided by González [2010]. Initially, the vehicle-bridge interaction was modeled using 1D continuous beam models subject to

simple moving loads [Frỳba, 2013] which is solvable in closed-form. By further development of computers and increasing use of the finite element method, the problem was reframed as a multi degrees of freedom (MDOF) system for the bridge interacting with simplified dynamical models of the vehicle. This approach has been broadly adopted for VBI modeling, mostly for short to mid-span bridges subject to a very limited number of vehicles with controlled motions. In this approach, once the models for the vehicle and the bridge are selected (based on required accuracy and fidelity), the dynamic equations of each component are separately built, in which the interaction forces between the vehicle and the bridge are coupled to the both sets of equations. Therefore, a numerical solver is required to solve the problem either iteratively or as a coupled system of equations.

The underlying principle of the approach, that is the interactive dynamic force acting between the vehicle and the bridge, has remained consistent throughout the literature. The uncoupled iterative algorithm is the most common method for VBI problems [Lin and Yang, 2005, Kim and Kawatani, 2008, OBrien et al., 2010, González et al., 2012, Yang and Yang, 2018]. Various versions of the algorithm have been developed based on the problem requirements, e.g., different vehicle models, single DOF, quarter-car, or half-car models as well as different bridge models with different fidelity levels (such as 2D, 3D, with or without material or geometrical nonlinearities). However, in the majority of these studies, a short- to mid-span bridge has been considered. As mentioned in González [2010], when the vehicle mass is negligible compared to the bridge mass (which is the case for medium to long bridges) and a smooth pavement is assumed, the dynamic model of the vehicle can be replaced with a moving mass model that simplifies the simulation process. Road irregularities increase the contribution of vehicle dynamics to the interaction force, which emphasize on the importance of a fully coupled model.

In the uncoupled iterative approach, the bridge model is analyzed multiple times

(once at the beginning, and at least once for each time step inside the compatibility convergence loop). In addition, as the bridge dimension grows, an accurate bridge model requires more degrees of freedom, which increases the computational costs. A limited number of studies have considered long-span bridges along with a dense vehicle network for the simulation purpose. Camara et al. [2019] recently modeled wind-bridge-vehicle interaction using the uncoupled iterative approach. The study could accurately model the system by adopting complex models for each component. The complexity of the approach implies that it requires great efforts to built such a high fidelity model, which may neither be a feasible nor cost effective solution for crowdsensing or other crude vehicle-bridge interacting scenarios. Moreover, bridge standards recommend lower dynamic factors for live loads in medium to long bridges compared to short bridges [AASHTO, 2008]; which means that the VBI interaction force is less dynamic and more similar to a constant moving load. These challenges and specifications suggest that it may not be required to use rigorous iterative solutions for VBI simulation of medium to long bridges subject to high traffic loads. This study intends to demonstrate that a simplified simulation approach inspired by the conventional uncoupled iterative algorithm [González, 2010] is able to simulate VBI problems with high accuracy and dramatically less computational effort.

Figure 4.1 shows how the same notion is applicable in the VBI simulation. This figure demonstrates a scenario of interest in which the bridge is subject to a random traffic network. The objective is to simulate the system and finally calculate the collected response of the sensing agent. In a brute-force approach, the spatial coordinates and mechanical properties of every single vehicle in the network are required to fully determine the complex model. Such an accurate information setting is quite impractical and unnecessary. Alternatively, one can simulate the collective loading effect of the vehicle network (the sensing agent excluded) by ambient random load (as shown in Figure 4.1 - b). If the spatio-temporal ambient random load is repre-

sented as a matrix $\boldsymbol{F}_0$, the conventional algorithm for simulating the VBI problem is as shown in Algorithm 4.

Algorithm 4 Conventional iterative VBI simulation.

1: **Input**: $\boldsymbol{M}_{brg}, \boldsymbol{C}_{brg}, \boldsymbol{K}_{brg}, \boldsymbol{M}_{vcl}, \boldsymbol{C}_{vcl}, \boldsymbol{K}_{vcl}, \boldsymbol{F}_0, rgh$
2: $\boldsymbol{Y}_{brg} = Newmark\beta(\boldsymbol{M}_{brg}, \boldsymbol{C}_{brg}, \boldsymbol{K}_{brg}, \boldsymbol{F}_0)$
3: **for** t = 1, $\cdots$, T **do**
4: Initiate $r := 0, r_n :=$ *some large value*
5: **while** $abs(r - r_n) < threshold$ **do**
6: $r = \boldsymbol{Y}_{brg}(t)$
7: $wv = rgh(t) + r$
8: $wv' = rgh'(t) + \boldsymbol{Y}'_{brg}(t)$
9: $y_{vcl}(t) = ODE45(\boldsymbol{M}_{vcl}, \boldsymbol{C}_{vcl}, \boldsymbol{K}_{vcl}, wv, wv')$
10: $F_t = -\boldsymbol{K}_{vcl}[2] * (y_{vcl}(t) - wv) - \boldsymbol{C}_{vcl}[2] * (y'_{vcl}(t) - wv')$
11: $R = -\boldsymbol{M}_{vcl}g - F_t$
12: $\boldsymbol{F} = \boldsymbol{F}_0$
13: $\boldsymbol{F}(t) = R$
14: $\boldsymbol{Y}_{brg} = Newmark\beta(\boldsymbol{M}_{brg}, \boldsymbol{C}_{brg}, \boldsymbol{K}_{brg}, \boldsymbol{F})$
15: $r_n = \boldsymbol{Y}_{brg}(t)$
16: $F_0 = F$
17: **Return** $\boldsymbol{Y}_{brg}, y_{vcl}$

In this algorithm, $\boldsymbol{M}_{brg}, \boldsymbol{C}_{brg}, \boldsymbol{K}_{brg}$ and $\boldsymbol{M}_{vcl}, \boldsymbol{C}_{vcl}, \boldsymbol{K}_{vcl}$ characterize mechanical properties of the bridge and the vehicle, respectively. rgh is a vector of roughness profile elevations at bridge DOFs. The algorithm performs the following steps:

1. The bridge is subjected to random ambient load $\boldsymbol{F}_0$ at different physical locations.
2. A vehicle starts moving from one side of the bridge and at each time instance, the bridge response (displacement) from the previous step in addition to the local roughness intensity (i.e., $rgh(t)$) is input to the vehicle system.
3. The vehicle response to the applied force from the previous step is then analyzed using a MATLAB ordinary differential equation (ODE) solver to calculate its displacement response (line 9 in Algorithm 4). Based on this response, the interacting force between the sensing vehicle and the bridge is calculated as: $F_t = -\boldsymbol{K}_{vcl}[2](y_{vcl}(t) - wv) - \boldsymbol{C}_{vcl}[2](y'_{vcl}(t) - wv')$ (where [2] stands for the $2nd$

DOF of the vehicle, i.e., the tire). Note that if $F_t < 0$, it is replaced with zero since it means that the vehicle lost its contact.

4. The interaction force from the vehicle to the bridge F_t upgrades the original loading matrix $\boldsymbol{F}_0$ to produce $\boldsymbol{F}$. At this location, the bridge is required to be analyzed again with the updated force matrix. Here, Newmark-β method is used for bridge dynamics analysis [Newmark et al., 1959].

5. If the difference between the updated bridge displacement and the one that was applied in Step 2 is higher than a predefined threshold, the process should be repeated from Step 2 onward by the updated bridge response. Otherwise, the vehicle moves to the next DOF on the bridge.

Step 5 in this process (i.e., the `while` loop in Algorithm 4) is expensive since it results in multiple full bridge analysis iterations within a time step. This is quite significant when the bridge is discretized with a large number of DOFs or is modeled with nonlinear elements. Figure 4.2 summarizes the approaches one can take for calculation of the sensing vehicle's measurement. In case (a), the brute-force approach is shown in which all the vehicles are coupled with the bridge.

4.2.3 Simplified Model

This study proposes a fast and accurate simulation approach for VBI problems in which: (1) the bridge span is medium to long and it is flexible, and (2) the vehicle network load is modeled as a random spatio-temporal load over the bridge span. The second condition refers to the ambient vibrations caused by a network of moving vehicles [De Roeck et al., 2000, Ren et al., 2004, Ren and Zong, 2004, Pakzad et al., 2008].

Figure 4.2b shows a simplified representation of Figure 4.1a, in which the traffic network (the sensing agent excluded) is replaced with an applied ambient white

noise load while the sensing agent is still interacting with the bridge in a coupled fashion. While this approach is significantly computationally less expensive, the coupled system still requires iterations to reach the compatibility between the vehicle and the bridge at each time step. In this study, we present an approach in which the compatibility calculations between two interacting components are not iterative, as shown in Figure 4.2c. In this approach, we posit that the dynamical effect of an individual sensing agent on a bridge response is negligible when the bridge is medium to long and the cumulative effect of other loads (the individual vehicle excluded) is significantly greater than a single vehicle. The approach is presented in Algorithm 5:

Algorithm 5 Simplified non-iterative VBI simulation.

1: **Input**: $\boldsymbol{M}_{brg}, \boldsymbol{C}_{brg}, \boldsymbol{K}_{brg}, \boldsymbol{M}_{vcl}, \boldsymbol{C}_{vcl}, \boldsymbol{K}_{vcl}, \boldsymbol{F}_0, rgh$
2: $\boldsymbol{Y}_{brg} = Newmark\beta(\boldsymbol{M}_{brg}, \boldsymbol{C}_{brg}, \boldsymbol{K}_{brg}, \boldsymbol{F}_0)$
3: **for** t = 1, $\cdots$, T **do**
4: $\quad r = \boldsymbol{Y}_{brg}(t)$
5: $\quad wv = rgh(t) + r$
6: $\quad wv' = rgh'(t) + \boldsymbol{Y}'_{brg}(t)$
7: $\quad y_{vcl}(t) = ODE45(\boldsymbol{M}_{vcl}, \boldsymbol{C}_{vcl}, \boldsymbol{K}_{vcl}, wv, wv')$
8: **Return** $\boldsymbol{Y}_{brg}, y_{vcl}$

In this algorithm, the bridge is only analyzed once at the beginning under $\boldsymbol{F}_0$. The bridge response is then linearly superimposed with rgh and then, applied to the vehicle dynamical model. In fact, the approach is similar to the constant force method proposed in González [2010]. However, in our approach the vehicle dynamics is incorporated in the vehicle response, which was not the case in a moving mass model. The approach has not been proposed or utilized previously; yet needs to be fully justified and evaluated. In the rest of this study, we first propose a theoretical proof on a simplified case of the coupled VBI problem. This part intends to demonstrate that bridge to vehicle mass and stiffness ratios are the keys to determine the coupling degree. In the next step, VBI responses of multiple bridges with different characteristics and vehicles are numerically simulated using coupled (i.e., conventional) and uncoupled (i.e., simplified) procedures and results are compared. Discussions and comparison of

the numerical results are also supplemented in the last sections.

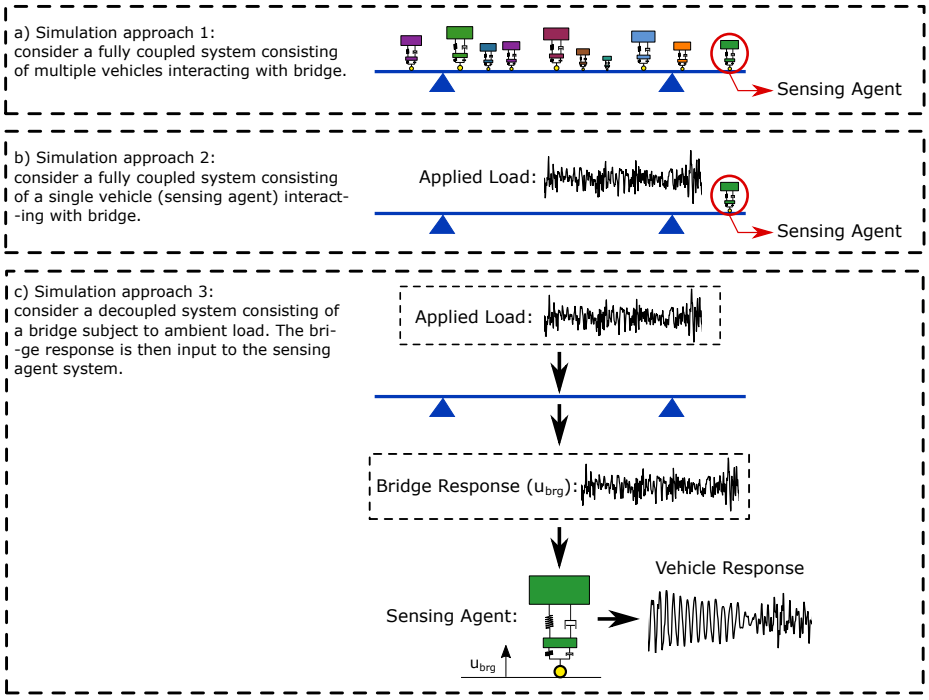

Figure 4.2: Simulation approaches: a) a complex and coupled system of a vehicle network interacting with a bridge; b) a coupled system of the sensing vehicle interacting with the bridge. The bridge is separately subject to an ambient load to capture the vehicle network's load; c) the proposed approach in which the bridge is only subject to the ambient load. The response is then applied to an uncoupled model of the sensing vehicle to produce the vehicle output.

4.3 Theoretical Approach

In this section, a closed-form theoretical proof for validity of the simplified model is presented. Generally, vehicle-bridge interaction is a complex model to be solved in closed-form, however, simplified models can be used for proof of concept [Frỳba, 2013, Yang et al., 2004b]. The objective here is to show that a coupled VBI system subject to external stochastic excitations produces bridge and vehicle responses that are very close to the responses of an uncoupled system, especially if the bridge is long and heavy. For this purpose, the mass and spring system shown in Figure 4.3 is considered in which the vehicle is located at the mid-span of the beam with no

motion and in full interaction (no damping is considered for simplicity). The random spatio-temporal load of the bridge is also lumped into an effective point load that is applied to the bridge mass. In particular, the proof intends to show that the coupling of the bridge response x_b to the vehicle interaction decays as the bridge dimensions grow.

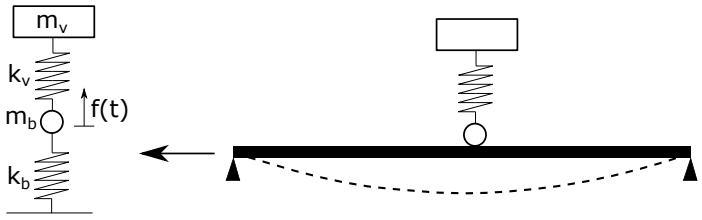

Figure 4.3: schematic of the coupled setup

From Figure 4.3, the beam is modeled as a unidirectional spring, while the vehicle is a single DOF system. The bridge spring represents the first modal stiffness of the beam. The bridge mass is lumped at the contact point of the two components. The setup constitutes a 2 DOF coupled system with the equation of motion shown in Equation 4.1. Using this simplified setup, both responses are calculated in closed-form:

$$\begin{bmatrix} m_b & 0 \\ 0 & m_v \end{bmatrix} \begin{bmatrix} \ddot{x}_b \\ \ddot{x}_v \end{bmatrix} + \begin{bmatrix} k_b + k_v & -k_v \\ -k_v & k_v \end{bmatrix} \begin{bmatrix} x_b \\ x_v \end{bmatrix} = \begin{bmatrix} f(t) \\ 0 \end{bmatrix} \tag{4.1}$$

where m_b and m_v are the bridge and vehicle masses, respectively; Also, k_b and k_v are the stiffnesses for two components. For further calculations, it is assumed that $m_b = \alpha m_v = \alpha m$ and $k_b = \beta k_v = \beta k$ in which α and β are bridge to vehicle mass and stiffness ratios, respectively, and $\alpha > \beta$. Therefore, using relative mass and stiffness ratios, Equation 4.1 can be states as:

$$\begin{bmatrix} \alpha m & 0 \\ 0 & m \end{bmatrix} \ddot{X} + \begin{bmatrix} (1+\beta)k & -k \\ -k & k \end{bmatrix} X = \begin{bmatrix} f(t) \\ 0 \end{bmatrix} \tag{4.2}$$

in which $X = [x_b; x_v]$ contains the bridge and vehicle responses, respectively. In order to solve this equation for X, the first step is to decouple it by using modal transformation using eigenvalue analysis shown in Equation 4.3.

$$det \begin{pmatrix} (\beta+1)k - \alpha m\omega^2 & -k \\ -k & k - m\omega^2 \end{pmatrix} = ((\beta+1)k - \alpha m\omega^2)(k - m\omega^2) - k^2 = 0 \tag{4.3}$$

By assuming $\frac{m\omega^2}{k} = \lambda$ and dividing both sides by k^2 we have:

$$\begin{aligned} (\beta+1) - (\beta+1)\lambda - \alpha\lambda + \alpha\lambda^2 - 1 = 0 \\ \lambda = \frac{\alpha+\beta \pm \sqrt{(\alpha+\beta+1)^2 - 4\alpha\beta}}{2\alpha} \end{aligned} \tag{4.4}$$

One can simply assume that $\alpha + \beta + 1 \approx \alpha + \beta$ since ratios are significantly large (especially the mass ratio α) when considering commercial vehicles and mid- to long-span bridges. This helps further simplifications as shown in Equation 4.5:

$$\begin{aligned} \lambda &= \frac{\alpha+\beta \pm \sqrt{(\alpha+\beta)^2 - 4\alpha\beta}}{2\alpha} = \frac{\alpha+\beta \pm (\alpha-\beta)}{2\alpha} \\ \lambda_1 &= 1 \Rightarrow \omega_1 = \sqrt{\frac{k}{m}} = \omega_v \\ \lambda_2 &= \frac{\beta}{\alpha} \Rightarrow \omega_2 = \sqrt{\frac{\beta}{\alpha}}\omega_v \end{aligned} \tag{4.5}$$

It is worth noting that from Equation 4.5, one of the natural frequencies is equal to the vehicle's fundamental frequency. Once the eigenvalues are found, eigenvectors can be derived to allow for modal superposition. For brevity, this calculation is summarized and the final mode shapes are presented in Equation 4.6.

$$\Phi = \begin{bmatrix} \frac{1}{\beta-\alpha+1} & \frac{\alpha-\beta}{\alpha} \\ 1 & 1 \end{bmatrix} = \begin{bmatrix} \phi_{11} & \phi_{12} \\ \phi_{21} & \phi_{22} \end{bmatrix} \tag{4.6}$$

In Equation 4.1, $f(t)$ is the applied load function, which is ultimately assumed as an ambient white noise for a random traffic network (i.e., Gaussian white noise $\sim \mathcal{N}(0, \sigma^2)$). In order to calculate the response of the system to such loads, one approach is to convert it to a sum of sinusoidal waves using Fourier transform. For a white noise, the spectral density function is a continuous function of a constant value (the value equals σ^2). Therefore, for simplicity, the response of the system subject to a single sinusoidal load is found in closed-form and then, the effect of different frequencies is evaluated by parametric study to determine whether the same conclusion is valid over the entire frequency band. Therefore, $f(t) = A_e sin(\omega_e t)$ is defined, in which A_e and ω_e are the sinusoidal amplitude and frequency, respectively. To convert the equation of motion shown in Equation 4.1 to modal coordinates, we premultiply both sides by Φ^T. The modal force vector and modal stiffness are then calculated as shown in Equation 4.7:

$$\Phi^T F(t) = \begin{bmatrix} \frac{1}{\beta-\alpha+1} & 1-\frac{\beta}{\alpha} \\ 1 & 1 \end{bmatrix}^T \begin{bmatrix} A_e sin(w_e t) \\ 0 \end{bmatrix} = \begin{bmatrix} \frac{A_e}{\beta-\alpha+1} sin(w_e t) \\ \frac{A_e(\alpha-\beta)}{\alpha} sin(w_e t) \end{bmatrix}$$

$$\hat{K} = \Phi^T K \Phi = \begin{bmatrix} \hat{k_1} & 0 \\ 0 & \hat{k_2} \end{bmatrix} = \begin{bmatrix} \left[\frac{\alpha}{(\beta-\alpha+1)^2} + \frac{\alpha-\beta-2}{\beta-\alpha+1}\right] k & 0 \\ 0 & \left[\frac{\beta^3+(1-2\alpha)\beta^2+\beta\alpha^2}{\alpha^2}\right] k \end{bmatrix}$$

$$x_b = \phi_{11} q_1 + \phi_{21} q_2$$

$$\hat{m_1}\ddot{q_1} + \hat{k_1} q_1 = \frac{A_e}{\beta-\alpha+1} sin(w_e t)$$

$$\hat{m_2}\ddot{q_2} + \hat{k_2} q_2 = \frac{A_e(\alpha-\beta)}{\alpha} sin(w_e t) \tag{4.7}$$

The steady-state responses of the single-degree of freedom systems subject to a harmonic load have the following form shown in Equation 4.8:

$$q_1(t) = \frac{\frac{A_e}{\beta-\alpha+1}}{\hat{k_1}} \frac{1}{1-\gamma^2} . sin(\omega_e t)$$

$$q_2(t) = \frac{\frac{A_e(\alpha-\beta)}{\alpha}}{\hat{k_2}} \frac{1}{1-\frac{\alpha}{\beta}\gamma^2} . sin(\omega_e t) \tag{4.8}$$

in which $\gamma = \omega_e/\omega_v$. For a unit amplitude of the external load (i.e., $A_e = 1$) and by substitution of stiffness from Equation 4.7 to Equations 4.8, the harmonic amplitudes are calculated as follows:

$$amp(q_1) = \frac{\beta-\alpha+1}{(\gamma^2-1)(\alpha^2-2\alpha\beta-4\alpha+\beta^2+3\beta+2)k}$$

$$amp(q_2) = \frac{\alpha(\alpha-\beta)}{(\beta-\alpha\gamma^2)(\alpha^2-2\alpha\beta+\beta^2+\beta)k} \tag{4.9}$$

Finally, by modal superposition of two modal responses, the amplitude of the total

harmonic vibration of the bridge is calculated as shown in Equation 4.10:

$$amp(x_b) = \phi_{11} \times amp(q_1) + \phi_{21} \times amp(q_2) =$$
$$\frac{1}{k}\left[\frac{1}{(\gamma^2-1)(\alpha^2-2\alpha\beta-4\alpha+\beta^2+3\beta+2)} + \frac{(\alpha-\beta)^2}{(\beta-\alpha\gamma^2)(\alpha^2-2\alpha\beta+\beta^2+\beta)}\right] \tag{4.10}$$

So far, the bridge response from the fully coupled setup is derived. In order to find the bridge response using the second approach (i.e., the simplified model), the setup shown in Figure 4.4 is assumed. The bridge model is individually subject to the external load and responds to it. The response is then applied to an isolated vehicle model to produce the vehicle response. The closed-form solution for the bridge response in such an uncoupled setup is trivial and shown in Equation 4.11.

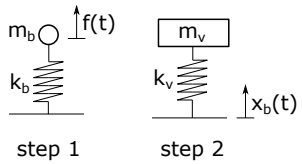

Figure 4.4: schematic of the uncoupled setup

$$\begin{aligned} m_b\ddot{x}_b + k_b x_b &= A_e sin(\omega_e t) \\ x_b &= \frac{A_e}{k_b}.\frac{1}{1-\frac{\omega_e}{\omega_b}^2}.sin(\omega_e t) \\ amp(x_b) &= \frac{1}{k(\beta+\alpha\gamma^2)} \end{aligned} \tag{4.11}$$

Once Equations 4.10 and 4.11 are derived, the parametric study can take place. Both equations are functions of α, β, and γ. By plotting the response error between these two solutions for different ranges of these three parameters, the extent of the error in the simplified decoupled model can be investigated. Intuitively, as the bridge

size increases, the stiffness of the structure decreases (i.e., longer bridges are more flexible), and the mass increases, resulting lower fundamental frequencies. The main objective is to observe the sensitivity of the error to the bridge size. Therefore, different mass and stiffness ratio pairs are plugged into both equations and errors are calculated. In addition, different loading frequencies are also examined. The mass and stiffness ratios (α and β) used for this purpose range $[50 : 10,000]$ and $[500 : 10]$, respectively, modeling short (stiff) bridges to long (flexible) ones. Loading frequencies spread exponentially from 10^{-3}Hz to 10^{3}Hz to envelope a sufficiently wide range of loading frequencies. Figure 4.5 summarizes the outcomes of the parametric study. Note that the x axis corresponds to different mass and stiffness ratio pairs, which is normalized to better convey the qualitative aspect of the plot (i.e., 0 is the stiffest bridge while 1 stands for the most flexible one).

Figure 4.5 demonstrates that based on the closed-form solutions, what would be the extent of error in the simplified simulation method for different types of bridges. As the bridge size increases, the error between two methods decays substantially (e.g., below 0.1% error for long bridges). This supports the idea that an uncoupled simplified solution is accurate enough when the bridge length increases. The figure also shows that there is a range of bridges in which the error is not negligible (for relatively short bridges the error can be up to 50% when the loading frequency resonate with the natural frequency of the vehicle). Also notice that the same trend occurs for different loading frequencies, with maximum error near the vehicle resonance frequency.

In this part, using our simplified model we showed that the uncoupled simulation approach yields accurate results when compared to the fully coupled approach, especially when the bridge size grows. In the next section, the results from a more detailed numerical simulation of the vehicle-bridge interaction are presented in order to incorporate other aspects of the VBI problems, such as vehicle motions and road roughness profile.

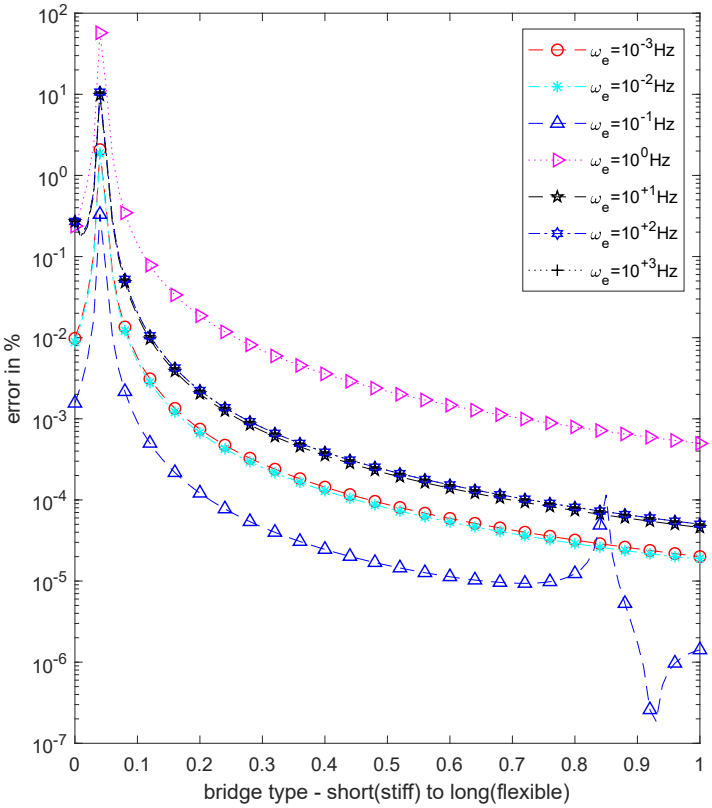

Figure 4.5: Results of the theoretical approach: parametric study shows the extent of the error for different bridge types and loading frequencies when using the simplified bridge-vehicle simulation approach.

4.4 Numerical Analysis

In this section, the VBI problem is modeled numerically in MATLAB and the results are compared with the signals from the simplified simulation approach. In this numerical case study, six bridges with different span lengths are modeled in SAP2000 and two simulation approaches are implemented. The exact numerical approach for modeling the bridge response interacting with a moving vehicle (roughness included) is adopted from González et al. [2012] as presented in Algorithm 4.

The bridge setup is shown in Figure 4.6. The span varies from 15 m (very short and stiff bridge) to 500 m (long and flexible bridge), with mechanical properties shown

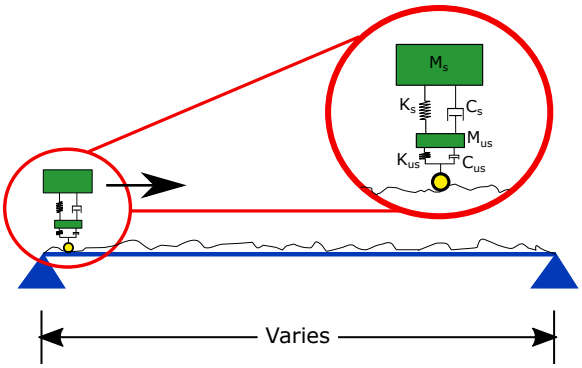

Figure 4.6: Schematic of simulated model - roughness profile is also included

in Table 4.1. The bridge is 3D modeled in SAP2000 using prismatic beams with box cross-sections. Note that the considered single span simply-supported bridge is the use case for the majority of numerical studies in the VBI community [Yang et al., 2004a, OBrien et al., 2010]. Since one of the objectives of our study is to propose a simplified numerical approach for VBI analysis, the same geometry and boundary condition are considered in the first numerical case study. The reason for a 3D model of the bridge is to have a physical sense of the dimensions of the deck section and better visualization. The modeling process is as follows: The bridge geometry and material are defined in the SAP model. The stiffness and mass matrices of the SAP model are then exported to a MATLAB script within which bridge dynamic analyses as well as vehicle-bridge interactions are held. The accuracy of the bridge models is verified by examining bridge natural frequencies. The fundamental modes in shorter bridges are vertical (longitudinal) while for very long spans, torsional modes dominate. Note that the torsional modes are not within the scope of this study and are excluded from modal analyses. In this case study, bridges are all simply-supported; however, a different geometry is evaluated in Section 5. The structural behavior is assumed linear elastic for consistency with operational modal analysis. The study does not take large deformations and nonlinearities into account based on the fact that the method is being proposed for numerical simulation of bridges under operational mode. In particular, no material nonlinearity is expected here. In terms

of geometry nonlinearity, we expect that it may be effective for very long bridges.

In this study, bridge models are deterministic and no uncertainty for material and geometry is included. In fact, the study is focused on studying the extent of bridge-vehicle interaction with respect to bridge dimensions and traffic level. Ni et al. [2019] showed that by incorporating uncertainties in bridge modeling, the modal properties are changed, however, this variation is dramatically lower for the fundamental modes compared to higher ones. In addition, Yang and Lin [2005] showed that in a vehicle-bridge interaction scenario, the bridge response is highly dominated by the first natural mode. Considering these, uncertainty propagation analysis is neglected in this study. The road roughness profile is adapted according to ISO standard for a road class 'A' [de Normalización , Ginebra] which is the case for a well maintained highway road condition. At each time instance, the bridge model is analyzed dynamically using Newmark-β method using matrices imported from SAP2000. For the vehicle, first a quarter-car model is adopted with the properties shown in Table 4.2. This vehicle simulates suspension properties of a commercial vehicle with high damping and low natural frequency (which are critical factors for a comfortable ride [Milliken et al., 2002]). The second vehicle is a quarter-car model of a heavy truck adopted from Harris et al. [2007], Elhattab et al. [2016] with properties shown in Table 4.3. The second vehicle is selected to investigate the approximation error of using the simplified method for heavy sensing agents when the weight is not negligible.

Table 4.1: Bridge spans and cross-section dimensions

Span length [m]	*15m*	*30m*	*50m*	*100m*	*200m*	*500m*
Outside depth [m]	0.60	1.10	1.60	2.40	3.00	5.00
Outside width [m]	0.3	0.50	1.30	2.00	2.50	4.00
Flange thickness [m]	0.04	0.05	0.10	0.15	0.15	0.50
Web thickness [m]	0.02	0.03	0.05	0.10	0.10	0.25
Fundamental freq. [Hz]	8.03	3.63	2.05	0.75	0.24	0.06

For a fair comparison, the vehicle's speed is kept constant among all bridge spans

Table 4.2: Commercial vehicle properties

Property Name	*Value*	*Units*
Unsprung Mass	69.9	Kg
Sprung Mass	466.0	Kg
Tire Damping	0.0	Ns/m
Suspension Damping	2796.0	Ns/m
Tire Stiffness	3043.0	N/m
Suspension Stiffness	290.3	N/m
Fundamental Frequency	1.2	Hz

Table 4.3: Heavy truck properties

Property Name	*Value*	*Units*
Unsprung Mass	700.0	Kg
Sprung Mass	17,300.0	Kg
Tire Damping	0.0	Ns/m
Suspension Damping	1.0×10^4	Ns/m
Tire Stiffness	1.75×10^6	N/m
Suspension Stiffness	4.0×10^5	N/m
Fundamental Frequency	0.69	Hz

($10m/sec$). Finally, the traffic load is modeled as a random ambient load uniformly applied over the span with the amplitude proportional to the number of vehicles. In particular, for n vehicles, a random and sparse matrix is generated in which the sum of forces in each row (i.e., for each time instance) is equal to $n \times 2,000 \times g$ N, assuming $2,000$ kg for the average weight of a commercial vehicle and g is the gravity acceleration. Four traffic levels are considered for each span length with $n = 0, 10, 20, 50$ ($n = 0$ models an isolated bridge while $n = 50$ models a bridge with 50 vehicles moving while being scanned by the sensing agent). The bridge is modeled as a MDF system with $0.1m$ spatial discretization (e.g., 15 m long bridge is modeled with 150 DOFs). The $0.1m$ discretization is selected based on a trade-off between computation time and maximum avoidance for displacement interpolation when the vehicle's location falls inside a bridge segment. 0.1m-long bridge segmentation yields exact vehicle displacement calculation when vehicles' speed is set to 10m/sec. For vehicles moving

faster than this speed, discretization of vehicle's time and space coordinates causes some gaps in locations of consecutive time steps. This gap causes a simplification in the vehicle's initial condition (particularly the initial speed) calculation. However, in this study the damping of the unsprung mass is set to zero which disconnects the vehicle's dynamic analysis to its initial speed. For simulating responses using the decoupled model, Algorithm 5 is adopted: the random traffic load is firstly applied to the bridge with no consideration for the sensing vehicle. The bridge responses at the vehicle locations are then aligned in space and applied to the model of the sensing vehicle. The vehicle processes the input through its dynamical model (shown in Tables 4.2 and 4.3) and produce the vehicle response.

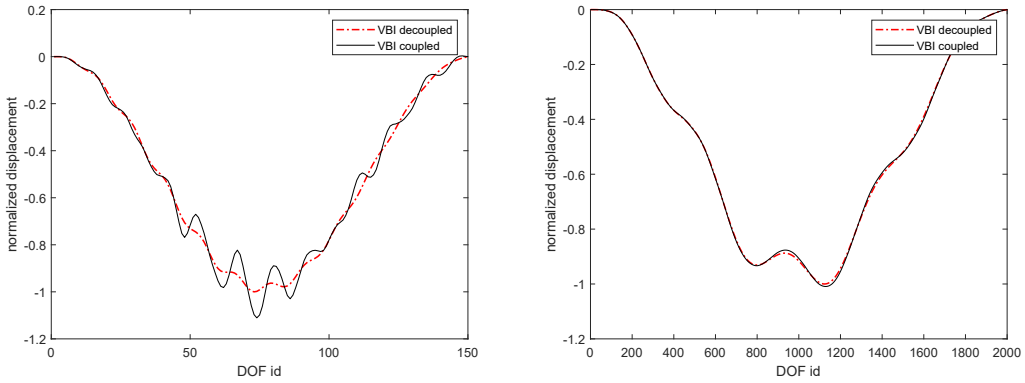

(a) 15 m bridge (b) 200 m bridge

Figure 4.7: Bridge displacement simulation results for the commercial vehicle

The performance of the simplified model is evaluated in terms of the bridge response as well as the vehicle response. From Section 4.3 it is expected that the simplified model yield more accurate response estimations as the length of the bridge span increases. For the conventional simulation approach, the acceptance threshold for the bridge response is set to 1.5×10^{-12} m. For each bridge span and traffic level pairs, bridge and vehicle response signals are simulated using two approaches (in total 24 runs for each vehicle); and the errors between two signals are measured in time and frequency domains using the mean squared error (MSE). For more consistency,

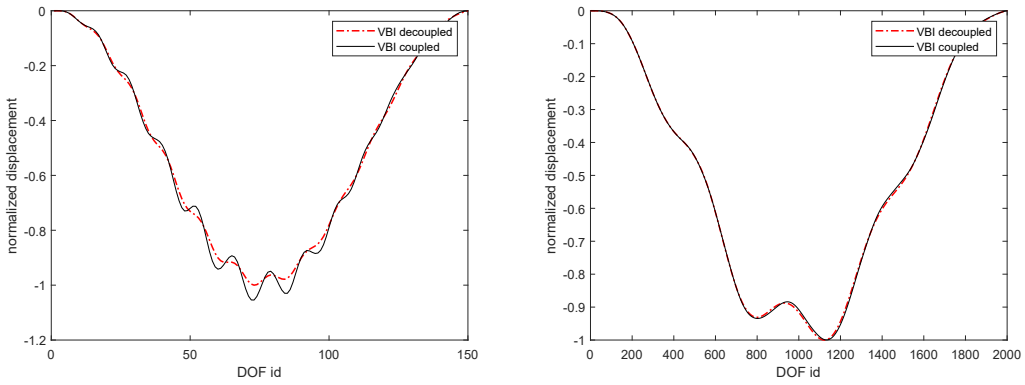

(a) 15 m bridge (b) 200 m bridge

Figure 4.8: Bridge displacement simulation results for the heavy truck

the responses are scaled by the absolute maximum values of the displacement signals found from the conventional method.

Simulated displacement signals for two spans (15 m and 200 m) are shown in Figures 4.7 and 4.8. For both vehicle types, the bridge response differs noticeably between the conventional and simplified VBI simulations for the 15 m bridge. However, as expected from Section 4.3, as the bridge length increases, the discrepancy between two simulation approaches shrinks in bridge response estimation. The MSE values versus bridge length are also presented in Figures 4.9 and 4.10 for the commercial vehicle and Figures 4.11 and 4.12 for the heavy truck to further quantify this observation. Figures 4.9 and 4.11 (error in the bridge response simulations) show a strictly decreasing MSE value as the bridge length increases. In addition, in both cases, as the traffic level increases (i.e., from $n = 0$ to $n = 50$), the estimation error reduces. This is more evident for the commercial vehicle. Note that the same patterns are deduced from the frequency representation plots.

Figures 4.9 and 4.11 show the extent of error for simulating stationary sensors' data that are attached to the bridge. However, what a mobile sensing agent records while scanning the bridge, is not the bridge pure vibrations, but the vehicle response to it. Therefore, Figures 4.10 and 4.12 show the accuracy of the vehicle response subject

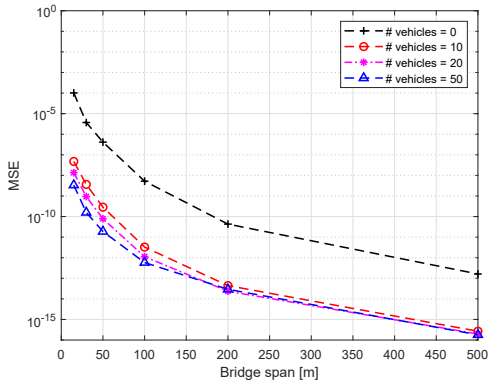

(a) Time signal comparison

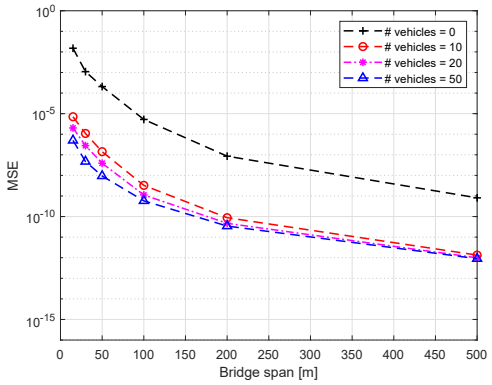

(b) Frequency comparison

Figure 4.9: Bridge response comparison for the commercial vehicle in terms of the MSE: The trends show more accurate simulation results as bridge span or traffic volume increases.

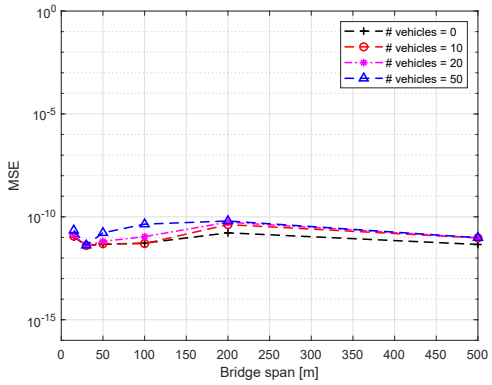

(a) Time signal comparison

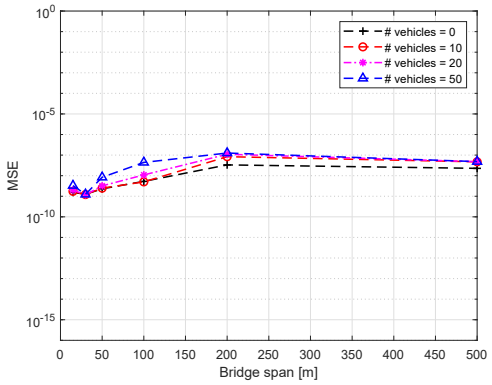

(b) Frequency comparison

Figure 4.10: Vehicle response comparison for the commercial vehicle in terms of the MSE: The trends show invariance to the span and the traffic level.

to the bridge motion when comparing the simplified model with the conventional approach. In this case, two sensing agents (i.e., the commercial vehicle versus the heavy truck) react differently. For the commercial vehicle, the responses are relatively insensitive to the span and traffic level and the errors are consistently low for all cases. However, from Figure 4.12, the truck response is simulated less accurately when the bridge span grows from 15 m to 100 m (for longer bridges, a decaying error trend is observed again). In particular, the frequency estimation error for the heavy vehicle crossing a 100 m long bridge is quite noticeable when using the simplified model. From

Table 4.3, the fundamental frequency of the truck is 0.69Hz which is near resonance for the 100 m long bridge (from Table 4.1, $f = 0.75$Hz). Moreover, the vehicle weight is significant, which results in higher interaction forces applied to the bridge and the vehicle itself. In fact, this case highlights that when the bridge and the vehicle have near resonance frequencies, the simplified model works more accurately when the vehicle is lightweight. To validate this, the properties from Table 4.3 are downscaled by a factor of 5 (i.e., the same natural frequency while being lighter) and simulation for 100 m long bridge is repeated. The MSE value for $n = 50$ from 1.19×10^{-4} reduced to 5.46×10^{-6}.

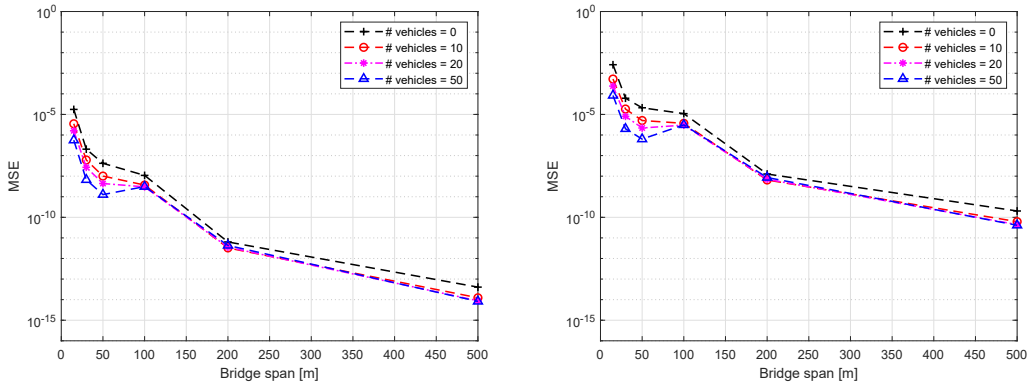

(a) Time signal comparison (b) Frequency comparison

Figure 4.11: Bridge response comparison for the heavy truck in terms of the MSE: The trends show more accurate simulation results as the bridge span or the traffic volume increases.

4.5 Computational Cost Evaluation

The main objective of the simplified model is to improve the computational performance of simulations while having a minimal impact on the accuracy of the results. In Figure 4.13 the computational runtimes for the commercial vehicle simulation case are compared between two methods (the heavy vehicle yields a very similar plot as well). The figure elaborates that while the runtime increases linearly in the simpli-

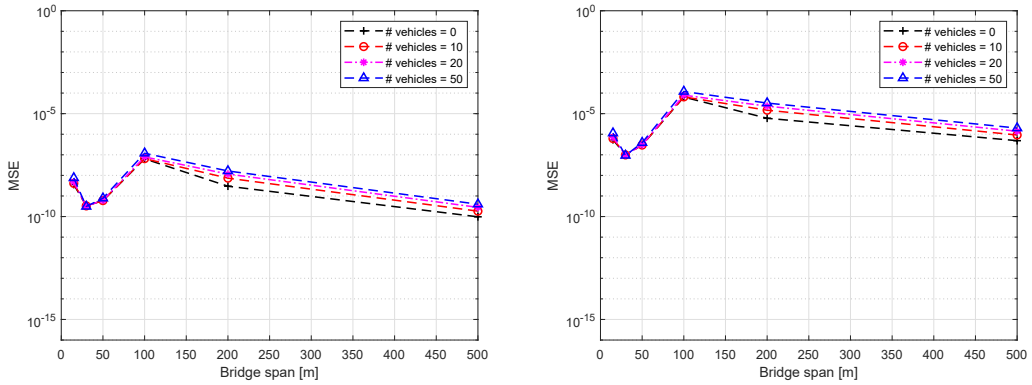

(a) Time signal comparison (b) Frequency comparison

Figure 4.12: Vehicle response comparison for the heavy truck in terms of the MSE: The trends show that the error peaks when the bridge and the vehicle have close fundamental frequency values.

fied model, it grows exponentially when using the conventional approach for longer bridges. For instance, using a single Intel Core i5 CPU, the entire VBI simulation process for the 500 m long bridge takes 1.8 sec using the simplified model, while the same process takes nearly $2,250.0$ sec using the conventional method (more than $1,000\times$ slower). This dramatic runtime difference is resulted by the inner iterations of the conventional approach (see Algorithm 4) that guarantee the compatibility. Within this iteration, the entire bridge model has to be analyzed repeatedly for the modified interaction force as long as the stopping criterion is not met, which is computationally very expensive. This is a bottleneck for the numerical computation, especially when the bridge length increases or models with higher fidelity is of interest (i.e., MDF model grows in size). Alternatively, the simplified model fully decouples the bridge model from the vehicle systems, which yields a one-time bridge analysis (see Algorithm 5). This significant speedup enables to perform VBI simulations for medium- to long-span bridges with fine spatial discretization, which is required for numerical studies on crowdsensing-based health monitoring.

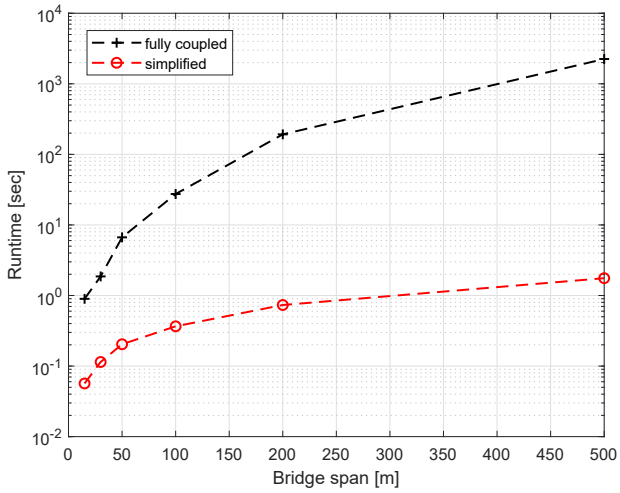

Figure 4.13: Runtime comparison between the conventional and simplified models: the conventional approach is computationally $> 1,000\times$ slower than the simplified model for the 500 m bridge with no significant gain in the accuracy of response estimations.

4.6 Fully Coupled Vehicle Network Simulation

In this section, a fully coupled network of vehicles is analyzed to verify the followings: (1) the premise of ambient white noise on behalf of a random traffic load is valid and (2) the simplified method yields accurate results for bridges with different geometries. Regarding that, a continuous bridge with four 50m-long spans with elastic steel material is modeled and shown in Figure 4.14 (beam cross-section is shown as well). The bridge length is discretized with 0.1m grids, resulting a 2,001 DOF system. The roughness profile is introduced with the same setup as before. In this case, instead of applying a spatio-temporal random load to model random traffic loads, the bridge is subjected to different levels of traffic caused by deterministic vehicle trajectories (as shown in Figure 4.2a). All vehicles are interacting with the bridge in the same fashion as given in Algorithm 4. In summary, the convergence loop continues until all vehicles have reached acceptable displacement errors.

In these analyses, each vehicle in the network has certain speed and mechanical properties. The mechanical properties are randomly selected with a lognormal distri-

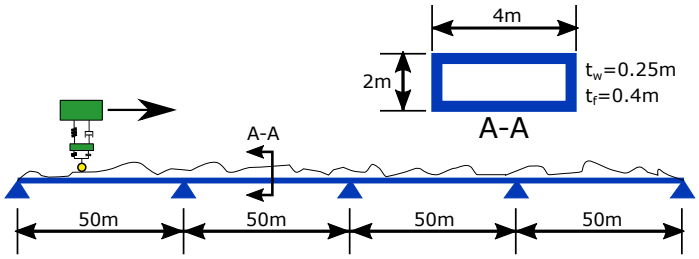

Figure 4.14: Geometry of four-span continuous bridge and cross-section.

bution. The mean values for each property is set to the values given in Table 4.2 for the commercial vehicle. Standard deviation σ is also set to 0.35 for all components of the property table. The map of vehicle network trajectories for two levels of traffic is shown in Figure 4.15. In this figure, each column contains momentary response of the bridge at all DOFs. Each trajectory is represented by a line in the spatio-temporal response matrix. Different slopes show different directions and speeds (close to horizontal shows very low speed vehicles while nearly vertical ones show very fast bridge crossings). The random trajectory generator allows for fixed vehicles as well.

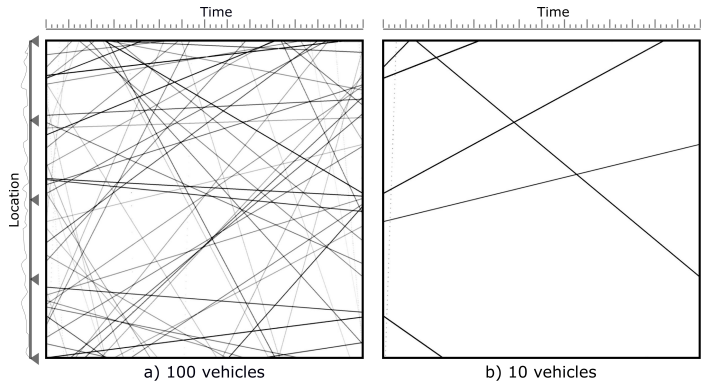

Figure 4.15: Random vehicles trajectory in the time-space matrix. Each solid line represents a single vehicle's motion over the bridge. Vehicles have different speeds and directions and all are fully interacting with the bridge. Two levels of traffic are shown.

The first objective is to show the spatio-temporal load determined by the vehicle network and bridge interaction has statistical characteristics of a 2D white noise. The resulted loading matrix for a random traffic case (with 200 random vehicle trajectories) is derived from the coupled dynamic analysis and the Fourier transform is shown

in Figure 4.16 along with the same representation of a white noise loading matrix. By comparison, both plots show uniform content everywhere with no coherent frequency peaks. This implies that a realistic loading scenario with deterministic vehicle motions has the similar effect to a random white noise.

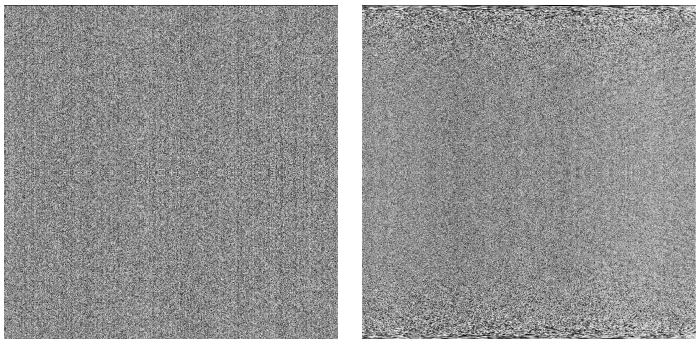

Figure 4.16: Frequency representation of spatio-temporal load applied to the bridge. (a) white noise spatio-temporal load considered in analyses in Section 3. (b) actual load resulted from a traffic network of random vehicles with full consideration for the vehicle-bridge interaction. Similarity between two representations confirm the random nature of traffic load.

In the next step, a mobile sensing agent is added to the traffic networks and the bridge interaction is considered with (1) conventional (Algorithm 4) and (2) simplified (Algorithm 5) approaches and results are compared. Three different speeds for the sensing agent are considered: $10m/sec$, $20m/sec$, and $30m/sec$. The MSE error between vehicle and bridge response estimations of the simplified and conventional approach is calculated and plotted in Figure 4.17. In all three speed cases, the error significantly drops when the network includes higher number of vehicles. This figure confirms that even in a realistic simulation of the traffic network, the simplified approach yields accurate estimations for the majority of cases (i.e., when the network is sufficiently crowded). As for the sensing agent's speed effect, except for a slightly higher errors for higher speeds, other variations are not conclusive. By comparing these plots with Figures 4.9 and 4.10, the trends are consistent. The variations in the magnitude of the MSEs can be explained due to different bridge boundary conditions

and more realistic loading pattern.

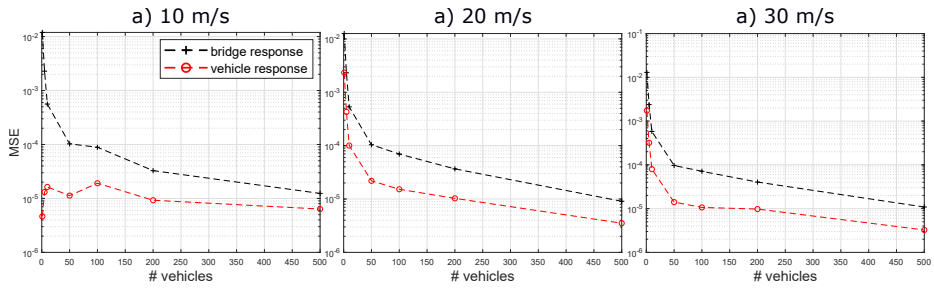

Figure 4.17: Bridge and vehicle response comparison for a commercial sensing vehicle in terms of the MSE: the plots confirm that as the number of traffic fleet increases, the error in simplified approach reduces. In general, once the number of fleet tops 50, the accuracy of the proposed method is very high.

4.7 Conclusions

In this study, a modified simulation algorithm was proposed for vehicle-bridge interaction (VBI) problems concerning medium- to long-span bridges with random traffic excitation. The primary deliverable of this study to the SHM community is to enable a fast and accurate numerical analysis method that can be used in different bridge infrastructure management levels, such as (1) evaluation of crowdsensing-based methods for bridge modal identification and (2) probabilistic and life-cycle analysis of bridges subjected to vehicle networks under various uncertainties (e.g., road profile, vehicle dynamics, traffic level, and environmental variations). Our main contribution is the result that as the bridge flexibility increases (longer spans), the degree of coupling between the vehicle and the bridge reduces notably. Conventional VBI simulation algorithms require iterations within each time step in order to reach a desired level of compatibility between the vehicle and the bridge, which is computationally expensive. We show that the proposed simple, decoupled model is efficient for simulations of the vehicle-bridge interacting systems in such cases, with an accuracy that increases with bridge flexibility. In particular, the theoretical analysis showed that the response

of a coupled continuous beam and vehicle setup subject to a random load becomes more independent to the vehicle dynamics as the bridge mass grows and the stiffness reduces. Therefore, for longer or flexible bridges, the dynamics are practically independent. Moreover, the numerical simulation validated that the bridge size and traffic load intensity both affect the accuracy of the bridge vibration estimations using the simplified model. For commercial vehicles, the simplified method yields accurate response estimations. In the case of a heavy vehicle with a natural frequency near the bridge's fundamental frequency, e.g., heavy vehicles and flexible bridges, the error associated with the simplified model is noticeable. In terms of the computational cost, a comparative study showed that the cost of the conventional model behaves exponentially while the cost of the simplified model is linear.

Chapter 5

Wavelet Platform for Crowdsensed Modal Identification of Bridges

5.1 Abstract

This study presents a flexible approach for bridge modal identification using smartphone data collected by a large pool of passing vehicles. With each trip of a mobile sensor, the spatio-temporal response of the bridge is sampled, plus various sources of noise, e.g., vehicle dynamics, environmental effects, and road profile. This study provides further evidence to support the hypothesis that through trip aggregation, such noise effects can be mitigated and the true bridge dynamics are exhibited. In this study, the continuous wavelet transform is applied to each trip, and the results are combined to estimate the structural modal response of the bridge. The Crowdsourced Modal Identification using Continuous Wavelets (CMICW) method is presented and validated in an experimental setting. In summary, the method successfully identifies natural frequencies and absolute mode shapes of a bridge with high accuracy. Notably, these results are the first to extract torsional mode shape information from mobile sensor data. Moreover, the influence of vehicle speed on the estimation accu-

racy is investigated. Finally, a hybrid simulation framework is proposed to account for the vehicle dynamics within the raw mobile sensing data. The proposed method is successful in removing vehicle dynamic effects and identifying modal properties. These results contribute to the growing body of knowledge on the practice of mobile crowdsensing for physical properties of transportation infrastructure.

5.2 Introduction

Infrastructure is a vital component of transportation systems and a vibrant economy. In many countries, monitoring and maintenance of existing infrastructure have turned into a significant concern for urban planners and decision makers, especially in the US, Europe, and Asia [Lancefield, 2017, Willsher et al., 2018, Pérez-Peña, 2018]. Nearly one of every nine bridges in the US is structurally deficient according to ASCE [of Civil Engineers, 2017]. The global state of infrastructure indicates a demand for large-scale health monitoring solutions with reduced setup costs that can rapidly produce information on existing mechanical properties, damage location, and extent of deterioration in bridges. Among available health monitoring methods, vibration-based systems have become popular as data acquisition is relatively inexpensive and the resulting data is an asset to a bridge management system.

5.2.1 Crowdsourcing for Urban Transportation Sensing

Through widespread presence of smart devices, datastreams are available that are primarily collected for personalized, comfort-intended tasks, such as adaptive screen lighting or navigation, but they can be further analyzed for widely-impacted socio-economical secondary objectives. Smartphones are equipped with numerous sensors for motion measurement and have an ability to continuously record data at high rates. Of course, in comparison to more dedicated instruments, smartphone sensors

are generally less precise and are expected to produce noisier data; nevertheless, the datasets produced by phones can be extremely large and include simultaneous measurements from dozens of sensing channels. In some cases, the vast size of these datasets can help overcome shortcomings in data quality. Recent research explored the possibility of using such data from vehicle networks for urban planning and transportation applications. A real-time framework was introduced that is able to create urban dynamic maps using smartphone data, such as traffic conditions and pedestrian movements in Rome [Calabrese et al., 2010]. In Wang et al. [2012] by combining GIS and smartphone data the patterns of road usage and origins of the cars were detected, which are applicable for transportation planning. A crowdsourced-based algorithm was proposed by Shin et al. [2015] for automated transportation mode detection using smartphone sensing data including acceleration. Other applications such as road incident reporting and real-time parking space information based on crowdsourcing data from drivers are proposed as well [Wang et al., 2017, Shi et al., 2018]. A review study on smartphone data crowdsourcing for vehicle positioning and drivers' behavior monitoring is conducted by Kanarachos et al. [2018]. The study elaborated that smartphones are advantageous for crowdsourcing application due to the market penetration, *Internet of Things* connectivity, and data sharing capabilities.

Smartphones as sensors is an emerging paradigm which is not limited to traffic monitoring and has recently been applied towards health monitoring of transportation infrastructure. The state of practice in vibration based structural health monitoring (SHM) is to utilize dedicated accelerometers at fixed locations and periodically monitor the output. However, mobile sensors have offered a great potential to dramatically overhaul this conventional paradigm. Some studies proposed smartphone acceleration and GPS data for real-time localization and characterization of road bumps from vehicle networks [Mednis et al., 2011, Kumar et al., 2016, Mukherjee and Majhi, 2016]. More recently, a vision-based approach for road condition assessment based on images

from dashboard-mounted smartphones has been proposed and experimentally tested [Maeda et al., 2018]. These successful applications encourage SHM community to develop crowdsensing-based methodologies for bridges.

5.2.2 Bridge Health Monitoring

Over the past twenty years, there has been extensive research on wireless sensor networks for structural health monitoring (SHM) and nondestructive testing applications. These sensor networks are economical, easy to implement and can support denser networks when compared with traditional wired systems [Pakzad et al., 2008, Lynch and Loh, 2006, Kim et al., 2007, Harms et al., 2010, Hackmann et al., 2013]. There is a plethora of important studies that successfully implemented dense wireless sensor networks on real-world bridges and have shaped the SHM field [Kim et al., 2007, Lynch et al., 2005]. With the emergence of wireless sensors, *spatial coverage* and *spatial density* have become increasingly important features of any sensor network as they broadly affect the veracity of key applications, e.g. damage localization, model updating, etc. The primary approach for enhancing spatial density of the identified modal properties is simply to design sensor networks with additional sensors [Lynch and Loh, 2006, Kim et al., 2007]; the drawbacks of this approach are an increased complexity in data acquisition and transmission systems and higher setup costs.

Mobile Sensing for Bridge Health Monitoring

Over the years, the capabilities of mobile sensor networks in SHM have been demonstrated both in theory and in practice. Mobile sensors have outstanding benefits: (1) the data can contain rich spatial information; (2) ubiquitous smartphones are great candidates for mobile sensors. (3) when combined with vehicle networks or fleets, mobile sensors routinely scane transportation infrastructure.

There has been progress in developing general purpose modal identification meth-

ods for mobile sensor data that are not necessarily tied to vehicles. The structural identification using expectation maximization (STRIDEX) [Matarazzo and Pakzad, 2018] utilized data from multiple mobile sensors for comprehensive modal identification (frequencies, damping ratios, and determine mode shapes) and further quantified the superior spatial information that can be produced with mobile sensor networks. With only two mobile sensors, STRIDEX identified the fundamental mode shape with 248 points - that is, two mobile sensors captured spatial information that was comparable to 120 fixed sensors [Matarazzo and Pakzad, 2018]. The modal identification through matrix completion (MIMC) method [Eshkevari et al., 2019, Eshkevari and Pakzad, 2020b, Sadeghi Eshkevari et al., 2020d] is a sparse sensing approach for processing large-scale sensing scenarios (mobile, fixed, or hybrid). A benefit of this method is that it can handle data from a very large number of moving sensors with arbitrary bridge trajectories.

Simultaneously, "indirect monitoring" research has considered measurements of vehicle vibrations collected while passing over bridges, which are subject to vehicle-bridge interaction [Yang et al., 2004a, Lin and Yang, 2005, Yang and Chang, 2009, Siringoringo and Fujino, 2012, González et al., 2012]. These studies have mostly considered one vehicle, simplistic traffic cases, and have been limited to partial modal identification of the bridge, e.g., frequencies only, damping ratios only. In these studies, a coupled dynamical system including both the vehicle and the bridge is usually developed, which is subject to a controlled load from the moving vehicle. A recent study by Sadeghi Eshkevari et al. [2020e] showed that in certain traffic scenarios, the vehicle dynamic response is nearly decoupled from the bridge system when the collective traffic loads on the bridge are effectively random.

Crowdsensing for Bridge Health Monitoring

The previous studies focused on mobile sensing for bridge health monitoring, yet did not strictly analyze smartphones for crowdsensing. Early studies with on-board smartphone acceleration sensors for structural health monitoring applications provided preliminary validation of smartphone sensor accuracy in a laboratory setting [Yu et al., 2015, Feng et al., 2015, Ozer et al., 2015].

An advantage of smartphones is that they contain other useful sensors such as GPS, gyroscopes, magnetometers, etc. which facilitates sensor data fusion and cross-validation among reference sensors [Guzman-Acevedo et al., 2019]. For example the integration of Intelligent Transportation Systems (ITS) including traffic video camera and bridge structure instrumentation with dedicated sensor data was suggested in order to enhance the estimation accuracy for structural health monitoring applications [Gandhi et al., 2007, Khan et al., 2016]. A particular application of interest is of course crowdsourcing smartphone data to assess the condition of existing infrastructure, e.g., bridges. Matarazzo et al. [2017] analyzed call detail record (CDR) data to estimate the number of smartphones that cross the Harvard bridge each month. Such estimates help quantify the crowdsensed data potential for specific urban infrastructure based on human mobility patterns. A later study aggregated smartphone data collected from forty-two vehicle trips over the Harvard bridge and extracted consistent indicators of the first three modal frequencies [Matarazzo et al., 2018]. This study was the first to support the hypothesis that smartphone data, collected within vehicles passing over a bridge, can be used to detect several bridge modal frequencies. Other studies involving mobile smartphone sensors have developed methods that can successfully track damage-sensitive features in a laboratory setting [Mei and Gül, 2018, Liu et al., 2020].

A recent study at MIT's Senseable City Lab proposed a wavelet-based statistical methodology which aggregates smartphone vehicle-trip data to estimate the most

probable modal frequencies (MPMFs) of a bridge. The study considered a large number of controlled and uncontrolled vehicle trips and successfully estimated the first three modal frequencies of the Golden Gate Bridge using the proposed framework. The method uses synchrosqueezed wavelet transformations to produce a stack of spatial-frequency maps whose local maxima represent bridge modal properties. The primary advantage of the proposed method is that it does not require synchronized sensing. In other words, sensor data aggregation is performed regardless of the sensing time for individual scans. This study builds on the same strategy by proposing a new wavelet-based methodology that is able to identify the modal frequencies and absolute mode shapes from crowdsourced mobile smartphone data.

5.2.3 Spatio-temporal Transformations

In this study, the primary objective is to estimate natural frequencies and absolute values of mode shapes by crowdsourcing mobile smartphone data. As explained in Eshkevari et al. [2019] and Matarazzo et al. [2018], bridge dynamics produce a spatio-temporal response which consists of modal responses. For instance, a bridge under a uniform ambient load produces a stationary signal at the fixed locations (since the signal is not a function of space), while a mobile sensor that drives by a bridge collects a nonstationary signal. Time-frequency transformations are designed to represent a nonstationary or nonlinear signal by a map of its time-dependent frequencies. Short-time Fourier transform (STFT) is a common approach that stacks FFTs (fast Fourier transforms) of sliding windows of a signal to create a 2D time-frequency representation (TFR) [Zhang et al., 2012, Malekjafarian and OBrien, 2014a]. Continuous wavelet transform (CWT) is numerically more stable and computationally less expensive. In CWT, a mother wavelet is applied on the signal to detect associated frequency contents and then repeatedly scaled up to represent lower frequency contents. The method has been extensively used for damage detection and modal identification.

A modified version of wavelet-based methods is synchrosqueezed wavelet transform (WSST), which was used in recent study at MIT's Senseable City Lab, yielding promising results. This algorithm is designed to remove the frequency smearing effect of CWT by squeezing adjacent frequency ridges into the most powerful band.

The continuous wavelet transform of a signal collected by a mobile sensor creates a 2D time-frequency representation, in which the time axis is interchangeable with location since $x = f(v, t)$ (where, x is the location, v is the vehicle speed, and t is the time; when vehicle speed is constant, $x = v \times t$). If the structural properties remain linear, this 2D representation includes ridges at the natural frequencies of the bridge. The magnitudes of the ridges are directly dependent on the location. For instance, for a simple beam, the ridge associated with the second mode has zero magnitude at the midspan since the second mode shape has zero magnitude there. Expanding the same argument, it is deduced that the magnitudes of each ridge are directly associated with the absolute amplitudes of the corresponding mode shape at that location. The idea is better explained in Figure 5.1. In this figure, stationary sensors collect signals and their CWTs are calculated (the complex Morlet wavelet transform used in this example is equivalent to the Fourier transform [Bentley and McDonnell, 1994]). Among all CWTs, the outstanding frequencies are identical, but their magnitudes vary between locations. By stacking these frequency representations in their spatial order, the envelopes of each modal frequency represents the absolute natural mode shapes.

5.2.4 Motivations and Contributions

Previous studies on mobile sensing have proposed effective solutions for a variety of mobile sensing scenarios [Matarazzo and Pakzad, 2018, Eshkevari et al., 2019]. Despite their appealing performance and high accuracy, they are limited to scenarios in which higher quality accelerometers (not smartphones) are available. This study, pro-

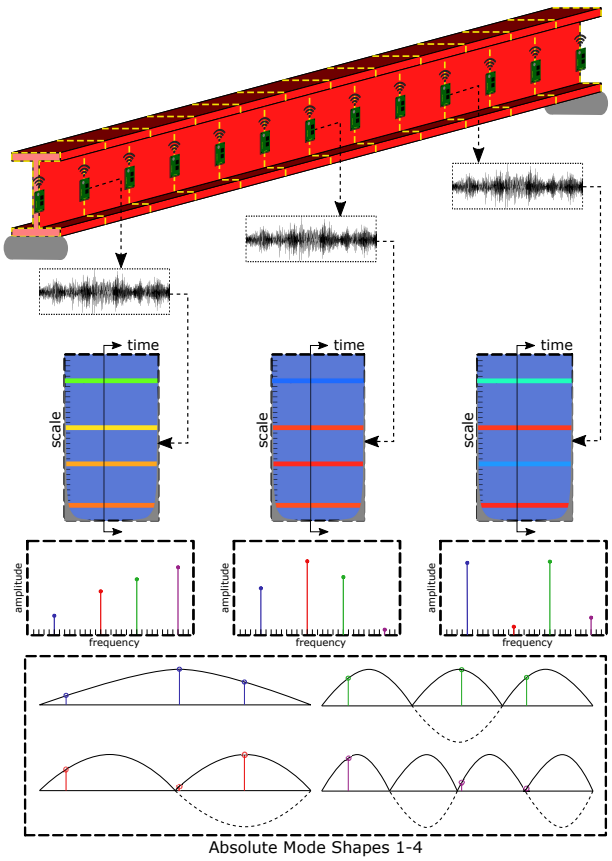

Figure 5.1: Spatial variation of CWTs: the simply-supported beam is equipped with fixed sensors. The CWT plots of using signals from different fixed sensors are shown. In each CWT plot, the modal bands have amplitudes that are proportional to the spatial amplitude of the natural modes. Frequency bands are consistently color-coded with respect to their intensity. By stacking these CWTs in spatial order, absolute mode shapes are identified.

poses crowdsourced modal identification using continuous wavelets (CMICW) which is designed to process smartphone data as a "collection" rather than, one-by-one. The method is able to estimate both natural frequencies and the absolute natural mode shapes (vertical and torsional). Notably, CMICW is the first method with an ability to extract torsional mode shape information from mobile sensor data (in a generic sense, not only smartphone data). The method also has beneficial computational features as the estimation process is scalable with respect to the number of datasets.

The approach relies on complex Morlet wavelet transform to convert individual mobile scans into a 2D map of bridge location versus frequency. By crowdsourcing a

large number of one-way scans and producing a library of 2D CWT plots, aggregation minimizes estimation biases through canceling out trivial ridges and intensifying consistent ridges, i.e., absolute natural mode shapes. In such a crowdsourcing scenario, the number of scans in the aggregation pool is the controlling parameter and directly influences the confidence and accuracy of the estimations. In Section 5.3, an overview of the designed pipeline is introduced and its components are justified. Section 5.4 will present the procedure and results of experimental case studies consisting of a laboratory-scale beam setup. Smartphones moving at various speeds collect vibration data when the beam is subjected to trains of random impulsive loads. The effect of sensors speed variations is also demonstrated. Moreover, a hybrid simulation procedure is designed to integrate vehicle suspensions effect to sensors measurements and the effect is investigated. In section 5.5, results are further discussed and the study is summarized.

5.3 Methodology

A schematic plan of the CMICW pipeline is shown in Figure 5.2. In this figure, the starting point is data collection using passerby sensors over the bridge. Each individual scan is fully independent and can happen with or without the presence of other scanning devices. The mobile sensor collects a time history of the bridge vibration responses at different time-location coordinates, depending on the speed of the vehicle. In the next step, this signal is transformed into a time-frequency domain using CWT. For a sensor with constant speed, the time axis can be linearly scaled to a bridge location axis. The CWT yields a 2D map of instantaneous frequencies at different bridge locations. For an individual signal, the 2D frequency map is highly contaminated by trivial contents caused by ambient loads, measurement noises, and stochastic events. Therefore, the process of collecting signals and applying CWT is

repeated in order to populate a crowdsourced pool of CWT maps. Once the pool is sufficiently large, an average of 2D maps converges to the frequency-location map of the bridge, i.e., natural frequencies and absolute mode shapes. However, since mobile sensors may have different speeds while sensing, the CWT maps have different resolutions and may not be readily consistent in size (dimensions of the CWT map depends on the length of the signal, which itself relies on the vehicle speed). Hence, the CWTs are 2D interpolated to a predefined global grid. Despite its desired spatio-temporal representation, CWT results in distorted values near the ends of the signal, widely known as the edge effect [Montanari et al., 2015]. To minimize the distortion, the proposed approach from [Montanari et al., 2015] is adopted. After aggregation, the 2D map shows strong ridges on the natural frequencies and minimal noise bed elsewhere, since the noisy contents cancel out each other. These intensified ridges are then automatically detected using a peak-picking algorithm and the aggregated map is section-cut at those frequencies. The final product of the pipeline is the identified absolute mode shapes, which have very high spatial resolution (final output of the procedure shown in Figure 5.2). The detailed components of the pipeline are presented in Figure 5.3.

In addition to the vertical modes, the method is also capable of reconstructing torsional modes and creating 3D representations. For this purpose, the pipeline is implemented separately for different lanes of the bridge. For the torsional modes, the values of the identified ridges vary between lanes. For instance, torsional modes have zero amplitude when centerline of a beam is considered while the edges reflect these modes with maximum amplitude. Extracting modal ridges in different lanes and placing them in parallel with the same order as the actual lanes construct a 3D representation of the torsional mode shapes.

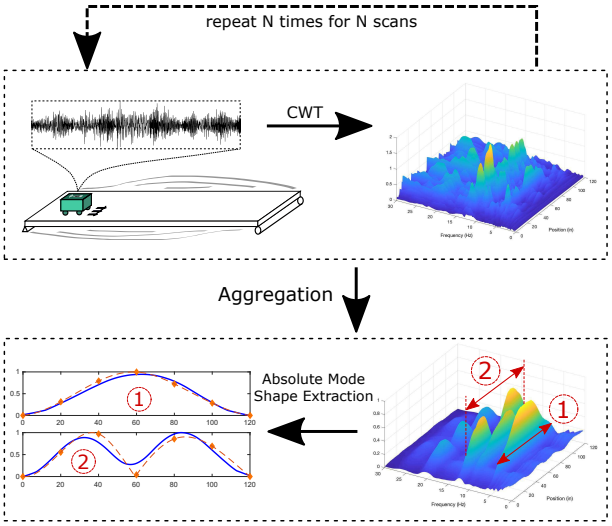

Figure 5.2: Crowdsourcing schematic for CMICW: each one-way vehicle scan collects a bridge response signal in a mobile fashion. The CWT of each signal includes ridges associated with natural modes that are severely mixed with noises (ambient ridges). However, once a large pool of CWT maps from different signals is collected, the average CWT map yields clear ridges on natural modes with minimal noisy contents. Note that each scan is independent to the rest (temporally and spatially).

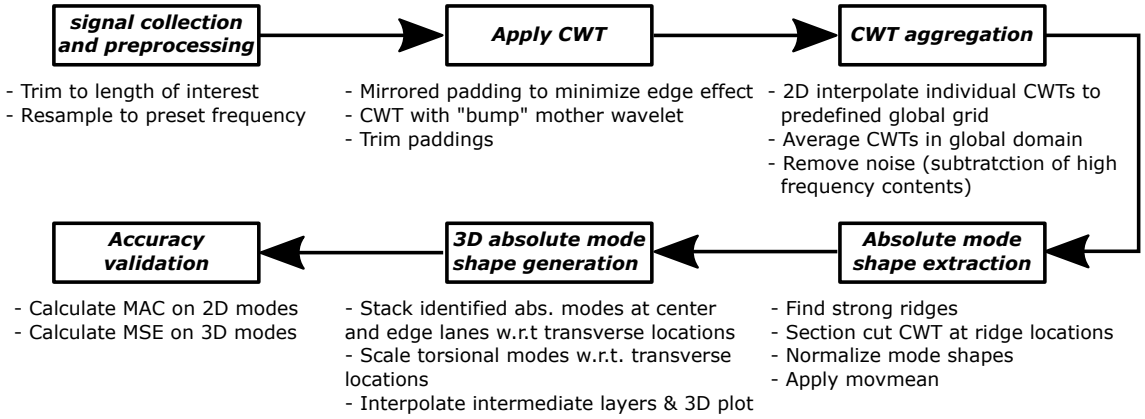

Figure 5.3: Detailed components of the CMICW pipeline.

5.4 Experimental Case Study

This section presents the setup of the laboratory-scale experiment and the results obtained from implementing the proposed method for modal identification along with validating estimations using fixed sensors as a benchmark. The test mimics a bridge subjected to random ambient load, monitored by moving sensors at random time intervals that are independent. Results show that the procedure successfully identifies

three vertical modes and two torsional modes using mobile smarthphone data.

5.4.1 Test Setup

The test setup consists of a steel beam that is 3.66m long, 0.635m wide and 6.35mm thick with two 4.33kg weights attached at midspan. The steel plate is placed on pin supports at 30cm to the both ends, and a hydraulic jack located below the bridge applies an adjustable, horizontal, post-tensioning force. The post-tensioning system allows for control over the stiffness of the model bridge. As seen in Figure 5.4, mobile sensors traversed the bridge using a pulley system. An AppliedMotion STAC6-Si motor towed mobile sensors on four different lanes. The application Si Programmer was used for motion planning and scheduling.

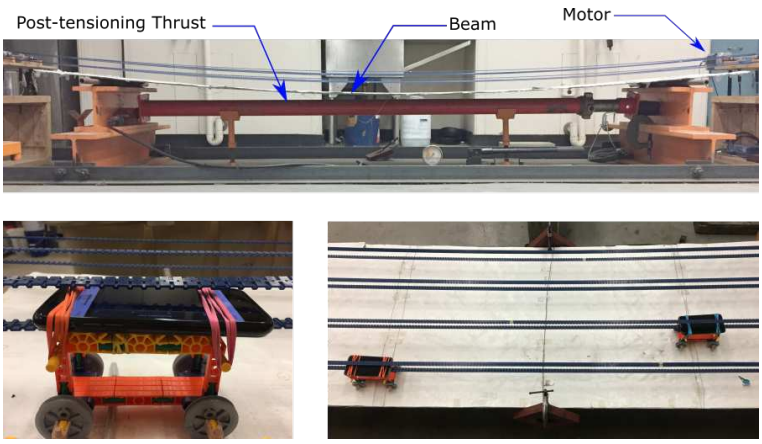

Figure 5.4: Layout of the test setup: (top) side view of the beam, (bottom-left) individual mobile sensing node, and (bottom-right) mobile sensors in motion.

Mobile sensors comprised of carts made from K'NEX with rubber bands binding a smartphone to each cart. The phones used the application Sensor Kinetics Pro to collect data at the maximum sampling rate (100 Hz) with no signal filtering. During testing, six iPhones ranging in model from iPhone6 to iPhone10 were used. Although the application set the sampling rate to 100 Hz, the actual sampling rate varied between phones. Each test required a lab assistant applying moderate-sized, random impulses along the bridge as the cart traveled down the bridge. The goal of the

excitation was to simulate an ambient random loads. The cart motion was planned to scan the bridge one way, then pause, and return to the starting position. Therefore, each test consisted of two scans of the bridge by each mobile phone. After collecting a large pool of one-way scans, the data passed through the pipeline shown in Figure 5.3.

In addition to the mobile sensing tests, the beam was monitored using stationary sensors to create a baseline for validation. Two separate stationary sensing tests were completed. For the first test, five smartphones evenly spaced in the longitudinal direction collected data and then the phones were rearranged to capture torsional modes along two parallel lanes in the transverse direction. The signals were trimmed to 30-second segments for analysis. Finally, the data channels were processed using SMIT [Chang and Pakzad, 2013b], a MATLAB-based modal identification software to identify natural frequencies and modes shapes. The software allows for selecting a desired SID method among multiple common algorithms. In this study, the ERA-NEXT-AVG method [Chang and Pakzad, 2012] was used for processing the stationary data. The resulting frequencies are found in Table 5.1 and the natural mode shapes are presented as the baseline in multiple figures (e.g., Figures 5.5 and 5.6) and used for MAC value calculations.

5.4.2 Mobile Scans with Constant Speed

In the first case, the test includes aggregation of mobile sensors with constant speed to simplify and validate that the proposed pipeline functions properly. In order to achieve this, 240 one-way scans of the bridge with the smartphone-equipped carts were performed. The speed of the sensors was set to 11.38cm per second (one way scan was 26.4sec). Aggregating the scans using the pipeline, the test yields the results shown in Figure 5.5. This figure displays the aggregated CWT maps in 2D and 3D. Within these maps, the ridges are then picked automatically by a pick-peaking

algorithm. The section-cuts of the maps at these peaks are presented in Figure 5.6. Through aggregation, the undesired random noise in single scans diminishes, leaving the consistently occurring mode shapes. Note that CWT calculates the absolute amplitudes of instantaneous frequencies. In this case, phase information is unavailable since the datasets are not recorded simultaneously. Therefore, the resulting ridges of the CWT map represent the absolute mode shapes of the bridge.

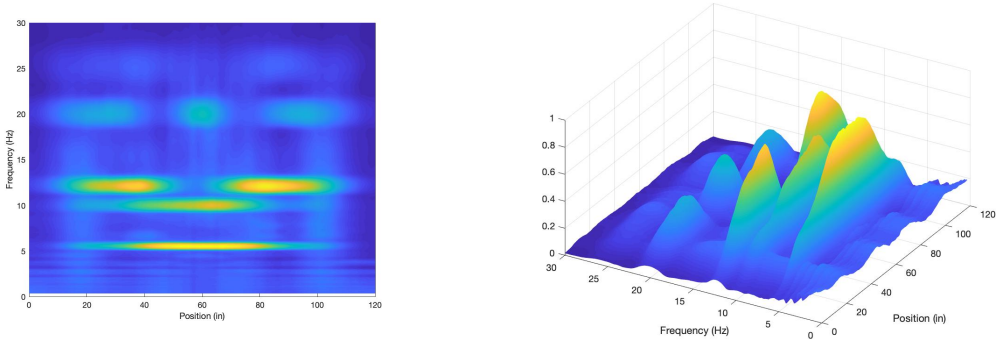

Figure 5.5: Aggregated CWTs of 240 one-way scans on the edge lane of the model bridge at medium speed

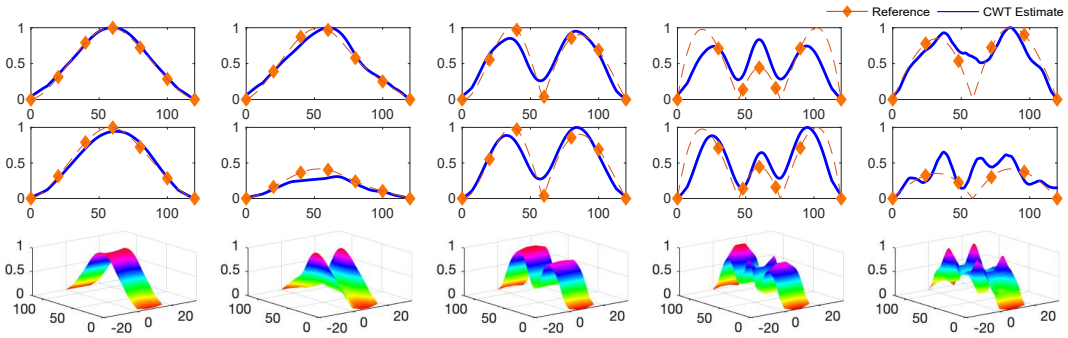

Figure 5.6: Three vertical and two torsional absolute mode shapes from 240 scans at medium speed on the edge and middle lane of model bridge.

The accuracy of identified modal parameters is presented in Table 5.1. The MAC values for the first three modes are above 0.95 (first two modes above 0.99) when compared to the fixed sensor baseline, indicating high accuracy in the estimation at lower modes. The accuracy of the estimated mode shapes at two higher modes is also fairly high. Additionally, all the identified frequencies are within 1.5% of the fixed

Table 5.1: Identification accuracy measures for the single speed case. Est. stands for estimation.

	Mode 1	*Mode 2*	*Mode 3*	*Mode 4*	*Mode 5*
Reference freq. [Hz]	5.51	9.93	12.34	20.26	24.99
CMICW freq. [Hz]	5.57	10.07	12.32	20.13	25.36
Est. error [%]	1.09	1.41	0.16	0.64	1.48
Edge lane, MAC [%]	99.81	99.19	95.60	90.16	97.23
Mid lane, MAC [%]	99.43	99.26	94.69	98.67	82.64

sensor reference found in Table 5.1. These results confirm that CMICW functions as expected and yields high accuracy.

5.4.3 Speed Variations Effect

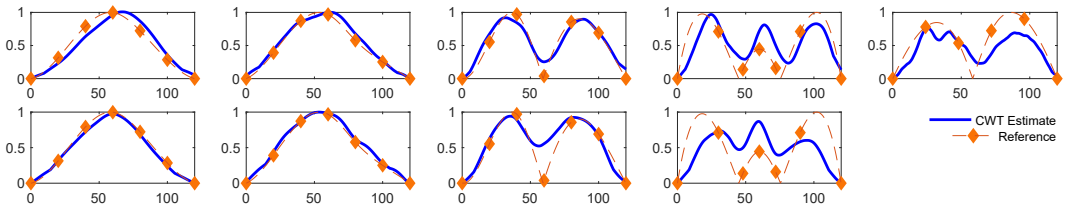

Figure 5.7: Identified absolute mode shapes with 80 one-way scans using slow sensors (top row) and fast sensors (bottom row). Note that the fifth mode is not identified using fast moving sensors.

Table 5.2: Identified accuracy measures for different speed cases. Est. stands for estimation.

	Mode 1	*Mode 2*	*Mode 3*	*Mode 4*	*Mode 5*
Reference freq. [Hz]	5.51	9.93	12.34	20.26	24.99
Slow CMICW freq. [Hz]	5.49	10.21	12.32	20.13	25.00
Fast CMICW freq. [Hz]	5.57	10.07	11.79	19.84	-
Est. error, Slow [%]	0.36	2.82	0.16	0.64	0.04
Est. error, Fast [%]	1.09	1.41	4.46	2.07	-
Edge lane MAC, Slow [%]	97.55	99.59	95.87	85.91	94.53
Edge lane MAC, Medium [%]	99.41	98.97	95.22	91.45	96.79
Edge lane MAC, Fast [%]	99.87	99.78	90.12	82.47	-

The previous experiment is limited to cases in which all scanning carriers retained constant speed. To generalize the application, two additional pools of scans containing

(a) 80 slower scans (9.50cm per second) and (b) 80 faster scans (14.53cm per second) were collected. Three datasets (slow, medium, and fast speeds) are then processed using CMICW (shown in Figure 5.3) and results are compared in Figure 5.7 as well as Table 5.2. Plot in Figure 5.7 present the identified absolute mode shapes from slow and fast datasets. All five modes were identified accurately in the case of slow speeds. However, with carts moving faster the accuracy of higher modes rapidly decreases. Examining the noise beds - detectable from the local minima of the identified modes at the valleys of the mode shapes - are noticeably higher in the fast speed case (e.g., in the third mode). In other words, as the speed increases, the accuracy of sharp curvature changes in the mode shapes reduce significantly. This can be explained by the fact that faster carriers noticeably magnify noises (e.g., road bumps) compared to slower counterparts. This observation will be further discussed in the following sections and is consistent with existing literature [Yang and Chang, 2009].

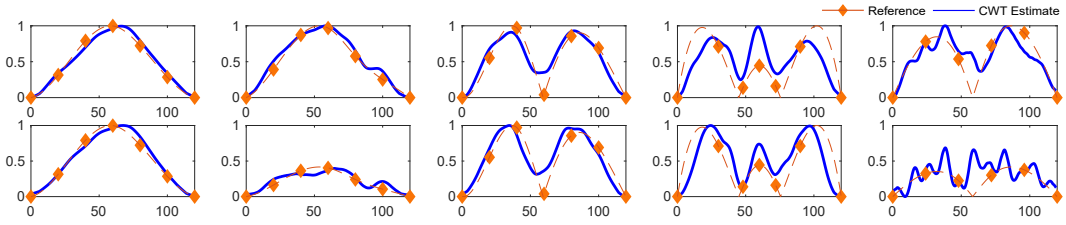

Figure 5.8: Identified absolute mode shapes through aggregating 80 slow, medium, and fast signals (240 one-way scans total). Top and bottom rows show the edge and middle lane results, respectively.

Table 5.3: Identification accuracy measures for the aggregated speed case. Est. stands for estimation.

	Mode 1	*Mode 2*	*Mode 3*	*Mode 4*	*Mode 5*
Reference freq. [Hz]	5.51	9.93	12.34	20.26	24.99
CMICW freq. [Hz]	5.50	10	12.25	20.25	25.25
Est. error [%]	0.18	0.70	0.73	0.05	1.04
Edge lane, MAC [%]	99.39	98.78	95.19	88.40	96.12
Mid lane, MAC [%]	99.17	94.93	95.01	97.94	90.73

5.4.4 Mobile Scans with Varying Speeds

The objective of this test is to show that the proposed method can incorporate generic car speeds since each car is analyzed independently. A database of 240 CWT scans is composed of 80 one-way scans with slow, medium, and fast speed. The speed-dependent map is interpolated to a preset global space-frequency grid so that it can be aggregated with other scans. Following the same process described in section 5.3, the mode shapes are extracted and compared to fixed sensor results in Figure 5.8. All five mode shapes that were previously identified in the slow and medium tests are successfully identified in this random aggregation case as well. The aggregated results from different speeds show a comparable accuracy with respect to the constant medium speed test, which has the same sample size. This trial demonstrates that CMICW is applicable for mobile sensors with generalized speeds. Note that the sample pool using which these results are derived is still quite small compared to the data collected on real-world bridges. Bridges that serve a large volume of vehicles daily represent a wealth of information that can be captured by mobile smartphones. It is expected that as the sample size grows, the variance of the estimated modal properties decreases. This is discussed in Section IV.

Table 5.4: Mechanical properties of vehicles used in simulation.

	V1	*V2*	*V3*	*V4*	*Units*
Suspension Stiffness	62.30	128.7	2.7e5	5700	N/m
Suspension Damping	6.0	3.86	6000	290	Ns/m
Sprung Mass	1	1	3400	466.5	Kg
Unsprung Mass	0.15	0.162	350	49.8	Kg
Tire Stiffness	653	643	9.5e5	1.35e5	N/m
Tire Damping	0	0	300	1400	Ns/m

5.4.5 Incorporating Suspension Effect - a Hybrid Simulation

The mobile carts used in the experiments were stiff; in a real-world scenario with a moving vehicle, the measured accelerations would be affected by the suspension system. This section describes a technique to simulate smartphone-in-vehicle scenarios using a quarter car suspension model to consider a more realistic dynamical response [Malekjafarian and OBrien, 2014a]. The process is as described previously with a new step preceding modal identification: the experimental mobile sensor measurements are fed into a vehicle suspension model. Each individual signal is processed through a linear state-space model which corresponds to the mechanical properties of a quarter-car. To consider the case of multiple vehicle sources, the vehicle properties were selected randomly from the candidates presented in Table (5.4) [Sun et al., 2001, Bogsjö et al., 2012, Florin et al., 2013, Gillespie and Sayers, 1985]. With this model, both vehicle speeds and suspension systems can be randomized to better simulate real traffic on a bridge. The transfer functions of the four cars are found in Figure 5.10. Note that the candidate car types were adopted from other studies, mimicking real-world vehicles in their dynamical properties. Due to the ride comfort concerns, the fundamental mode of vehicle suspensions is around 1.0 Hz, and the highly damped second natural frequency is approximately 10.0 Hz.

Figure 5.9 shows the absolute mode shapes identified by aggregating 80 constant speed slow scans compared to aggregating 240 one-way scans with mix speed aggregation, as seen in Section 5.4.4. Additionally, the post-process for both tests remained the same for a fair comparison. Results are consistent with previous experiments. The first three modes are found with high accuracy as presented in Table 5.5. Due to the shape of the transfer functions, certain ranges of the bridge frequency contents are amplified and others diminish substantially, as depicted in Figure 5.10 (e.g., the fifth mode, at 25 Hz, has nearly vanished). Overall, this effect reduced the contribution of higher modes. In addition, Figure 5.10, includes a vertical pattern at five different

locations, which is not present in Figure 5.5(a). This pattern corresponds to noise generated by the bumps in the experimental setup. Because different speeds have been aggregated, the bump-induced impulses affect the entire frequency spectrum. When the vehicle speed is slow, the effect of these impulses on mode shape estimation is less significant. The result is an accuracy that is comparable with an analysis using only one-third the sample size. To mitigate the "bump effects", an average of the noise bed over the CWT map is removed from the aggregated map.

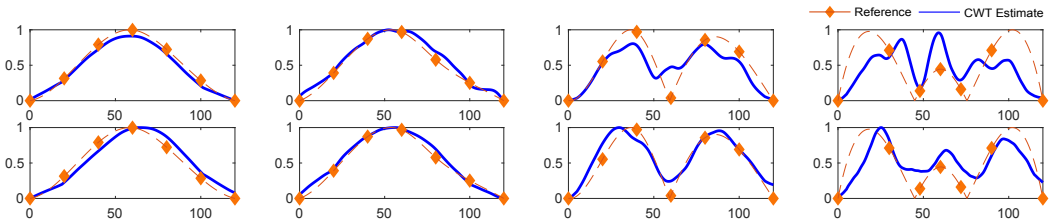

Figure 5.9: Identified absolute mode shapes from hybrid simulation using only slow moving sensors (top row) and aggregation of different speeds (bottom row).

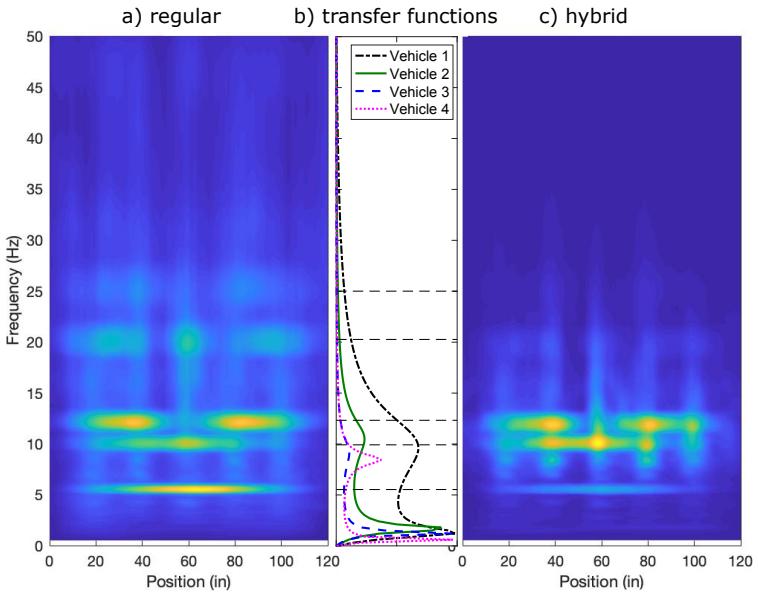

Figure 5.10: CWT map before and after the hybrid simulation. From (b), higher frequency contents of the bridge are filtered out by the low amplitude tails of the transfer functions, resulting no absolute bridge mode extraction within this high frequency range in (c). This implies that sensing vehicles have to be chosen carefully in order to observe desired frequency range.

Table 5.5: Identification accuracy measures for the hybrid simulation. Agg. and est. stand for aggregated and estimation, respectively.

	Mode 1	*Mode 2*	*Mode 3*	*Mode 4*
Reference freq. [Hz]	5.51	9.93	12.34	20.26
CMICW slow freq. [Hz]	5.72	9.67	12.15	20.31
CMICW agg. freq. [Hz]	5.72	10.42	13.38	19.81
Est. error, Slow [%]	3.81	2.62	1.54	0.25
Est. error, Agg. [%]	3.81	4.93	8.43	2.22
Edge lane MAC, Slow [%]	99.52	99.35	94.16	87.76
Edge lane MAC, Agg. [%]	99.86	99.31	89.94	78.35

5.5 Discussion and Conclusion

5.5.1 Statistical Analysis

CMICW can operate exclusively from crowdsourcing. In the previous sections, it was shown that when the sample size is large, more accurate results are expected. However, the confidence of estimations with respect to the sample size has not been investigated. Figure 5.11 presents the identification accuracy of the fundamental mode using 20 samples versus 480 samples (selected from medium speed scans). The lines show the average of mode shapes from all individual scans and the shady area around centerlines indicate the 95% confidence intervals in the estimations. The figure demonstrates that by increasing the number of samples, not only the accuracy of the estimations increase (i.e., shape of the mode), but also the confidence of estimations. In the lower part of the figure, the trend of confidence interval width versus the sample size is presented, consistent with this finding. The fact that the mode shape identification result eventually becomes more reliable (e.g., 30% reduction in CI when number of scans grow from 50 to 100) show the promising strength of this crowdsourcing-based method.

To generalize the scalability of the method, in Figure 5.12, the trends of the identified modes' MSE and MAC values are analyzed with respect to the sample size.

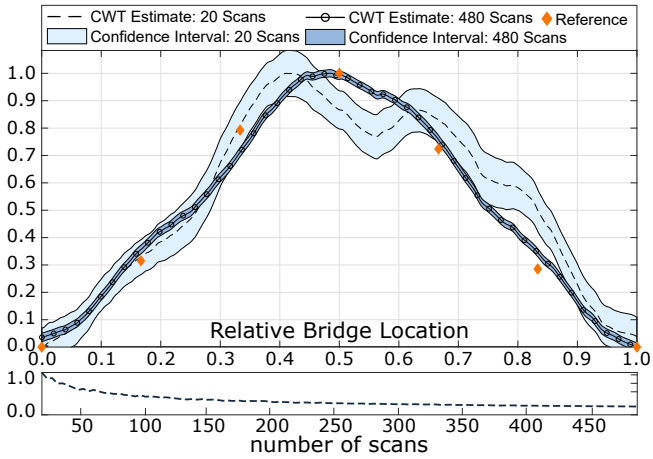

Figure 5.11: Identified fundamental mode using 20 scans versus 480 scans: the confidence interval of the identified points has significantly narrowed by crowdsourcing more data. Below the confidence interval width vs. number of aggregated scans is plotted.

For maximum fairness of the trial, 100 random sample sets are picked for each sample size, and results are averaged. In all cases, as the size of the aggregation pool increases, it is more likely to predict modal properties accurately. Note that in some cases, one may pick a very nice subset of the scans, using which the estimation outperforms the estimations with more samples. This supports the idea that by aggregation of larger pool of data, the reliability of estimations increases, because they gradually become less and less sensitive to the quality of individual samples.

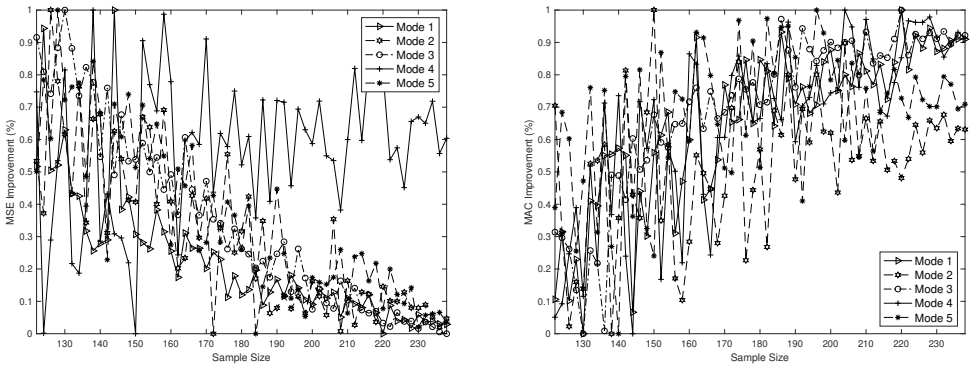

(a) MSE trend on 3D modes (b) MAC trend on edge lane

Figure 5.12: Accuracy measures vs. sample size. Both figures confirm that as the number of scans increases, the error reduces and the accuracy also improves.

CMICW is prone to intrinsic biases when it comes to the spatial information. These biases were visible in Figure 5.11 where the reference points (found using fixed sensors) fall outside the band of confidence interval (e.g., with 480 scans). In other words, the plot shows that in some locations, the aggregation yields a confident estimation that is slightly inaccurate (e.g., the reference point at relative location 0.83 in Figure 5.11). In this context, the bias is explained as an unreducible error in the mode shape amplitudes caused by consistent physical obstacles for a smooth sensing, such as expansion joints and speed bumps (note that road irregularity is not a consistent obstacle since it may or may not appear in a single scan). These obstacles (among other variables) introduce an undesired content to every scan, causing a bias in the final amplitude of the modal ridges at those location. Since this effect happens in every scan, it is not reducible by adding more scans to the pool. To better examine these, Figure 5.13 shows errors in identified mode shapes via different sample sizes. The red lines indicate the errors in the estimated fundamental absolute mode shape when compared with the stationary sensors result. The bias between small and large sample sizes is reduced considerably (in particular, 92% bias reduction between 20 scans and 480 scans), nevertheless, the error is still present in the case with the larger sample size.

In our experimental setup, there were transversal wires that act as speed bumps and joints, which can explain the unreducible errors in those locations. To remove this undesired content, blind source separation techniques can be applied as proposed in Sadeghi Eshkevari et al. [2020b], Eshkevari and Pakzad [2019b]. In this approach, given multiple scans over a certain portion of the bridge, algorithms such as ICA or SOBI can extract the common content - consistent road bumps or joints - as one of the sources. Once it is extracted, mobile scans can be filtered and the aggregation will be performed on the filtered signals. The method is implemented here and the final effect on the unreducible error is presented in Figure 5.14. In this figure, a

comparison between error values before and after applying ICA demonstrate that the decontamination technique enhanced the performance of the algorithm. In particular, the effect on higher modes is more significant.

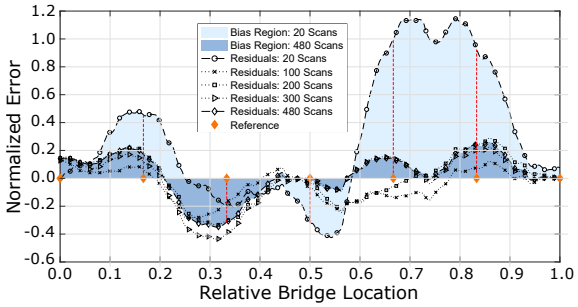

Figure 5.13: Unreducible bias analysis based on the first mode shape. As the sample size grows, the error at stationary locations reduces. However, the error does not reach zero due to the presence of consistent physical obstacles (here, transversal wires).

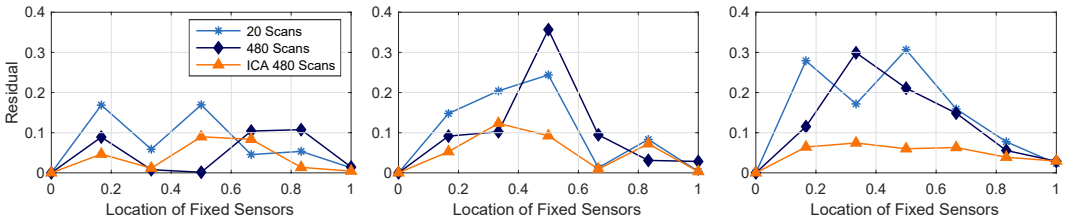

Figure 5.14: Identified mode shape error before and after applying ICA for separation of the effects of consistent obstacles (here, wire bumps) for the first three modes. For higher modes, ICA dramatically helped to reduce the error. In particular, the accuracy of the third mode (right) has improved by 70% after ICA post-processing.

5.5.2 Final Remarks

This study presented and experimentally validated a novel crowdsensing approach for bridge health monitoring using smartphones. In particular, CMICW method is able to estimate natural frequencies and absolute mode shapes. The method aggregates spatio-temporal maps of the individual signals collected by mobile smartphones to estimate the modal properties of a bridge. In this study, we showed that the approach has the following advantages:

- CMICW is a fully crowdsourcing based approach using widely available smartphones for bridge modal identification.
- This method does not require synchronized or simultaneous sensors, which maximizes its implementation.
- The MAC accuracy of identified mode shapes enhances as more data become available. In addition, by aggregating more data, the estimations become more reliable (i.e., narrower CI).
- This method is adoptive over time. If bridge properties change over time, CMICW gradually updates its estimations based on new data and identify the variations.
- Vehicle suspension results in a loss of higher modes; however, as long as the suspension properties of the vehicles that are used in a large dataset are random, the frequency contents of the suspension itself vanish through the aggregation process and the lower modes are accurately identified.
- By aggregation of results from different lanes of a bridge, a 3D representation of the identified modes is achievable.

CMICW was validated using an experimental setup. In summary, the first five natural modes of the beam setup were targeted for the modal identification (three vertical and two torsional modes). Three test cases were conducted: (a) 240 medium speed scans, (b) 80 scans with fast and slow speeds (each), and (c) hybrid simulation of vehicle suspension. By aggregation of the samples with constant speeds, we were able to identify all five modes for the slow and medium speed cases and first four modes with the fast speed case (e.g., first two natural modes with MAC 99% and frequency estimations within 1.4% error). In the second aggregation strategy, 80 scans from each speed were picked randomly to simulate a more realistic sample set.

The aggregation resulted all five modes with MAC estimation of $> 95\%$ for the first three modes and frequency estimations within 1.0% error. In the final aggregation strategy, the same sample set described previously was passed through a random group of quarter-car suspension models in order to simulate vehicle manipulation of signals. From this hybrid simulation, the first four modes were identified (e.g., the first three modes yielded MAC values $> 90\%$). The fifth mode was not identifiable due to its overlap with the low amplitude range of the vehicle transfer function. The hybrid simulation also was repeated using only 80 slow scans, that resulted in higher estimation accuracy (e.g., the first three modes yielded MAC values $> 94\%$).

CMICW is a promising solution for large-scale, fully data-driven, crowdsourcing-based method for the structural health monitoring of bridges.

Chapter 6

DynNet: Physics-based neural architecture design for linear and nonlinear structural response modeling and prediction

6.1 Abstract

Data-driven models for predicting dynamic responses of linear and nonlinear systems are of great importance due to their wide application from probabilistic analysis to inverse problems such as system identification and damage diagnosis. In this study, a physics-based recurrent neural network model is designed that is able to learn the dynamics of linear and nonlinear multiple degrees of freedom systems given a ground motion. The model is able to estimate a complete set of responses, including displacement, velocity, acceleration, and internal forces. Compared to the most advanced counterparts, this model requires smaller number of trainable variables while the accuracy of predictions is higher for long trajectories. In addition, the architecture

of the recurrent block is inspired by differential equation solver algorithms and it is expected that this approach yields more generalized solutions. In the training phase, we propose multiple novel techniques to dramatically accelerate the learning process using smaller datasets, such as hardsampling, utilization of trajectory loss function, and implementation of a trust-region approach. Numerical case studies are conducted to examine the strength of the network to learn different nonlinear behaviors. It is shown that the network is able to capture different nonlinear behaviors of dynamic systems with very high accuracy and with no need for prior information or very large datasets.

6.2 Introduction

Dynamic response prediction of structural systems has been a great tool for design and assessment of individual buildings as well as reliability analysis of infrastructure and large urban areas. Traditionally, this process is executed by building numerical models of dynamic systems and predicting responses using numerical differential equation solvers such as Newmark-β method. However, this approach is suitable for structures with known physical properties (i.e., mass, stiffness, and damping matrices) with very accurate analytical modals for nonlinear components of the structures. Structural health monitoring (SHM) methods have been effective in identifying mechanical properties of the existing structures. Yet, the dynamic response simulation of an existing system requires a comprehensive SHM phase for model updating [Yuen et al., 2006, Ching and Beck, 2004, Johnson et al., 2004, Shahidi and Pakzad, 2014]. In addition, for an accurate simulation of a structure with nonlinear components, emerging technologies such as real-time hybrid simulation are proposed [Christenson et al., 2008, Ahmadizadeh et al., 2008, Al-Subaihawi et al., 2020]. This approach is also limited to individual nonlinear structural components and requires advanced

experimental and numerical devices.

Artificial intelligence has been one of the most useful and promising tools in science and technology over the past few decades. In particular, machine learning has demonstrated a great potential for learning and predicting nonlinear behaviors and trends in large and noisy datasets [Deng et al., 2014]. Neural Networks (NN) have shown an exceptional potential as universal function approximators with minimal need for prior information about the underlying knowledge of a problem [Cybenko, 1989, Leshno et al., 1993]. However, in engineering applications, black-box function approximators are less favored due to the fact that for many of those, solid underlying equations/models exist. Knowledge-based machine learning approach intends to bridge this gap by contributing governing equations into machine learning models [Towell et al., 1990].

6.2.1 Artificial Intelligence in Civil Engineering

In general, the major applications of machine learning in civil engineering can be divided into following categories: (a) system identification (SID); (b) damage detection; and (c) dynamic response prediction of structures. A detailed overview of machine learning algorithms for damage detection is given in Worden and Manson [2007], Ying et al. [2013]. In summary, the methods use machine learning algorithms (e.g., support vector machines (SVM) and multi-layer perceptrons (MLP)) for classification between damaged and undamaged states of structural components based on low-level inputs (e.g., motion sensor data). A multi-stage damage detection method is proposed by Yi et al. [2013] in which signal features are extracted using wavelet transforms and an MLP network diagnoses whether damage has occurred. Gui et al. [2017] proposed a method for feature extraction from sensor data time series and damage classification based on these extracted features using SVM. More recently, end-to-end damage detection algorithms are emerging in which feature extraction and

damage detection stages are combined in a single estimator. Abdeljaber et al. [2017] proposed a vibration-based convolutional neural network (CNN) for direct damage detection and localization based on sensor time signals. Gulgec et al. [2019] proposed a one-step vision-based damage detection and localization method via CNN which uses 2D strain fields as input.

Fewer studies have investigated data-driven methods for system identification due to the inherited model-dependency of this problem. Some efforts have been made to reconstruct underlying equations using data-driven algorithms. Brunton et al. [2016] proposed a look-up approach to reconstruct the governing equation of dynamic systems using sparse identification. More recent studies investigate machine learning solutions with model-guided constraints. Raissi and Karniadakis [2018] introduced hidden physics models that are able to identify underlying physics of dynamic systems using small datasets. In civil engineering, Sadeghi Eshkevari et al. [2020d] proposed a data-driven approach for bridge modal identification using mobile sensing data. The model is highly constrained by the modal superposition law of structural dynamics and could successfully identify complete modal properties.

In addition to diagnosis and monitoring tasks that are objectives of the previous studies, data-driven approaches for dynamic response prediction of structural systems has been of great importance and interest. Finite element analysis (FEA) along with nonlinear time history analysis (NTHA) has enabled very accurate dynamic response estimations; however, both techniques are computationally expensive and require detailed information of the system. By emergence of probabilistic reliability analyses of individual and clusters of structures subject to hazards (e.g., earthquake), it is realistically impractical to carry out extensive FEA and NTHA analyses of increasingly larger systems [Song and Ok, 2010, Mahsuli and Haukaas, 2013]. Therefore, faster, more flexible, and reliable approaches are highly required.

6.2.2 Data-driven Dynamic Response Prediction

Dynamic response prediction of structures using statistical methods have been widely investigated over the last few years. The approaches span from model-based predictions to data-driven models such as autoregressive moving average (ARMA) models or neural networks. A model-based full state predictor is proposed that incorporates a prior nonlinear model of the building for experimental response prediction [Roohi et al., 2019]. Mattson and Pandit [2006] proposed an autoregressive model to predict major trends of the dynamic response; however, the effect of exogenous input was remained and considered as residual. In fact, despite their simplicity, ARMA-based models are limited to stationary and linear systems. To address that, Bornn et al. [2009] proposed an autoregressive SVM that incorporates nonlinear functionalities within the prediction equation. Neural networks (NN) have been the most recent approach for dynamic response prediction due to their flexibility and great performance in regression problems. The pioneer studies were focused on simple MLP models for partial one-step ahead response prediction (i.e., predictions include some but not all of the followings: displacement, velocity, acceleration, and internal force of all degrees of freedom). Lightbody and Irwin [1996] proposed a single layer neural network in which the output is a weighted sum of multiple trainable AR models with *Tanh* activation. The study was a breakthrough that enhanced estimator complexities from individual linear model to a nonlinear ensemble of linear models. By recent computational developments, deeper MLP networks were utilized for more comprehensive dynamic response predictions of nonlinear cases. Lagaros and Papadrakakis [2012] proposed a MLP for one-step ahead response prediction of nonlinear buildings. The method showed great performance both numerically and experimentally, however, the prediction was limited to displacement time histories. Note that in general there is no guarantee for reasonable predictions of other response components (e.g., velocity and accelerations) using a single component when using data-driven regression methods.

Therefore, yet more comprehensive predictive models are required.

Theoretically speaking, MLPs are ideal when the input features are fully independent. In dynamic response prediction problem, however, a high inter-dependency between responses at consequent time steps exist. Therefore, other neural network architectures have been also utilized for this specific problem. CNNs are known for their strength in extracting local (e.g., spatial or temporal) features and inter-dependency of input nodes [Sainath et al., 2015]. In addition, the state-space model of the training variables is dramatically reduced since fixed sized kernels are being trained rather than large variable matrices from fully-connected layers. CNNs are mostly used for computer vision applications in which 2D kernels are applied on pixel pallets. In signal processing, 1D kernels are more proper choices. A dynamic response predictor for linear systems using CNNs is introduced in Sun et al. [2017]. More recently, Wu and Jahanshahi [2019] introduced a CNN-based algorithm for different partial dynamic response predictions. The most advanced case included prediction of acceleration response at the roof level of a multi degrees of freedom (MDOF) system given the ground motion.

Comprehensive dynamic response prediction of nonlinear systems has been investigated in a few recent studies. Zhang et al. [2019a] confirms that recurrent neural networks (RNN) are structurally great candidates for structural dynamic response modeling, however, technically they suffer from gradient-vanishing issue during training process. In fact, RNN models have been a frequently used architecture in the previously mentioned models (i.e., all one-step ahead response prediction models are basically RNN models). Based on this argument, Zhang et al. [2019b] proposes a long short-term memory (LSTM) architecture for the response modeling in order to address the gradient-vanishing issue. The primary difference of LSTM models compared to vanilla RNN models is the special architecture that allows for learning long-term temporal dependencies. The study successfully predicted displacements,

velocities, accelerations, and internal forces using the ground motion in different non-linear cases. However, the model consisted of a large trainable variable space and required very long training process (i.e., 50,000 epochs).

The same research team has also recently introduced physics-guided models using CNN and LSTM architectures for dynamic response prediction problem [Zhang et al., 2019a, 2020]. The studies propose an additional term in the loss function of the problem which penalizes deviations in the equation of motion when predicted outputs are plugged in. The studies showed that imposing this new physical constraint helped to enhance the prediction accuracy. Despite their high accuracy and completeness, the NN architectures are vanilla versions of the common NN types with no guidance from the physics. This results in over-complicated networks that require high number of training epochs. In addition, LSTM model requires a fixed signal length which is limiting.

In our study, we focus on designing architecture of a recurrent neural cell that updates the state from current time step to the next (i.e., one-step ahead predictor) with the neural connections that are inspired by exact numerical differential equation solvers. We believe that an ideal network is able to predict a response merely based on current time step of a full state space, as it is hardcoded in the simulation algorithms such as Newmark-β.

6.2.3 Motivation

As the ubiquity of data-driven methods grows, the generalization and reliability of these models become more important. The vast majority of the available research train neural networks with no consideration for solid knowledge that governs the actual problem in hand. In addition, for engineering applications as opposed to data science problems, the available data is not extremely large and does not cover the entire domain of application possibilities (e.g., data is available for a limited domain

of linear response in operational conditions). These two concerns demand for incorporating physics constraints into the architecture design of the NNs. On the other hand, as the problem holds more constraints, the training process eventually becomes harder. This study proposes a new approach to impose a special architecture that is inspired by implicit equation of motion solvers into a recurrent cell for full response prediction of nonlinear MDOF systems. The proposed network is called DynNet in this article, standing for dynamic network. Moreover, this study recommends multiple techniques so that the training process becomes smoother and more reliable.

DynNet is a recurrent cell that performs one-step ahead prediction of the full state space of MDOF nonlinear dynamic system given a desired ground motion. The schematic structure of the network is presented in Figure 6.1. This architecture has no limitation for the length of the signal. Our contribution is to design the architecture based on implicit dynamic simulation algorithms for nonlinear time history analysis (e.g., nonlinear Newmark-β method). The key idea is that if the numerical algorithm is suitable and exact for nonlinear response analysis, a similar architecture has to be successful in learning the same nonlinear model from raw data. In addition, the architecture design is inspired by Residual Networks (i.e., ResNet) [He et al., 2015] that have shown outstanding performances in learning partial differential equations from raw data. DynNet has significantly smaller dimension compared to the most accurate counterparts.

In terms of network optimization, this study utilizes second order trust region method which dramatically reduces required training iterations. Training dynamic blocks for one-step ahead prediction is highly sensitive to instability. To overcome this challenge, we introduce projection loss function. In addition, to accelerate learning ability of the network for nonlinear transitions, a hardsampling technique is proposed and implemented. Although DynNet is strongly constrained which results in harder training, its smaller variable space and high constraints enable network training with

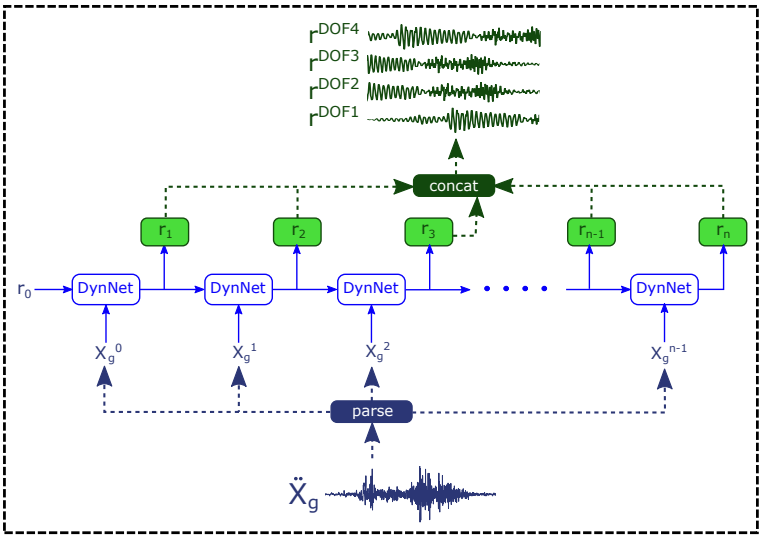

Figure 6.1: Schematic diagram of DynNet and conversion from ground motion to the structural response.

very limited amount of data. The physical interpretability of DynNet also helps to model highly severe nonlinear behaviors as well as very long signals, as we will show in the next sections.

In the following section, the detailed architecture of the network is elaborated. In Section 6.4 the technical approaches for faster and more robust training process of DynNet are presented (e.g., the optimization algorithm, loss function, and hardsampling technique). In Section 6.5 two numerical case studies are presented in which different types of nonlinearity are imposed. The summary of the method along with the highlights are presented in Section 6.6.

6.3 Physics-based Neural Network Architecture Design

6.3.1 Numerical Solution for Direct Problems

For simulation of dynamic systems, implicit solvers analyze responses at time step i to derive response at time step $i+1$. In fact, regardless of the complexity and level of non-

linearity of the problem, simulators require no further information for one-step ahead prediction. Relying on this fact, an ultimate simulator that learns from data should be a dynamic cell that is able to perform one-step ahead prediction with high accuracy and low cumulative error. In addition, considering the causality of the dynamic system as well as its short memory (i.e., a few recent samples are sufficient for the next step prediction), LSTM models seem unnecessarily over-complicated. DynNet is a robust one-step ahead dynamic cell that is very sharp in learning nonlinearities as well as robust to noise. In this study, we do not use a simplified version of existing networks such as CNN or LSTM, but instead design the internal cell connections in a way that conforms with common dynamic simulation solvers. The nonlinear version of Newmark's algorithm is shown in Algorithm 6 [Riddell and Newmark, 1979].

Algorithm 6 Newmark's Method for Nonlinear Systems.

Input: $u_i, \dot{u}_i, \ddot{u}_i, S_i, \ddot{x}_i^g$, TangentStiffness(.), NonlinearForce(.)
$a_1, a_2, a_3, C_1, C_2, C_3, C_4, C_5, C_6, M, \Gamma :=$ Constant
$\hat{p}_{i+1} = M\Gamma\ddot{x}_i^g + a_1 u_i + a_2 \dot{u}_i + a_3 \ddot{u}_i$
$R^{(0)} = \hat{p}_{i+1}$
$j = 0$
$K_i^t =$TangentStiffness$(u_i, \dot{u}_i, \ddot{u}_i, S_i)$
while $abs(R^{(j)}) < threshold$ **do**
    $R^{(j)} = \hat{p}_{i+1} - S_{i+1}^{(j)} - a_1 u_{i+1}^{(j)}$
    $(K_{i+1}^t)^{(j)} = (K_{i+1}^t)^{(j)} + a_1$
    $\Delta u^{(j)} = ((K_{i+1}^t)^{(j)})^{-1} R^{(j)}$
    $u_{i+1}^{(j+1)} = u_{i+1}^{(j)} + \Delta u^{(j)}$
    $S_{i+1}^{(j+1)} =$ NonlinearForce$(u_{i+1}^{(j+1)}, S_i^{(j)})$
    $j = j + 1$
$u_{i+1} = u_{i+1}^{(j)}$
$S_{i+1} = S_{i+1}^{(j)}$
$\dot{u}_{i+1} = C_1(u_{i+1} - u_i) + C_2 \dot{u}_i + C_3 \ddot{u}_i$
$\ddot{u}_{i+1} = C_4(u_{i+1} - u_i) + C_5 \dot{u}_i + C_6 \ddot{u}_i$
Return $u_{i+1}, \dot{u}_{i+1}, \ddot{u}_{i+1}, S_{i+1}$

In this algorithm, $u_i, \dot{u}_i, \ddot{u}_i$ are displacement, velocity, and acceleration vectors of current time step i, respectively. S_i and $\ddot{x}_i^g$ are respectively the internal force vector and ground motion acceleration at time i. In this algorithm, the detailed expressions

for constant coefficients are discounted. The algorithm consists of a majority of linear expressions and some nonlinear functions - TangentStiffness(.) and NonlinearForce(.) - that depend on the defined nonlinearity of the system (the first function returns tangent stiffness and the second function derives nonlinear story forces based on the nonlinear model). In particular, the algorithm can be divided into three blocks: (a) initialization; (b) equilibrium solver; and (c) post-processing. In this organization, blocks (a) and (c) merely include linear operations. For instance, in Line 16, the relationship between displacement and velocity of the future time step is a linear expression.

In addition, block (b) contains a `while` loop which certifies the equilibrium (i.e., Newton-Raphson root finding solution). Intuitively, this while loop incrementally adds up values to its estimation of u_{i+1} every time the loop runs. This mechanics resemble the mechanics of Residual Networks (ResNet) [He et al., 2015] in which the output of the network is added to the input and fed back to the network repeatedly. Studies have shown that ResNets outperform other architectures in learning differential equations from data due to their inherited resemblance to the Euler's method [Lu et al., 2017, Chen et al., 2018].

6.3.2 DynNet Components

DynNet is designed to benefit from two intuitive ideas: (1) inspired by the structure of numerical implicit simulators; and (2) ResNet structure for nonlinearity learning. The architecture of the network is given in Figure 6.2. The input of the network is identical to the Newmark's algorithm. All connections in the network are linear expect for the internal connections of the ResNet block. The network initially adjusts the dimension of the input vector via a linear embedding layer. Then, velocity and acceleration of the structure in addition to the ground motion acceleration of the current time step are fed into a linear layer to produce R_u^n (equivalent to R in Algorithm 6). Then,

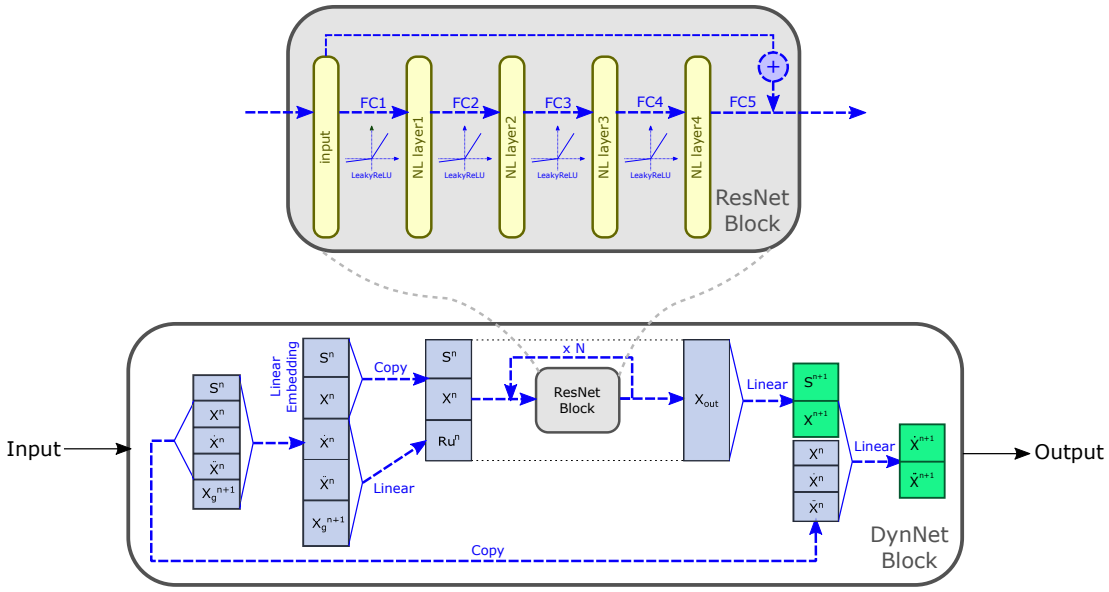

Figure 6.2: DynNet recurrent cell components.

internal force, displacement, and R_u are concatenated and passed into the ResNet block. The ResNet block is expanded in Figure 6.2 as well. This block is the sole component of the network that is able to learn the nonlinear behavior of the dynamic system. The block is conveniently arranged with stacked fully-connected layers that are connected with leaky rectified linear units (i.e., LeakyReLU activation functions). The output of the fifth fully-connected layer is added to the input of the ResNet block to produce the terminal state of the ResNet block. This terminal state is fed back to the ResNet block N times (N is a user defined parameter). After N repetitions, the output is linearly mapped to S_{i+1} and X_{i+1}. Given X_{i+1}, the velocity and acceleration of the next time step are derived by another linear map. Once the prediction of time step $i+1$ is found, it will be fed back to DynNet for the response prediction of the consecutive time step (e.g., $i+2$).

The concentrated learning ability that is placed in the ResNet block enables easy replacement of the simple MLP network with other nonlinear structures (e.g., CNN or deeper networks). This feature decouples the nonlinearity learning and state transitioning tasks of the network. In other words, for very involved types of nonlinearities,

one simply requires to modify the structure of the ResNet block (e.g., add extra layers). However, in this study we found a five layer MLP sufficiently strong for the test cases. The variable space of the network is highly dependent to the user-defined embedding dimension. In this study, embedding size is set to eight for all cases, yielding $5,320$ trainable variables. The dimension is significantly lower compared to other recently developed networks for the same purpose.

6.4 Accelerating Techniques for the Training Phase

6.4.1 Selecting Optimizer

Stochastic first-order methods, including SGD [Robbins and Monro, 1951] and Adam [Kingma and Ba, 2014], are currently standard optimization methods for training neural network problems. These methods have a low per-iteration cost, enjoy optimal complexity, and are easy to implement and applicable to many machine learning tasks. However, these methods have several issues: (i) they are highly sensitive to the choice of hyper-parameters (such as batch size and learning rate); and more importantly (ii) they are not effective for ill-conditioned problems, meaning that for a small change in the inputs, the outputs can change dramatically. The second issue is quite likely when dealing with nonlinear structural systems. For instance, in an elasto-plastic model, there is a bounded relationship between force and displacement within the elastic range. However, the variations of displacements become extremely large when the system experiences larger forces (i.e., forces beyond the elastic limit).

On the other hand, second-order methods by utilizing second-order (i.e., curvature) information can address the aforementioned issues. One class of second-order methods are Hessian-free methods, in which no Hessian is needed to be constructed explicitly, and only Hessian-vector multiplications are needed in order to update the neural network parameters. In our study, we utilize a method in the Hessian-free

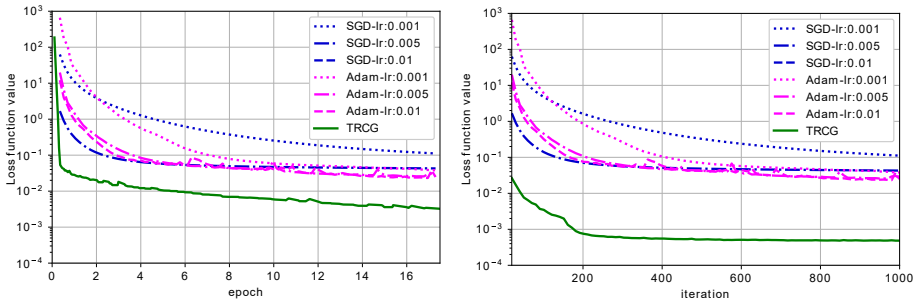

Figure 6.3: Optimization trends using different optimizers.

class which is called *Newton trust-region approach* (TRCG). This is motivated by the results presented in Figure 6.3 that illustrate the performance of TRCG and some of the well-known stochastic first-order methods with different choices of hyperparameters. As is clear from the results, the performance of TRCG by utilizing the curvature information is noticeably better than the stochastic first-order methods in terms of loss function value with respect to both iteration and epoch number. Similar behaviour is also observed in Berahas et al. [2019], Xu et al. [2020]. In every iteration of TRCG, the following non-convex quadratic sub-problem needs to be solved:

$$\begin{aligned} p_k \in \underset{p\in\mathbb{R}^d}{\arg\min}\ Q_k(p) =& p^T g_k + \tfrac{1}{2} p^T H_k p \\ &\text{s.t. } \|p\| \leq \Delta_k, \end{aligned} \tag{6.1}$$

where g_k is the (stochastic) gradient, H_k is the (stochastic) Hessian, and Δ_k is the trust-region radius at iteration k. The above sub-problem can be approximately and efficiently solved using CG-Steihaug [Nocedal and Wright, 2006] which is summarized in Algorithm 7. The output of Algorithm 7, p_k, is the search direction in order to update the neural network parameters. In other words, assume we are at k^{th} iteration, and the neural network parameters are updated as $\omega_{k+1} := \omega_k + p_k$. More details regarding the trust-region algorithm, the strategy for updating Δ_k, accepting or rejecting the steps can be found in Nocedal and Wright [2006].

Algorithm 7 CG-Steihaug [Nocedal and Wright, 2006].

Input: ϵ (termination tolerance), g_k (current gradient).

Set $z_0 = 0$, $r_0 = g_k$, $d_0 = -r_0$
if $\|r_0\| < \epsilon$ **then**
    return $p_k = z_0 = 0$
for $j = 0, 1, 2, ...$ **do**
    if $d_j^T H_k d_j \leq 0$ **then**
        Find $\tau \geq 0$ such that $p_k = z_j + \tau d_j$ minimizes $m_k(p_k)$ and satisfies $\|p_k\| = \Delta_k$
        return p_k
    Set $\alpha_j = \dfrac{r_j^T r_j}{d_j^T H_k d_j}$ and $z_{j+1} = z_j + \alpha_j d_j$
    if $\|z_{j+1}\| \geq \Delta_k$ **then**
        Find $\tau \geq 0$ such that $p_k = z_j + \tau d_j$ and satisfies $\|p_k\| = \Delta_k$
        return p_k
    Set $r_{j+1} = r_j + \alpha_j H_k d_j$
    if $\|r_{j+1}\| < \epsilon_k$ **then**
        return $p_k = z_{j+1}$
    Set $\beta_{j+1} = \dfrac{r_{j+1}^T r_{j+1}}{r_j^T r_j}$ and $d_{j+1} = -r_{j+1} + \beta_{j+1} d_j$

6.4.2 Projection Loss

In order to train a recurrent block for one-step ahead prediction, the simplest approach is to minimize the residue between the predictions and the actual values over a mini-batch in each iteration. However, this approach for training produces very unstable networks, which are prone to divergence when predicting a long trajectory of responses given the initial conditions. To address this issue, we introduce and utilize projection loss that is the basis for the training process in this study.

Projection loss is calculated as the mean squared error of a sequence of responses predicted by DynNet when compared with the corresponding actual responses. To produce the sequence of predicted responses, the only given value is the initial conditions at some randomly selected time step. This initial condition is then fed into the DynNet and the responses are fed back for N times to predict a trajectory starting from the random initial condition (N is a user-defined projection length). Compared to the conventional loss function, the projection loss can effectively control the insta-

bility issue of the neural network. Figure 6.4 demonstrates the effect of loss functions with different projection lengths on the testing loss.

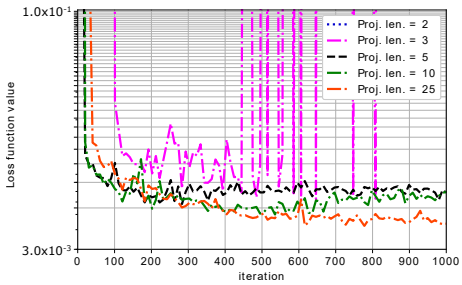

Figure 6.4: Optimization trends using different projection lengths.

As shown in Figure 6.4, the length of the projection directly affects the robustness of the optimization. In fact, when the projection length is two, the network's inference diverges (i.e., after multiple steps of recurrence, DynNet outputs explode and it is outside the shown range in the figure). The best results on the testing data are observed when the projection length equals to 25. Note that as the projection length in the loss function increases, the model becomes more optimal for longer trajectory predictions, however, the training time linearly increases as well. In fact, for loss functions with longer projection lengths, the forward pass and backpropagation steps take longer and these computations cannot be distributed over the processing resources (due to the sequential nature of the network inference). In addition, by comparing results from projection length = 5 and projection length = 25, it is observed that the former performs better initially (i.e., in lower iterations) while the latter shows its advantage later on. From this observation, we adopt a sequentially increasing projection length model in this study. In the following section, the models are trained for loss functions with projection lengths equal to 5, 10, and 25, respectively; for each, the models are trained for a fixed number of iterations.

6.4.3 Hardsampling Technique

For learning highly nonlinear systems, samples may be distributed extremely unevenly in different behavioral regions. For instance, elasto-plastic systems normally respond linearly to the major portion of a ground motion, regardless of the intensity of the motion. In other words, the system undergoes nonlinear deformations occasionally when a large impact occurs in the input. As a result, the portion of one-step ahead response transitions that are within elastic region is dramatically larger than the inelastic region. This induces a severe imbalance in the training data distribution, which turns out to be detrimental for model's robustness. Importance sampling is a technique for online batch selection that is used to circumvent the problem with unevenly distributed data.

A review of more common batch selection methods are given in Section 7 of Loshchilov and Hutter [2015]. One of the simplest and most effective approaches for adaptive batch selection is rank-based selection [Schaul et al., 2015, Loshchilov and Hutter, 2015]. In this method, during the training phase, samples of each batch are sorted in descending order based on their function value, and then, their probability of re-selection is updated based on their ranking. The idea was first employed for reinforcement learning using temporal difference (TD) as the reference for sample sorting, and later was adopted for deep learning applications and based on loss function value. In this study, a similar approach is introduced which is inspired by the notion of ranked-based batch selection.

In the implemented hardsampling technique, a hardsampling rate r is defined which is the proportion of samples in the batch that are eventually selected from the hardsamples. The model starts with randomly selected samples in the first iteration. At the end of the iteration, the N (is a user-defined hyperparameter) samples with the maximum contributions in the total batch loss are added to a list of hardsamples. In fact, the list of hardsamples is a bag of samples that are not learned well by the

model yet. In the next iteration, the batch samples are selected such that b_1 samples are randomly selected from the entire training samples and b_2 samples are randomly selected from the the list of hardsamples and $b2 = \lfloor r \times (b_1 + b_2) \rfloor$. At the end of the iteration, the list of hardsamples is updated and passed to the next iteration. The process continues accordingly.

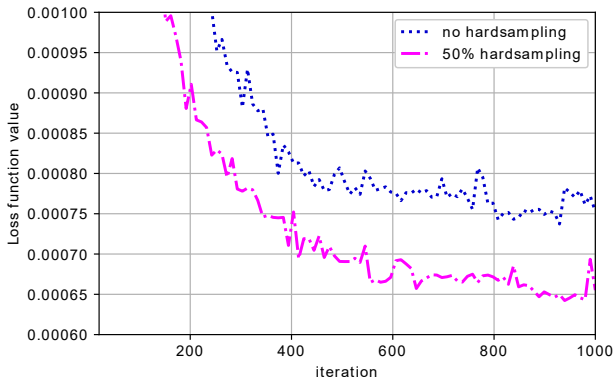

Figure 6.5: Optimization trends using different hard sampling ratios.

To evaluate the effectiveness of the technique, the optimization process is performed with and without hardsampling technique and results are compared in Figure 6.5. In this example, the rate of hardsampling r is 50%. The result clearly confirms the advantage of hardsampling technique in fast learning and better learning of the model. Therefore, in this study this technique is also used in the training process of the models. The approach is adaptive, meaning that the training process automatically picks hardsamples throughout the training process. In engineering problems, we may have an *a-priori* hypothesis about the hardsamples. For instance, in the elastoplastic models, it is expected that one-step ahead response transitions that are beyond the elastic limit are hardsamples. In the next section, we will confirm that our adaptive hardsampling technique automatically detects these samples.

6.5 Numerical Case Studies

In this section, two case studies are considered to validate the strengths of DynNet in response prediction of different nonlinear systems. These case studies differ in terms of the type of introduced nonlinearity to the systems. The first case is a four degrees of freedom (DOF) system with elastic perfectly plastic springs. The second model consists of a four-DOF system equipped with nonlinear (3^{rd} order) elastic stiffeners (schematics of the force displacement behaviors are shown in Figure 6.6). The governing equations of motion (EOM) for these two nonlinear systems are shown in Equations 6.2 and 6.3.

$$m\ddot{x} + c\dot{x} + f(x) = -m\Gamma\ddot{x}_g. \tag{6.2}$$

$$f_1(x) = \begin{cases} k_0 x & x \leq \Delta_y, \\ F_y & x > \Delta_y. \end{cases} \tag{6.3}$$

$$f_2(x) = k_1 x + k_2 x^3.$$

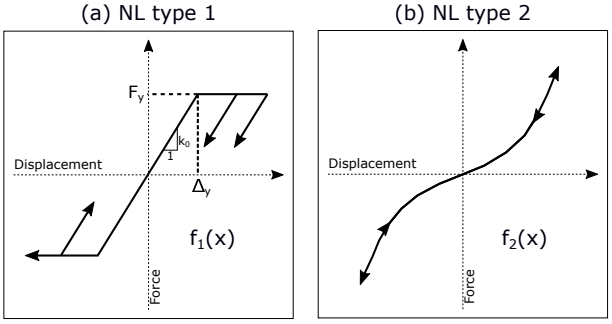

Figure 6.6: Force-displacement relationships of two nonlinear cases.

For the numerical simulation, Newmark's method for nonlinear systems is used in MATLAB. For this purpose, 20 strong ground motions are randomly selected from Center for Engineering Strong Motion Database (CESMD) [Haddadi et al.]. In addition to that, 10 band limited random time series are synthesized and added to

the the library of input signals. The earthquake ground motions are scaled using the wavelet algorithm proposed by Hancock et al. [2006]. The target matched spectra for twenty earthquake ground motions as well as the mean matched and target spectra are shown in Figure 6.7. The algorithm scales the time histories in a way that the response spectrum optimally matches with the target spectrum within the range of $0.2T_1$ to $1.5T_1$ (T_1 is the structure's natural period of the first mode).

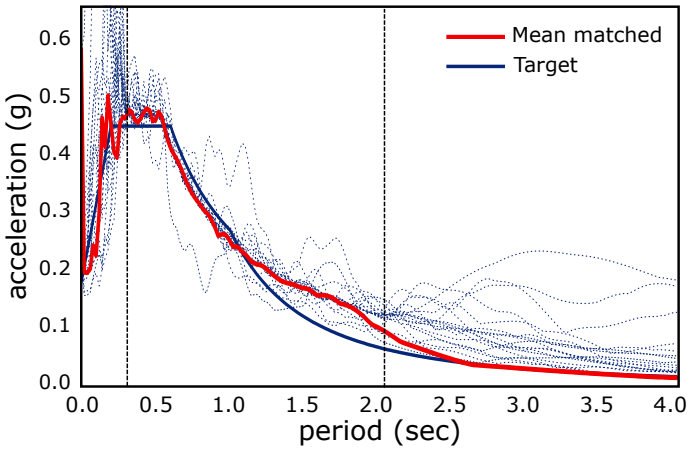

Figure 6.7: Earthquake response spectra matched with respect to the target spectrum and the mean spectrum.

For each case study, the scaled earthquake ground motions as well as random time histories are simulated to predict structure's responses (i.e., displacement, velocity, and acceleration) at all four DOFs. This data include both training and testing datasets. From 30 simulated ground motions, eight ground motions are randomly picked to be used as the training dataset and the rest for testing. Note that since DynNet is heavily constrained by the physics of the problem and enjoys low training variable space, it is expected that the model is easily trainable with small amount of training data and also is desirably generalized for a wide range of testing data.

6.5.1 Case 1: Elastic-Perfectly Plastic Model (NL type 1)

In this section, the results on the first test case - a four DOF shear building with elastic-perfectly plastic stiffness - are presented. The mechanical properties of the

structure is presented in Table 6.1. In this table, $M1 - M4$ and $K1 - K4$ stand for mass and elastic stiffness values of DOF1 to DOF4, respectively. Fy shows the stories' yielding force. To consider the robustness of DynNet, three levels of noise are also considered (0%, 5%, and 10% noise levels). The network is trained to predict the full response at all DOFs including displacement, velocity, and acceleration time histories given the earthquake ground motion.

Table 6.1: Mechanical properties for NL type 1.

Mechanical props.	*Values*	*Units*
M1	0.259	$kip.s^2/in$
M2/M1	1	-
M3/M1	0.75	-
M4/M1	0.5	-
Fy	50	$kips$
K1	168	$kips/in$
K2/K1	7/9	-
K3/K1	1/3	-
K4/K1	1/4	-

As concluded in the previous section, the network is trained in a multilevel manner: 1000 iterations with 10-step projection loss, then 1000 iterations with 25-step projection loss, and finally, 1000 iterations with 50-step projection loss. During the training process, batch size was set fixed at 1024 (i.e., 1024 one-step ahead transitions). In total, the network is trained for less than 100 epochs using TRCG optimizer. The learning curve is presented in Figure 6.8 (nonlinear (NL) type 1). The figure demonstrates that by increasing the length of projection in the custom loss function, a sharp drop in the loss function occurs.

As previously explained, the training phase incorporates the proposed hardsampling technique. To evaluate the physical interpretation of automatically selected hard samples, Figure 6.9 is presented. In this figure, the entire training dataset (including eight signals) are shown and divided by vertical lines. The signal portions that are labelled as hardsamples are color coded in red. Interestingly, hardsamples

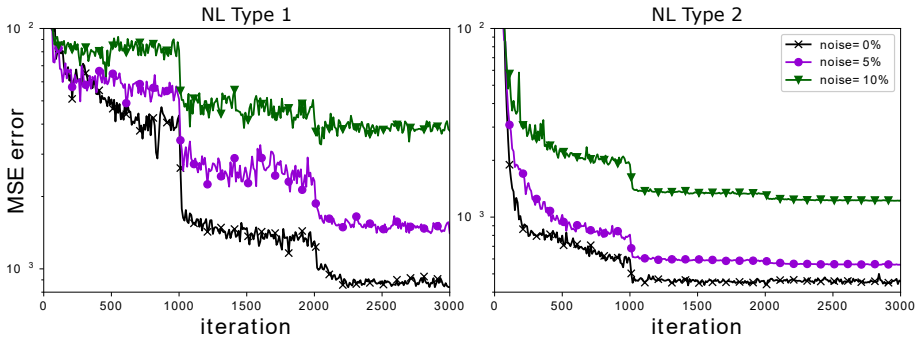

Figure 6.8: Loss function reduction versus iteration: the projection length for loss function calculation changes at iteration 1000 and 2000 (length equals to 10, 25, and 50 for each portion). The sudden drops in the loss function values at those iterations show the effectiveness of the proposed training technique.

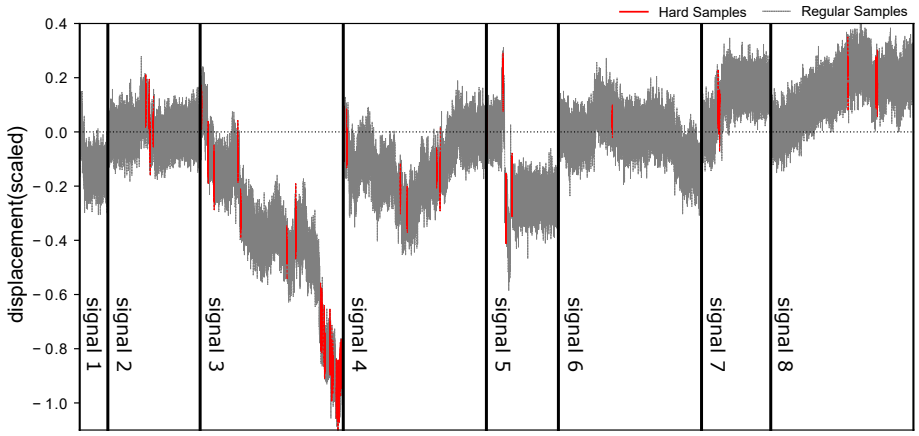

Figure 6.9: Locations of hard samples for adaptive sampling in the nonlinearity type 1: as expected, the majority of hard samples are located when large residual displacements occur.

are mostly found when a sudden drop (due to a severe nonlinear behavior) has happened. This observation confirms that the algorithm reuses highly nonlinear samples to intensify its learning ability.

To evaluate the prediction performance of the trained network, the prediction results on one randomly picked testing signal with 5% noise for short and long trajectories are presented in Figures 6.10 and 6.11. The predictions are compared with the reference signals in both time and frequency domains (velocity predictions are neglected for brevity). For short trajectories (i.e., five second prediction in Figure 6.10), the performance is promising. Note that the nonlinear baseline variations are accu-

rately predicted in the displacement time signals. In terms of frequency, the accuracy of predicted signal is very high. For longer trajectories (i.e., 40 second prediction in Figure 6.11), the prediction accuracy is as high. The modal peaks in frequency domain are captured accurately. Notably, all the baseline variations in the displacement time signal are predicted accurately using the trained network. Such high accuracy for predicting severely nonlinear responses are unprecedented in the literature.

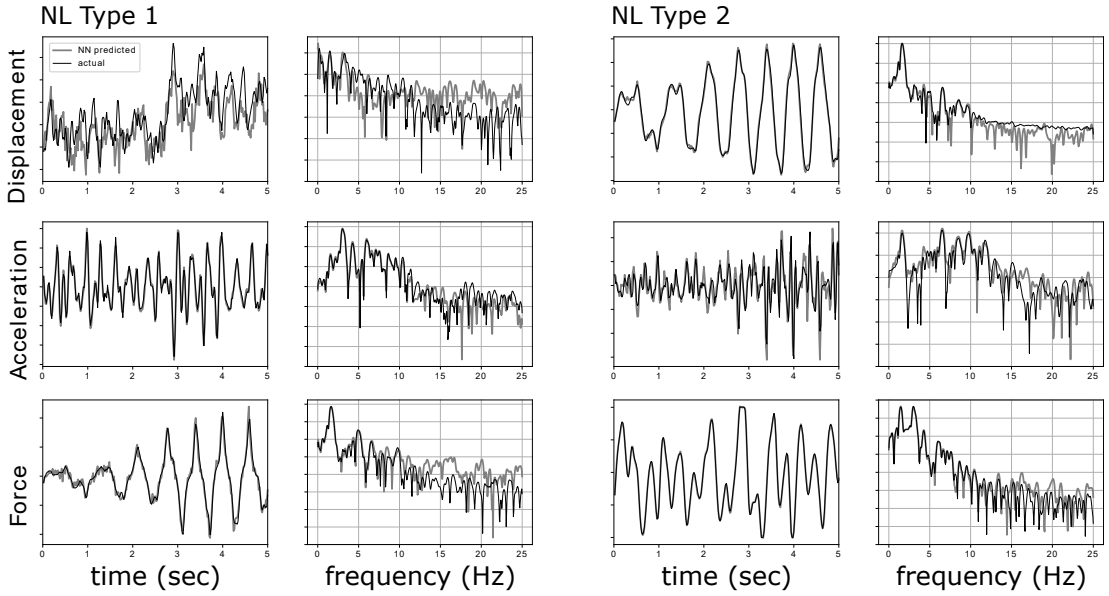

Figure 6.10: Predicted signals for 5 seconds with 5% noise. The plots show that the network is very accurate in predicting responses for a short future. The same level of accuracy is visible in both time and frequency representations of the signals.

To further quantify the accuracy of the predictions in all the testing signals, Pearson correlation coefficients (PCC) are calculated between predicted and ground truth signals (40 second predictions) and presented in Figure 6.12. PCC is a measure to quantify the fitness of predicted trajectories with respect to the ground truth signals [Weisstein, 2006]. The results for all three noise levels are presented. The histograms demonstrate the distribution of different prediction accuracy. In general, for all predicted quantities (i.e., displacement, acceleration, and internal force) and all noise levels, more than 90% of DynNet's predictions have PCC above 0.8. Particularly, force and acceleration predictions are exceptionally accurate. Note that in the noisy

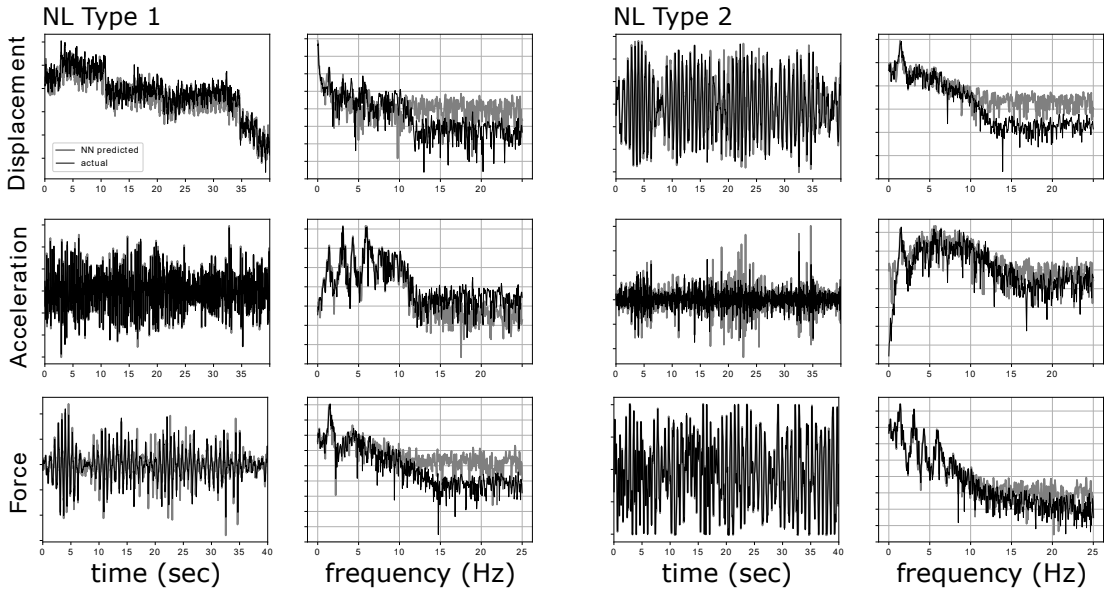

Figure 6.11: Predicted signals for 40 seconds with 5% noise. The plots show that the network is still accurate in predicting responses for a longer time. The same level of accuracy is visible in both time and frequency representations of the signals. Notice that the displacement prediction for the NL type 1 is strongly nonlinear. However, the network successfully estimated it.

cases, the likelihood of having very high PCC is inevitably low due to the irreducible noise. Still, DynNet shows a very good performance in response predictions subjected to these highly nonlinear signals.

In general, recurrent networks are prone to instability in longer trajectories [Salehinejad et al., 2017]. Error accumulation due to feeding the output of the network back is reported as the main source of this instability [Holden et al., 2017]. In this study, by physically constraining the network as well as utilizing projection loss for training, the model enjoys stability for longer trajectory predictions. Figure 6.13 shows prediction errors for different noise levels with respect to different projection lengths. For the noiseless case, the mean squared error (MSE) gradually increases as the trajectory lengthens. However, the error is still very low for very long trajectories (i.e., $10,000$ one-step ahead predictions equivalent to 200 seconds). Interestingly, for two noisy cases, except for the lower range of trajectories, the error remains constant for longer trajectories. This implies that: (1) DynNet is quite stable regardless of the

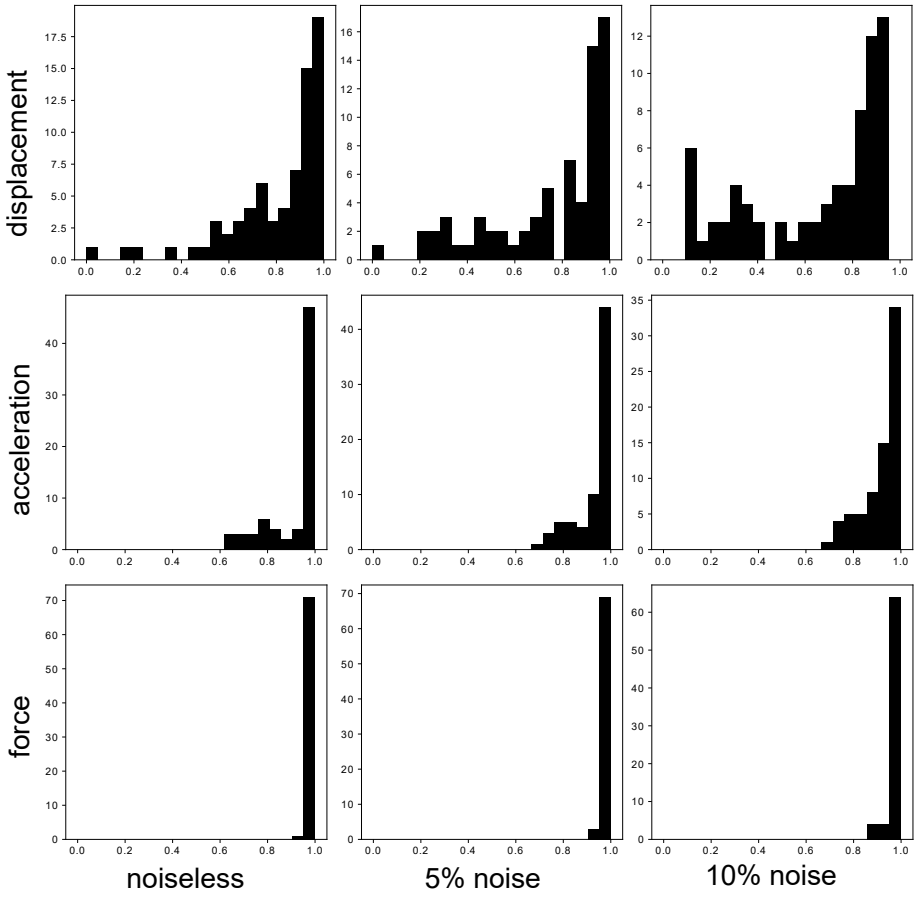

Figure 6.12: Pearson correlation coefficient histogram for predicted responses - nonlinearity type 1.

trajectory length; and (2) noisier data tends to discount the increasing error issue for longer trajectories.

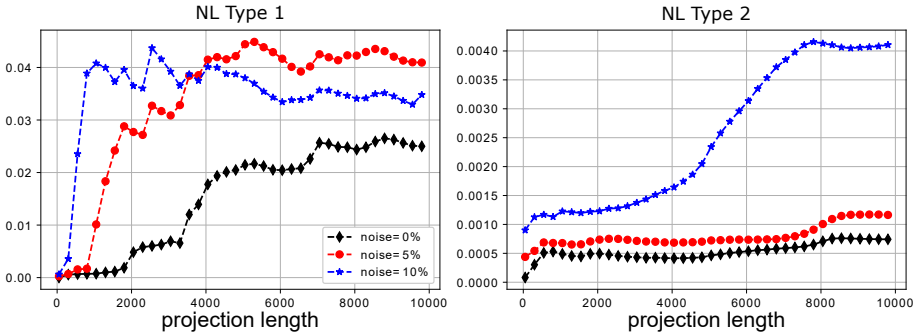

Figure 6.13: MSE error of the predicted signals vs. the length of projection. As expected, the error increases as the projection length is longer. However, in all cases after a rapid jump in the error at the beginning, the error flattens for longer projections. Notice as expected, noisier signals have higher MSE errors.

Finally, to verify the strength of DynNet in identifying the nonlinear behavior, hysteresis diagrams for a randomly picked signal and different noise levels are shown in Figure 6.14. The DynNet estimated signals could very accurately capture the linear tangent of the spring force. In addition, the transition to nonlinear region is learned very accurately (normalized force values are exactly bounded within -1 to 1). The same level of accuracy is noticeable in all noise cases.

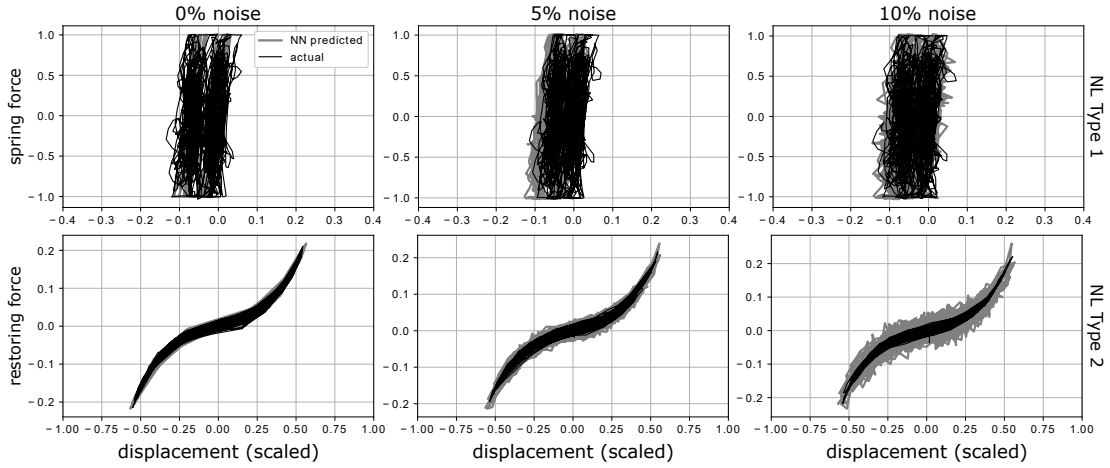

Figure 6.14: Hysteresis diagram in two nonlinearity cases at the first floor and for different noise levels. Both sets of results confirm the promising performance of the network in learning different nonlinear behaviors.

To further investigate the scalability and generalization of the trained DynNet, the nonlinear responses of the structure subjected to different magnitudes of a selected earthquake ground motion are inferred and compared with the numerical solutions. Four levels of magnitude are considered in this analysis: 0.5x, 0.85x, 1.0x, and 1.2x (compared to the normalized ground motion). The results are presented in Figure 6.15. In this plot, dotted lines show exact simulation results while solid lines represent DynNet predictions. Results of internal forces and displacements for the 1^{st} DOF are shown for brevity. Internal forces are very accurately predicted in all four levels of magnitude of the ground motion. The accuracy is lower in the displacement predictions, however, the relative trends and lower amplitudes are carefully captured by DynNet. Note that the selected ground motion contains a strong shock-wave at

$\sim 380^{th}$ time step which causes severe nonlinear response and baseline shift (residual deformation) in the displacement predictions. The model, however, is still successful in following the exact variations of the building responses.

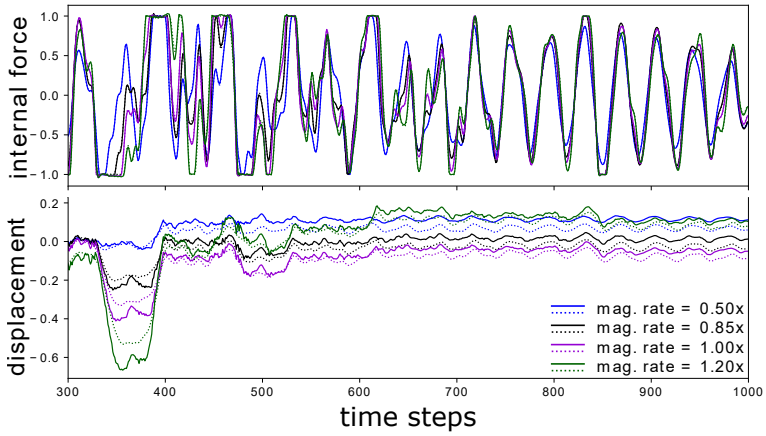

Figure 6.15: Response predictions for a ground motion with different magnitudes. This figure demonstrates the generalization of the trained NN model. Note that dashed lines show the actual responses from the numerical simulation. Despite strong nonlinear behavior, all four different magnitudes are predicted very accurately.

6.5.2 Case 2: Nonlinear Elastic Model (NL type 2)

In the second case study, a 4-DOF structure with nonlinear elastic springs is studies. For the nonlinear springs, a 3^{rd} order polynomial behavior is introduced which can model a hardening after initial pseudo-linear phase (see Figure 6.6). Due to the elasticity of the model, no residual displacements are expected here. Mechanical properties of the building are presented in Table 6.2. In this table, M's and K's are defined as explained before. $k1$ and $k2$ are coefficients of the 3^{rd} order restoring force equation (Equation 6.3). The training process is identical to the previous case study. DynNet requires no pre-processing or special accommodation for different nonlinear models. The model is trained for the same number of iterations and epochs as the previous test case. Loss function variation over the iterations is shown in Figure 6.8. Again, sudden drops in loss values are detected when the projection length of the custom loss increases.

Table 6.2: Mechanical properties for NL type 2.

Mechanical props.	*Values*	*Units*
M1	0.340	$kip.s^2/in$
M2/M1	0.8	-
M3/M1	0.75	-
M4/M1	0.6	-
K1	100	$kips/in$
K2/K1	3/4	-
K3/K1	1/2	-
K4/K1	1/4	-
k1	1	-
k2	10	in^2

The nonlinear response predictions for a randomly picked ground motion from testing data are presented in Figures 6.10 and 6.11 (short and long trajectories, respectively). As before, DynNet shows a promising performance in nonlinear response predictions, both in time and frequency domains, regardless of the length of trajectory. To evaluate the predicting performance of the trained neural network on the entire testing data, PCC coefficients are calculated and the distributions are shown in Figure 6.16. Note that similar to the previous test case, three levels of measurement noise are considered for both training and evaluation phases of the network loss function.

In Figure 6.16, the general note is that the number of very high accuracy predictions (i.e., with PCC above 0.8) is not as high as the previous case, especially when measurement noise is introduced. However, for noiseless and 5% additive noise cases, the results show high accuracy. Histogram of displacement and internal force response predictions show a unimodel distribution with the mode at PCC $\in [0.95, 1.0]$. In terms prediction stability for longer trajectories, regression MSE error with respect to length of prediction trajectory is presented in Figure 6.13. Again, as observed in the PCC histograms, two lower noise cases show a steady trend of MSE loss as the trajectory length increases while the 10% noise case is not as stable. Notice that the

values of MSE errors generally are significantly lower in the NL type 2 (nonlinear elastic case) compared to the NL type 1 (elastic-perfectly plastic) while histograms show higher accuracy for prediction of the latter model. This observation is explained by the inelastic behavior of the NL type 1 model which can cause baseline shifts (i.e., residual deformations). We showed that DynNet is successful in capturing baseline variations, even though a small discrepancy causes much larger MSE errors for these response predictions. The baseline variations are not expected in the elastic model.

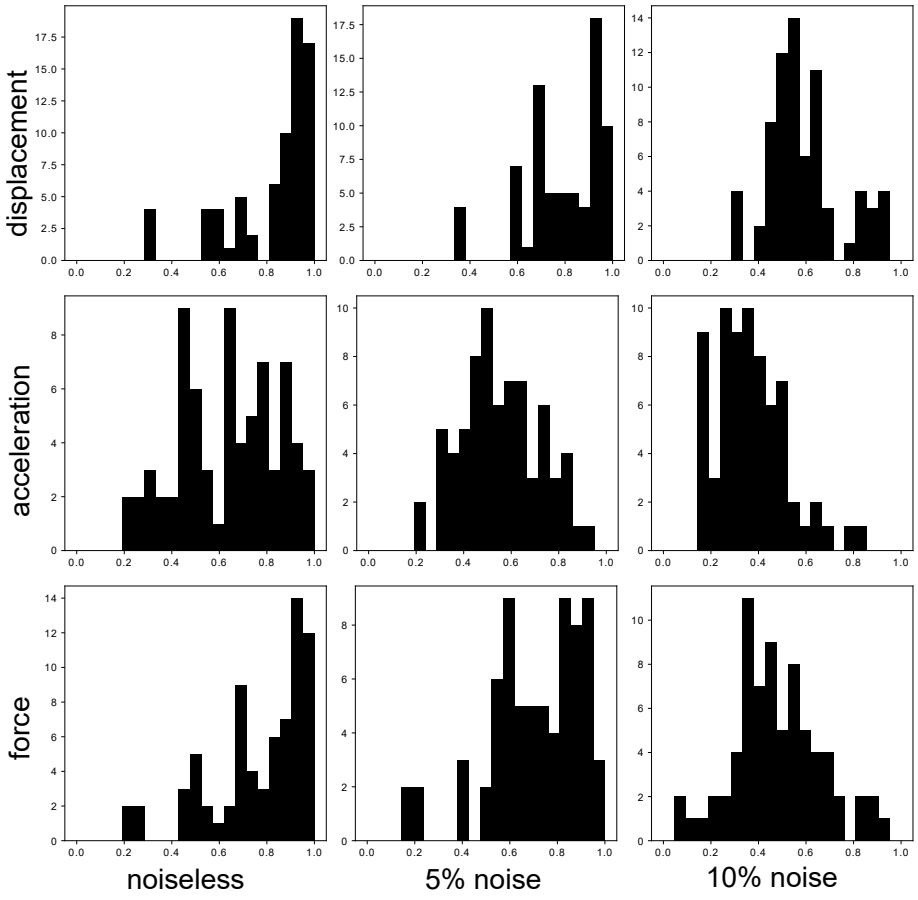

Figure 6.16: Pearson correlation coefficient histogram for predicted responses - nonlinearity type 2.

Finally, in order to validate the ability of the neural network to predict nonlinear elastic behavior of the spring forces, hysteresis diagrams are plotted in Figure 6.14. The restoring force here includes both the elastic spring force and the damping force (i.e., $c\dot{x} + f(x)$ in Equation 6.2). According to these plots, DynNet predictions very

accurately match with the simulation results. The 3^{rd} order behavior of the spring as well as the small energy dissipation area caused by the damper force is identified and correctly predicted. In higher noise levels, the prediction shows higher fluctuations around the exact plots which can be simply explained by the high level of noise.

6.6 Conclusion

In this study, we proposed a data-driven approach for comprehensive prediction of nonlinear dynamic responses of multi degrees of freedom (DOF) systems using Neural Networks. In particular, inspired by common implicit dynamic analysis algorithms, DynNet block is designed as a one-step ahead response predictor. By repeatedly inferring the block, long response trajectories are predicted. Compared to the most advanced data-driven methods, DynNet has significantly smaller variable space, resulting less computational effort per iteration. Due to physics-based constraints of the proposed architecture, the network required more advanced optimizers for a smooth and efficient learning process. With this regard, trust-region approach using CG-Steihaug (TRCG) algorithm was implemented. In addition, for more efficient learning, a simple hardsampling technique as well as trajectory loss function was developed and implemented which resulted in faster learning of severely nonlinear transitions.

For verification, DynNet was tested in two nonlinear case studies: a four DOF shear building (1) with elastic perfectly plastic stiffness, and (2) with nonlinear elastic (3^{rd} order) stiffness. For each test case, three levels of measurement noise were included to evaluate the noise propagation characteristics of the proposed network. The networks were trained using less than 30% of the available data and evaluated using the remaining 70%. In both test cases, we showed that the network quite successfully was able to predict a complete set of nonlinear responses including displacement, velocity, acceleration, and internal force time histories at all DOFs given

the applied ground motion only. The stability of the predictions for longer trajectories was analyzed and concluded that for the majority of cases, DynNet holds the error level stably as the trajectory length grows. In addition, using hysteresis diagrams, we showed that the performance of DynNet in capturing nonlinear behaviors of the springs is promising.

Data-driven function estimators are extremely popular in science and technology, however, in engineering applications due to the availability of accurate governing equations and numerical solutions, fully black-box function estimators are less accepted. This study tries to bridge the gap between black-box models and available exact solutions to create a fast learner function estimator. It is believed that DynNet can create a great potential for faster regional disaster sustainability and health monitoring analyses.

Chapter 7

Input Estimation of Nonlinear Systems using Probabilistic Neural Network

7.1 Abstract

Mobile sensors that are carried by drive-by vehicles are great candidates for crowdsensing of transportation infrastructure. The primary challenge for free and widespread utilization of such sensors is low signal to noise ratio. Vehicle scans are highly contaminated by road profile roughness as well as the dynamics of the vehicle suspension system. In this research, a learning-based filter is designed to decontaminate the vehicle-collected signals in order to extract the input. In other words, the neural network is a nonlinear deconvolution filter for a specific vehicle. Given this filter, one can simply collect data within the vehicle cabin and deconvolve it to achieve its input, which is a more pure version of structural dynamics. The proposed network architecture is trained and tested with real data collected by different vehicles and simple set of sensors. The study demonstrates that the proposed recurrent architec-

ture successfully estimates the input of the vehicle systems. In general, the proposed methodology is for estimating a nonlinear transfer function between two locations of a dynamical system in which the sensing-desired location is inaccessible while the other location is in reach.

7.2 Introduction

7.2.1 Vehicle Input Estimation using Neural Networks

The problem of input estimation has been of great interest among researchers in many fields, such as mechanical, structural, and aerospace engineering. In this problem, the objective is to estimate the driving forces of a dynamic system (e.g., linear or nonlinear) given a subset of the system's state. As expected, the problem can be formulated in a variety of complexities: single input and single output (SISO), multiple input and multiple output (MIMO), and any combinations in between. In case of a building subjected to a base excitation (e.g., an earthquake), a full state vector includes vibration responses at all degrees of freedom (e.g., story accelerations) while the input is applied on only one degree of freedom (e.g., the ground level), resulting a single input and multiple output (SIMO) system. With the same logic, a vehicle suspension system can be observed as a MIMO system considering each tire as an input point and cabin translational and rotational accelerations as outputs.

The applications of input estimation vary depending on the nature of the problem and the field. In earthquake engineering, it is desired to estimate the ground motions in the buildings that are not comprehensively instrumented on the ground level. This problem has been thoroughly investigated, mostly by using structural models (e.g., finite element) as the baseline. One popular approach to this problem is to concatenate the input vector to to the state vector to produce an augmented state and perform state tracking algorithms such as various versions of Kalman Filter

[Gillijns and De Moor, 2007, Lourens et al., 2012, Maes et al., 2016]. Despite the wide applicability of the methods, they are found to be susceptible to instability and un-observability issues [Naets et al., 2015]. One primary challenge for the application of such methods is their reliance on an available baseline model of the structure. This can be partially overcome with preliminary or simultaneous system identification. Nevertheless, the baseline model is not always available and additional system identification may not be possible.

For the main application of this thesis (e.g., mobile sensing using vehicle-carried sensors), the vehicle input is considered to be significantly less contaminated by the vehicle suspension and less noisy, resulting in more suitable signals for bridge health monitoring or road condition assessment. In fact, in the field of indirect bridge health monitoring, contact point (CP) response is found significantly more informative and less disrupted [Yang et al., 2018, Nayek and Narasimhan, 2020, Eshkevari et al., 2020]. In fact, the vehicle suspension acts as a band-limited transfer function that filters out and manipulate the content that enters the systems through the CPs at the tire level. Therefore, by reversing this filter, a substantially more informative data can be extracted.

Recently, a few studies proposed input estimation methods based on simplified linear vehicle models. Yang et al. [2018] proposed a closed-form solution for calculating the contact point input of a SDF vehicle suspension model given its cabin response. The solution is based on a fully known vehicle model. Despite the simplifying assumptions, the study could demonstrate the substantial improvement in the bridge system identification results when CP estimations are used instead of the cabin responses. The improvements could minimize the detrimental impact of high speed sensing as well the overlap between vehicle and bridge modal frequencies. The study has been fully based on numerical analysis. A Gaussian process latent force model is proposed to jointly estimate the state and the input of a known MDF vehicle system by Nayek

and Narasimhan [2020]. The proposed model is evaluated using numerical trials and found beneficial for bridge modal identification, in particular, to retrieve information regarding the higher bridge modes that were overshadowed by the vehicle transfer function.

However, due to the nonlinearity, complexity, and variety of the vehicle physical models, it is preferred to design an approach that accomplishes the the input estimation with no need for a baseline model or simplifying assumptions such as a simplified and linear vehicle suspension and fully known vehicles. However, the majority of commercial vehicles are equipped with nonlinear suspension systems (nonlinear stiffness and damping) [Demir et al., 2012] in order to maximize the ride comfort. The same argument is also valid for built structures; modern controlling and lateral resisting systems are nonlinear. Considering these, In this study a recurrent neural network framework is introduced that is able to learn the nonlinear transformation between the input and the output of dynamic system and exploits the learned information to estimate future inputs of the system in order to expand the applicability and minimize the limiting constraints.

7.2.2 Network Architecture and Training

Deep learning has shown great potential as universal function approximators for learning complex relationships and patterns from raw data. In particular, recurrent neural architectures have been widely used for signal regression tasks over the past years. In linear time invariant dynamic systems, the exact transfer function of a system can be replaced with a finite impulse response (FIR) filter. However in nonlinear systems, the previously mentioned impractical. The state transition equation of a dynamic system is shown in Equation 7.1.

$$X_{k+1} = AX_k + Bp_k \tag{7.1}$$

where X_k is the full state vector of the system at time step k, A and B are characteristic matrices of the system, and p_k is the applied load at time step k. For nonlinear systems, A and B are not constant matrices but functions of time or a transformation of the state vector. This state equation usually pairs with an observation equation using which the measurement vectors and full state vectors are related. In the direct problem, given p_k and initial state X_0, we showed in Chapter 6 that the full state space can be estimated in a data driven fashion with no need for available estimates for A and B. In this chapter, the idea is to study the inverse problem: given X_k for $k \in 1:T$ and a prior estimate for p_T, it is desired to estimate p_k for $k \in 1:T-1$. This problem is equivalent to deconvolution of the system's response. Note that in case of linear systems, the methods proposed in Chapter 3 or Yang et al. [2018] are right candidates. Here, the proposed neural network functions as a nonlinear deconvolution filter to estimate the system's input.

A schematic overview of the proposed framework is given in Figure 7.1. In this figure, the neural network is represented as a recurrent neural network (RNN) block that at each time step, processes the input and output values inside the L-shaped binder to predict the one-step backward estimation of the input (e.g., contact point force in vehicle systems). This process is repeated until the maximum possible length of the input signal is estimated. In this framework, the input and output signals correspond to the CP and the cabin accelerations, respectively. Note that the figure depicts a SISO case in which the number of response channels equals to one. However, in multi degrees of freedom systems, the network dimensions grow accordingly with no change in the structure or the pipeline.

As it is shown, the network unravel the input signal in a reverse order. This is not a necessity, however, it is more practical to estimate the initial force at the same time as the latest entry of the response slice. On the other hand, the forward-unraveling option is more desired for real-time input estimation. In this study, the

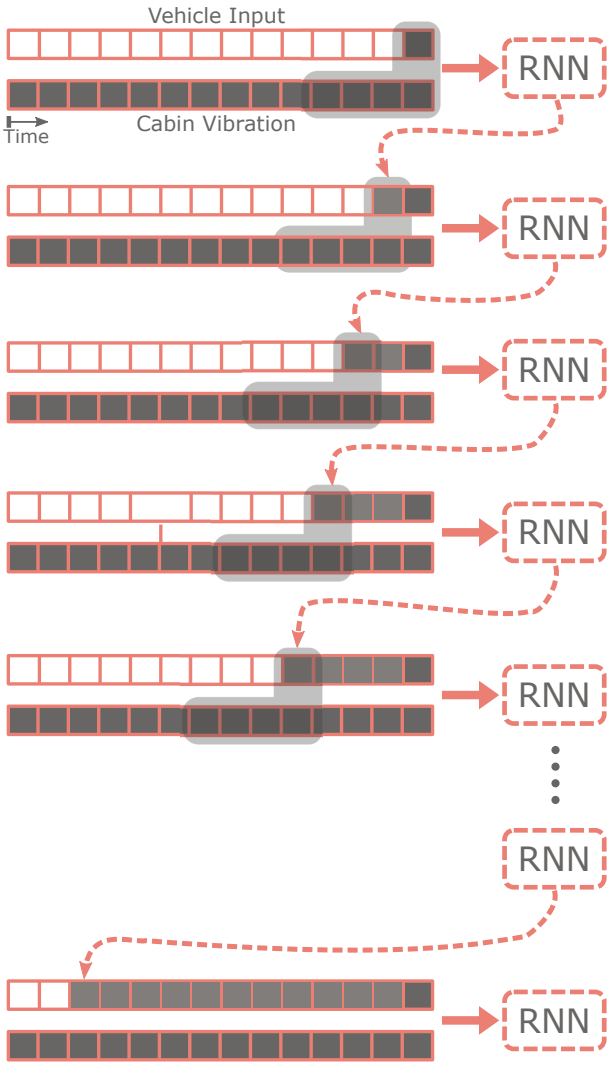

Figure 7.1: Schematic diagram of the input estimator network.

reverse-unraveling approach is adopted due to its slightly better performance. The structure of the RNN block is given in Figure 7.2.

The architecture incorporates fully-connected layers for transitioning between two consecutive time steps. The data flows through two stages in the network: shared layers and channel-specific layers. Channels can be either different output axes, degrees of freedom, or types (here by output we refer to the network. However, physically speaking, the output of the network is the input of the dynamic system). By using the shared layers, the number of trainables is reduced significantly. In contrary, our preliminary experiments showed that by solely defining shared layers, the performance

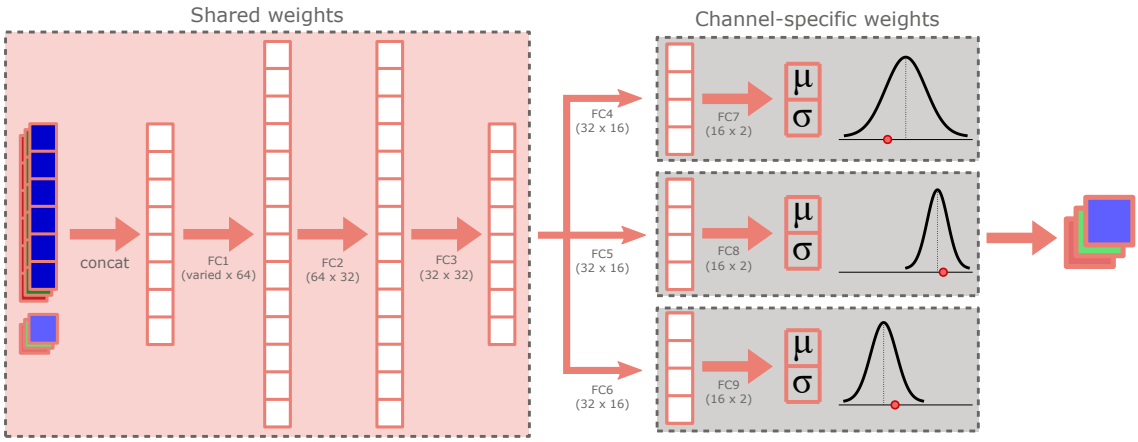

Figure 7.2: Details of the network architecture.

is noticeably lower.

A general shortcoming of the learning-based regression models is that the prediction is a deterministic tensor (e.g., a scalar or a set of values). In classification task, however, the final output of the network is class probabilities which is useful for uncertainty analysis. For example, In case of risk-averse problems, by setting higher bars for the classification probabilities, it is possible to enhance the accuracy of the classification predictions with the expense of lowering the recall. Such estimation reliability analyses are not possible when the neural network outputs deterministic results. To address that, we introduce a probabilistic learning-based regression model that estimates a normal distribution, instead of a single value, for the regressed prediction. During the training process, the optimization objective is to push the mean values of the normal distributions to the actual labels and shrink the variance for highly confident estimations. For inference, one can either sample randomly from the normal distributions or merely pick the mean values (i.e., the most probably estimation value). From Figure 7.2, the last layer of each channel-specific network predicts μ and σ using which the normal distribution is constructed. The standard deviation σ is a good indicator of network's confidence regarding a regression prediction.

7.2.3 Training Process and the Objective Function

To train the novel probabilistic regression model, conventional loss functions are not applicable. In contrast, the loss function has to follow the same formulation as of the policy gradient methods in reinforcement learning applications [Sutton and Barto, 2018]. The RNN block can be interpreted as a policy network in which the state is defined as the input of the neural network (i.e., a slice of the system's response) and the action is the best estimate of the neural network's output (i.e., the system's input - base excitation or CP vibration) at the previous time step. With this analogy, the loss function is defined as the following:

$$\mathcal{L}(\theta) = -\log(p(a|\pi^{\theta}(s))) + \mathcal{L}_{proj}(\pi^{\theta}, n_{proj}) \tag{7.2}$$

$p(a|\pi^{\theta}(s))$ is the probability of taking action a in state s given policy π^{θ}. The second term of the loss function is the projection loss (introduced previously in Chapter 6) with the projection length of n_{proj} and using policy π^{θ}. In the first term, s includes the inputs of the neural network and a is the corresponding output values. As this term becomes smaller, we ensure that the network's output distribution is more likely to predict values that are close to the actual outputs. The second term of the loss function also attempts to enhance the regression results for longer projections in a conventional MSE minimization manner. In this term, an increasing geometric factor is element-wise multiplied to the outputs to put more weight on the accuracy of further estimations.

For the training using this loss function, Newton trust-region approach is adopted due to its outstanding performance compared to linear methods such as Adam. The training process consists of two phases: 50 epochs with projection length of five and 20 epochs with projection length of 50. Depending on the experiment, the architecture of the network is modified in order to handle the proper number of output channels. This

variation causes different number of trainable parameters. Regardless, the dimension of the RNN has been always less than $15K$.

In the following sections, different case studies are investigated and results are discussed. In Section 7.3, a quarter-car model is numerically simulated and the input is estimated. In Section 7.4, a real-world building is studied and the ground excitations are estimated. Finally, in Section 7.5, the experimental data collected by a real-world vehicle is analyzed and the input prediction task is performed.

7.3 Case One: Numerical Vehicle Input Estimation

To evaluate the performance of the proposed network, a linear quarter-car model of a commercial vehicle is simulated in MATLAB for synthetic data generation. The model car travels over different rough roads with roughness profiles generated in accordance to the ISO8608:2016 spectrum [ISO, 2016] (road class C). in each simulation, the vehicle drives over a 1000 meters long road with a fixed speed of 5.0 meters per second. The vehicle's cabin acceleration as well as the input vibration (tire level acceleration) are saved respectively as the output and the input of the system. The objective is to predict the tire level accelerations given the cabin acceleration respond using the trained neural network.

In total, five scans are simulated: four used for training and one for testing. In addition, to investigate the noise effect the network is trained for three different signal-to-noise ratios.

As shown in Figure 7.1, the input of the RNN block includes a slice of the cabin vibrations and one value of the vehicle input. The slice length is a hyper-parameter of the proposed method. Based on our preliminary trials, slice length of 10 is found to outperform other values. In Figures 7.3 and 7.4 the estimated input signal for

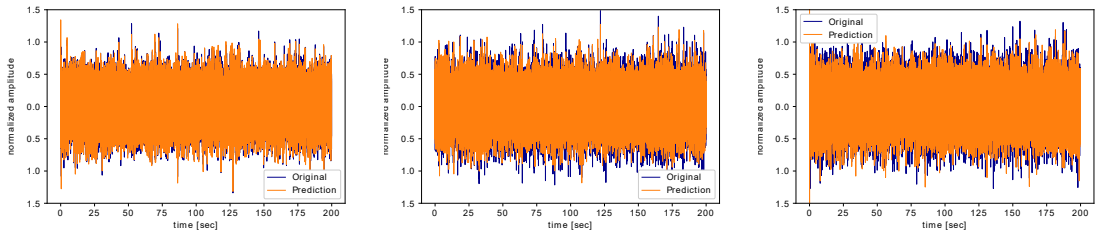

Figure 7.3: Input estimation at different noise levels. Time window is 200.0 seconds. From left to right: SNR = 100, SNR = 20, and SNR = 10.

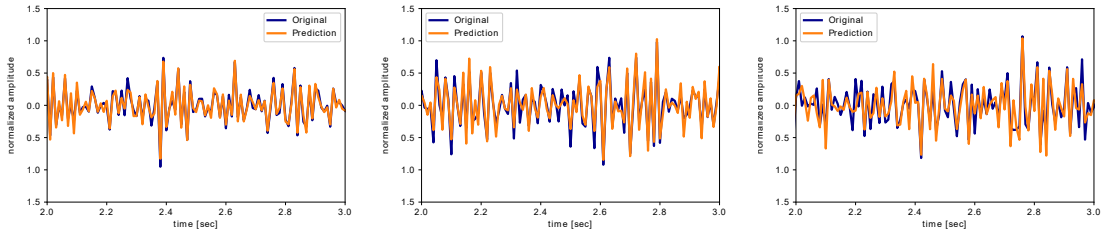

Figure 7.4: Input estimation at different noise levels. Time window is 1.0 second. From left to right: SNR = 100, SNR = 20, and SNR = 10.

the testing case are compared with the original signal in two different scales. The frequency domain comparison is also presented in Figure 7.5. In general, the input estimation is very accurate in all cases. An expected drop in accuracy is noticed with the SNR decreases. Root mean square error (RMSE) values of the power spectral density (PSD) differences are also given in Figure 7.5 which confirms higher accuracy in less noisy cases.

To quantify the uncertainty of the regression estimations of network, the probabilistic neural network predicts an standard deviation for each estimation. This value is associated to the confidence level for that estimation. In other words, when the standard deviation of a prediction is lower, the network estimates the value with higher confidence. In Figure 7.6, histograms of standard deviations are plotted for different noise levels. The spike with the lowest range corresponds to the least noisy case and the range increases for noisier cases, confirming that the model is quite confident about its regression predictions when the model is less noisy. This finding

is anticipated when the additive noise is manually included. However, when dealing with real data, the histogram of standard deviations enables to quantify the confidence of regression predictions or to distinguish less noisy channels of data, to name a few application. Consequently, due to the recurrent nature of the network inference, as the extent of standard deviation values increases, the neural network estimations accumulate larger errors.

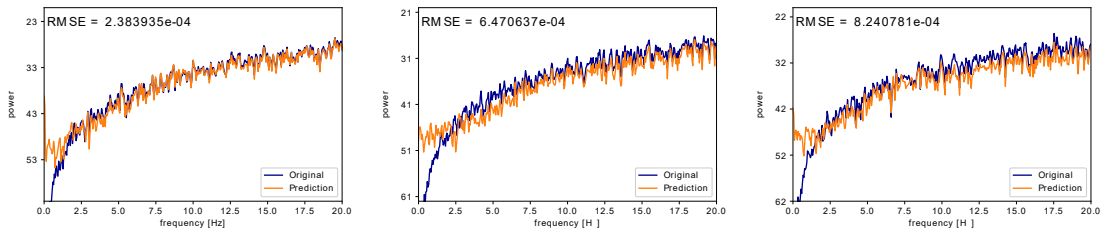

Figure 7.5: PSD of the input estimations at different noise levels. From left to right: SNR = 100, SNR = 20, and SNR = 10.

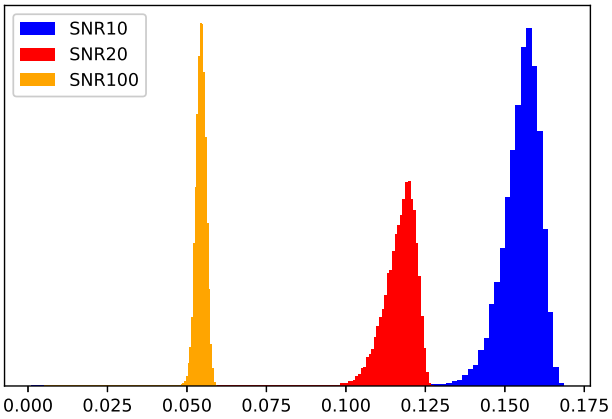

Figure 7.6: Histogram of standard deviations for different noise case: as the noise level increases, the standard deviations increase implying less confident regression estimations.

Learning-based solutions for engineering problems are often being criticized for their lack of interpretability. In recent years, deep learning community has been focused on developing fair methods to interpret and attribute the outputs of the network directly to its input features. Doing so, one can analyze whether the trained

network make predictions by heavily relying on theoretically-related features or not. In this study, we use integrated gradients which represents the integral of gradients with respect to the inputs throughout the network's depth from a given output back to the input layer [Sundararajan et al., 2017]. The final product of this method is a relative importance map of the input features with respect to one channel of the output. The results of this analysis is presented in Figure 7.7.

In this case study, the input and output signals are unidirectional, meaning that the system's input has only one channel and therefore one importance map can be produced. The feature importance analyses of all three noise levels are presented in the same figure. From Equation 7.1, it is expected that in a noiseless scenario, given the full state vectors in two consecutive times (e.g., X_{k+1}, X_k), the input p_k can be estimated (in a linear time invariant system). Since the used signals in this case study are accelerations, the full state vector can be derived by numerical integration. Therefore, in a noiseless case, it is expected that the network only requires a few sequential acceleration samples right before time k in order to predict p_k. Interestingly, this can be confirmed in Figure 7.7. In case of SNR 100 (the lowest noise), the accelerations at the three latest time steps almost fully determine the network prediction. As the noise level increases, however, the effect of previous output (u_{t-1}) value as well as more distant acceleration samples increase. This finding is fully in accordance to our expectation from the physics of the problem.

7.4 Case Two: Real-World Building Input Estimation

The application of interest in this study is to propose a data-driven solution for vehicle input estimation since it is a critical step for indirect bridge health monitoring. Yet, in this case study a real-world multi degrees of freedom building is considered

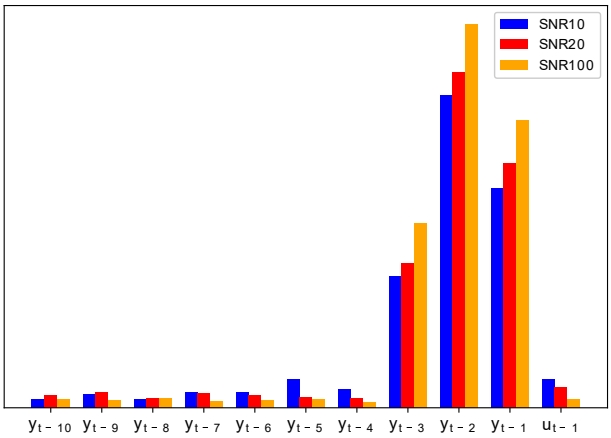

Figure 7.7: Feature importance analysis of the trained neural network: as the noise level increases, the importance of samples with further time differences increase.

to elaborate on the application of the proposed network for input estimation of other types of dynamic systems. For this purpose, the vibration data from a six-story Hotel in San Bernardino, California is exploited which is provided by the Center for Engineering Strong Motion Data (CESMD). The database provides building vibrations in two horizontal axes for multiple earthquake incidents, among which, 12 earthquake recordings are used for this case study. The data is split equally to training and testing. The building geometry as well as the sensor layouts are presented in Figure 7.8.

Since the ground motion is not available from the sensing data, the vibrations of first floor is considered as the the input to the upper stories (channels 1 and 3 from Figure 7.8), and data collected at the roof and the third floor is used as the output (channels 4, 5, 7, and 8 from Figure 7.8). The objective is to predict the earthquake acceleration in the first floor given the response at the roof and the third floor. The acceleration slice window is set as 10 as before. The network training process is also exactly as explained in the previous case study. After training, the input estimation results for one of the testing earthquakes is plotted and presented in Figures 7.9 to 7.10.

As the figures present, the accuracy of earthquake estimation is remarkably high in

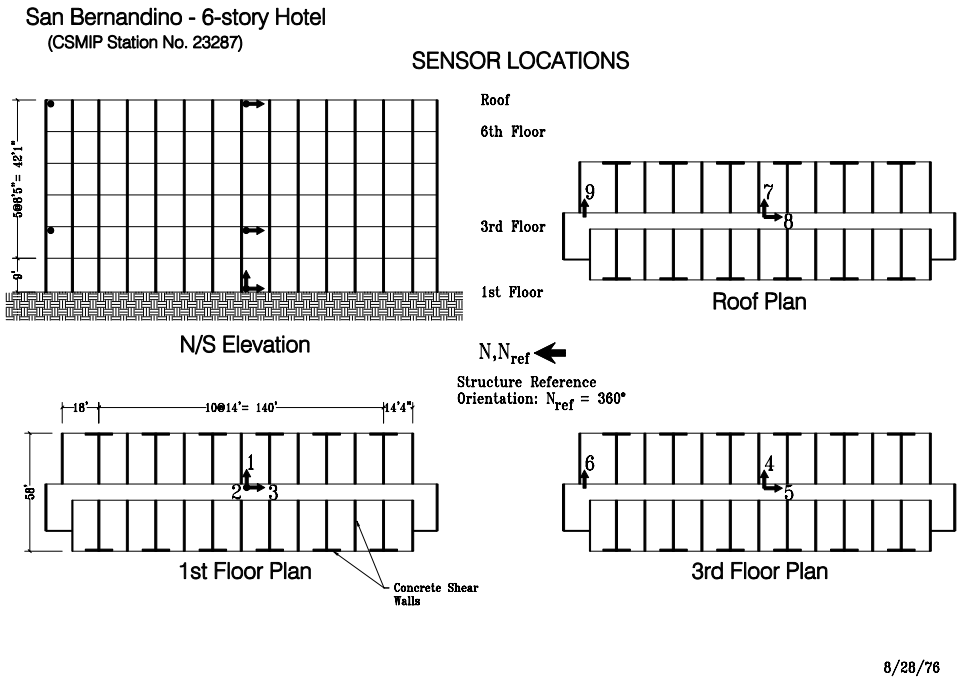

Figure 7.8: Six-story hotel building in San Bernardino, CA: plan and sensor layout (adopted from www.strongmotioncenter.org).

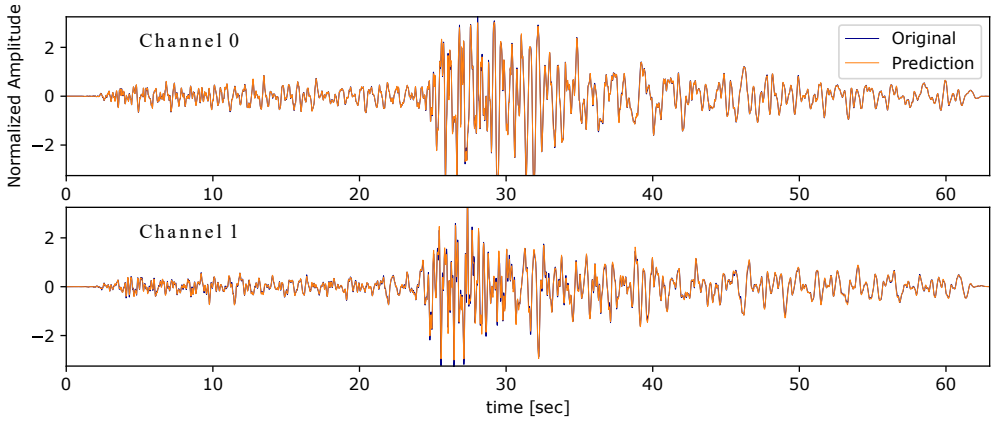

Figure 7.9: Input signal predictions in two horizontal axes. Long time projection is presented ($\sim$ 60 seconds).

both channels. The prediction comparison in the frequency domain also demonstrates that the prediction captures peaks and valleys quite precisely, especially in lower half of the frequency band. By visual inspection of the figures, it is noticeable that the

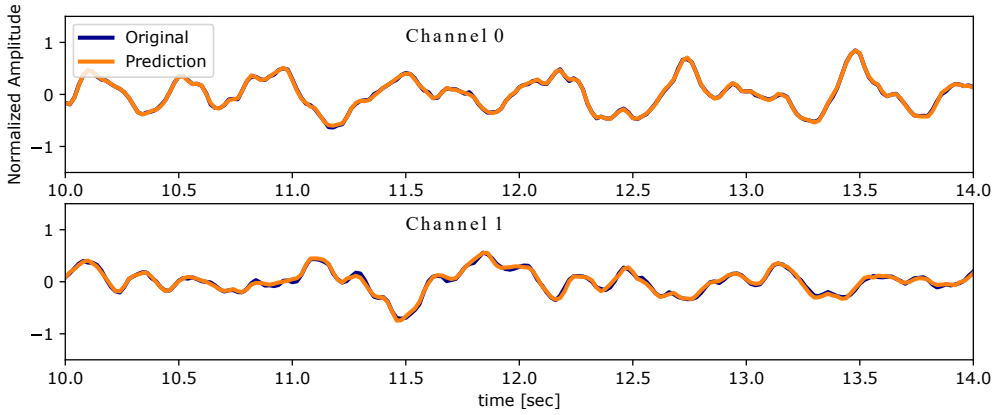

Figure 7.10: Input signal predictions in two horizontal axes. Short time projection is presented (4 seconds).

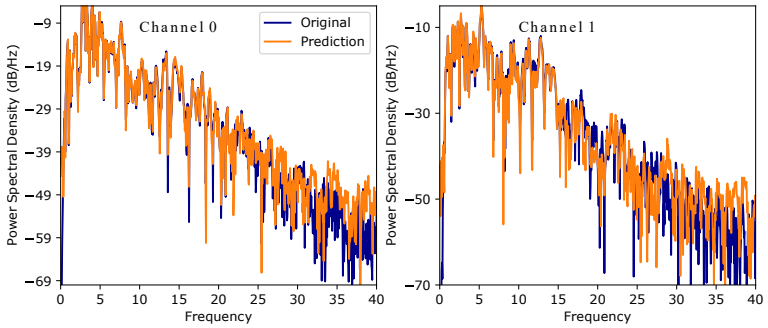

Figure 7.11: PSDs of the input signal predictions in two horizontal axes.

predictions in channel 0 are slightly more accurate compared to channel 1. To quantify the input estimation performance of the trained network for all testing signals, the network is inferred repeatedly with the different testing earthquakes, random starting points, and projection lengths. The accuracy measures of all these test cases are presented in Figure 7.12.

The figure shows that the correlation coefficients of the input estimations are almost always near one (i.e., exact). In terms of the MSE of the time signals, the distribution is located very close to zero while the range of values in channel 0 is significantly narrower compared to channel 1. The same pattern is found also in the frequency domain MSEs. The near perfect input estimations for this real-world case study confirms that the proposed learning based method is quite feasible for input estimation in different mechanical systems. In terms of different levels of accu-

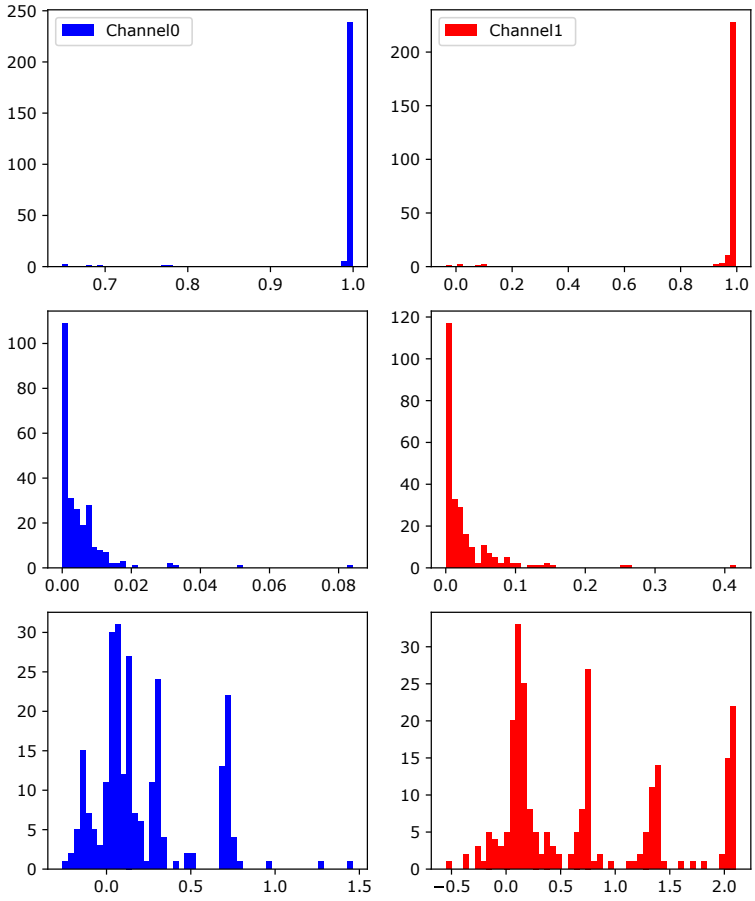

Figure 7.12: Histograms of the accuracy measures over the testing signals: (top) correlation coefficinet, (center) MSE in time domain, and (bottom) MSE in frequency domain.

racy between input channels, one can judge the network's performance by evaluating the confidence of the network predictions. For that, the histograms of predictions' standard deviations for both channels are presented in Figure 7.13.

From Figure 7.13, one can realize that the network is less confident about regressing values of channel 1 compared to channel 0. This result is consistent with the previous findings in Figure 7.12. Again, the probabilistic nature of the regression predictions in our proposed method enables to quantify prediction confidences in different channels with no need for evaluation with labelled data.

Finally, to interpret the contributions of the neural network features, the inter-

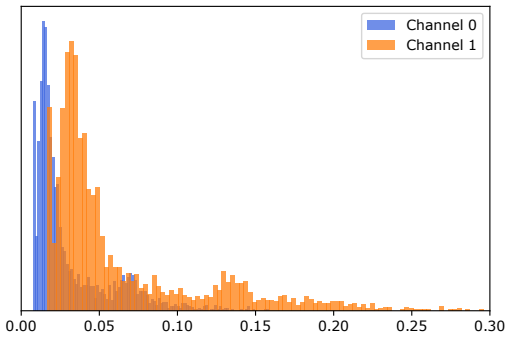

Figure 7.13: Histograms of standard deviations for two axes.

pretability analysis in accordance to Sundararajan et al. [2017] is performed on the trained network. The importance maps for both channels are presented in Figures 7.14 and 7.15. Channel ids match the indices previewed in Figure 7.8. As expected, for predicting building input at channel 0 (east-west direction), the output channels that are in parallel to it contribute more noticeably (e.g., channels 4 and 7). The same is also true for the perpendicular channels. In addition to that, it is found that the importance decreases for the output samples with more distant times. Interestingly, this decaying importance observation is less obvious in channel 1. This can suggest that the building response in the north-south direction is not as linear as the other direction which results in a stronger dependency to the distant outputs.

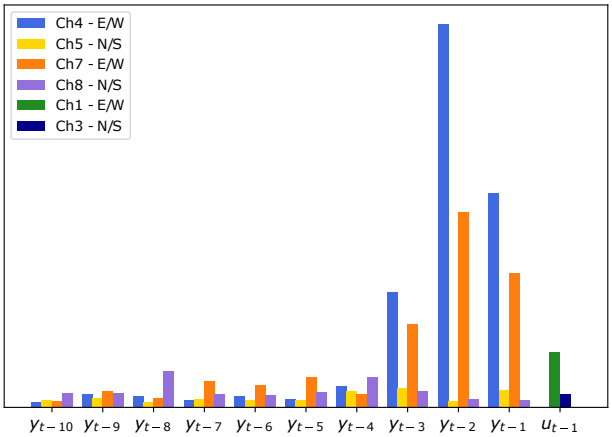

Figure 7.14: Importance map of the network features with respect to channel 0.

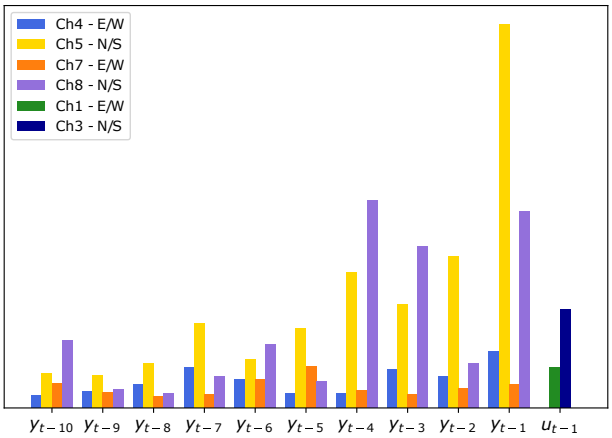

Figure 7.15: Importance map of the network features with respect to channel 1.

7.5 Case Three: Real-World Vehicle Input Estimation

In the final case study, an experiment was designed and conducted in order to collect data from a real-world vehicle at two locations: vehicle cabin and in proximity to the contact point. The contact point of the vehicle is practically inaccessible for a sensor device. Therefore, a practically feasible location is chosen and a manually assembled sensor bundle was attached to that location. The sensor was wirelessly communicating with a computer which was held by the operator in the passenger's front seat. The cabin sensor was attached to the dashboard of the vehicle. The sensor layout is presented schematically in Figure 7.16. As it is show in this figure, sensor 2 is mounted on the lower control arm which is found to be one of the most suitable locations for the vehicle input collection. The arm is a solid beam attached to the rim and is located right before the spring and the shock absorber throughout the pathway starting from the tire's contact point to the vehicle cabin.

The sensor bundle used for vehicle input sensing is shown in Figure 7.17 (similar configuration is used for the cabin sensor). The bundle consists of three components: (1) Raspberry Pi board, (2) ADXL345 accelerometer, and (3) power source. The Raspberry Pi is selected for data processing and storage due to its low cost, easy

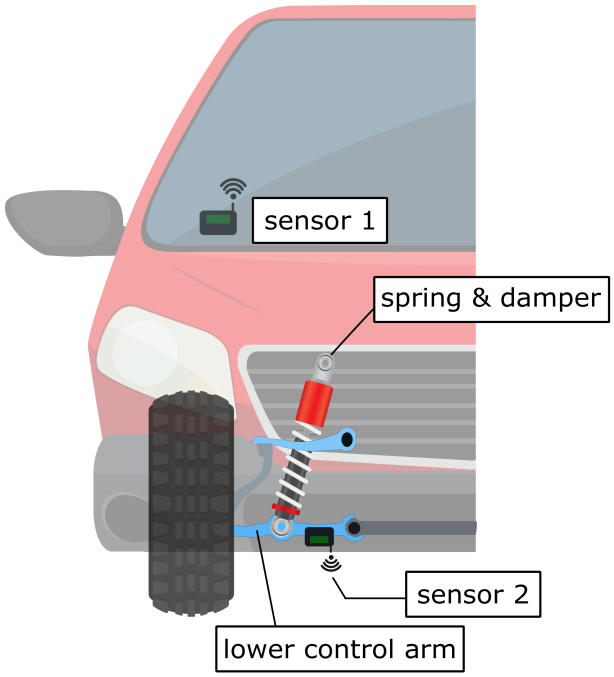

Figure 7.16: Schematic view of quarter-car model and sensor locations.

programming, and wireless connectivity. ADXL345 is a low cost 3-axis accelerometer which is compatible with Raspberry Pi and easily programmable. The acceleration range and sampling frequency can be tuned based on the application and required accuracy. To select these parameters, a lab-scale experiment was conducted on a single degree of freedom system and the accuracy of network predictions were compared for data collected with different sensor settings. Based on this preliminary study, the sampling frequency of $500Hz$ and acceleration range of $\pm 16.0g$ were set for the final experimental trial.

For the road test, a Kia Forte 2020 was equipped with the sensor sets. The instrumented vehicle was driven over roads with different roughness conditions, including recently paved, poor condition, and gravel roads near Lehigh University campus area. In total, 23 scans of $50,000$ samples were collected. The vehicle speed was mostly kept within $10 - 12.5$mph, however, in rare situations of traffic accumulation behind the testing car, the speed varied. The collected data were then preprocessed to be prepared for the training. The preprocessing phase included the following steps: (1)

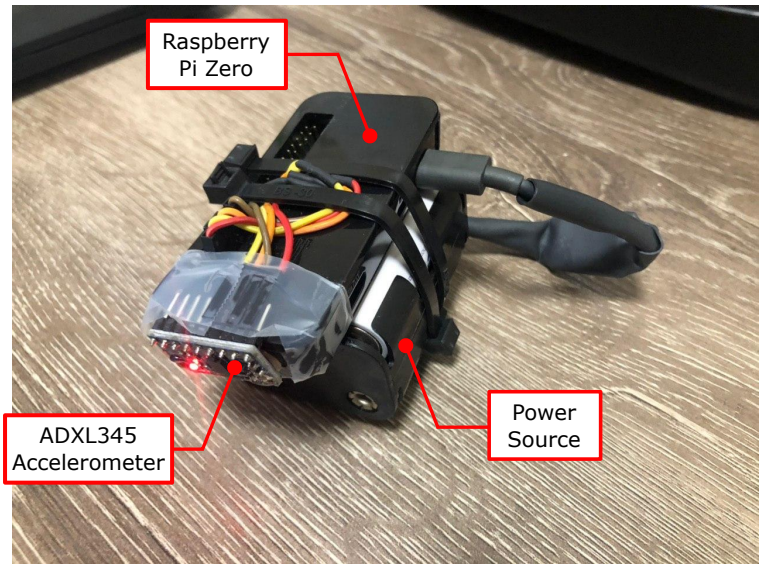

Figure 7.17: Assembled sensor setup: the main board is a Raspberry Pi and the sensing device is an ADXL345 accelerometer.

signal resampling in order to even the time intervals between samples, (2) signal filtering using a band-limited filter, and (3) downsampling to 100Hz. Filtering and downsampling steps reduce high frequency noise as well as measurement drifts in the collected signals. After preprocessing, signals are normalized linearly by a factor of $a_i = \mu_i + 3\sigma_i$ in which i is the index of a randomly picked signal. μ_i and σ_i are mean and standard deviation of the samples in signal i. This approach for normalization is found to yield better performances compared to other conventional methods.

7.5.1 Results

The training process of the real-world vehicle experiment is the same as the previous case studies. From 23 scans, 10, 1, and 12 are randomly picked for training, evaluation, and testing, respectively. Note that the majority of data are kept unseen for better performance assessment. As an important note, in this experiment the vehicle's suspension system is assumed as a quarter-car. Based on this assumption, the objective is to predict 3-axis vibrations at sensor 2 given collected responses at sensor 1. However to be more accurate, the vehicle can receive input from all four

tires, meaning that a more realistic scenario is to train the network based on inputs at all four tires given a complete set of vehicle cabin vibrations. In this study, the simplified version of the problem is investigated in expense of a lower input prediction accuracy.

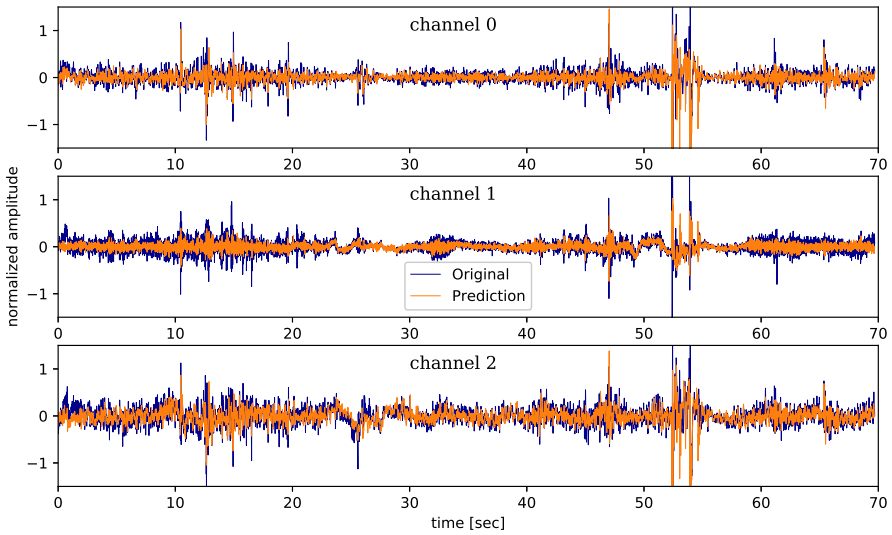

Figure 7.18: Input signal predictions in three axes. Long time projection is presented (70 seconds).

To evaluate the performance of the input estimations, the reconstructed input signals for one of the testing samples are presented in Figures 7.18 to 7.20. Figures generally confirm that the input estimation is performed quite accurately in all three axes. The nonstationary nature of the input is evident in the time signals (e.g., several high amplitude spikes). Still, the trained network successfully estimated the patterns. Figure 7.20 presents a comparison between predicted and original signals in the frequency domain. The trends, peaks, and baselines of the original PSDs are carefully represented in the predicted signals as well.

To quantify the accuracy of the input estimations, from each testing sample, 50 input projections with randomly picked length and starting point are made. In this analysis, the lower bound of the projection length is set to 200. For each projection,

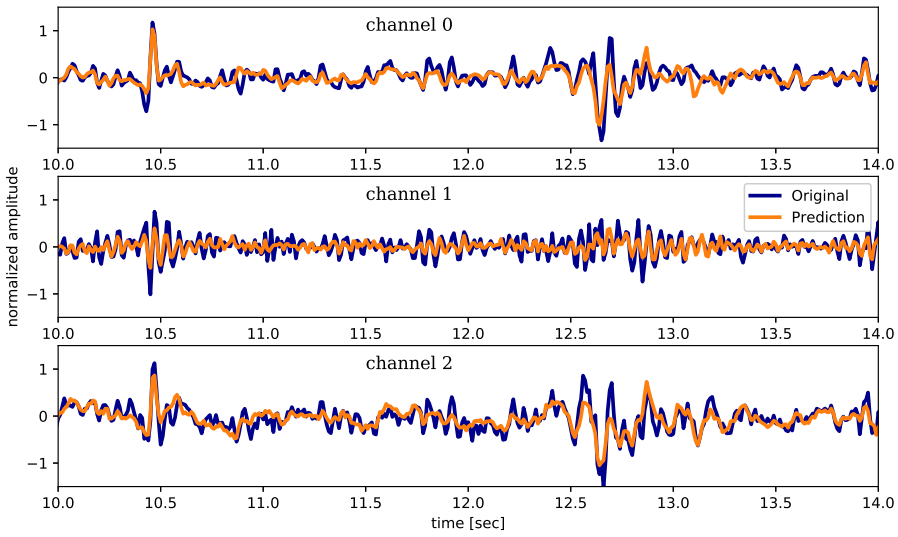

Figure 7.19: Input signal predictions in three axes. Short time projection is presented (4 seconds).

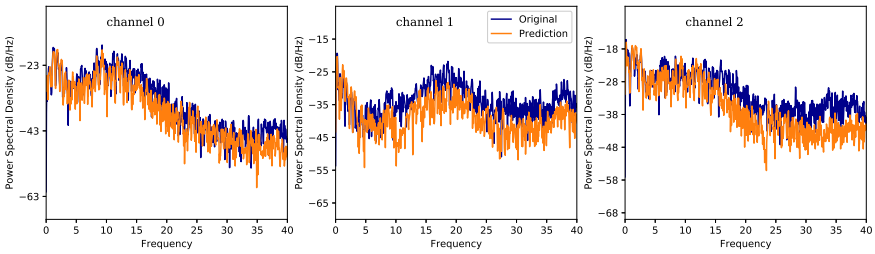

Figure 7.20: PSDs of the input signal predictions in three axes.

the accuracy is measured using the correlation coefficient, the MSE of the signal in time domain, and the MSE of the signals in frequency domain. The accuracy measures from this analysis are presented in Figure 7.21. Figure 7.21 (top) demonstrates that the distributions of the correlation coefficients are located in different ranges depending on the axis. For instance, in channel 2 the upper bound of the coefficients is 0.9 with an average near 0.75. These numbers are lower for channel 0 and channel 1, respectively. The correlation coefficient is a good measure to quantify the general coherence of two signals. However, for more detailed comparison, the MSE histograms are also presented.

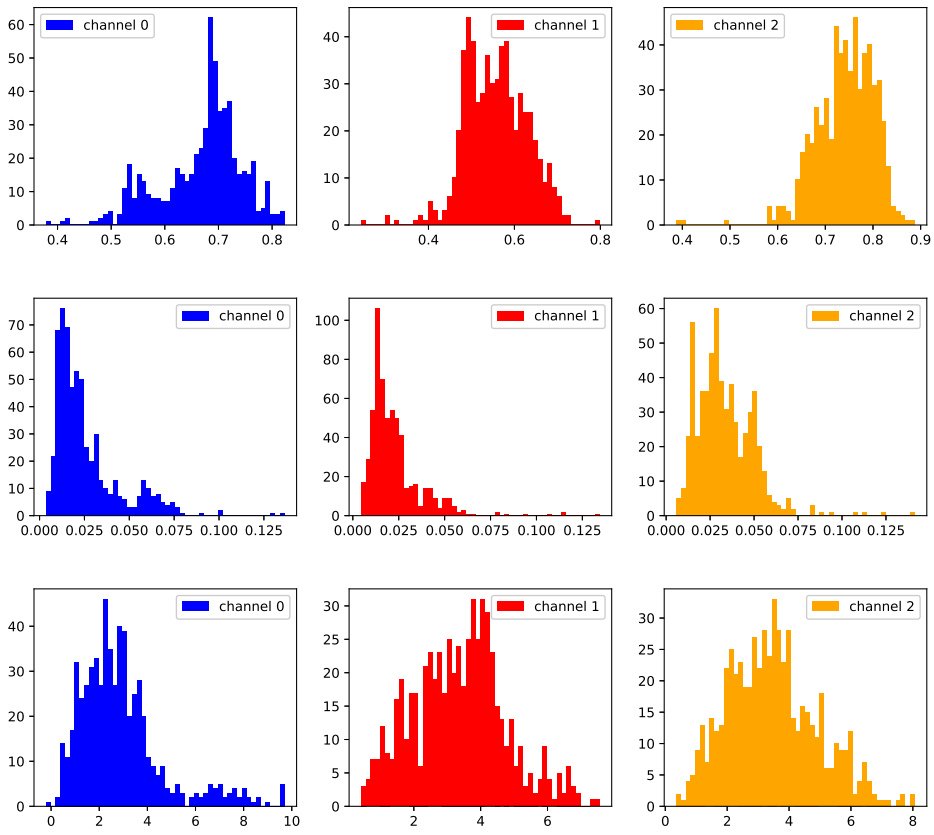

Figure 7.21: Histograms of the correlation coefficients (top), the MSEs in time (center), and the MSEs in frequency (bottom) from 50×12 random projections. Results are presented for three different axes.

From Figure 7.21 (center and bottom), it is hard to distinguish the channel with the most accuracy in the time and frequency predictions since the range and mean values are quite similar. This implies that the trained network should have had nearly the same confidence for predicting regression values in all three channels. To investigate that, the histograms of standard deviations are presented in Figure 7.22. In this figure, in contrast to the case shown in Figure 7.6, the standard deviations are not very different. One can notice that channel 0 is marginally inclined to the left (implying higher confidence in this channel), however, the difference is not strong. In other words, given the histograms of Figure 7.22, it is expected that performance of the trained network in all three axes is nearly identical. More importantly, this

finding is not a result of post-analysis using an available or labelled dataset, but it is readily available through the inference of the probabilistic network.

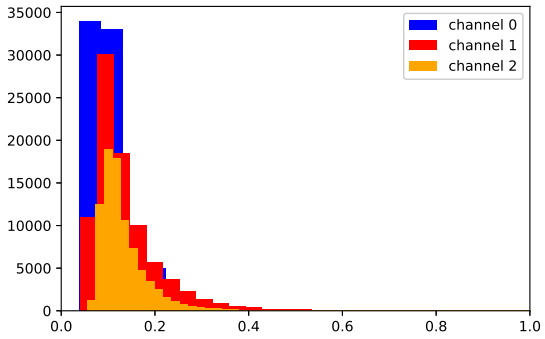

Figure 7.22: The histograms of standard deviations for three axes.

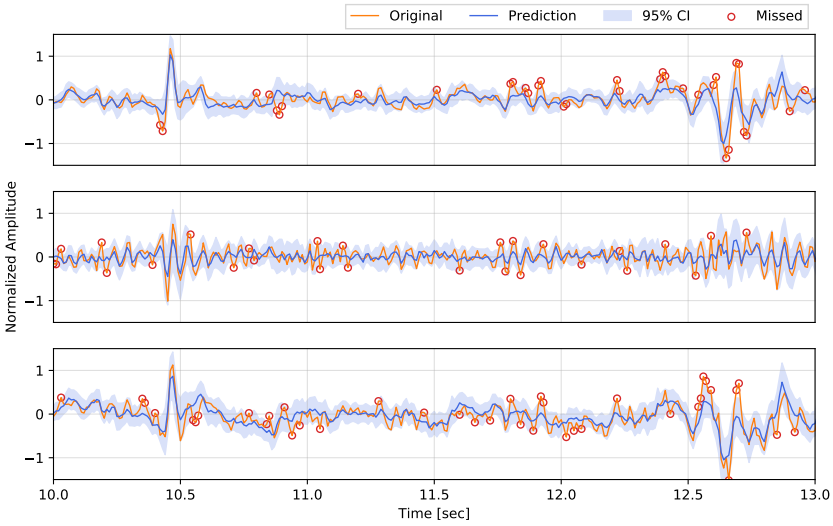

Figure 7.23: Input signal prediction with 95% confidence interval band: low confident points are marked with circles.

In addition to general confidence assessment over the entire signal or output channel, the resulted standard deviations are useful to detect low confidence predictions in a local scale. Figure 7.23 present the predicted and original signals and also highlight the 95% confidence interval of the predictions. The strong majority of the predicted samples fall inside the confidence band which confirms the strength of the trained

network. The outliers marked with circles indicate samples that the model cannot predict successfully, even considering the confidence interval. The number of such points can also be a good measure of the network performance. Finally, the interpretability of the trained network is analyzed. Figure 7.24 presents the importance factors of the network's input features. As expected, due to the highly nonlinear nature of the vehicle suspension, severely noisy data, and the contribution of vehicle inputs from other tires, the importance patterns are not as explainable as in the previous cases. Yet, in all three channels the importance of the more distant time steps decreases. This is consistent with our general expectation regarding causal dynamic systems. In addition, the cross-channel contributions are quite common in the experimental case (i.e., the contributions of channels perpendicular to the output channel are high). For instance, all three channels of the vehicle's input are strongly contributing in predicting neural network output at channel 1 (Figure 7.24b) which is dissimilar to the findings of the previous test cases. In this test, the alignment of sensors at the two locations (Figure 7.16) were dictated by the best available attaching surface; therefore, the sensors are mounted with arbitrary angles with respect to each other. As a result, the projections of multiple channels are expected to influence the prediction of each sensor channel in the vehicle's cabin.

In comparison to Figures 7.7 and 7.14, it is noticed that the real vehicle case has higher dependency to the input of the last time step (u_{t-1}). Intuitively, in all three case studies, the proposed neural network has two objectives: (a) to estimate the different of vehicle's inputs in two consecutive times steps (i.e., $u_{t-1} - u_{t-2}$) and (b) to estimate the vehicle's input at the unavailable time step given the available input value (e.g., to predict u_{t-2} given u_{t-1}). When u_{t-1} is available, the second task is quite trivial. Still, in the two first case studies the importance factors of u_{t-1} were comparatively small meaning that the networks were easily able to to predict the unavailable vehicle's input directly from the vehicle's output (i.e., the networks did

not require the supplemented u_{t-1} to find u_{t-2}). Nevertheless, in the third case, the critical role of the given vehicle's input is more clear. The trained network learned to fulfill task (a), but was disabled to estimate the initial vehicle's input directly. Therefore, the supplemented initial value could play a critical role and contribute significantly in the regression accuracy.

7.6 Conclusion

In this chapter, the inverse problem is dynamical systems was investigated in which the objective is to estimate the input given the dynamic response of the system. The problem is of great importance in different engineering fields. In particular, to achieve a realistic and accurate framework for bridge health monitoring using vehicle data crowdsourcing, the estimation of the vehicle's contact point input is critical. Thus, a probabilistic neural network architecture is proposed to learn the nonlinear and complex connection between the output and the input of the dynamic system with no prior characteristic information about the system. The network is then a robust filter for estimating the input of the dynamic system. The findings of this chapter are as follows:

- the study showed that the idea of using neural networks for input estimation of nonlinear systems is feasible and can yield to high accuracy input estimations.
- Compared to the alternatives, (1) this method is not limited to linear systems, (2) is fully based on practically available data types such as acceleration, and (3) requires no prior information of the physical system.
- The common approach for signal estimation is to utilize regression models. A probabilistic neural network is proposed to enable probabilistic perspective towards the predictions of regression models. Using this approach, one can quantify the certainty of the model for a given prediction.

- Using network interpretability methods, the importance maps of input features were presented and intuitively explained.
- Three case studies were explored, among which two were based on real-world structures (a building and a vehicle). In both applications, the proposed method resulted in accurate input predictions in all available data channels.
- In the case of real-world vehicle, an inexpensive sensor bundle is introduced and assembled. The Raspberry Pi based sensor bundle can be easily used for vibration analysis of structures in other research areas.

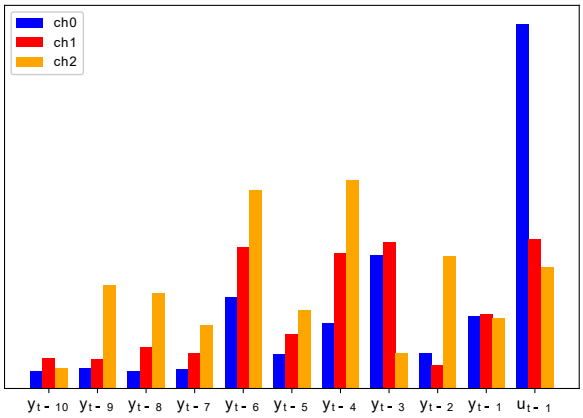

(a) channel 0

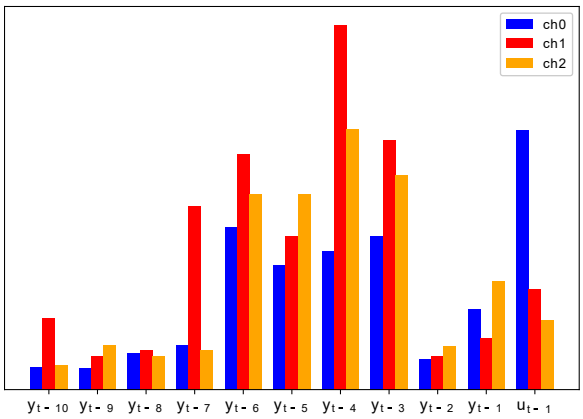

(b) channel 1

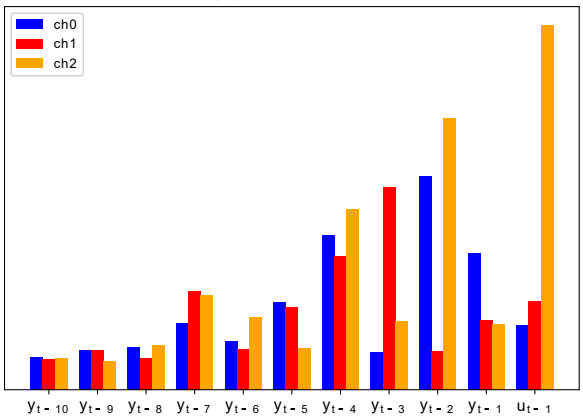

(c) channel 2

Figure 7.24: Importance map of the network features with respect to different channels.

Bibliography

ASCE. 2017 infrastructure report card. ASCE Reston, VA, 2017.

Thomas J Matarazzo and Shamim N Pakzad. Scalable structural modal identification using dynamic sensor network data with stridex. *Computer-Aided Civil and Infrastructure Engineering*, 33(1):4–20, 2018.

Soheil Sadeghi Eshkevari, Shamim N Pakzad, Martin Takáĉ, and Thomas J Matarazzo. Modal identification of bridges using mobile sensors with sparse vibration data. *Journal of Engineering Mechanics*, 2020a.

Y-B Yang, CW Lin, and JD Yau. Extracting bridge frequencies from the dynamic response of a passing vehicle. *Journal of Sound and Vibration*, 272(3-5):471–493, 2004a.

Yeong-Bin Yang, JD Yau, Zhongda Yao, and YS Wu. *Vehicle-bridge interaction dynamics: with applications to high-speed railways*. World Scientific, 2004b.

Arturo González, Eugene J OBrien, and PJ McGetrick. Identification of damping in a bridge using a moving instrumented vehicle. *Journal of Sound and Vibration*, 331(18):4115–4131, 2012.

Johannio Marulanda, Juan M Caicedo, and Peter Thomson. Modal identification using mobile sensors under ambient excitation. *Journal of Computing in Civil Engineering*, 31(2):04016051, 2016.

Eugene J OBrien and Abdollah Malekjafarian. A mode shape-based damage detection approach using laser measurement from a vehicle crossing a simply supported bridge. *Structural Control and Health Monitoring*, 23(10):1273–1286, 2016.

Thomas J Matarazzo and Shamim N Pakzad. Truncated physical model for dynamic sensor networks with applications in high-resolution mobile sensing and bigdata. *Journal of Engineering Mechanics*, 142(5):04016019, 2016a.

Eugene J OBrien, Daniel Cantero, Bernard Enright, and Arturo González. Characteristic dynamic increment for extreme traffic loading events on short and medium span highway bridges. *Engineering Structures*, 32(12):3827–3835, 2010.

Albert-Laszlo Barabasi. The origin of bursts and heavy tails in human dynamics. *Nature*, 435(7039):207, 2005.

H. Wang, F. Calabrese, G. Di Lorenzo, and C. Ratti. Transportation mode inference from anonymized and aggregated mobile phone call detail records. *In Intelligent Transportation Systems (ITSC), 2010 13th International IEEE Conference on Intelligent Transportation Systems*, pages 318–323, 2010.

Pu Wang, Timothy Hunter, Alexandre M Bayen, Katja Schechtner, and Marta C González. Understanding road usage patterns in urban areas. *Scientific reports*, 2: 1001, 2012.

Lauren Alexander, Shan Jiang, Mikel Murga, and Marta C González. Origin–destination trips by purpose and time of day inferred from mobile phone data. *Transportation research part c: emerging technologies*, 58:240–250, 2015.

Remi Tachet, Oleguer Sagarra, Paolo Santi, Giovanni Resta, Michael Szell, SH Strogatz, and Carlo Ratti. Scaling law of urban ride sharing. *Scientific reports*, 7:42868, 2017.

Remi Tachet, Paolo Santi, Stanislav Sobolevsky, Luis Ignacio Reyes-Castro, Emilio Frazzoli, Dirk Helbing, and Carlo Ratti. Revisiting street intersections using slot-based systems. *PloS one*, 11(3):e0149607, 2016.

Amin Anjomshoaa, Fábio Duarte, Daniël Rennings, Thomas Matarazzo, Priyanka de Souza, and Carlo Ratti. City scanner: Building and scheduling a mobile sensing platform for smart city services. *IEEE Internet of Things Journal*, 2018.

Mohammed M Vazifeh, P Santi, G Resta, SH Strogatz, and C Ratti. Addressing the minimum fleet problem in on-demand urban mobility. *Nature*, 557(7706):534, 2018.

Kevin Robert Gurney, Paty Romero-Lankao, Karen C Seto, Lucy R Hutyra, Riley Duren, Christopher Kennedy, Nancy B Grimm, James R Ehleringer, Peter Marcotullio, Sara Hughes, et al. Climate change: Track urban emissions on a human scale. *Nature News*, 525(7568):179, 2015.

Emanuele Massaro, Chaewon Ahn, Carlo Ratti, Paolo Santi, Rainer Stahlmann, Andreas Lamprecht, Martin Roehder, and Markus Huber. The car as an ambient sensing platform [point of view]. *Proceedings of the IEEE*, 105(1):3–7, 2017.

Sandeep Sony, Shea Laventure, and Ayan Sadhu. A literature review of next-generation smart sensing technology in structural health monitoring. *Structural Control and Health Monitoring*, 26(3):e2321, 2019.

Shamim N Pakzad, Gregory L Fenves, Sukun Kim, and David E Culler. Design and implementation of scalable wireless sensor network for structural monitoring. *Journal of infrastructure systems*, 14(1):89–101, 2008.

Jerome P Lynch and Kenneth J Loh. A summary review of wireless sensors and sensor networks for structural health monitoring. *Shock and Vibration Digest*, 38 (2):91–130, 2006.

Masahiro Kurata, Junhee Kim, Yilan Zhang, Jerome P Lynch, GW Van Der Linden, Vince Jacob, Ed Thometz, Pat Hipley, and Li-Hong Sheng. Long-term assessment of an autonomous wireless structural health monitoring system at the new carquinez suspension bridge. In *Nondestructive Characterization for Composite Materials, Aerospace Engineering, Civil Infrastructure, and Homeland Security 2011*, volume 7983, page 798312. International Society for Optics and Photonics, 2011.

Thomas J Matarazzo, Paolo Santi, Shamim N Pakzad, Kristopher Carter, Carlo Ratti, Babak Moaveni, Chris Osgood, and Nigel Jacob. Crowdsensing framework for monitoring bridge vibrations using moving smartphones. *Proceedings of the IEEE*, 106(4):577–593, 2018.

Qipei Mei, Mustafa Gül, and Marcus Boay. Indirect health monitoring of bridges using mel-frequency cepstral coefficients and principal component analysis. *Mechanical Systems and Signal Processing*, 119:523–546, 2019.

Qipei Mei and Mustafa Gül. A crowdsourcing-based methodology using smartphones for bridge health monitoring. *Structural Health Monitoring*, page 1475921718815457, 2018.

AJ Kleywegt and KC Sinha. Tools for bridge management data analysis. *Transportation Research Circular*, (423), 1994.

Ian FC Smith. Studies of sensor data interpretation for asset management of the built environment. *Frontiers in Built Environment*, 2:8, 2016.

CW Lin and YB Yang. Use of a passing vehicle to scan the fundamental bridge frequencies: An experimental verification. *Engineering Structures*, 27(13):1865–1878, 2005.

YB Yang and KC Chang. Extracting the bridge frequencies indirectly from a passing vehicle: Parametric study. *Engineering Structures*, 31(10):2448–2459, 2009.

Jennifer Keenahan, Eugene J OBrien, Patrick J McGetrick, and Arturo Gonzalez. The use of a dynamic truck–trailer drive-by system to monitor bridge damping. *Structural Health Monitoring*, 13(2):143–157, 2014.

Patrick J McGetrick, Chul-Woo Kim, Arturo González, and Eugene JO Brien. Experimental validation of a drive-by stiffness identification method for bridge monitoring. *Structural Health Monitoring*, 14(4):317–331, 2015.

Wei-ming Li, Zhi-hui Jiang, Tai-long Wang, and Hong-ping Zhu. Optimization method based on generalized pattern search algorithm to identify bridge parameters indirectly by a passing vehicle. *Journal of Sound and Vibration*, 333(2):364–380, 2014.

Rune Brincker, Lingmi Zhang, and Palle Andersen. Modal identification of output-only systems using frequency domain decomposition. *Smart materials and structures*, 10(3):441, 2001.

J-N Juang and Richard S Pappa. An eigensystem realization algorithm for modal parameter identification and model reduction. *Journal of guidance, control, and dynamics*, 8(5):620–627, 1985.

GH James, Thomas G Carne, James P Lauffer, et al. The natural excitation technique (next) for modal parameter extraction from operating structures. *Modal Analysis-the International Journal of Analytical and Experimental Modal Analysis*, 10(4): 260, 1995.

Bart Peeters and Guido De Roeck. Stochastic system identification for operational modal analysis: a review. *Journal of Dynamic Systems, Measurement, and Control*, 123(4):659–667, 2001.

Siu-Kui Au. Fast bayesian fft method for ambient modal identification with separated modes. *Journal of Engineering Mechanics*, 137(3):214–226, 2011.

Shamim N Pakzad, Guilherme V Rocha, and Bin Yu. Distributed modal identification using restricted auto regressive models. *International Journal of Systems Science*, 42(9):1473–1489, 2011.

Minwoo Chang and Shamim N Pakzad. Observer kalman filter identification for output-only systems using interactive structural modal identification toolsuite. *Journal of Bridge Engineering*, 19(5):04014002, 2013a.

S Dorvash and SN Pakzad. Stochastic iterative modal identification algorithm and application in wireless sensor networks. *Structural Control and Health Monitoring*, 20(8):1121–1137, 2013.

Thomas J Matarazzo and Shamim N Pakzad. Structural identification for mobile sensing with missing observations. *Journal of Engineering Mechanics*, 142(5):04016021, 2016b.

Fang Gensun. Whittaker–kotelnikov–shannon sampling theorem and aliasing error. *Journal of approximation theory*, 85(2):115–131, 1996.

Thomas Schanze. Sinc interpolation of discrete periodic signals. *IEEE Transactions on Signal Processing*, 43(6):1502–1503, 1995.

SO Reza Moheimani, Dunant Halim, and Andrew J Fleming. *Spatial control of vibration: theory and experiments*, volume 10. World scientific, 2003.

Abdul J Jerri. The shannon sampling theorem—its various extensions and applications: A tutorial review. *Proceedings of the IEEE*, 65(11):1565–1596, 1977.

Shay Maymon and Alan V Oppenheim. Sinc interpolation of nonuniform samples. *IEEE Transactions on Signal Processing*, 59(10):4745–4758, 2011.

Soheil Sadeghi Eshkevari, Thomas J. Matarazzo, and Shamim N. Pakzad. Bridge modal identification using acceleration measurements within moving vehicles. *Me-*

chanical Systems and Signal Processing, 141:106733, 2020b. ISSN 0888-3270. doi: https://doi.org/10.1016/j.ymssp.2020.106733.

Soheil Sadeghi Eshkevari and Shamim Pakzad. Bridge structural identification using moving vehicle acceleration measurements. In *Dynamics of Civil Structures, Volume 2*, pages 251–261. Springer, 2019a.

Abdollah Malekjafarian, Patrick J McGetrick, and Eugene J OBrien. A review of indirect bridge monitoring using passing vehicles. *Shock and vibration*, 2015, 2015.

Abdollah Malekjafarian and Eugene J OBrien. Identification of bridge mode shapes using short time frequency domain decomposition of the responses measured in a passing vehicle. *Engineering Structures*, 81:386–397, 2014a.

Soheil Sadeghi Eshkevari and Shamim N Pakzad. Signal reconstruction from mobile sensors network using matrix completion approach. In *Topics in Modal Analysis & Testing, Volume 8*, pages 61–75. Springer, 2020a.

Prateek Jain, Praneeth Netrapalli, and Sujay Sanghavi. Low-rank matrix completion using alternating minimization. In *Proceedings of the forty-fifth annual ACM symposium on Theory of computing*, pages 665–674. ACM, 2013.

Dave Zachariah, Martin Sundin, Magnus Jansson, and Saikat Chatterjee. Alternating least-squares for low-rank matrix reconstruction. *IEEE Signal Processing Letters*, 19(4):231–234, 2012.

B Kramer and S Gugercin. Tangential interpolation-based eigensystem realization algorithm for mimo systems. *Mathematical and Computer Modelling of Dynamical Systems*, 22(4):282–306, 2016.

Sriram S Krishnan, Zhuoxiong Sun, Ayhan Irfanoglu, Shirley J Dyke, and Guirong Yan. Evaluating the performance of distributed approaches for modal identification.

In *Sensors and Smart Structures Technologies for Civil, Mechanical, and Aerospace Systems 2011*, volume 7981, page 79814M. International Society for Optics and Photonics, 2011.

Boris Kramer and Alex A Gorodetsky. System identification via cur-factored hankel approximation. *SIAM Journal on Scientific Computing*, 40(2):A848–A866, 2018.

Edward L Wilson, Ming-Wu Yuan, and John M Dickens. Dynamic analysis by direct superposition of ritz vectors. *Earthquake Engineering & Structural Dynamics*, 10 (6):813–821, 1982.

Jian-Feng Cai, Emmanuel J Candès, and Zuowei Shen. A singular value thresholding algorithm for matrix completion. *SIAM Journal on Optimization*, 20(4):1956–1982, 2010.

Emmanuel J Candès and Benjamin Recht. Exact matrix completion via convex optimization. *Foundations of Computational mathematics*, 9(6):717, 2009.

Ciyou Zhu, Richard H Byrd, Peihuang Lu, and Jorge Nocedal. Algorithm 778: L-bfgs-b: Fortran subroutines for large-scale bound-constrained optimization. *ACM Transactions on Mathematical Software (TOMS)*, 23(4):550–560, 1997.

Fabien Poncelet, Gaëtan Kerschen, J-C Golinval, and Damien Verhelst. Output-only modal analysis using blind source separation techniques. *Mechanical systems and signal processing*, 21(6):2335–2358, 2007.

Mark Eisen, Aryan Mokhtari, and Alejandro Ribeiro. Large scale empirical risk minimization via truncated adaptive newton method. *arXiv preprint arXiv:1705.07957*, 2017.

Stephen Wright and Jorge Nocedal. Numerical optimization. *Springer Science*, 35 (67-68):7, 1999.

Randall J Allemang and David L Brown. A correlation coefficient for modal vector analysis. In *Proceedings of the 1st international modal analysis conference*, volume 1, pages 110–116. SEM Orlando, 1982.

Anil K Chopra. Dynamics of structures. theory and applications to. *Earthquake Engineering*, 2017.

Ian Jolliffe. Principal component analysis. In *International encyclopedia of statistical science*, pages 1094–1096. Springer, 2011.

YQ Ni, Y Xia, WY Liao, and JM Ko. Technology innovation in developing the structural health monitoring system for guangzhou new tv tower. *Structural Control and Health Monitoring: The Official Journal of the International Association for Structural Control and Monitoring and of the European Association for the Control of Structures*, 16(1):73–98, 2009.

P Andersen, Rune Brincker, Bart Peeters, Guido De Roeck, L Hermans, and C Krämer. Comparison of system identification methods using ambient bridge test data. In *Proc. of the 17th International Modal Analysis Conference, Kissimee, Florida*, pages 7–10, 1999.

Mustafa Gul and F Necati Catbas. Statistical pattern recognition for structural health monitoring using time series modeling: Theory and experimental verifications. *Mechanical Systems and Signal Processing*, 23(7):2192–2204, 2009.

Siavash Dorvash, Shamim Pakzad, Clay Naito, Ian Hodgson, and Ben Yen. Application of state-of-the-art in measurement and data analysis techniques for vibration evaluation of a tall building. *Structure and Infrastructure Engineering*, 10(5):654–669, 2014.

Dapeng Zhu, Jiajie Guo, Chunhee Cho, Yang Wang, and Kok-Meng Lee. Wire-

less mobile sensor network for the system identification of a space frame bridge. *Ieee/Asme Transactions On Mechatronics*, 17(3):499–507, 2012.

Kay Smarsly, Kincho H Law, and Dietrich Hartmann. Multiagent-based collaborative framework for a self-managing structural health monitoring system. *Journal of computing in civil engineering*, 26(1):76–89, 2011.

Tracy Kijewski-Correa, Dae Kun Kwon, Ahsan Kareem, Audrey Bentz, Yanlin Guo, Sarah Bobby, and Ahmad Abdelrazaq. Smartsync: an integrated real-time structural health monitoring and structural identification system for tall buildings. *Journal of Structural Engineering*, 139(10):1675–1687, 2012.

Yilan Zhang, Sean M O'Connor, Gwendolyn W van der Linden, Atul Prakash, and Jerome P Lynch. Senstore: a scalable cyberinfrastructure platform for implementation of data-to-decision frameworks for infrastructure health management. *Journal of Computing in Civil Engineering*, 30(5):04016012, 2016.

HY Guo, L Zhang, LL Zhang, and JX Zhou. Optimal placement of sensors for structural health monitoring using improved genetic algorithms. *Smart materials and structures*, 13(3):528, 2004.

Sang-Hyo Kim, Chongyul Yoon, and Byoung-Jin Kim. Structural monitoring system based on sensitivity analysis and a neural network. *Computer-Aided Civil and Infrastructure Engineering*, 15(4):189–195, 2000.

Minwoo Chang and Shamim N Pakzad. Optimal sensor configuration for flexible structures with multi-dimensional mode shapes. *Smart Materials and Structures*, 24(5):055012, 2015.

Michele Meo and G Zumpano. On the optimal sensor placement techniques for a bridge structure. *Engineering structures*, 27(10):1488–1497, 2005.

Jakob Eriksson, Lewis Girod, Bret Hull, Ryan Newton, Samuel Madden, and Hari Balakrishnan. The Pothole Patrol: Using a Mobile Sensor Network for Road Surface Monitoring. In *The Sixth Annual International conference on Mobile Systems, Applications and Services (MobiSys 2008)*, Breckenridge, U.S.A., June 2008.

G Alessandroni, LC Klopfenstein, S Delpriori, M Dromedari, G Luchetti, B Paolini, A Seraghiti, E Lattanzi, V Freschi, A Carini, et al. Smartroadsense: Collaborative road surface condition monitoring. *Proc. of UBICOMM-2014. IARIA*, pages 210–215, 2014.

Rajiv Kumar, Abhijit Mukherjee, and VP Singh. Community sensor network for monitoring road roughness using smartphones. *Journal of Computing in Civil Engineering*, 31(3):04016059, 2016.

Maria Feng, Yoshio Fukuda, Masato Mizuta, and Ekin Ozer. Citizen sensors for shm: Use of accelerometer data from smartphones. *Sensors*, 15(2):2980–2998, 2015.

Soheil Sadeghi Eshkevari and Shamim N Pakzad. Signal reconstruction from mobile sensors network using matrix completion approach. In *Topics in Modal Analysis & Testing, Volume 8*, pages 61–75. Springer, 2020b.

Branko Ristic, Sanjeev Arulampalam, and Neil Gordon. Beyond the kalman filter. *IEEE Aerospace and Electronic Systems Magazine*, 19(7):37–38, 2004.

Simo Särkkä. Unscented rauch–tung–striebel smoother. *IEEE Transactions on Automatic Control*, 53(3):845–849, 2008.

Daniel Cantero, Patrick McGetrick, Chul-Woo Kim, and Eugene OBrien. Experimental monitoring of bridge frequency evolution during the passage of vehicles with different suspension properties. *Engineering Structures*, 187:209–219, 2019.

KC Chang, CW Kim, Sudanna Borjigin, et al. Variability in bridge frequency induced by a parked vehicle. In *Proceedings of the 4th KKCNN Symposium on Civil Engineering*, pages 75–79, 2014.

Dionysius M Siringoringo and Yozo Fujino. Estimating bridge fundamental frequency from vibration response of instrumented passing vehicle: analytical and experimental study. *Advances in Structural Engineering*, 15(3):417–433, 2012.

Abdollah Malekjafarian and Eugene J OBrien. Identification of bridge mode shapes using short time frequency domain decomposition of the responses measured in a passing vehicle. *Engineering Structures*, 81:386–397, 2014b.

Yao Zhang, Longqi Wang, and Zhihai Xiang. Damage detection by mode shape squares extracted from a passing vehicle. *Journal of Sound and Vibration*, 331(2): 291–307, 2012.

Abdollah Malekjafarian and Eugene J OBrien. On the use of a passing vehicle for the estimation of bridge mode shapes. *Journal of Sound and Vibration*, 397:77–91, 2017.

Yufen Zhou and Suren Chen. Fully coupled driving safety analysis of moving traffic on long-span bridges subjected to crosswind. *Journal of Wind Engineering and Industrial Aerodynamics*, 143:1–18, 2015.

A Camara, I Kavrakov, K Nguyen, and G Morgenthal. Complete framework of wind-vehicle-bridge interaction with random road surfaces. *Journal of Sound and Vibration*, 2019.

Soheil Sadeghi Eshkevari, Thomas J Matarazzo, and Shamim N Pakzad. Simplified vehicle-bridge interaction for medium to long-span bridges subject to random traffic load. *Journal of civil structural health monitoring*, 9(2):201–215, 2020c.

SJ Elliott and PA Nelson. The active control of sound. *Electronics & communication engineering journal*, 2(4):127–136, 1990.

J-F Cardoso. Blind signal separation: statistical principles. *Proceedings of the IEEE*, 86(10):2009–2025, 1998.

Norden E Huang, Zheng Shen, Steven R Long, Manli C Wu, Hsing H Shih, Quanan Zheng, Nai-Chyuan Yen, Chi Chao Tung, and Henry H Liu. The empirical mode decomposition and the hilbert spectrum for nonlinear and non-stationary time series analysis. In *Proceedings of the Royal Society of London A: mathematical, physical and engineering sciences*, volume 454, pages 903–995. The Royal Society, 1998.

Adel Belouchrani, Karim Abed-Meraim, J-F Cardoso, and Eric Moulines. A blind source separation technique using second-order statistics. *IEEE Transactions on signal processing*, 45(2):434–444, 1997.

David Cebon. *Handbook of vehicle-road interaction*. 1999.

Gaëtan Kerschen, Fabien Poncelet, and J-C Golinval. Physical interpretation of independent component analysis in structural dynamics. *Mechanical Systems and Signal Processing*, 21(4):1561–1575, 2007.

A Sadhu, S Narasimhan, and J Antoni. A review of output-only structural mode identification literature employing blind source separation methods. *Mechanical Systems and Signal Processing*, 94:415–431, 2017.

Andrzej Cichocki and Shun-ichi Amari. *Adaptive blind signal and image processing: learning algorithms and applications*, volume 1. John Wiley & Sons, 2002.

Seungjin Choi, Andrzej Cichocki, Hyung-Min Park, and Soo-Young Lee. Blind source separation and independent component analysis: A review. *Neural Information Processing-Letters and Reviews*, 6(1):1–57, 2005.

Aapo Hyvärinen and Erkki Oja. Independent component analysis: algorithms and applications. *Neural networks*, 13(4-5):411–430, 2000.

Lang Tong, VC Soon, YF Huang, and RALR Liu. Amuse: a new blind identification algorithm. In *Circuits and Systems, 1990., IEEE International Symposium on*, pages 1784–1787. IEEE, 1990.

Ahmed M Abdel-Ghaffar and Magdi A Khalifa. Importance of cable vibration in dynamics of cable-stayed bridges. *Journal of Engineering Mechanics*, 117(11):2571–2589, 1991.

Jian-Huang Weng, Chin-Hsiung Loh, Jerome P Lynch, Kung-Chun Lu, Pei-Yang Lin, and Yang Wang. Output-only modal identification of a cable-stayed bridge using wireless monitoring systems. *Engineering Structures*, 30(7):1820–1830, 2008.

Frank McKenna, Gregory L Fenves, Michael H Scott, et al. Open system for earthquake engineering simulation. *University of California, Berkeley, CA*, 2000.

Gabriel Rilling and Patrick Flandrin. One or two frequencies? the empirical mode decomposition answers. *IEEE transactions on signal processing*, 56(1):85–95, 2008.

Minwoo Chang and Shamim N Pakzad. Observer kalman filter identification for output-only systems using interactive structural modal identification toolsuite. *Journal of Bridge Engineering*, 19(5):04014002, 2013b.

Alena Bilošová. Modal testing. *VŠB-Tech. Univ. Ostrava, Ostrava, Czech Republic, Tech. Rep*, pages 63–64, 2011.

Lu Sun, Zhanming Zhang, and Jessica Ruth. Modeling indirect statistics of surface roughness. *Journal of transportation engineering*, 127(2):105–111, 2001.

Klas Bogsjö, Krzysztof Podgórski, and Igor Rychlik. Models for road surface roughness. *Vehicle System Dynamics*, 50(5):725–747, 2012.

Patrick Flandrin, Gabriel Rilling, and Paulo Goncalves. Empirical mode decomposition as a filter bank. *IEEE signal processing letters*, 11(2):112–114, 2004.

Miroslav Pastor, Michal Binda, and Tomáš Harčarik. Modal assurance criterion. *Procedia Engineering*, 48:543–548, 2012.

William F Milliken, Douglas L Milliken, and Maurice Olley. *Chassis design: principles and analysis*, volume 400. Society of Automotive Engineers Warrendale, 2002.

Matt Giaraffa. Tech tip: Springs & dampers, part one. *Optimum G: Technical Papers*, 2017.

E Esmailzadeh and HD Taghirad. Ride comfort and roll characteristics of tandem-axled trucks. Technical report, SAE Technical Paper, 1995.

Yvan Champoux, Simon Richard, and Jean-Marc Drouet. Bicycle structural dynamics. *Sound and vibration*, 41(7):16–25, 2007.

Andronic Florin, Manolache-Rusu Ioan-Cozmin, and Pătuleanu Liliana. Passive suspension modeling using matlab, quarter-car model, input signal step type. *New technologies and products in machine manufacturing technologies*, pages 258–263, 2013.

Thomas D Gillespie and Michael W Sayers. *Measuring Road Roughness and its Effects on User Cost and Comfort: A Symposium*, volume 884. ASTM International, 1985.

SR Chen and CS Cai. Equivalent wheel load approach for slender cable-stayed bridge fatigue assessment under traffic and wind: Feasibility study. *Journal of Bridge Engineering*, 12(6):755–764, 2007.

XQ Zhu and Siu-Seong Law. Structural health monitoring based on vehicle-bridge interaction: accomplishments and challenges. *Advances in Structural Engineering*, 18(12):1999–2015, 2015.

XQ Zhu and Siu-Seong Law. Recent developments in inverse problems of vehicle–bridge interaction dynamics. *Journal of Civil Structural Health Monitoring*, 6(1): 107–128, 2016.

YB Yang and Judy P Yang. State-of-the-art review on modal identification and damage detection of bridges by moving test vehicles. *International Journal of Structural Stability and Dynamics*, 18(02):1850025, 2018.

Yufen Zhou and Suren Chen. Vehicle ride comfort analysis with whole-body vibration on long-span bridges subjected to crosswind. *Journal of Wind Engineering and Industrial Aerodynamics*, 155:126–140, 2016.

Soheil Sadeghi Eshkevari, Shamim N Pakzad, Martin Takáč, and Thomas J Matarazzo. Modal identification of bridges using mobile sensors with sparse vibration data. *Journal of Engineering Mechanics*, 142(4):04015109, 2020d. doi: 10.1061/(ASCE)EM.1943-7889.0001733.

Kevin P O'Keeffe, Amin Anjomshoaa, Steven H Strogatz, Paolo Santi, and Carlo Ratti. Quantifying the sensing power of vehicle fleets. *Proceedings of the National Academy of Sciences*, 116(26):12752–12757, 2019.

Francesco Calabrese, Massimo Colonna, Piero Lovisolo, Dario Parata, and Carlo Ratti. Real-time urban monitoring using cell phones: A case study in rome. *IEEE Transactions on Intelligent Transportation Systems*, 12(1):141–151, 2010.

Yan Yu, Ruicong Han, Xuefeng Zhao, Xingquan Mao, Weitong Hu, Dong Jiao, Mingchu Li, and Jinping Ou. Initial validation of mobile-structural health monitoring method using smartphones. *International Journal of Distributed Sensor Networks*, 11(2):274391, 2015.

Ekin Ozer, Maria Feng, and Dongming Feng. Citizen sensors for shm: Towards a crowdsourcing platform. *Sensors*, 15(6):14591–14614, 2015.

Thomas J Matarazzo and Shamim N Pakzad. Stride for structural identification using expectation maximization: iterative output-only method for modal identification. *Journal of Engineering Mechanics*, 142(4):04015109, 2016c.

Arturo González. Vehicle-bridge dynamic interaction using finite element modelling. In *Finite element analysis*. IntechOpen, 2010.

Ladislav Frỳba. *Vibration of solids and structures under moving loads*, volume 1. Springer Science & Business Media, 2013.

Chul-Woo Kim and Mitsuo Kawatani. Pseudo-static approach for damage identification of bridges based on coupling vibration with a moving vehicle. *Structure and infrastructure engineering*, 4(5):371–379, 2008.

LRFD AASHTO. Bridge design specifications (2007). *American Association of State Highway and Transportation Officials, Washington, DC*, 4, 2008.

Nathan Mortimore Newmark et al. A method of computation for structural dynamics. American Society of Civil Engineers, 1959.

Guido De Roeck, Bart Peeters, and Wei-Xin Ren. Benchmark study on system identification through ambient vibration measurements. In *Proceedings of IMAC-XVIII, the 18th International Modal Analysis Conference, San Antonio, Texas*, pages 1106–1112, 2000.

Wei-Xin Ren, Issam E Harik, George E Blandford, M Lenett, and Baseheart TM. Roebling suspension bridge. ii: Ambient testing and live-load response. *Journal of Bridge Engineering*, 9(2):119–126, 2004.

Wei-Xin Ren and Zhou-Hong Zong. Output-only modal parameter identification of civil engineering structures. *Structural Engineering and Mechanics*, 17(3-4):429–444, 2004.

Pinghe Ni, Yong Xia, Jun Li, and Hong Hao. Using polynomial chaos expansion for uncertainty and sensitivity analysis of bridge structures. *Mechanical Systems and Signal Processing*, 119:293–311, 2019.

YB Yang and CW Lin. Vehicle–bridge interaction dynamics and potential applications. *Journal of sound and vibration*, 284(1-2):205–226, 2005.

Organización Internacional de Normalización (Ginebra). *Mechanical vibration-road surface profiles-reporting of measured data*. ISO, 1995.

Niall K Harris, Eugene J OBrien, and Arturo González. Reduction of bridge dynamic amplification through adjustment of vehicle suspension damping. *Journal of Sound and Vibration*, 302(3):471–485, 2007.

Ahmed Elhattab, Nasim Uddin, and Eugene OBrien. Drive-by bridge damage monitoring using bridge displacement profile difference. *Journal of Civil Structural Health Monitoring*, 6(5):839–850, 2016.

N Lancefield. Thousands of uk bridges at risk of collapse, warns rac, 2017.

K Willsher, L Tondo, and J Henley. Bridges across europe are in a dangerous state, warn experts. *The Guardian*, 2018.

R. Pérez-Peña. After italy collapse, europe asks: how safe are our bridges?, 2018.

American Society of Civil Engineers. 2017 infrastructure report card. 2017.

Dongyoun Shin, Daniel Aliaga, Bige Tunçer, Stefan Müller Arisona, Sungah Kim, Dani Zünd, and Gerhard Schmitt. Urban sensing: Using smartphones for transportation mode classification. *Computers, Environment and Urban Systems*, 53: 76–86, 2015.

Xiong Wang, Jinbei Zhang, Xiaohua Tian, Xiaoying Gan, Yunfeng Guan, and Xinbing Wang. Crowdsensing-based consensus incident report for road traffic acquisition. *IEEE transactions on intelligent transportation systems*, 19(8):2536–2547, 2017.

Fengrui Shi, Di Wu, Dmitri I Arkhipov, Qiang Liu, Amelia C Regan, and Julie A McCann. Parkcrowd: Reliable crowdsensing for aggregation and dissemination of parking space information. *IEEE Transactions on Intelligent Transportation Systems*, 2018.

Stratis Kanarachos, Stavros-Richard G Christopoulos, and Alexander Chroneos. Smartphones as an integrated platform for monitoring driver behaviour: The role of sensor fusion and connectivity. *Transportation research part C: emerging technologies*, 95:867–882, 2018.

Artis Mednis, Girts Strazdins, Reinholds Zviedris, Georgijs Kanonirs, and Leo Selavo. Real time pothole detection using android smartphones with accelerometers. In *2011 International conference on distributed computing in sensor systems and workshops (DCOSS)*, pages 1–6. IEEE, 2011.

Abhijit Mukherjee and Subhra Majhi. Characterisation of road bumps using smartphones. *European Transport Research Review*, 8(2):13, 2016.

Hiroya Maeda, Yoshihide Sekimoto, Toshikazu Seto, Takehiro Kashiyama, and Hiroshi Omata. Road damage detection using deep neural networks with images captured through a smartphone. *arXiv preprint arXiv:1801.09454*, 2018.

Sukun Kim, Shamim Pakzad, David Culler, James Demmel, Gregory Fenves, Steven Glaser, and Martin Turon. Health monitoring of civil infrastructures using wireless sensor networks. In *Proceedings of the 6th international conference on Information processing in sensor networks*, pages 254–263. ACM, 2007.

Tyler Harms, Sahra Sedigh, and Filippo Bastianini. Structural health monitoring of bridges using wireless sensor networks. *IEEE Instrumentation & Measurement Magazine*, 13(6):14–18, 2010.

Gregory Hackmann, Weijun Guo, Guirong Yan, Zhuoxiong Sun, Chenyang Lu, and Shirley Dyke. Cyber-physical codesign of distributed structural health monitoring with wireless sensor networks. *IEEE Transactions on Parallel and Distributed Systems*, 25(1):63–72, 2013.

Jerome Peter Lynch, Yang Wang, Kincho H Law, Jin Hak Yi, Chang Geun Lee, and Chung Bang Yun. Validation of a large-scale wireless structural monitoring system on the geumdang bridge. In *Proceedings of 9th International Conference on Structural Safety and Reliability*, pages 19–23, 2005.

Soheil S Eshkevari, Shamim N Pakzad, Martin Takac, and Thomas J Matarazzo. Modal identification of bridges using mobile sensors with sparse vibration data. *Journal of Engineering Mechanics*, 142(4):04015109, 2019.

Soheil Sadeghi Eshkevari, Thomas J Matarazzo, and Shamim N Pakzad. Simplified numerical simulation of vehicle-bridge interaction for long-span bridges subject to random traffic load. *arXiv preprint arXiv:1801.09454*, 2020e.

G Michel Guzman-Acevedo, G Esteban Vazquez-Becerra, Jesus R Millan-Almaraz, Hector E Rodriguez-Lozoya, Alfredo Reyes-Salazar, J Ramon Gaxiola-Camacho, and Carlos A Martinez-Felix. Gps, accelerometer, and smartphone fused smart sensor for shm on real-scale bridges. *Advances in Civil Engineering*, 2019, 2019.

Tarak Gandhi, Remy Chang, and Mohan Manubhai Trivedi. Video and seismic sensor-based structural health monitoring: Framework, algorithms, and implementation. *IEEE Transactions on intelligent transportation systems*, 8(2):169–180, 2007.

Sakib Mahmud Khan, Sez Atamturktur, Mashrur Chowdhury, and Mizanur Rahman. Integration of structural health monitoring and intelligent transportation systems for bridge condition assessment: current status and future direction. *IEEE Transactions on Intelligent Transportation Systems*, 17(8):2107–2122, 2016.

Thomas Matarazzo, Mohammad Vazifeh, Shamim Pakzad, Paolo Santi, and Carlo Ratti. Smartphone data streams for bridge health monitoring. *Procedia engineering*, 199:966–971, 2017.

Jingxiao Liu, Siheng Chen, Mario Bergés, Jacobo Bielak, James H Garrett, Jelena Kovačević, and Hae Young Noh. Diagnosis algorithms for indirect structural health monitoring of a bridge model via dimensionality reduction. *Mechanical Systems and Signal Processing*, 136:106454, 2020.

Paul M Bentley and JTE McDonnell. Wavelet transforms: an introduction. *Electronics & communication engineering journal*, 6(4):175–186, 1994.

Lorenzo Montanari, Biswajit Basu, Andrea Spagnoli, and Brian M Broderick. A padding method to reduce edge effects for enhanced damage identification using wavelet analysis. *Mechanical Systems and Signal Processing*, 52:264–277, 2015.

Minwoo Chang and Shamim N Pakzad. Modified natural excitation technique for stochastic modal identification. *Journal of Structural Engineering*, 139(10):1753–1762, 2012.

Soheil Sadeghi Eshkevari and Shamim Pakzad. Bridge structural identification using moving vehicle acceleration measurements. In *Dynamics of Civil Structures, Volume 2*, pages 251–261. Springer, 2019b.

Ka-Veng Yuen, James L Beck, and Lambros S Katafygiotis. Efficient model updating and health monitoring methodology using incomplete modal data without

mode matching. *Structural Control and Health Monitoring: The Official Journal of the International Association for Structural Control and Monitoring and of the European Association for the Control of Structures*, 13(1):91–107, 2006.

Jianye Ching and James L Beck. New bayesian model updating algorithm applied to a structural health monitoring benchmark. *Structural Health Monitoring*, 3(4): 313–332, 2004.

Erik A Johnson, Heung-Fai Lam, Lambros S Katafygiotis, and James L Beck. Phase i iasc-asce structural health monitoring benchmark problem using simulated data. *Journal of engineering mechanics*, 130(1):3–15, 2004.

S Golnaz Shahidi and Shamim N Pakzad. Generalized response surface model updating using time domain data. *Journal of Structural Engineering*, 140(8):A4014001, 2014.

Richard Christenson, Yi Zhong Lin, Andrew Emmons, and Brent Bass. Large-scale experimental verification of semiactive control through real-time hybrid simulation. *Journal of Structural Engineering*, 134(4):522–534, 2008.

M Ahmadizadeh, G Mosqueda, and AM Reinhorn. Compensation of actuator delay and dynamics for real-time hybrid structural simulation. *Earthquake Engineering & Structural Dynamics*, 37(1):21–42, 2008.

Safwan Al-Subaihawi, Chinmoy Kolay, Thomas Marullo, James M Ricles, and Spencer E Quiel. Assessment of wind-induced vibration mitigation in a tall building with damped outriggers using real-time hybrid simulations. *Engineering Structures*, 205:110044, 2020.

Li Deng, Dong Yu, et al. Deep learning: methods and applications. *Foundations and Trends® in Signal Processing*, 7(3–4):197–387, 2014.

George Cybenko. Approximation by superpositions of a sigmoidal function. *Mathematics of control, signals and systems*, 2(4):303–314, 1989.

Moshe Leshno, Vladimir Ya Lin, Allan Pinkus, and Shimon Schocken. Multilayer feedforward networks with a nonpolynomial activation function can approximate any function. *Neural networks*, 6(6):861–867, 1993.

Geoffrey G Towell, Jude W Shavlik, and Michiel O Noordewier. Refinement of approximate domain theories by knowledge-based neural networks. In *Proceedings of the eighth National conference on Artificial intelligence*, volume 861866. Boston, MA, 1990.

Keith Worden and Graeme Manson. The application of machine learning to structural health monitoring. *Philosophical Transactions of the Royal Society A: Mathematical, Physical and Engineering Sciences*, 365(1851):515–537, 2007.

Yujie Ying, James H Garrett Jr, Irving J Oppenheim, Lucio Soibelman, Joel B Harley, Jun Shi, and Yuanwei Jin. Toward data-driven structural health monitoring: application of machine learning and signal processing to damage detection. *Journal of Computing in Civil Engineering*, 27(6):667–680, 2013.

Ting-Hua Yi, Hong-Nan Li, and Hong-Min Sun. Multi-stage structural damage diagnosis method based on. *Smart Structures and Systems*, 12(3_4):345–361, 2013.

Guoqing Gui, Hong Pan, Zhibin Lin, Yonghua Li, and Zhijun Yuan. Data-driven support vector machine with optimization techniques for structural health monitoring and damage detection. *KSCE Journal of Civil Engineering*, 21(2):523–534, 2017.

Osama Abdeljaber, Onur Avci, Serkan Kiranyaz, Moncef Gabbouj, and Daniel J Inman. Real-time vibration-based structural damage detection using one-dimensional convolutional neural networks. *Journal of Sound and Vibration*, 388:154–170, 2017.

Nur Sila Gulgec, Martin Takáč, and Shamim N Pakzad. Convolutional neural network approach for robust structural damage detection and localization. *Journal of Computing in Civil Engineering*, 33(3):04019005, 2019.

Steven L Brunton, Joshua L Proctor, and J Nathan Kutz. Discovering governing equations from data by sparse identification of nonlinear dynamical systems. *Proceedings of the national academy of sciences*, 113(15):3932–3937, 2016.

Maziar Raissi and George Em Karniadakis. Hidden physics models: Machine learning of nonlinear partial differential equations. *Journal of Computational Physics*, 357: 125–141, 2018.

Junho Song and Seung-Yong Ok. Multi-scale system reliability analysis of lifeline networks under earthquake hazards. *Earthquake engineering & structural dynamics*, 39(3):259–279, 2010.

M Mahsuli and T Haukaas. Seismic risk analysis with reliability methods, part i: Models. *Structural Safety*, 42:54–62, 2013.

Milad Roohi, Eric M Hernandez, and David Rosowsky. Nonlinear seismic response reconstruction and performance assessment of instrumented wood-frame buildings—validation using neeswood capstone full-scale tests. *Structural Control and Health Monitoring*, 26(9):e2373, 2019.

Steven G Mattson and Sudhakar M Pandit. Statistical moments of autoregressive model residuals for damage localisation. *Mechanical Systems and Signal Processing*, 20(3):627–645, 2006.

Luke Bornn, Charles R Farrar, Gyuhae Park, and Kevin Farinholt. Structural health monitoring with autoregressive support vector machines. *Journal of Vibration and Acoustics*, 131(2), 2009.

Gordon Lightbody and George W Irwin. Multi-layer perceptron based modelling of nonlinear systems. *Fuzzy sets and systems*, 79(1):93–112, 1996.

Nikos D Lagaros and Manolis Papadrakakis. Neural network based prediction schemes of the non-linear seismic response of 3d buildings. *Advances in Engineering Software*, 44(1):92–115, 2012.

Tara N Sainath, Brian Kingsbury, George Saon, Hagen Soltau, Abdel-rahman Mohamed, George Dahl, and Bhuvana Ramabhadran. Deep convolutional neural networks for large-scale speech tasks. *Neural Networks*, 64:39–48, 2015.

Shan-Bin Sun, Yuan-Yuan He, Si-Da Zhou, and Zhen-Jiang Yue. A data-driven response virtual sensor technique with partial vibration measurements using convolutional neural network. *Sensors*, 17(12):2888, 2017.

Rih-Teng Wu and Mohammad R Jahanshahi. Deep convolutional neural network for structural dynamic response estimation and system identification. *Journal of Engineering Mechanics*, 145(1):04018125, 2019.

Ruiyang Zhang, Yang Liu, and Hao Sun. Physics-guided convolutional neural network (phycnn) for data-driven seismic response modeling. *arXiv preprint arXiv:1909.08118*, 2019a.

Ruiyang Zhang, Zhao Chen, Su Chen, Jingwei Zheng, Oral Büyüköztürk, and Hao Sun. Deep long short-term memory networks for nonlinear structural seismic response prediction. *Computers & Structures*, 220:55–68, 2019b.

Ruiyang Zhang, Yang Liu, and Hao Sun. Physics-informed multi-lstm networks for metamodeling of nonlinear structures. *arXiv preprint arXiv:2002.10253*, 2020.

Kaiming He, Xiangyu Zhang, Shaoqing Ren, and Jian Sun. Deep residual learning for image recognition. corr abs/1512.03385 (2015), 2015.

Rafael Riddell and Nathan Mortimore Newmark. Statistical analysis of the response of nonlinear systems subjected to earthquakes. Technical report, University of Illinois Engineering Experiment Station. College of . . . , 1979.

Yiping Lu, Aoxiao Zhong, Quanzheng Li, and Bin Dong. Beyond finite layer neural networks: Bridging deep architectures and numerical differential equations. *arXiv preprint arXiv:1710.10121*, 2017.

Tian Qi Chen, Yulia Rubanova, Jesse Bettencourt, and David K Duvenaud. Neural ordinary differential equations. In *Advances in neural information processing systems*, pages 6571–6583, 2018.

Herbert Robbins and Sutton Monro. A stochastic approximation method. *The Annals of Mathematical Statistics*, pages 400–407, 1951.

Diederik P Kingma and Jimmy Ba. Adam: A method for stochastic optimization. *arXiv preprint arXiv:1412.6980*, 2014.

Albert S Berahas, Majid Jahani, and Martin Takáč. Quasi-newton methods for deep learning: Forget the past, just sample. *arXiv preprint arXiv:1901.09997*, 2019.

Peng Xu, Fred Roosta, and Michael W Mahoney. Second-order optimization for non-convex machine learning: An empirical study. In *Proceedings of the 2020 SIAM International Conference on Data Mining*, pages 199–207. SIAM, 2020.

Jorge Nocedal and Stephen J. Wright. *Numerical Optimization*. Springer Series in Operations Research. Springer, second edition, 2006.

Ilya Loshchilov and Frank Hutter. Online batch selection for faster training of neural networks. *arXiv preprint arXiv:1511.06343*, 2015.

Tom Schaul, John Quan, Ioannis Antonoglou, and David Silver. Prioritized experience replay. *arXiv preprint arXiv:1511.05952*, 2015.

Hamid Haddadi, A Shakal, C Stephens, W Savage, M Huang, W Leith, and J Parrish. Center for engineering strong-motion data (cesmd).

Jonathan Hancock, Jennie Watson-Lamprey, Norman A Abrahamson, Julian J Bommer, Alexandros Markatis, EMMA McCOY, and Rishmila Mendis. An improved method of matching response spectra of recorded earthquake ground motion using wavelets. *Journal of earthquake engineering*, 10(spec01):67–89, 2006.

Eric W Weisstein. Correlation coefficient. 2006.

Hojjat Salehinejad, Sharan Sankar, Joseph Barfett, Errol Colak, and Shahrokh Valaee. Recent advances in recurrent neural networks. *arXiv preprint arXiv:1801.01078*, 2017.

Daniel Holden, Taku Komura, and Jun Saito. Phase-functioned neural networks for character control. *ACM Transactions on Graphics (TOG)*, 36(4):1–13, 2017.

Steven Gillijns and Bart De Moor. Unbiased minimum-variance input and state estimation for linear discrete-time systems with direct feedthrough. *Automatica*, 43(5):934–937, 2007.

E Lourens, Edwin Reynders, Guido De Roeck, Geert Degrande, and Geert Lombaert. An augmented kalman filter for force identification in structural dynamics. *Mechanical Systems and Signal Processing*, 27:446–460, 2012.

Kristof Maes, AW Smyth, Guido De Roeck, and Geert Lombaert. Joint input-state estimation in structural dynamics. *Mechanical Systems and Signal Processing*, 70: 445–466, 2016.

Frank Naets, Javier Cuadrado, and Wim Desmet. Stable force identification in structural dynamics using kalman filtering and dummy-measurements. *Mechanical Systems and Signal Processing*, 50:235–248, 2015.

YB Yang, Bin Zhang, Yao Qian, and Yuntian Wu. Contact-point response for modal identification of bridges by a moving test vehicle. *International Journal of Structural Stability and Dynamics*, 18(05):1850073, 2018.

Rajdip Nayek and Sriram Narasimhan. Extraction of contact-point response in indirect bridge health monitoring using an input estimation approach. *Journal of Civil Structural Health Monitoring*, pages 1–17, 2020.

Soheil Sadeghi Eshkevari, Thomas J Matarazzo, and Shamim N Pakzad. Bridge modal identification using acceleration measurements within moving vehicles. *Mechanical Systems and Signal Processing*, 141:106733, 2020.

Ozgur Demir, Ilknur Keskin, and Saban Cetin. Modeling and control of a nonlinear half-vehicle suspension system: a hybrid fuzzy logic approach. *Nonlinear Dynamics*, 67(3):2139–2151, 2012.

Richard S Sutton and Andrew G Barto. *Reinforcement learning: An introduction*. MIT press, 2018.

ISOBS ISO. 8608: 2016 mechanical vibration–road surface profiles–reporting of measured data. *BSI Standards Publication: London, UK*, 2016.

Mukund Sundararajan, Ankur Taly, and Qiqi Yan. Axiomatic attribution for deep networks. *arXiv preprint arXiv:1703.01365*, 2017.

N Senroy and S Suryanarayanan. Two techniques to enhance empirical mode decomposition for power quality applications. In *2007 IEEE Power Engineering Society General Meeting*, pages 1–6. IEEE, 2007.

Appendix A

Discussion on the Generality of the Methods

In this part, we implement the proposed pipelines on a shorter bridge (300m single span) with a road roughness profile adopted from ISO8608:2016 [ISO, 2016] (considering road class C). In this case, the possibility of the methods is examined in (a) a shorter bridge, (b) with a realistic road profile roughness spectrum, and (c) with closely-spaced vehicle and the bridge frequency contents. The bridge is supported by rigid constraints from both ends and is modeled as a $5,000$ DOF concrete beam in Opensees. The nodal mass of each DOFs is set to 1039 Kg with $10.4m^2$ and $51.5m^4$ cross-sectional area and moment of inertia, respectively. Based on these mechanical properties, the first four natural modes of the bridge have the following frequencies: 0.40 Hz, 1.11 Hz, 2.18 Hz, and 3.61 Hz. The vehicle properties are adopted based on Table 3.1 and the sensing pattern is identical with the previous cases. From the frequency values, the vehicle natural mode is located closely after the fourth natural mode of the bridge which adds complexity, especially for applying Method 2.

Figure A.1 shows the deconvolution effect on the vehicle response FRF and Figure A.2 presents identification results from applying Method 1. Deconvolution using the

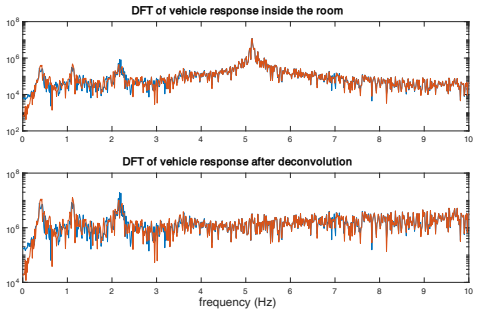

Figure A.1: FRF deconvolution results for ISO8606 roughness and 300m bridge

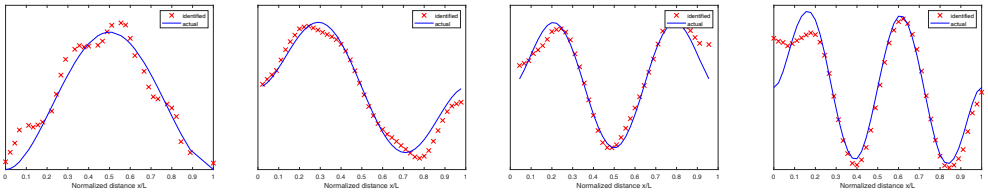

Figure A.2: FRF+SOBI with ISO8606 roughness and 300m bridge

transfer function could extract the highly-damped mode at frequency about 5Hz that associates with the vehicle fundamental model. In addition, from Figure A.2, the natural mode shapes are acceptably identified (MAC values ranging from 0.9195 to 0.9718).

For Method 2, the primary challenge is that the 4^{th} natural mode of the bridge is very close to the frequency content of the vehicle and EEMD is not able to perfectly extract the vehicle mode out the mixed signal. To address this problem, frequency shifting approach [Senroy and Suryanarayanan, 2007] can be adopted. In this approach, the frequency contents can be modulated into a lower range while keeping their distance. This helped to escape the undesired frequency ratio ([Rilling and Flandrin, 2008]) and allows EEMD to separate modes. Modal identification results from Method 2 are presented in Figures A.3 and A.4. Figure A.3 demonstrated that EEMD-based method can be successful for the deconvolution tasks in cases with closely-spaced frequencies. Identification results also are fairly acceptable with MAC values ranging from 0.7870 for the fourth mode to 0.9185 for the first mode (as expected, mode 4 has the least accuracy because of its closeness to the vehicle

frequency). Generally it is concluded that the proposed methods are suitable for a wide variety of bridges, however, the frequency contents proximity or overlap has a detrimental effect on the final output. In addition, note that the simulation algorithm used in this study is a simplified method which is very accurate for slowly-moving vehicles that cross long bridges in operational mode [Sadeghi Eshkevari et al., 2020c]. This sensing situation is a very practical case; however, further analyses are required to generalize the applicability of the proposed SID algorithms for scenarios that are different from our base case.

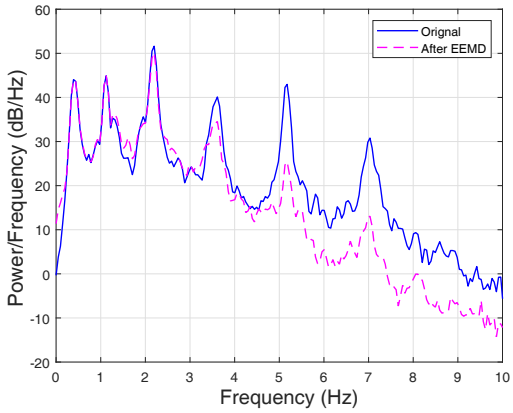

Figure A.3: EEMD deconvolution results for ISO8606 roughness and 300m bridge

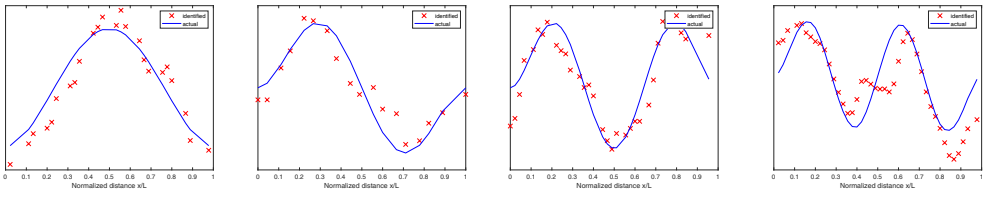

Figure A.4: EEMD+SOBI with ISO8606 roughness and 300m bridge

Appendix B

Modal Aggregation

In STRIDEX, MSR function maps mobile measurements to stationary virtual probing locations (VPLs) and iteratively calculate the best estimate for structural parameters using expectation maximization (EM) algorithm. In the original studies of STRIDEX, the minimum model size is selected such that the number of VPLs is equal to the number of moving sensors. The number of VPLs can be set to $p \times N$, where N is the number of mobile sensors and p is the model order. With an increased p, a higher spatial resolution is produced for the identified mode shapes can be achieved. For this study, however, the same number of VPLs as mobile sensors has been considered. Four model orders, $p = 1, 2, 3,$ and 4 have been analyzed here. For each model order, 11 VPL sets have been presumed and superposed to enhance mode shape resolutions. Each VPL set consists of eight VPLs with equal spacing, and with a certain eccentricity. In total, for each analysis, $11 \times 4 = 44$ output sets exist, each consists of estimated modal properties. For aggregating these, an automated algorithm has been adopted. For a certain desired mode, the algorithm automatically produces a perfect sine-shaped mode shape estimation (e.g., half-sine for mode one, full-sine for mode two), and check the dissimilarity between identified mode shape and this preliminary estimation for each file. Those sets that have dissimilarity measures

less than a certain threshold (used 0.72 to 0.74), are selected and combined to shape the final identified mode shapes. The dissimilarity measure used in this study is the second norm of $y - \tilde{y}$ or $y + \tilde{y}$. If the second expression governs, it means that the mode shape is accurate but inverted. In addition to the dissimilarity condition for output selection, sets with damping ratios over %30 are excluded as well. This automated algorithm accelerate mode shape reconstruction process significantly and keep it more controlled.

Appendix C

Auxiliary Identifications - Road Profile and Vehicle Suspension

The procedure of bridge signal extraction consists of distinct steps for vehicle effect separation and roughness-caused vibration separation. With this notion, one may be interested to exploit byproducts of the processes for different objectives, i.e. road roughness profile estimation and vehicle suspension identification. SOBI as the linear mix separator of both methods computes two signal channels, one of which was used as bridge vibration for SID. The other channel theoretically shall correspond to the road roughness profile. In Figure C.1 the second extracted channels from SOBI (identified roughness profiles) are compared with three predesignated profiles.

Location domain shown in Figure C.1 is just a small portion of the entire path that is selected for more clarity. FRF approach is more successful in accurately estimating roughness profile. In fact, in the case of random profile, EEMD method does not extract an acceptable signal as the road profile estimation. An important difference between the two approaches in this study is the necessity of pre-identification of the vehicle. In fact, FRF approach needs vehicle characteristics as a given which was created by a preliminary SID of the vehicle while traveling over normal roads.

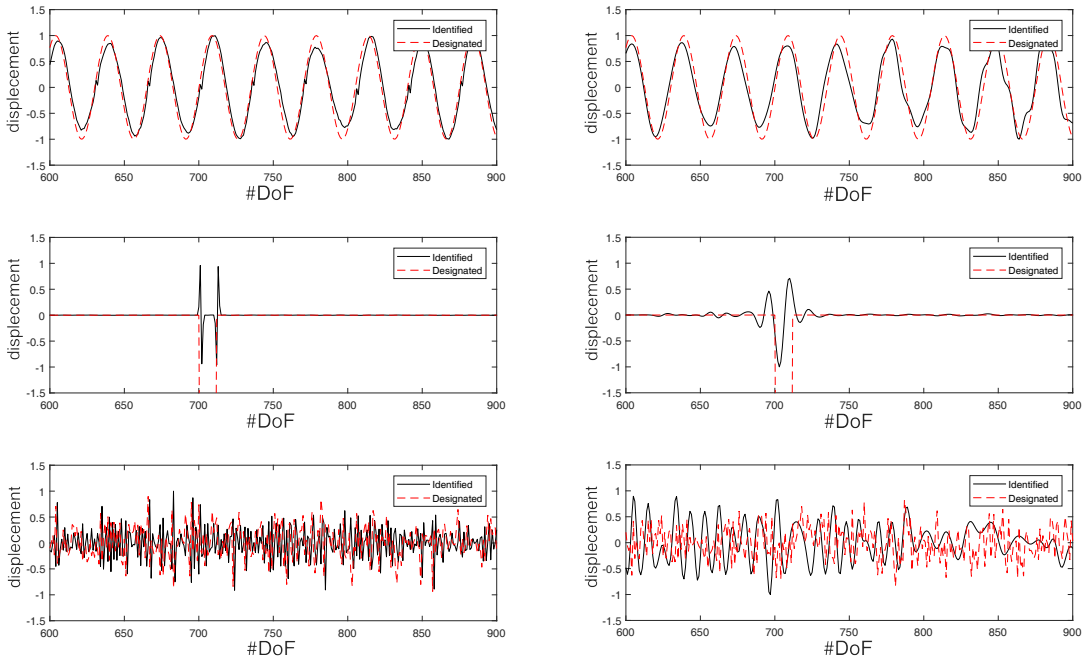

Figure C.1: Roughness profile estimation - FRF method on left, EEMD on Right

However, in EEMD approach, vehicle identification is not required and the method can produce the vehicle effect as an IMF. Therefore, this IMF is assumed to be the pure vehicle response and by representing it into the frequency domain, the vehicle natural frequencies shall be identified. Figure C.2 shows these analyses for the three cases of interest.

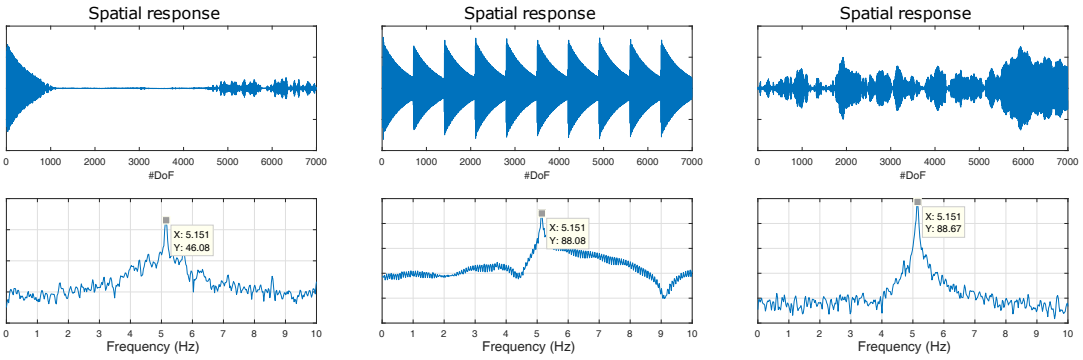

(a) Sinusoidal roughness (b) EJ roughness (c) Random roughness

Figure C.2: IMF corresponding to vehicle - spatial and frequency representation

Figure C.2 illustrates that the IMF extracted as the vehicle response is exactly showing a large spike on the location of the vehicle fundamental mode. Note that

because of the low sampling frequency for the discrete simulation of the vehicle, the second natural frequency is not clearly visible.

Biography

Soheil Sadeghi Eshkevari is a Ph.D. Candidate in the Department of Civil and Environmental Engineering at Lehigh University. He received his Bachelor's degree from University of Tehran in Civil Engineering in 2013. He also received a Master's degree in Structural Engineering from Sharif University of Technology in 2016. His research interests include mobile sensing, applications of artificial intelligence and machine learning in civil engineering and urban planning, information crowdsourcing, and smart cities. Soheil was the recipient of D. J. DeMichele Scholarship Award from Society of Experimental Mechanics in 2019. He is Rossin Doctoral Fellow since 2019 and received Dean's Doctoral Assistantship Award in 2014.

In Summer 2019, Soheil spend an internship with Thornton Tomasetti as Machine Learning Data Scientist for four months. During this time, he could contribute in AI-based software development efforts. In addition to his main pursuit of research, Soheil worked on vision-based system identification of buildings and active structural control of nonlinear buildings using Reinforcement Learning. During his Ph.D., Soheil has published three journal papers in ASCE Journal of Engineering Mechanics, Journal of Mechanical Systems and Signal Processing, and Journal of Civil Structural Health Monitoring. He also submitted two manuscripts, published and presented four technical papers at IWSHM and IMAC conferences. In September 2020, Soheil will be joining MIT Senseable City Lab as Postdoctoral Researcher.